SPIN DYNAMICS IN 2D AND 3D CONFINED MAGNETIC STRUCTURE AND THIN FILM HETEROSTRUCTURES

THESIS SUBMITTED FOR THE DEGREE OF

DOCTOR OF PHILOSOPHY (SCIENCE)

IN

PHYSICS (EXPERIMENTAL)

BY

SOURAV SAHOO

DEPARTMENT OF PHYSICS

UNIVERSITY OF CALCUTTA

2021

Abstract

Ferromagnetic nanostructures and thin film heterostructures have long been interesting systems due to their interesting spin configuration, spin dynamics and damping as well as their potential applications in high density magnetic storage, memory, logic, transistor and communication devices. Therefore, realization and control over high-frequency spin dynamics, commonly known as magnetization dynamics, in magnetic nanostructures and thin films may lead to paradigm-shifting, next generation devices including high density spintronics and neuromorphic systems. The aim of this thesis is to explore and control spin-waves in ferromagnetic thin film heterostructures and nanoscale structures of different shapes, geometry and dimensions. We have employed Brillouin light scattering (BLS) spectroscopy and time-resolved magneto-optical Kerr effect (TRMOKE) techniques for studying the frequency-resolved and time-resolved magnetization dynamics, respectively.

In this thesis, we have investigated experimentally and numerically the magnetization dynamics in $Ni_{80}Fe_{20}$ (permalloy) connected nanodot arrays of varying filling fractions to understand the role of rectangular-connector nanochannels to control the spin-wave modes of magnetic nanodots. This study paves the way for the designing of the spin-wave based demultiplexer. Subsequently, we have investigated the effect of field reversal study of spin-wave modes in a two-dimensional (2D) square artificial spin ice (ASI) system made of permalloy. We have explored the role of magnetic microstates of the 2D ASI on its spin-wave modes. Two anticrossing between the spin-wave branches were observed with the anticrossing gap of around 1 GHz due to coupling between magnonic and phononic degrees of freedom. The latter was excited by the femtosecond laser as a result of the variation of thermal expansion of permalloy and silicon.

We have studied the precessional magnetization dynamics in a three-dimensional (3D) cobalt tetrapod structure fabricated by two-photon lithography and electrodeposition using TRMOKE microscope. Three distinct spin-wave modes were observed with frequencies spanning up to 30 GHz. The 3D spin-wave mode profiles were calculated using micromagnetic simulations, which revealed the presence of uniform and standing spin-wave modes in the nanowires forming the tetrapod structure. However, due to the isolated nature of the 3D structure, it was unable to provide coherent spin waves extending through a 3D network. To explore that we have further studied the coherent

spin waves in a permalloy connected nanowire network arranged in a 3D diamond bond lattice geometry forming a 3D-ASI structure. We have measured the spin-wave modes in this 3D-ASI system using BLS spectroscopy as a function of the bias magnetic field. Two clear spin-wave modes with nearly monotonic bias-field dispersion over a broad magnetic field range were observed. The spin-wave mode profiles along the different planes of the 3D structure were calculated to obtain insights into the spatial nature of the modes in this complex connected structure.

Finally, we have studied the modulation of Gilbert damping in thin film heterostructures made of Ta(t)/CoFeB(3 nm)/SiO_2(2 nm) with varying Ta thickness by sending charge current through the Ta layer. The pure spin current generated by the spin Hall effect in the Ta layer was injected in the adjacent CoFeB layer exerting a damping-like spin-orbit torque (SOT). The damping-like SOT efficiency was found to be large and stable over the wider range of Ta thickness regime (3 - 20 nm) maintaining a stable β-Ta phase.

List of Publications

Included in the thesis:

1. "Ultrafast Magnetization Dynamics in a Nanoscale Three-Dimensional Cobalt Tetrapod Structure", **S. Sahoo**, S. Mondal, Gwilym Williams, A. May, S. Ladak and A. Barman; Nanoscale **10**, 9981 (2018).

2. "Nanochannels for Spin-Wave Manipulation in $Ni_{80}Fe_{20}$ Nanodot Arrays", **S. Sahoo**, S. N. Panda, S. Barman, Y. Otani and A. Barman; J. Magn. Magn. Mater. **522**, 167550 (2020).

3. "Observation of Coherent Spin Waves in a Three-dimensional Artificial Spin Ice Structure", **S. Sahoo**, A. May, A. Berg, A. K. Mondal, S. Ladak and A. Barman; Nano Lett. **21**, 4629 (2021).

4. "All-Optical Detection of Spin-Orbit Torque Driven Modulation of Gilbert Damping in Ta/CoFeB/SiO_2 Heterostructures", **S. Sahoo**, S. Mondal, S**.** Choudhury, J. Sinha and A. Barman (Manuscript under preparation).

5. "All-Optical Study of Magnetization Dynamics in a Square Artificial Spin Ice Nanostructure", **S. Sahoo** et al. (Manuscript under preparation).

Relevant publications not included in the thesis:

6. "Direct Observation of Interfacial Dzyaloshinskii-Moriya Interaction in W/CoFeB/SiO_2 Heterostructures Using Brillouin Light Scattering", A. K. Chaurasiya, C. Banerjee, S. Pan, **S. Sahoo**, S. Choudhury, J. Sinha and A. Barman; Sci. Rep. **6**, 32592 (2016).

7. "Field Controlled Ultrafast Magnetization Dynamics in Two-Dimensional Nanoscale Ferromagnetic Antidot Arrays", A. De, S. Mondal, **S. Sahoo**, S. Barman, Y. Otani, R. K. Mitra and A. Barman; Beilstein J. Nanotechnol. **9**, 1123 (2018).

8. "Hybrid Magneto-dynamical Modes in a Single Magnetostrictive Nanomagnet on a Piezoelectric Substrate Arising from Magnetoelastic Modulation of Precessional Dynamics", S. Mondal, M. A. Abeed, K. Dutta, A. De, **S. Sahoo**, A. Barman, and S. Bandyopadhyay; ACS Appl. Mater. Interfaces, **10**, 43970 (2018).

9. "Shape Dependent High Frequency Spin-Wave Dynamics in Nanoscale Magnonic Crystal", A. De, S. Mondal, S. Choudhury, **S. Sahoo**, S. Majumder, S. Barman, Y. Otani and A. Barman; J. Magn. Magn. Mater. **487**, 165263 (2019).

10. "Tunability of Domain Structure and Magnonic Spectra in Antidot Arrays of Heusler Alloy", S. Mallick, S. Mondal, T. Seki, **S. Sahoo**, T. Forrest, F. Maccherozzi, S. Barman, A. Barman, K. Takanashi, and S. Bedanta; Phys. Rev. Appl. **12**, 014043 (2019).

11. "Reliability of Magneto-elastic Switching of Non-ideal Nanomagnets with Defects: A Case Study for the Viability of Straintronic Logic and Memory", D. Winters, M. A. Abeed, **S. Sahoo**, A. Barman and S. Bandyopadhyay; Phys. Rev. Appl. **12**, 034010 (2019).

12. "The Effect of Material Defects on Resonant Spin Wave Modes in a Nanomagnet", M. A. Abeed, **S. Sahoo**, D. Winters, A. Barman and S. Bandyopadhyay; Sci. Rep. **9**, 16635 (2019).

13. "Large Nonlinear Ferromagnetic Resonance Shift and Strong Magnon-Magnon Coupling in $Ni_{80}Fe_{20}$ Nano-Cross Array", K. Adhikari, **S. Sahoo**, A. K. Mondal, Y. Otani and A. Barman; Phys. Rev. B **101**, 054406 (2020).

Book chapters and review articles:

14. "Precessional Magnetization Dynamics and Spin Waves in 3D Ferromagnetic Nanostructures**",** S. Mondal, **S. Sahoo**, and A. Barman in Three-Dimensional magnonics, Ed. G. Gubbiotti, CRC Press, ISBN 9789814800730 - CAT# K426145 (2019).

15. "Magnetization Dynamics of Nanoscale Magnetic Materials: A Perspective" A. Barman, S. Mondal, **S. Sahoo** and A. De; J. Appl. Phys. 1**28**, 170901 (2020).

16. "Spin-Orbit Effects in Magnonics", A. Barman, **S. Sahoo** and J. Sinha; The 2021 Magnonics Roadmap; J. Phys.: Condens. Matter **33**, 413001 (2021).

Acknowledgements

Throughout the long journey of my dissertation work, I always received endearing support and assistance. First and foremost, I would like to thank my supervisor, Prof. Anjan Barman for mentoring me by guiding how to be a part of a world-class experimental facility. His expertise was priceless for articulating the problems and methodologies for this dissertation. I would also like to thank him for always being patient and guiding me throughout this long path. His experiences and insightful counsel pushed me to conceive new thoughts to shape the research problems to a higher level. I joined his research group as a project student in the summer of 2015. I still remembered our first meeting which started with the plotting of a hysteresis loop and subsequently continued with several discussions on the basic concepts of magnetism which immensely helped me to understand the research field. Throughout this long journey, he gave me several inspiring talks which helped me a lot not only in my research work but also in my personal life. I am very lucky to have a mentor like him who used to invest a lot of time in each of his students to make them successful researchers. I was fortunate to attend my first foreign conference: "Magnonics" in Italy, with him. It is a lifelong experience for me. I would also like to thank him for giving me opportunities to be a part of the review articles besides my research works. These few sentences will never suffice my gratitude for him for all the things I have learned for him throughout this 6.5-year long journey.

I would like to acknowledge Dr. Sam Ladak (Cardiff University, UK), Prof. YoshiChika Otani (Riken, Japan) and Dr. Will Branford (Imperial College, London) for sending us the interesting samples which are the backbone of this thesis work. I sincerely thank Dr. Saswati Barman for her support in LLG micromagnetic simulator.

I would like thank to all the lab members of the UFNML family ("Spintronics and Spin Dynamics Group"). Throughout this long journey, I spent most of my time in our laboratories with the lab members. During my project works, I got the opportunity to share the lab space with some of my super seniors; Dr. Semanti Pal, Dr. Bipul Kumar Mahato, Dr. Susmita Saha, Dr. Ruma Mandal and Dr. Arnab Ganguly. Their friendly behaviour helped me to easily adapt to the lab culture and work ethic. I am thankful to Dr. Chandrima Banerjee for her guidance throughout my projects which was a part of my master's degree. She taught me the measurement and alignment procedure of the Brillouin light scattering technique. She helped me to learn the presentation and

interpretation of experimental results from scratch. I would like to thank Mr. Avinash Kumar Chaurasiya from whom I got a great deal of help and inputs during my projects. I would like to convey my sincere thanks to Dr. Jaivardhan Sinha for his valuable advice during my projects and the initial days of my PhD. I would like to thank Dr. Sucheta Mondal for instructing me on the time-resolved magneto-optic Kerr effect technique. I learnt the analysis of time-resolved data and micromagnetic simulations from her. I would like to thank Dr. Samiran Choudhury for always being there for any kind of help and suggestions. I would like to thank Dr. Santanu Pan and Mr. Kartik Adhikari for their friendly advice for my research works. I would also like to thank Mrs. Anulekha De for her help in all the difficulties in my professional and personal life. My heartiest thank to all my lab juniors; Surya Narayan Panda, Sudip Majumder, Arundhati Adhikari, Amrit Kumar Mondal, Koustuv Dutta, Pratap Kumar Pal, Sreya Pal, Soma Dutta and Suchetana Mukhopadhyay for maintaining a professional and friendly environment in the lab. With them, I have shared a lot of memories during this long journey. I would like to thank Dr. Arpan Bhattacharyya for his help during my thesis writing. I am mesmerized to be able to share the lab space with the nicest people. This journey was very joyful which was not possible without you. I have learnt several life lessons by sharing many experiences (good or bad) with all of you. The presence of Gaurav Patel, Shubham Shukla, Anuj Kumar Dhiman, Biswajit Sahoo, Gyandeep Pradhan, Daisy Gogoi, Kajal Tiwari, Abhilash Mishra, Bikash Das Mohapatra and Ankan Mukhopadhyay in the lab during their projects were quite joyful.

I would like to thank my I-PhD batchmates; Amit Barh, Ananda Gopal Maity, Balwant Singh Bisht, Arunava Adak, Debsuvra Mukhopadhyay, Manas Pratim Das, Neha Jha and Ruchi Pandey for all the memories of the master's degree. Amit and Ananda always stood by my side throughout the ups and downs of this long journey. I am fortune of having friends like them.

I would also like to thank all the seniors, colleagues and Juniors at our institute for making a homely environment inside the campus. I would also like to thank the cooking team and mess committee (I was part of it for 1 year) members for maintaining the student mess and providing the best quality food throughout the years.

My journey from a small village boy to a PhD student was not possible without the sacrifices of my family. My father always supported my decision. He had a lot of faith in me. He never forced me to do anything. His words always push me to work hard.

Unfortunately, he is no more to bless me for this milestone of my life. I think that he would be happy to see me being able to complete my work for the degree and advise me to sincerely work in the future. My mother and brother always showed great faith in me. They always understood my situation and supported me. I would like to express my sincere thanks to Khokon Kaku (Amit Pradhan) for his careful guidance throughout my school and college days. He always guided me towards the right path. Besides my family, my friends always played a crucial role in my life and without them I could not reach this milestone. I would like to thank all of my school and college friends. My heartiest thanks to two of my childhood friends; Amit Panda and Swapan Das for their support for any kind of my family contingencies, so that I can focus on my research work. My special thanks to Nabanita Pal and her family for their love and support throughout my PhD.

My sincere thanks to all my teachers. Their teaching has inspired me a lot to be able to reach this stage. I would also like to acknowledge all the staff of the technical cell of our institute for their assistance while using the characterization tools.

Finally, I would like to thank S N Bose National for Basic Sciences for giving me the opportunity as an I-PhD student and providing the junior and senior research fellowship for my PhD. The financial support from the institute gave me opportunities to attend several national conferences which enriched my knowledge and immensely helped me with my research work.

Sourav Sahoo
S.N. Bose National Centre for Basic Sciences
Salt Lake, Kolkata, India

List of Abbreviations

1D	: One-dimensional
2D	: Two-dimensional
3D	: Three-dimensional
AFM	: Atomic force microscopy
AOM	: Acousto-optic modulator
ASI	: Artificial spin ice
BBO	: β-barium borate
BCC	: Body centred cubic
BLS	: Brillouin light scattering
BV	: Backward-volume
CND	: Connected nanodot
CSN	: Crescent shaped nanowires
CVD	: Chemical vapour deposition
DE	: Damon-Eshbach
(i)DMI	: (Interfacial) Dzyloshinskii Moriya interaction
DLT	: Damping-like torque
DE	: Damon-Eshbach
EBL	: Electron-beam lithography
EDX	: Energy dispersive X-ray
EM	: Edge mode
FCC	: Face centred cubic
FEBID	: Focused electron beam ion deposition
FFT	: Fast Fourier transformation
FLT	: Field-like torque
FM	: Ferromagnet
FMR	: Ferromagnetic resonance
FPI	: Fabry-Pérot interferometer
fs	: Femtosecond
GMR	: Giant magneto resistance
GVD	: Group velocity dispersion
HCP	: Hexagonal close-packed

HDD : Hard disk drive
HM : Heavy-metal
HNB : Horizontal nanobar
HNC : Horizontal nanochannel
IR : Infrared
LBO : Lithium triborate
MD : Multidomain
MFM : Magnetic force microscopy
MO : Microscope objective
MOD : Modulation of damping
MOF : Modulation of frequency
MOKE : Magneto-optical Kerr effect
MRAM : Magnetic random-access memory
MTJ : Magnetic tunnel junction
NC : Nanochannel
ns : Nanosecond
OBD : Optical bridge detector
PMA : Perpendicular magnetic anisotropy
ps : Picosecond
PVD : Physical vapour deposition
PWM : Plane wave method
QM : Quantized mode
RR : Retro-reflector
SAW : Surface acoustic wave
SC : Simple cubic
SEM : Scanning electron microscopy
SHE : Spin Hall effect
(i)SHE : (Inverse) spin Hall effect
SHG : Second harmonic generator
SOC : Spin-orbit coupling
SOI : Spin-orbit interaction
SOT : Spin-orbit torque
ST-FMR : Spin-torque ferromagnetic resonance

STT : Spin-transfer torque

TFPI : Tandem Fabry-Pérot interferometer

TMR : Tunnelling magnetoresistance

TPL : Two-photon lithography

TRMOKE : Time-resolved magneto-optical Kerr effect

UM : Uniform mode

VNB : Vertical nanobar

VNC : Vertical nanochannel

XRD : X-ray diffraction

θ_{SH} : Spin Hall angle

μs : Microsecond

Contents

Abstract i

List of Publications iii

Acknowledgements v

List of Abbreviations viii

Contents xi

List of Figures xv

1. Introduction 1

1.1 Interfacial Properties of Heavy-metal/Ferromagnet Layer Structure 4

1.2 Ferromagnetic Nanostructures: Antidot and Connected Nanodot Lattice 6

1.3 Artificial Spin Ice 8

1.4 Three Dimensional Magnetic Nanostructures 10

1.5 Objective of the Thesis 14

References 16

2. Theoretical Background 30

2.1 Different Magnetic Energies 30

2.1.1 Zeeman Energy 31

2.1.2 Exchange Energy 31

2.1.3 Dipolar Energy 32

2.1.4 Anisotropic Energy 33

2.2 Magnetization Dynamics 36

2.2.1 Laser Induced Magnetization Dynamics 37

2.2.2 Precessional Magnetization Dynamics 37

2.2.3 Spin-wave and Ferromagnetic Resonance 39

2.3 Damping 40

2.3.1 Intrinsic Mechanisms 41

2.3.2 Extrinsic Mechanisms 42

2.3.3 Manipulation of Magnetic Damping 42

References 46

3. Methods 49

3.1 Sample Fabrication 50

3.1.1 Electron-beam Lithography 50
3.1.2 Two-photon Lithography 50
3.1.3 Electrodeposition 51
3.1.4 Thermal Evaporation 52
3.1.5 Electron-beam Evaporation 53
3.1.6 Sputtering 54
3.1.7 Ion Milling and Lift off Process 55

3.2 Sample Characterization 56

3.2.1 Scanning Electron Microscopy 56
3.2.2 Energy Dispersive X-ray 57
3.2.3 X-ray Diffraction 57
3.2.4 Atomic Force Microscopy 58
3.2.5 Magnetic Force Microscopy 59
3.2.6 Magneto Optic Kerr Effect 60

3.3 Experiment Tools for Magnetization Dynamics 63

3.3.1 Time-Resolved Magneto Optic Kerr Microscope 63
3.3.2 Non Colinear Time-Resolved Magneto Optic Kerr Magnetometry 69
3.3.3 Brillouin Light Scattering Technique 76

3.4 Numerical Methods 83

3.4.1 OOMMF 85
3.4.2 MuMax3 86
3.4.3 LLG Simulator 87
3.4.4 DotMag 88

References 89

4. Nanochannels for Spin-Wave Manipulation in $Ni_{80}Fe_{20}$ Nanodot Arrays 92

4.1 Introduction 92
4.2 Experimental Details 93
4.3 Results and Discussions 95

4.4 Conclusion 102
References 103
5. All-Optical Study of Magnetization Dynamics in a Square Artificial Spin Ice Nanostructure 106
5.1 Introduction 106
5.2 Experimental Details 108
5.3 Results and Discussions 109
5.3.1 Magnetoelastic Interaction 119
5.3.2 Overlap Between Magnetic and Elastic Modes 121
5.4 Conclusion 122
References 123
6. Ultrafast Magnetization Dynamics in a Nanoscale Three-Dimensional Cobalt Tetrapod Structure 127
6.1 Introduction 127
6.2 Experimental Details 128
6.3 Results and Discussions 130
6.4 Conclusion 135
References 136
7. Observation of Coherent Spin Waves in a Three-Dimensional Artificial Spin Ice Structure 138
7.1 Introduction 138
7.2 Experimental Details 140
7.3 Results and Discussions 142
7.4 Conclusion 147
References 148
8. All-Optical Detection of Spin-Orbit Torque Driven Modulation of Gilbert Damping in Ta/CoFeB/SiO_2 Heterostructures 151
8.1 Introduction 151
8.2 Experimental Details 153
8.3 Results and Discussions 154

8.3.1 Modulation of Precessional Frequency in Presence of Charge Current 159
8.4 Conclusion 162
References 163
9. Summary and Outlook 166
9.1 Summary 166
9.2 Outlook 170
Appendix A: Chapter 4 173
A.1. Extraction of Magnetic Parameters of the $Ni_{80}Fe_{20}$ Thin Film 173
A.2. Spin-Wave in Isolated Nanodots and Nanochannels 173
Appendix B: Chapter 7 176
B.1. Bias Field Dependent of Spin-Wave Frequency 176
B.2. Static Magnetization Configuration of the Sample 177
B.3. Collective Nature of Spin-Wave Modes 178
B.4. Calculated Spin-Wave Mode Profiles of Additional Modes Observed Only in the Simulation 178

List of Figures

Figure 2. 1. (a) Broadside and (b) head to tail configuration for ferromagnetically coupled magnetic moments. The latter is lower in energy. 34

Figure 2. 2. Precessional motion of magnetization (***M***) with respect to effective magnetic field ($\boldsymbol{H_{eff}}$) is shown. Different torque terms of LLG equation are shown. 39

Figure 2. 3. (a) Ground state spin configuration of a ferromagnetic material. (b) Non uniform precessional motion, and (c) uniform precessional motion are shown. 40

Figure 2. 4. (a) Schematic of bulk spin Hall effect in heavy metal (HM) is shown. Flow of charge current direction (I_{dc}), spin current direction (I_s) are shown. 44

Figure 3. 1. Schematic of a two-photon lithography (TPL). 51

Figure 3. 2. Schematic of electrodeposition 52

Figure 3. 3. Schematic of thermal evaporation 53

Figure 3. 4. Schematic of electron-beam evaporation. 54

Figure 3. 5. Schematic of RF-DC magnetron sputtering 55

Figure 3. 6. Schematic of scanning electron microscope (SEM) and energy dispersive X-ray (EDX) is shown. The monitor at right and left captures the SEM image and EDX spectra, respectively. 56

Figure 3. 7. Schematic of (a) X-ray diffractometer and (b) diffraction of X-ray from the atomic planes are shown. 58

Figure 3. 8. Schematic of atomic force microscopy. 59

Figure 3. 9. (a) Schematic of longitudinal, polar and transverse Kerr geometries, and (b) Kerr rotation (θ_k), Kerr ellipticity (ε_k) and two orthogonal components of electric field (***r*** and ***k***) in the ellipsoid are shown. 61

Figure 3. 10. Schematic of the static-MOKE system present in our laboratory at S.N. Bose National Centre for Basic Sciences. 62

Figure 3. 11. Schematic of the optical bridge detector (OBD). 63

Figure 3. 12. Schematic of the colinear TRMOKE system present in our laboratory at S.N. Bose National Centre for Basic Sciences. 67

Figure 3. 13. Photograph of the TRMOKE microscopy set-up present in our laboratory at S.N. Bose National Centre for Basic Sciences. 68

Figure 3. 14. Schematic of the noncolinear TRMOKE system present in our laboratory at S.N. Bose National Centre for Basic Sciences. 74

Figure 3. 15. Photograph of the noncolinear TRMOKE system present in our laboratory at the S.N. Bose National Centre for Basic Sciences. 75

Figure 3. 16. Transmission Spectra of FPI1 and FPI2 and in tandem operation. The transmitted spectra consist of an intense elastic peak (frequency: ω_L) and two weaker sidebands ($\omega_L \pm \omega$)...78

Figure 3. 17. Schematic of the pinhole and light modulator arrangement inside the TFPI of the BLS system. 79

Figure 3. 18. A schematic of the part of the BLS spectrum which passes through shutter (SH), (a) SH1 and (b) SH2 when another shutter remains closed. A superposition of the spectra in (a) and (b) is acquired when SH1 and SH2 operate in synchronization. 80

Figure 3. 19. Schematic of the BLS setup present in our laboratory at S.N. Bose National Centre for Basic Sciences..... 81

Figure 3. 20. Photograph of the BLS setup present in our laboratory at S.N. Bose National Centre for Basic Sciences..... 82

Figure 3. 21. Correlation between micromagnetics with ab-initio and macrospin model. 83

Figure 3. 22. Generation of spherical shape in – (a) finite difference method (cuboidal cell) and (b) finite element method (tetrahedral cell)..... 84

Figure 4. 1. Scanning electron micrographs are shown for (a) S1, (b) S2 and (c) S3. The scale bar is common to three samples, as shown in (b). A magnified view of the constituent nanodot with the four nanochannels is shown at the inset of each image. (d) A schematic of sample is shown where the dot size (*S*), and nanochannels length (*l*) and width (*w*) are marked..... 95

Figure 4. 2. (a) Schematic of experimental geometry is shown. Focusing of pump and probe beam and direction of applied magnetic field (*H*) are highlighted. Typical time resolved (b) reflectivity and (c) Kerr rotation data of sample S1 are shown at a bias magnetic field of 1.67 kOe. 96

Figure 4. 3. (a) Experimental time-resolved Kerr rotation showing precessional oscillation for all three samples at H = 1.67 kOe. The FFT power spectra of time-resolved (b) experimental and (c) simulated precessional oscillations are shown. Spin-wave modes are numbered in the ascending value of frequency. 97

Figure 4. 4. Simulated spatial distributions of power of spin-wave modes are shown. The corresponding phase profiles are shown in the inset. 98

Figure 4. 5. (a) Magnetostatic field distribution of all the samples at H = 1.67 kOe. Linescans of the magnetostatic field distributions taken along (b) horizontal nanochannels: HNCs (R1) and (c) vertical nanochannels: VNCs (R2) as shown by dotted lines on S1 of (a). (d) Variation of magnetostatic field with filling fraction. The difference in B_{in} between HNC and VNC is shown in the inset. 99

Figure 4. 6. (a) Simulated power spectra of only nanodots and nanochannels of S1 are shown. Modes are marked by numbers in order of ascending frequency value. (b) Simulated spatial distribution of power of spin-wave modes is shown. The corresponding phase profile is presented at the top right corner of each power map. The colour maps of power and phase profiles are shown at the top right side of (b). Black dashed lines are a guide to the eye to show the positions of nanodots or nanochannels. 100

Figure 4. 7. Simulations showing propagating nature of spin-wave modes (a) M3, (b) M5 and (c) M7. Spin-wave of desired frequency is excited at the centre (marked by *I*) of the array highlighted by dark blue coloured dashed line as shown in (c). Here 'O' corresponds to the output of the spin-wave propagation through the nanochannels. The colour map of spin-wave power is shown at the right side. 101

Figure 5. 1. (a) Atomic force microscope and (b) scanning electron microscope images of the Py square ASI structure. The length-scale bars are shown at bottom right corner. Some characteristic structural parameters of the ASI structure are marked in (a). (c) Energy dispersive x-ray spectrum showing elemental composition of the sample. The peak positions of different elements are identified in the spectrum..... 109

Figure 5. 2. (a) Magnetic hysteresis loop measured by static-MOKE showing the reversal mechanism of Py square ASI. (b) Remanent state MFM image is shown. Simulated (c) magnetic hysteresis loop, (d) remanent state MFM and (e) remanent state magnetization configuration is shown. Multidomain magnetic states are marked by dotted boxes in (d) and (e). The color bars and wheel are shown at top right corner. 110

Figure 5. 3. Experimental time-resolved Kerr rotation data is shown for four different bias magnetic field values. The FFT power spectra of the time-resolved (b) experimental and (c)

simulated precessional oscillations are shown. The spin-wave modes are numbered in the descending value of frequency. The magnetic field values are mentioned inside each panel. The spin-wave modes only observed in simulation are marked by * in the simulated spectra. 111

Figure 5. 4. (a) Surface plot of spin-wave power spectra with field (*H*) is shown. The solid symbols superposed on the surface plot represent peak frequencies of spin-wave modes obtained from the FFT power spectra. The color bar is shown at right. The spin-wave mode anticrossing regions are marked by black solid circles. Four important *H* values are marked by vertical dashed lines on the surface plot whose spin-wave spectra are shown in (b). In panels 1 and 4, the anticrossings and corresponding gaps are shown (b). In panels 2 and 3, M2 starts to show field dispersion. 112

Figure 5. 5. Magnetic field dispersion of experimental and simulated spin-wave frequencies is shown. Solid symbols represent experimental data, which are reproduced from Fig. 5.4(a), while the dotted and dash-dotted lines represent simulated frequencies. 113

Figure 5. 6. Equilibrium state magnetization configurations at six different magnetic fields (*H*) are shown. The magnetic field values are mentioned at the top of each image. Magnified views of magnetic microstates are shown in the bottom panels. The color wheel and the magnetic field geometry are shown at the bottom left. 115

Figure 5. 7. (a) Simulated spin-wave power profiles at different magnetic field values are shown. 116

Figure 5. 7. (b) Simulated spin-wave phase profiles at different magnetic field values are shown. 116

Figure 5. 8. (a) Simulated spin-wave power profiles at different magnetic field values are shown. 117

Figure 5. 8. (b) Simulated spin-wave phase profiles at different magnetic field values are shown. 117

Figure 5. 9. Correlation between magnetic microstates and spin-wave mode profile is shown. Magnetic microstates are shown on the left side and corresponding spin-wave power and phase profiles are presented at middle and right sides of each panel respectively. The colour bars and wheels are presented at bottom right. 118

Figure 5. 10. (a) Oscillations in time-resolved reflectivity data are shown for four different applied magnetic fields. (b) Surface plot of FFT power spectra of the time-resolved reflectivity is shown. Positions of different acoustic modes are marked by horizontal arrows, while the color bar is shown at the left side. Calculated acoustic frequencies are shown by dashed lines in (b). 120

Figure 6. 1. Scanning electron micrograph of (a) an array of tetrapod structures and (b) a single tetrapod structure. 129

Figure 6. 2. (a) Schematic diagram of the cobalt tetrapod and the experimental geometry. Typical time-resolved (b) reflectivity and (c) Kerr rotation data are shown at *H* = 3.92 kOe. 130

Figure 6. 3. (a) Time-resolved Kerr rotation data for three different bias magnetic field values. (b) Power spectra for the entire time-resolved data. (c) Power spectra for the marked region in time-resolved data. Corresponding values of bias magnetic fields are shown. 131

Figure 6. 4. Simulated (a) power spectra and (b) normalized static magnetization configuration (z-component) for ground state at three different bias magnetic fields are shown. 133

Figure 6. 5. Simulated spin-wave mode profiles for *H* = 3.40, 3.92 and 4.50 kOe. 134

Figure 6. 6. (a) Magnified view of mode profile and (b) sliced view of the tetrapod junction for different modes at *H* = 4.50 kOe. 134

Figure 7. 1. (a) Scanning electron micrograph showing top view of full array of 3D-ASI with size 50×50×10 μm^3, the scale bar is 25 μm. A constituent tetrapod element is shown in the inset by capturing a zoomed view of 3D array where the scale bar is 1 μm (b) A magnified view of the interconnected nanowires in the lattice is shown. Four sub-lattice layers are highlighted. Scale bar in (b) is 2 μm. (c) Magnetic hysteresis loop of the 3D-ASI sample measured using static magneto-optical Kerr effect. Applied magnetic field (H) geometry is shown in (b).....140

Figure 7. 2. (a) Schematic of BLS measurement geometry. The measurement was performed at θ = 0°. The applied field (H) direction is shown in the left inset and the scale bar is 2 μm. The 3D-ASI network is presented by a schematic on the right side of the image. (b) BLS spectra for three different magnetic field values are shown. Open circles present the experimental data points. Here, cyan and red color solid lines present the fitting of individual peak and the grey color solid line presents the resultant of the multi-peak fitting.....141

Figure 7. 3. (a) Spin-wave frequencies of mode 1 (M1) and mode 2 (M2) are plotted as a function of applied magnetic field. Here, symbols present the experimentally measured data points. The elastic peak fitted with a Gaussian function is shown at the inset. (b) Simulated spin-wave spectra for three intermediate field values are shown. The dotted lines in (a) present the simulated results.....142

Figure 7. 4. (a) Schematic of diamond-lattice unit cell. Here, the green color double lines present the bond position and blue spheres present the atom position. The dashed lines define the axes. (b) A representative simulated unit cell of 3D-ASI is shown. One unit cell consists of four tetrapod elements, each of them are highlighted by different color for better visualization. A one-to-one correspondence between the diamond bond lattice and 3D-ASI (omitting the atoms) could be found from (a) and (b). (c) Magnetization configuration of the equilibrium state (m_x component) at H = 1.6 kOe (along x-direction; in-plane) is shown. The color bar for m_x is shown next to the image.....144

Figure 7. 5. (a) A representative static magnetization profile (m_x component) along with the coordinate system. The red and black dashed lines show the slice taking positions to extract mode profiles parallel to different planes at positions 1 and 2. Spin-wave mode profiles are calculated at different points of 3D-ASI structure at H = 1.6 kOe by taking slice along: (b) x´-y´ plane at point 1, (c) y´-z´ plane at point 2 and (d) x-´z´ plane at point 1. The power profiles are shown in upper panels and corresponding phase profiles in the lower panels. The color bars for power and phase are shown at the bottom left corner.....146

Figure 8. 1. (a) X-ray diffraction patterns measured at grazing angle of incidence from Ta films of thicknesses of 4, 6, 10 and 15 nm are shown. Peaks correspond to β phase of Ta are marked in the plots. (b) Variation of inverse of sheet resistance of Ta(t)/$Co_{20}Fe_{60}B_{20}$(3 nm)/SiO_2(2 nm) as a function of Ta thickness (t) is plotted. (c) Atomic force microscope images showing the surface topography of the Ta(t)/$Co_{20}Fe_{60}B_{20}$(3 nm)/SiO_2(2 nm) samples with t = 4, 6, 10 and 20 nm are presented. The scale bar is same for all samples as shown in the images.....155

Figure 8. 2. (a) Schematic of the measurement geometry is shown. The applied current (J_c) and magnetic field (H_{eff}) directions are marked (green arrow). (b) A typical time-resolved Kerr rotation data for Ta (3 nm)/$Co_{20}Fe_{60}B_{20}$(3 nm)/SiO_2(2 nm) at H = 1.5 kOe is shown. (c) The bias magnetic field variation of precession frequency (solid black circles) is fitted with Kittel formula (blue solid line). The variation of damping parameter (α_0, solid red squares) with H is shown. The dotted line is a guide to the eye, which shows an invariance of α_0 with H.....156

Figure 8. 3. (a) Representative time-resolved precessional oscillations for extraction of damping under the influence of maximum positive and negative charge current densities (J_c) are shown at left and right panels. Here, Ta thickness is mentioned in the left panel. The estimated effective (α_{eff}) damping parameters are also presented inside each panel. Comparison of left and right panel reveals that α_{eff} changes with the polarity of charge current. (b) The MOD plot for Ta thicknesses

of 4, 7 and 20 nm are shown. Solid line is a linear fit to the MOD with J_c. Error bars correspond to the fitting error obtained during the estimation of damping.....158

Figure 8. 4. The modulation of frequency (MOF) for t = 6 nm (a) and 10 nm (c) are shown. The solid red line represents the parabolic fit of MOF with J_c. The corresponding change in normalized effective magnetization (M_{ej}/M_e) is plotted (blue solid circles). The blue solid line represents parabolic fitting. The modulation of damping (MOD) considering Joule heating effect (α_{ej}) is plotted for t = 6 nm (b) and 10 nm (d). The solid red line represents the fit with a function: a + bJ_c + cJ_c^2. The parameter b gives the MOD due to damping-like torque (DLT).....160

Figure 8. 5. Variation of DLT efficieny without (ξ_{DL}: solid blue circles) and with (ξ'_{DL}; solid red circles) Joule heating effect as a function of Ta thickness. The DLT efficiency remains invariant with Ta thickness. The dotted lines are a guide to the eye. 160

Figure A. 1. Bias field dependence of precession frequency of an unpatterned Py thin film is shown. The symbols represent experimental frequency values, whereas the solid line represents theoretical fit using equation A.1.....173

Figure A. 2. (a) Simulated power spectra of connected nanodots (CNDs), isolated nanodots (NDs) and isolated nanochannels (NCs) are shown for sample S2 at an applied bias magnetic field of H = 1.67 kOe. (b) Spatial distributions of spin-wave mode powers are shown, whereas the phase profiles are presented at the insets of corresponding power profiles. In isolated cases, black dashed lines are to guide the positions of the NDs and NCs.....174

Figure A. 3. (a) Simulated power spectra of connected nanodots (CNDs), isolated nanodots (NDs) and isolated nanochannels (NCs) are shown for sample S3 at an applied bias magnetic field of H = 1.67 kOe. (b) Spatial distributions of spin-wave mode powers are shown, whereas the phase profiles are presented at the insets of corresponding power profiles. In isolated cases, black dashed lines are to guide the positions of the NDs and NCs.....175

Figure B. 1. Experimental data of bias field dependent spin-wave frequency (open symbols) fitted with Kittel formula of equation B.1 (solid line). 176

Figure B. 2. Static magnetization configurations (m_x component) of the sample at bias magnetic field (H) of (a) 0.6 kOe, (b) 1.0 kOe and (c) 2.0 kOe are shown.....177

Figure B. 3. Static magnetization configuration of (a) m_z component and (b) m_y component of the 3D-ASI sample at H = 1.6 kOe applied in the plane of the sample (along x direction). 177

Figure B. 4. Simulated spin-wave spectra for one leg, one element and one unit cell of 3D-ASI at H = 1.6 kOe are shown. The positions of M1 and M2 are marked by black dashed lines. Representative simulated structures are shown on the left panels.....178

Figure B. 5. Simulated spin-wave spectra of the 3D-ASI sample at H = 1.6 kOe. The experimentally observed modes are marked by '#' while the additional modes observed explicitly in simulation are numbered as 'digit*' from lower to higher frequencies.....179

Figure B. 6. Spin-wave mode profiles calculated at different points of 3D-ASI structure at H = 1.6 kOe by taking slice along (a), (d) x´-y´ plane at point 1, (b), (e) y´-z´ plane at point 2 and (c), (f) x´-z´ plane at point 1. The mode profiles of M1, M2 and M3 are shown in (a), (b) and (c), while (d), (e) and (f) show the mode profiles of M4* and M5*. The x´-y-´z´ coordinate and positions (1 and 2) are presented in Fig. 7.5(a) of Chapter 7. The power profiles are shown in upper part and corresponding phase profiles in lower part of each panel. The color bars are presented at bottom right corner.....180

Chapter 1

1. Introduction

Magnetism is one of the fascinating and oldest research fields. It found its utility over the evolution of humankind, starting from the old-age marine compass to current data storage devices. Magnet is a part of human evolutionary history. All the applications were made possible by fundamental research of magnetism, search for new materials and discovery of novel phenomena. The story of magnetite (Fe_3O_4) to attract iron was known even around 2500 years ago. The word 'magnet' originates from the Greek word "magnesia". In ancient times, people found that a specific shape of floated magnetite aligned itself around the north-south direction of the earth. A needle-shaped iron rubbed on magnetite showed the same behaviour which gave rise to marine compass. The first-ever scientific study on magnetism was done by William Gilbert around 1600 AD when he published his classic book "On the Magnet" [1]. He demonstrated the behaviour of the earth's magnetic field by experimenting with loadstone and iron. Later on, the correlation between electricity and magnetism was anticipated by the different discoveries at the beginning of the nineteenth century by Oersted [2], Ampere and Faraday. However, a theoretical correlation was missing until the development of the unified theory of electricity and magnetism by Maxwell in 1865 [3] based on the mathematical works of Laplace, Poisson, Green, Gauss and Faraday's observations. The unified theory described light as propagation of electric and magnetic oscillation together. In the late 19th and early 20th centuries, different approaches were taken to understand magnetism such as Langevin theory [4] and Weiss molecular field theory [5]. The famous discovery of relativistic mechanics by Einstein [6], described the magnetic field to originate from current carrying wire as observed by Oersted but was not able to explain the origin of magnetization in loadstone. Until the progress of quantum mechanics at the beginning of the 20th century, the origin of magnetism in material (loadstone) was not understood. Some phenomenal work was done by Niels Bohr and Hendreka van Leeuwen independently (Bohr-van Leeuwen theory [7]), which states that from classical mechanics points of view, magnetization cannot exist at a finite temperature. The progress of quantum mechanics in the 1920s resulted in the description of diamagnetism

and paramagnetism in materials, and later, based on Heinsberg's discovery of exchange interaction [8] and Pauli's exclusion principle description of spontaneous magnetization in ferromagnet and ferrimagnet (loadstone) was possible. The first experimental observation of electron spin was made by Stern and Gerlach in 1922 [9]. Later on, it was theorized by Goudsmit and Uhlenbeck [10] to describe quantized angular momentum as observed by Stern and Gerlach. In 1928. Dirac gave his famous equation known as the 'Dirac equation' [11] which is a combination of relativity and quantum mechanics, two landmarks of modern physics to describe the origin of spin − the primary source of electron magnetism. The first part of the 20^{th} century was a revolution in theoretical physics. With the passing of the 20^{th} century, the research field of magnetism made its own revolution. In 1956, the pioneering work on surface anisotropy by Neel [12] suggested that the broken symmetry at an interface result in a surface magnetic anisotropy. Later on, the evolution of nanotechnology and nanoscience [13] opened the path for the exploration of the universe of nanomagnets. The nanomagnets show novel functionalities [14,15] which are not possible in their bulk counterparts. An important milestone in thin film magnetism research was the discovery of giant magnetoresistance (GMR) in 1988 by Fert [16] and Grunberg [17]. This discovery revolutionized hard disk drive (HDD) where GMR is now used as read head. Current HDD has a data density of more than 1000 Gb/in^2. Since the discovery of GMR, the research in spintronics, which deals with interactions between transported electron's spin and magnetization configuration and its dynamics, have been boosted. This leads to the designing of the magnetic tunnel junction (MTJ) where two magnetic layers (reference and free layer) are separated by an insulating (metallic layer used in GMR). The tunnelling magnetoresistance (TMR) [18] property of MTJ makes it suitable for magnetic memory devices. The MTJs have been used in magnetic random-access memory (MRAM) which can be employed as primary memory in computers. With the development of spin-transfer torque (STT) mechanism [19], STT based MRAM (STT-MRAM) [20,21] has emerged as non-volatile universal memory. Despite, its potential application, STT-MRAM faces issues of barrier breakdown and switching by small read current [22]. The spin-orbit torque (SOT) is emerging as an alternative for STT. The SOT mainly arises from the interfacial Rashba effect [23,24] and bulk spin Hall effect (SHE) [25,26]. The low power and high-speed switching using SOT [27] are promising for SOT-MRAM. The generation of spin current via SHE is a promising way to induce SOT in the magnetic layer. The SHE

was first observed in 2004 in semiconductor material [28] since its prediction in 1971 [25]. The SHE is majorly explored in heavy metal (HM)/ferromagnet (FM) structures. Besides the HMs, topological insulators [29] and noncollinear antiferromagnet [30] are promising for generating large SHE to induce SOT in FMs. Besides SHE, HM/FM heterostructures can possess different novel phenomena such as interfacial Dzyloshinskii Moriya interaction (iDMI) [31], perpendicular magnetic anisotropy (PMA) [32], spin pumping [33], inverse SHE (iSHE) [34] and interfacial Rashba effect [23]. These novel functionalities of HM/FM have made them an integral part of modern spintronics research. The study of spintronics gave rise to a number of sub-fields such as spin orbitronics [35], spin caloritronics [36], magnon spintronics [37], ultrafast spin photonics [38] and spin mechatronics [39]. The progress of spintronics is promising for the designing of next generation storage and information devices [38,40].

As spintronics deals with the transportation of spin, magnonics deals with the wave motion of spins in a magnetic system. The field of magnonics began with the desire to control and explore spin waves in periodically patterned magnetic structures with a goal to use spin waves as information encoders and processors instead of diffusive spin current. The periodically patterned structures are commonly known as magnonic crystals [41], a magnetic analogue of photonic crystal [42]. The concept of spin-wave was first proposed by F. Bloch in 1930 [43]. Spin waves can be described as propagation of ripple or perturbed energy in from of phase in a coupled magnetic system, like 'Mexican wave'. Spin waves like other waves of different origins (such photon, phonon) show wave characteristics, namely, reflection and refraction [44,45], propagation [46,47], interference [48], tunnelling [49] Doppler effect [50] and diffraction [51]. These wave properties of spin-wave promoted the study of the magnonic crystals which can be designed by periodic modulation of magnetic parameters (magnetization, anisotropy, exchange constant) or external parameters (magnetic field, stress, electric field, electrical current) in a magnetic thin film. Besides the fundamental interests, the magnonic crystals are a potential candidate to fulfil the ever-increasing demand for energy-efficient information carriers for data storage and processing [37,52]. Therefore, a large number of experimental and numerical studies on the static and dynamic responses of the magnonic crystals have been carried out in one-dimension (1D: magnonic waveguides [53], stripes [54], nanowires [55]), two-dimension (2D: dot [56], antidot [57], bi-component magnonic crystal [58]) and three-dimension (3D: arrays of sphere [59]). The

study of spin-wave dynamics in different dimensional magnonic crystals led to the observation of several interesting phenomena such as channelling of spin-wave [60], opening of magnonic bandgap [61], mode crossover [62], dynamic configuration anisotropy [63], mode splitting [64], magnon-magnon coupling [65], symmetric and asymmetric mode [66] to name a few. Further, the variation of constituent elements' width [67-69], aspect ratio [70,71], shape [72,73], lattice constant [56,74], lattice symmetry [75,76], base material [77,78] as well as the variation of external bias magnetic field strength and orientation [79-81] were explored to understand the spin-wave behaviours and also to achieve more control over the spin-wave dynamics. This leads to the designing of a number of miniaturized components and devices such as spin wave-based multiplexer [82], interferometer [83], grating [84], magnonic waveguides [85,86], phase shifters [87], directional couplers [88], nanomagnetic antenna [89] and many more. Further, the coupling between magnon with other quasiparticles such as phonon [90], optical and microwave photon [91,92], spin ensemble [92,93], fluxon [94] etc. are promising for 'hybrid magnonics' where more than one parameter can be useful for tuning spin-wave dynamics. These developments are promising to build a foundation for future all-magnon circuits [95], spin-wave based computing [96], neuromorphic [97] and quantum computing [98].

The recent emergence of artificial spin ice (ASI) as a reconfigurable magnetic structure with monopole defect states and the 3D magnetic structure with more dimensional flexibility (compared to 1D and 2D) have the potential to introduce new functionalities in the magnonic crystals for further progress towards future energy-efficient storage and information devices.

A brief overview of few aspects of magnonics and spintronics are presented in succeeding paragraphs which have inspired the present thesis work.

1.1 Interfacial Properties of Heavy-metal/Ferromagnet Layer Structure

As mentioned earlier, HM/FM thin film interfaces play a crucial role in spintronics devices. PMA can originate from the magnetic anisotropy at the interface between HM/FM such as Co/Pd(Pt) [32,99] multilayer system and heterostructure of HM (Ta [100], Ru [100], W [101], Mo [102], Hf [103])/CoFeB/MgO. Experimental studies showed that HM/FM interface is crucial for PMA. Although, in the case of HM/FM/Oxide structure

besides the HMs (Ta, Ru, W, Mo, Hf), the oxide layer (MgO) adjacent to the FM layer also plays an important role to induce PMA. The HM/FM structures have also been used as free layer [20], reference layer [104] and as both layers [100] in perpendicularly magnetized MTJs where high TMR ratios have been reported. These PMA structures were also used in synthetic antiferromagnets [105]. The antiferromagnetic state is induced via interlayer exchange coupling between two PMA bilayer systems (Co/Pt) separated by a spacer layer (Ru). The broken inversion symmetry at HM/FM interface can induce iDMI. The DMI was discovered by Dzyloshiskii [106] and Moriya [107] to describe weak ferromagnetism in an antiferromagnet. The iDMI favours canted spin texture which can stabilize topologically protected skyrmion [108] spin texture in HM/FM system. The study of iDMI is interesting for the exploration of asymmetric spin-wave propagation and stabilization of chiral spin textures. A large number of studies on iDMI have been reported for different HM/FM systems [109-116] to estimate the value of the iDMI constant which is a crucial parameter for stabilization of skyrmion texture. In most of the studies, Pt/FM systems were used. To avoid interfacial anisotropy induced by Pt, others HMs (W [117], Ta [113], Hf [118], TaN [119]) have been studied. Reduction in iDMI due to symmetric interfaces have been reported in [120]. The asymmetric HM/FM/HM structure with two different HMs of different DMI chirality (Pt and Ir) [121] enhances the iDMI strength. Recently, room temperature skyrmions [122,123] in HM/FM heterostructure have been observed. The combination of SOT with skyrmion [124] can lead to skyrmion based racetrack memory for application in MRAM. Although the implementation is facings difficult due to the skyrmion Hall effect which can be overcome using skyrmionium [125] and synthetic antiferromagnet [126]. Spin pumping is another phenomenon that occurs at the interfaces of HM/FM. The excitation of ferromagnetic resonance (FMR) in FM leads to the generation of macroscopic spin current in the adjacent HM which diffuses away from the interface [127,128]. It occurs due to time and spin-dependent scattering of magnetization precession at the interface. The spin pumping in HM/FM heterostructures [129,130] has been studied to determine the spin mixing conductance (related to interface quality) and diffusion length (related to spin-orbit coupling (SOC) strength in HM). In general HMs with high SOC possess a diffusion length of few nanometres [131,132]. This spin current (due to spin pumping from FM to HM) generates an electric current in HM which is known as iSHE. For this behaviour spin pumping phenomenon is also called a spin battery [133]. Spin pumping and SHE generate pure spin current over

the large interfacial area which is injected to HM from FM and FM to HM respectively. The charge current through an HM with high SOC generates spin current via SHE which can be transferred to adjacent FM layers to control its magnetization state and dynamics. The spin current exerts a torque on the FM layer magnetization, also known as SOT which is a combination of damping-like torque (DLT) and field-like torque (FLT). The SOT efficiency depends on spin-mixing conductance and spin Hall angle (θ_{SHJ}). The θ_{SH} represents the charge to spin conversion efficiency. Several studies have been carried out to determine θ_{SH} in different HMs [26,134-140]. Enhancement in θ_{SH} with increasing resistivity [139] and HM phase transition [140] have been reported. There are several experimental techniques to determine θ_{SH} spin current, such as, non-local spin valve technique [141], second harmonic generation [142], spin-torque FMR (ST-FMR) [136], iSHE measurement [34], static magneto-optical Kerr effect (static-MOKE) [143], etc. However, θ_{SH} reported from various techniques are found to vary over a wide range (e.g., between 0.0037 and 0.08 in Pt [52]). The determination of θ_{SH} using an all-optical detection technique based on a time-resolved MOKE (TRMOKE) magnetometer can be a reliable technique for measuring θ_{SH}. The all-optical TRMOKE method does not suffer from the effect of defects and inhomogeneities due to the large area averaging and it does not require any delicate micro-fabrication techniques for sample preparation. It can eliminate possible experimental artefacts involved in the electrical detection techniques [138,140]. Moreover, magnetization damping can be extracted directly from the decaying profile of time-resolved precessional oscillation, which is more advantageous than other available techniques.

1.2 Ferromagnetic Nanostructures: Antidot and Connected Nanodot Lattice

Periodically arranged grooves or holes are known as antidot lattice as known from photonics [144] and nanoelectronics [145]. The magnetic antidots are an integral part of magnonic crystals, with potential application in non-volatile memory [146], a mesh of connected waveguides [79], logic devices and others. In the case of antidots, the magnetic materials are physically connected all over the lattice, which means antidot lattices are exchange-dipole coupled magnetic systems. Therefore, the spin-wave frequency, group velocity and propagation lengths are much higher in comparison to isolated periodic nanostructure, i.e., dot lattice. Also, the superparamagnetic effect which is unavoidable in

isolated nanostructures [147], can be avoided during lowering of the magnetic element size. There have been several experimental [57,148-151] and numerical studies [79,152-154] on antidot lattices to understand spin-wave behaviour and the role of the magnetostatic interaction, dynamic dipolar interaction and demagnetizing field. The antidots can tune spin-wave dynamics properties such as the introduction of antidots on ferromagnetic stripe [85,155] can transmit a single-mode spin-wave by lowering the energy leakage. The antidots can also modify the static properties such as the tunability of the easy and hard axis which can be achieved by changing antidot lattice symmetries [156]. Pechan et al. [157] reported the first-ever experimental study of spin-wave modes in a permalloy antidot lattice using FMR and time-resolved Kerr microscopy. They observed localized spin-wave modes and magnetization precessional data was drastically modified at the vicinity of antidot edges. Subsequently, Neusser et al. [158] reported an extensive study on square antidot lattice. They observed extended and localized spin-wave modes and depending on the external magnetic field orientation, opening-closing of channels for spin-wave transmission. The same group also reported [80] an anisotropic damping behaviour originating from edge roughness of antidots, affecting spin-wave dynamics. Later on, the effect of inhomogeneity of internal field in square antidots on spin-wave dynamics led to the observation of magnetic normal modes [150] and weakly field-dependent localized mode in a strongly inhomogeneous regime [159]. Also, the tunable metamaterial response for spin-wave in the same type of antidot lattice was reported in [160]. This was followed by a number of studies on antidot lattices of varying shape [72], lattice symmetry [76], base material [77,161], lattice constant [74] and externally applied field amplitude and orientation [162] to get an internal and external control over spin-wave modes and band structure. Further studies have explored different phenomena such as bang gap opening at the boundary of Brillouin zone [163], formation of the mini band due to coupling between edge modes [164], mode conversion, positive and negative group velocity of spin-wave [81], mode hopping [165,166], mode softening [167] etc. Besides the regular antidot lattices, different types of magnonic quasicrystals such as octagonal [168-170], binary [171,172] and defective [173-175] antidot lattices have shown further tunability of spin-wave modes. Recently, connected nanodot (CND) [176,177] have attracted much attention to understand the role of nanochannels on spin-wave dynamics. In the case of CNDs, dots are connected

through regular shaped nanochannels as opposed to irregularly shaped nanochannels that occur in antidot lattices.

1.3 Artificial Spin Ice

The study of spin-wave dynamics in ASI is an emerging field due to its highly reconfigurable magnetic microstates. ASIs are tailor-made ferromagnetic nanostructure on the desired geometry to manifest the magnetic defect state or frustration. In a physical system, when all competitive energy terms can be minimized simultaneously to achieve the ground state then frustrations may occur. Pioneering work on geometrical frustration was reported in 1935 by Pauling [178] to describe the zero-temperature entropy [179] in water ice. The ambiguity to choose the hydrogen bonds in water ice leads to the "two-in-two-out" configuration in the lower energy state of water ice by positioning two hydrogen atoms close to an oxygen atom and two far away. In the early 1990s, researchers observed some unusual behaviour in some disordered magnetic materials (mostly antiferromagnetically coupled) [180,181] at lower temperatures. This observation boosted the study of frustration in magnetic systems. Later on, Harris et al. [182] observed water ice-like frustration in ferromagnetically interacting pyrochlore materials (such as $Ho_2Ti_2O_7$) obeying the ice rule. They named this frustrating behaviour as "spin ice". One of the salient features of spin ice is the existence of magnetic monopoles [183] also known as defect states. These monopoles are always created in pairs and linked via effective "Dirac String". These defect states are different from Dirac envisioned string and monopoles, and as a result, they do not impose any charge quantization in Maxwell's equation. The ASIs can mimic the observed monopole characteristics which could be studied in a more controlled manner to probe the topological defects locally and exploring possible applications in magnetic devices. Depending on the nano bar arrangement geometry, different types of ASI structure can be designed, namely, square [184], kagome [185], pinwheel [186,187], trident [188], tetris [189], brickwork [190], shakti [191], toroidal [192], square–kite tessellation [193], quadrupolar [194], pentagonal [195], dice [196] and Penrose tiling [197,198]. The first-ever experimental observation of spin ice behaviour in ASI (square geometry) was reported by Wang et al. [184] in 2006. In the same year, the spin ice behaviour in a kagome ASI was also demonstrated [185]. Subsequently, the direct imagining of the magnetic monopoles and effective Dirac string in ASI structures were observed [199,200]. The defects can affect

the quasistatic, equilibrium magnetization configuration and reversal process of ASI structure [201-203]. These observations provoked the study of high frequency response in such structures to explore the effect of monopole defects, i.e., microstates on global as well as local spin-wave modes for designing a magnonic device with new functionalities. The first ever high-frequency response of ASI was studied on square ASI geometry using a numerical method [204]. They explored the effects of monopole defects on spin-wave modes. The defects showed some distinguishing characteristics on the spin-wave spectra and mode profiles. This was followed by the experimental study of the field swept of spin-wave dynamics of square ASI [205]. They observed field history-dependent asymmetric behaviour of spin-wave modes around zero field which was claimed to be occurring from the local configuration of neighbouring nanobars. Later on, an extensive experimental and simulation study on square ASI [206] was reported. The spin-wave dynamics strongly depends on the field history. A systemic study on interconnected kagome ASI [207,208] was also reported around the same time. Here, a new spin-wave mode appeared in the spectra with the presence of monopoles during field reversal, and the mode intensity increased with the increasing monopole numbers. The resonance frequency variation was observed at the junctions of nanobars due to topological defects which can affect the exchange dominated spin waves. During the same year, spin-wave dynamics was reported for different types of ASI and anti-ASI structures [209]. They observed that the resonant modes were originated from different parts of the ASI and anti-ASI. Symmetry breaking Y-shaped units of kagome lattice [210] were able to manipulate spin-wave mode activation and deactivation by changing bias field direction. The microstate configuration can suppress a bulk mode in kagome ASI as reported in [211] using micromagnetic simulation. Symmetric mode in square ASI was also reported [212]. Some studies were reported on spin-wave dispersion in ASI structures [213-215]. Due to the weak interaction between the nanobars of square ASI, the spin wave field dispersion showed a flatter band [213]. The opening of the channel at a 45° angle led to the dispersive spin-wave band in a square anti-ASI system [214]. Theoretical calculation predicated that the band structure tunability could be achieved via the topological states in a square ASI [215]. More recently, a comprehensive study of spin-wave mode characteristics and selective mode behaviour in connected and disconnected kagome ASI nanostructures have been demonstrated [216]. It was observed that the spin-wave modes were strongly influenced by the ASI geometry as well as by the microstates. Most

of the experimental studies on spin-wave dynamics in ASI systems focused on global measurement. The simulation studies suggest that the local area response of the spin-wave spectra should differ from the global response. As a result, the current focus is shifting towards the local measurement of spin-wave dynamics in such a structure to demonstrate the correlation between the local magnetic microstates and the spin-wave spectra.

1.4 Three Dimensional Magnetic Nanostructures

Over the last few years, the research of 3D magnetic nanostructure has been gaining a huge momentum due to the revelation of a flurry of novel phenomena such as curvature induced anisotropy and DMI like spin texture [217,218], frustration in 3D ASI systems [219,220], 3D magnonic crystals [218,221], noncollinear spin textures such as twisted skyrmion [222], magnetic singularities, e.g. Bloch points [223,224], hopfions [225] and vortex domain walls [226] as well as its potential in future applications such as magnetic sensors [227], neuromorphic computing [97], ultra-dense data storage devices [228,229] and 2.5D spintronic devices [230]. The primary roadblocks to the study of 3D magnetic nanostructures have been the lack of standard tools for fabrication, characterization and numerical study. However, some of the 2D fabrication techniques such as physical vapour deposition (PVD), chemical vapour deposition (CVD) has been pushed for 3D magnetic structure fabrication. In a broad sense, the fabrication techniques can be categorized into three different subgroups, such as (a) combination of thin film deposition with some 3D structure fabrication or other mechanisms (strain engineering), (b) chemical synthesis and self-assembly methods and (c) 3D nano-printing or focused electron beam ion deposition (FEBID).

PVD and CVD techniques are majorly used to fabricate most of the 2D nano-patterns and thin films. The CVD has been used to deposit ferromagnetic layers on deep etched trenches and membranes [231-233] which resemble 3D-like nanostructures. PVD can be used to fabricate 3D magnetic structures by depositing materials on a pre-designed 3D skeleton [234]. This frame can be fabricated by using two-photon lithography (TPL). TPL is a powerful tool for the fabrication of 3D structures. For TPL, a femtosecond pulsed laser beam is focused on a polymer, which only interacts with the focused area without disturbing the neighbouring region which enables its ability to write a pattern inside a photoresist, leading to the fabrication of the 3D structure.

The characterization of the Co layer on buckyball [234] polymer 3D structure designed by TPL was studied by using ptychographic x-ray tomography. Helical 3D magnetic micromachines [235] were fabricated using TPL and e-beam evaporation. These structures can be useful for localized drug delivery. May *et al.* have demonstrated a large area 3D frustrated magnetic diamond lattice of connected Py nanowires by using TPL and e-beam evaporation [236]. Furthermore, free-standing nanoscale cobalt tetrapod structures [237] have been fabricated by using a combination of TPL and electrodeposition techniques. The curved magnetic structures can be fabricated by deposition of magnetic materials [238,239] on self-assembled spherical nonmagnetic nanoparticles. The multi-layered curved surfaces such as nanotubes [240] can be fabricated by using rolled up technology by strain engineering and self-assembled methods. Also, the self-assembly of colloidal particles [241,242] has been explored to fabricate 3D nanostructures.

FEBID is a direct writing nano-lithographic technique called as '3D nano printing' technique with the ability to fabricate 3D structures with dimensions of tens of nanometres within few seconds to few minutes. Recent advancement of the FEBID technique makes it capable of growing polycrystalline magnetic metals and alloys [243] and promotes it as a powerful and flexible technique for free form 3D complex-magnetic structure fabrication. One of the major drawbacks of the FEBID technique is the contamination of deposited material with oxygen and carbon. A 90% purity cobalt stricture has been achieved using the FEBID technique [244,245]. The MOKE loops obtained from FEBID fabricated cobalt nanowire with diameter 100 ±25 nm and length 4-12 μm [244] demonstrated high optical quality samples obtained from this technique. The purity of other magnetic materials [246-248] was tried to be improved by some additional processes such as thermal annealing. In the meantime, the combination of FEBID [249] with sputtered deposition [234] and thermal evaporation [250] has emerged as an alternative technique to fabricate 3D magnetic nanostructures by avoiding the bottleneck of material fabrication.

Initially, chemical synthesis techniques were commonly used in 3D nanostructure fabrication. The materials were deposited through the pores of pre-designed nano-templates such as anodic alumina templates, block-copolymer templates, track-etched polycarbonate (PCTE) and other self-assembly methods. 3D interconnected NiCo nanowire's structure [251] was fabricated by using PCTE membranes and

electrodeposition technique. However, this technique lacks the flexibility to design arbitrary shaped complex 3D nanostructure fabrication.

Simulation guided fabrication of 3D nanostructures [117] can also be used in desired 3D magnetic structure fabrication. However, large area fabrication of magnetostatically coupled and uncoupled 3D nanostructure with high material purity [252] requires new techniques and strategies of fabrication for a systematic understanding of magnetism in the third dimension. So far, the hybrid fabrication techniques which are combinations of 3D nanopatterning such as FEBID [249], TPL [253-256] with thin film deposition such as sputtering [234], electrodeposition [237] and thermal evaporation [220,250] have emerged as powerful ways to fabricate 3D complex magnetic nanostructures.

Some efforts have been made in the experimental and numerical studies of 3D magnetic nanostructure to explore its intriguing novel functionalities. Micromagnetic simulations revealed the Bloch-point vortex domain-wall [257] in a nanowire. Later, the Bloch-point in Py nanowire was experimentally observed and propagation of domain wall through such structure has been studied [223,224]. The current induced motion of topologically defective structure has been reported in [258]. Also, 3D nanomagnetic logic devices based on magnetic coupling between Fe nanopillar and nanowire [259], nanomagneto-mechanical actuators based cobalt nanorods [260] have been demonstrated. The domain wall motion in a magnetic ratchet [229] have been studied which is a promising candidate for future storage and logic devices. Recently, the theoretically predicated curvature induced DMI [261] has been demonstrated experimentally [217]. The evolution of vortex domain wall in a 3D micron sized disc was studied [226], which showed interesting spin texture in the 3D. The grown FeCo magnetic structures [262] have been proposed for 3D ASI. Magnetic monopole frustration and its propagation in a 3D ASI structure have been demonstrated recently [263]. These intriguing characteristics of 3D nanostructure have influenced the theoretical and experimental explorations of spin-wave dynamics. Some theoretical studies have been reported but there are very few experimental (most on quasi 3D structure) studies that can be found in literature as reported so far.

Theoretical studies of spin-wave properties in 3D magnetic structure have been performed by using different numerical methods such as the plane wave method (PWM) [59,221,264-267], linear combination of atomic orbitals [268] and micromagnetic simulations [221,269] The 3D structures have been studied in systems of ferromagnetic spheres arranged in sites of a simple cubic (SC) [59,264,267,268], body centred cubic

(BCC) [264], face centred cubic (FCC) [264,266] and hexagonal close-packed (HCP) [265,268] crystallographic structures, embedded in a matrix [59,264-267] of ferromagnetic materials. Numerically calculated band structures of 3D magnonic crystal were first reported in [59]. The dipolar interaction affects the bandwidth [264] and spin relaxation [268] in these structures. The magnonic band gaps were found to be sensitive to exchange and magnetization contrast in between magnetic materials of sphere and matrix. The bandgap opening occurred above a critical value of magnetization contrast (even without exchange contrast) depending on the lattice type. The exchange contrast also played an important role in magnonic bandgap opening, but it needed very large values for the opening of the bandgap in the absence of magnetization contrast. The normalized band gap varied almost linearly with both the contrasts. The band gaps also depended on lattice symmetry and scattering centre shape. Among the cubic lattice, the FCC structure showed the highest bandgap. A systematic study of ferromagnetic material combination effect on band gap in HCP lattice was reported in reference [265]. The highest band gap was found for Ni spheres embedded in the Fe matrix. The PWM calculations of 3D magnonic crystals have been extended for magnetoferritin based 3D magnonic crystals. In these calculations, inter-particle space was filled by ferromagnetic material. The introduction of ferromagnetic material ignited the magnonic band gap opening in these systems. The FCC lattice produced by self-assembled magnetoferritin nanoparticles is suitable for a magnonic band gap system. The damping of spin-wave in a homogeneous medium is independent of the direction of spin-wave propagation. This scenario changed for magnonic crystals. The damping has been considered in PWM calculations for spin waves in 3D magnonic crystals in reference [267]. The anisotropic nature and wave vector dependence of damping can be tuned by changing the magnetic material and filling fraction of magnonic crystals. Recently, the meander like structures, interconnected film segments placed at 90° to each other of YIG, fabricated on a pre-patterned substrate has been proposed for 3D magnonic crystals [221,269]. Spin-wave propagation and dispersion for isolated and coupled 3D magnonic crystals were studied by using the finite element method, micromagnetic simulation and transfer matrix method. The bandgap of Damon-Eshbach (DE) mode increased with the increment of the width of the groove. For the coupled case, the dispersion curve splits into two, symmetric and anti-symmetric modes. The calculation of spin-wave dispersion was extended for volume magnetostatic surface wave [221]. The dispersion curves become narrower with

the increment of groove width, which means volume waves can propagate with small wavenumbers. Both the volume modes can coexist in this magnonic crystal system. These mender shaped structures of single layer [270] and multilayers [271] have been studied experimentally. It was observed that the spin-wave band structures were controllable by varying geometrical parameters of the films. They claimed this structure as a 3D magnonic waveguide. The microwave response of self-assembled magnetoferritin nanoparticles [272] arranged in 3D FCC arrays and self-assembled rolled up multilayer nanowire [240] were also reported. Below the blocking temperature of nanoparticles, the linewidth of ferromagnetic resonance was broadened [272] due to the misalignment of crystal lattices of individual nanoparticles with respect to each other. The azimuthally quantized spin-wave mode was observed in multilayer nanowire [240] which was tailored by nanowire's radius and the number of layers. So far, the experimental dynamics in 3D like thin film structure, multilayer nanowire and magnetoferritin structure have been reported. The probing of spin-wave dynamics in a 3D lithographically grown structure is still in its infancy due to its high roughness, which is inevitable in 3D structures, besides the lack of measurement techniques. However, the spin-wave dynamics of vertically or tilted grown 3D nano and microstructures will be interesting to explore due to its rich static phenomena as well as for its basic understanding. Available spin-wave dynamics measurement techniques such as Brillouin light scattering (BLS), MOKE magnetometer and FMR can be useful to explore spin-wave dynamics in such structures.

1.5 Objective of the Thesis

The research work of the thesis is primarily based on the experimental study of spin-wave dynamics of thin film heterostructure of HM/FM/Oxide, different classes of 2D magnonic crystals and 3D magnetic nanostructures with the aid of TRMOKE magnetometer, TRMOKE microscopy and conventional BLS technique. The experimental studies are accompanied by numerical calculation and/or theoretical modelling. Broadly the studied systems can be categorized as follows:

i) 2D magnonic crystals in the form CNDs array: The role of nanochannels on spin-wave dynamics of CNDs with varying filling factors has been investigated.

ii) 2D magnonic crystals in form of square ASI: The influence of magnetic microstates on spin-wave characteristics and the interaction between an optically excited surface acoustic wave (SAW) with magnons have been studied.

iii) 3D magnetic nanostructures: The precessional magnetization dynamics in 3D cobalt tetrapod structure has been studied to explore spin-wave behaviour in a complex 3D structure. The evolution of spin-wave behaviour in a connected nanowire network forming a 3D ASI structure has also been studied.

iv) HM/FM heterostructures: The modulation of effective Gilbert damping parameter due to damping-like torque via SHE in Ta(t)/CoFeB(3nm)/SiO_2(2nm) heterostructure with varying Ta thickness (3-20 nm) has been studied.

References

[1] W. Gilbert, De Magnete (Dover Publications, 2013).
[2] S. J. Blundell, Magnetism: A Very Short Introduction (OUP Oxford, 2012).
[3] Maxwell JC (1865) A Dynamical Theory of the Electromagnetic Field. Philos Trans R Soc Lond 155:459–512.
[4] P. Langevin, Magnétisme et Théorie des Électrons; Ann. chim. et phys.**,** 203 (1905).
[5] P. Weiss, L'hypothèse du champ Moléculaire et la Propriété Ferromagnétique; J. Phys. Theor. Appl. **6,** 661 (1907).
[6] A. Einstein, Zur Elektrodynamik Bewegter Körper; Annalen der physik **4** (1905).
[7] J. M. D. Coey, Magnetism and Magnetic Materials (Cambridge University Press, 2010).
[8] W. Heisenberg, Mehrkörperproblem und Resonanz in der Quantenmechanik; Z. Phys. **38,** 411 (1926).
[9] W. Gerlach and O. Stern, Das magnetische Moment des Silberatoms; Z. Phys. **9,** 353 (1922).
[10] G. E. Uhlenbeck and S. Goudsmit, Spinning Electrons and the Structure of Spectra; Nature **117,** 264 (1926).
[11] P. A. M. Dirac and R. H. Fowler, The Quantum Theory of the Electron; Proceedings of the Royal Society of London. Series A, Containing Papers of a Mathematical and Physical Character **117,** 610 (1928).
[12] L. Néel, Anisotropie Magnétique Superficielle et Surstructures D'orientation; J. Phys. Radium **15,** 225 (1954).
[13] N. Taniguchi, "On the Basic Concept of 'Nano-Technology'," Proc. Intl. Conf. Prod. Eng. Tokyo, Part II, Japan Society of Precision Engineering, 1974.
[14] R. Skomski, Nanomagnetics; J. Phys.: Condens. Matter **15,** R841 (2003).
[15] S. D. Bader, Colloquium: Opportunities in Nanomagnetism; Rev. Mod. Phys. **78,** 1 (2006).
[16] M. N. Baibich, J. M. Broto, A. Fert, F. N. Van Dau, F. Petroff, P. Etienne, G. Creuzet, A. Friederich, and J. Chazelas, Giant Magnetoresistance of (001)Fe/(001)Cr Magnetic Superlattices; Phys. Rev. Lett. **61,** 2472 (1988).
[17] G. Binasch, P. Grünberg, F. Saurenbach, and W. Zinn, Enhanced Magnetoresistance in Layered Magnetic Structures with Antiferromagnetic Interlayer Exchange; Phys. Rev. B **39,** 4828 (1989).
[18] S. S. P. Parkin, C. Kaiser, A. Panchula, P. M. Rice, B. Hughes, M. Samant, and S.-H. Yang, Giant Tunnelling Magnetoresistance at Room Temperature with MgO (100) Tunnel Barriers; Nat. Mater. **3,** 862 (2004).
[19] J. C. Slonczewski, Current-driven Excitation of Magnetic Multilayers; J. Magn. Magn. Mater. **159,** L1 (1996).
[20] K. Yakushiji, T. Saruya, H. Kubota, A. Fukushima, T. Nagahama, S. Yuasa, and K. Ando, Ultrathin Co/Pt and Co/Pd Superlattice Films for MgO-based Perpendicular Magnetic Tunnel Junctions; Appl. Phys. Lett. **97,** 232508 (2010).
[21] Y. Huai, Spin-transfer Torque MRAM (STT-MRAM): Challenges and Prospects; AAPPS bulletin **18,** 33 (2008).
[22] W. S. Zhao, Y. Zhang, T. Devolder, J. O. Klein, D. Ravelosona, C. Chappert, and P. Mazoyer, Failure and Reliability Analysis of STT-MRAM; Microelectron. Reliab. **52,** 1848 (2012).
[23] G. Dresselhaus, Spin-Orbit Coupling Effects in Zinc Blende Structures; Phys. Rev. **100,** 580 (1955).
[24] I. M. Miron, T. Moore, H. Szambolics, L. D. Buda-Prejbeanu, S. Auffret, B. Rodmacq, S. Pizzini, J. Vogel, M. Bonfim, A. Schuhl, and G. Gaudin, Fast Current-induced Domain-wall Motion Controlled by the Rashba effect; Nat. Mater. **10,** 419 (2011).
[25] M. I. Dyakonov and V. I. Perel, Current-induced Spin Orientation of Electrons in Semiconductors; Phys. Lett. A **35,** 459 (1971).
[26] L. Liu, O. J. Lee, T. J. Gudmundsen, D. C. Ralph, and R. A. Buhrman, Current-Induced Spin waveitching of Perpendicularly Magnetized Magnetic Layers Using Spin Torque from the Spin Hall Effect; Phys. Rev. Lett. **109,** 096602 (2012).

[27] K.-S. Lee, S.-W. Lee, B.-C. Min, and K.-J. Lee, Threshold Current for Switching of a Perpendicular Magnetic Layer Induced by Spin Hall Effect; Appl. Phys. Lett. **102,** 112410 (2013).
[28] Y. K. Kato, R. C. Myers, A. C. Gossard, and D. D. Awschalom, Observation of the Spin Hall Effect in Semiconductors; Science **306,** 1910 (2004).
[29] Y. Fan, P. Upadhyaya, X. Kou, M. Lang, S. Takei, Z. Wang, J. Tang, L. He, L.-T. Chang, M. Montazeri, G. Yu, W. Jiang, T. Nie, R. N. Schwartz, Y. Tserkovnyak, and K. L. Wang, Magnetization Switching through Giant Spin–orbit Torque in a Magnetically Doped Topological Insulator Heterostructure; Nat. Mater. **13,** 699 (2014).
[30] M. Kimata, H. Chen, K. Kondou, S. Sugimoto, P. K. Muduli, M. Ikhlas, Y. Omori, T. Tomita, A. H. MacDonald, S. Nakatsuji, and Y. Otani, Magnetic and Magnetic Inverse Spin Hall Effects in a Non-collinear Antiferromagnet; Nature **565,** 627 (2019).
[31] J. Cho, N.-H. Kim, S. Lee, J.-S. Kim, R. Lavrijsen, A. Solignac, Y. Yin, D.-S. Han, N. J. J. Van Hoof, and H. J. M. Sweagten, Thickness Dependence of the Interfacial Dzyaloshinskii–Moriya Interaction in Inversion Symmetry Broken Systems; Nat. Commun. **6,** 1 (2015).
[32] P. F. Carcia, Perpendicular Magnetic Anisotropy in Pd/Co and Pt/Co Thin-Film Layered Structures; J. Appl. Phys. **63,** 5066 (1988).
[33] Y. Tserkovnyak, A. Brataas, and G. E. W. Bauer, Spin Pumping and Magnetization Dynamics in Metallic Multilayers; Phys. Rev. B **66,** 224403 (2002).
[34] E. Saitoh, M. Ueda, H. Miyajima, and G. Tatara, Conversion of Spin Current into Charge Current at Room Temperature: Inverse Spin-Hall Effect; Appl. Phys. Lett. **88,** 182509 (2006).
[35] W. Zhang, M. B. Jungfleisch, W. Jiang, J. Sklenar, F. Y. Fradin, J. E. Pearson, J. B. Ketterson, and A. Hoffmann, Spin Pumping and Inverse Spin Hall Effects—Insights for Future Spin-Orbitronics; J. Appl. Phys. **117,** 172610 (2015).
[36] G. E. W. Bauer, E. Saitoh, and B. J. van Wees, Spin Caloritronics; Nat. Mater. **11,** 391 (2012).
[37] A. V. Chumak, V. I. Vasyuchka, A. A. Serga, and B. Hillebrands, Magnon Spintronics; Nat. Phys. **11,** 453 (2015).
[38] A. Hoffmann and S. D. Bader, Opportunities at the Frontiers of Spintronics; Phys. Rev. Appl. **4,** 047001 (2015).
[39] M. Matsuo, E. Saitoh, and S. Maekawa, Spin-Mechatronics; J. Phys. Soc. Jpn. **86,** 011011 (2017).
[40] I. Žutić, J. Fabian, and S. D. Sarma, Spintronics: Fundamentals and applications; Rev. Mod. Phys. **76,** 323 (2004).
[41] S. A. Nikitov, P. Tailhades, and C. S. Tsai, Spin Waves in Periodic Magnetic Structures—Magnonic Crystals; J. Magn. Magn. Mater. **236,** 320 (2001).
[42] H. Kosaka, T. Kawashima, A. Tomita, M. Notomi, T. Tamamura, T. Sato, and S. Kawakami, Superprism Phenomena in Photonic Crystals; Phys. Rev. B **58,** R10096 (1998).
[43] F. Bloch, Zur Theorie des Ferromagnetismus; Z. Phys. **61,** 206 (1930).
[44] S.-K. Kim, S. Choi, K.-S. Lee, D.-S. Han, D.-E. Jung, and Y.-S. Choi, Negative Refraction of Dipole-Exchange Spin Waves through a Magnetic Twin Interface in Restricted Geometry; Appl. Phys. Lett. **92,** 212501 (2008).
[45] F. Goedsche, Reflection and Refraction of Spin Waves; Phys. Status Solidi B **39,** K29 (1970).
[46] J. R. Eshbach, Spin-Wave Propagation and the Magnetoelastic Interaction in Yttrium Iron Garnet; Phys. Rev. Lett. **8,** 357 (1962).
[47] Z. Liu, F. Giesen, X. Zhu, R. D. Sydora, and M. R. Freeman, Spin Wave Dynamics and the Determination of Intrinsic Damping in Locally Excited Permalloy Thin Films; Phys. Rev. Lett. **98,** 087201 (2007).
[48] S. Choi, K.-S. Lee, and S.-K. Kim, Spin-wave Interference; Appl. Phys. Lett. **89,** 062501 (2006).
[49] S. O. Demokritov, A. A. Serga, A. André, V. E. Demidov, M. P. Kostylev, B. Hillebrands, and A. N. Slavin, Tunneling of Dipolar Spin Waves through a Region of Inhomogeneous Magnetic Field; Phys. Rev. Lett. **93,** 047201 (2004).
[50] V. Vlaminck and M. Bailleul, Current-Induced Spin-Wave Doppler Shift; Science **322,** 410 (2008).

[51] S. Mansfeld, J. Topp, K. Martens, J. N. Toedt, W. Hansen, D. Heitmann, and S. Mendach, Spin Wave Diffraction and Perfect Imaging of a Grating; Phys. Rev. Lett. **108,** 047204 (2012).
[52] A. Barman, G. Gubbiotti, S. Ladak, A. O. Adeyeye, M. Krawczyk, J. Gräfe, C. Adelmann, S. Cotofana, A. Naeemi, V. I. Vasyuchka, B. Hillebrands, S. A. Nikitov, H. Yu, D. Grundler, A. V. Sadovnikov, A. A. Grachev, S. E. Sheshukova, J. Y. Duquesne, M. Marangolo, G. Csaba, W. Porod, V. E. Demidov, S. Urazhdin, S. O. Demokritov, E. Albisetti, D. Petti, R. Bertacco, H. Schultheiss, V. V. Kruglyak, V. D. Poimanov, S. Sahoo, J. Sinha, H. Yang, M. Münzenberg, T. Moriyama, S. Mizukami, P. Landeros, R. A. Gallardo, G. Carlotti, J. V. Kim, R. L. Stamps, R. E. Camley, B. Rana, Y. Otani, W. Yu, T. Yu, G. E. W. Bauer, C. Back, G. S. Uhrig, O. V. Dobrovolskiy, B. Budinska, H. Qin, S. van Dijken, A. V. Chumak, A. Khitun, D. E. Nikonov, I. A. Young, B. W. Zingsem, and M. Winklhofer, The 2021 Magnonics Roadmap; J. Phys.: Condens. Matter **33,** 413001 (2021).
[53] G. Gubbiotti, S. Tacchi, G. Carlotti, N. Singh, S. Goolaup, A. O. Adeyeye, and M. Kostylev, Collective Spin Modes in Monodimensional Magnonic Crystals Consisting of Dipolarly Coupled Nanowires; Appl. Phys. Lett. **90,** 092503 (2007).
[54] M. P. Kostylev, A. A. Stashkevich, and N. A. Sergeeva, Collective Magnetostatic Modes on a One-Dimensional Array of Ferromagnetic Stripes; Phys. Rev. B **69,** 064408 (2004).
[55] J. Topp, D. Heitmann, M. P. Kostylev, and D. Grundler, Making a Reconfigurable Artificial Crystal by Ordering Bistable Magnetic Nanowires; Phys. Rev. Lett. **104,** 207205 (2010).
[56] B. Rana, D. Kumar, S. Barman, S. Pal, Y. Fukuma, Y. Otani, and A. Barman, Detection of Picosecond Magnetization Dynamics of 50 nm Magnetic Dots down to the Single Dot Regime; ACS Nano **5,** 9559 (2011).
[57] O. N. Martyanov, V. F. Yudanov, R. N. Lee, S. A. Nepijko, H. J. Elmers, R. Hertel, C. M. Schneider, and G. Schönhense, Ferromagnetic Resonance Study of Thin Film Antidot Arrays: Experiment and Micromagnetic Simulations; Phys. Rev. B **75,** 174429 (2007).
[58] S. Choudhury, S. Saha, R. Mandal, S. Barman, Y. Otani, and A. Barman, Shape- and Interface-Induced Control of Spin Dynamics of Two-Dimensional Bicomponent Magnonic Crystals; ACS Appl. Mater. Interfaces **8,** 18339 (2016).
[59] M. Krawczyk and H. Puszkarski, Magnonic Excitations versus Three-Dimensional Structural Periodicity in Magnetic Composites; Cryst. Res. Technol. **41,** 547 (2006).
[60] V. E. Demidov, S. O. Demokritov, K. Rott, P. Krzysteczko, and G. Reiss, Nano-Optics with Spin Waves at Microwave Frequencies; Appl. Phys. Lett. **92,** 232503 (2008).
[61] D. Kumar, P. Sabareesan, W. Wang, H. Fangohr, and A. Barman, Effect of Hole Shape on Spin-Wave Band Structure in One-Dimensional Magnonic Antidot Waveguide; J. Appl. Phys. **114,** 023910 (2013).
[62] V. V. Kruglyak, A. Barman, R. J. Hicken, J. R. Childress, and J. A. Katine, Precessional Dynamics in Microarrays of Nanomagnets; J. Appl. Phys. **97,** 10A706 (2005).
[63] V. V. Kruglyak, P. S. Keatley, R. J. Hicken, J. R. Childress, and J. A. Katine, Dynamic Configurational Anisotropy in Nanomagnets; Phys. Rev. B **75,** 024407 (2007).
[64] K. Adhikari, S. Barman, R. Mandal, Y. Otani, and A. Barman, Tunable Angle-Dependent Magnetization Dynamics in $Ni_{80}Fe_{20}$ Nanocross Structures of Varying Size; Phys. Rev. Appl. **10,** 044010 (2018).
[65] K. Adhikari, S. Sahoo, A. K. Mondal, Y. Otani, and A. Barman, Large Nonlinear Ferromagnetic Resonance Shift and Strong Magnon-Magnon Coupling in $Ni_{80}fe_{20}$ Nanocross Array; Phys. Rev. B **101,** 054406 (2020).
[66] X. Zhu, M. Malac, Z. Liu, H. Qian, V. Metlushko, and M. R. Freeman, Broadband Spin Dynamics of Permalloy Rings in the Circulation State; Appl. Phys. Lett. **86,** 262502 (2005).
[67] U. Ebels, J. L. Duvail, P. E. Wigen, L. Piraux, L. D. Buda, and K. Ounadjela, Ferromagnetic Resonance Studies of Ni Nanowire Arrays; Phys. Rev. B **64,** 144421 (2001).
[68] S. Saha, S. Barman, Y. Otani, and A. Barman, All-Optical Investigation of Tunable Picosecond Magnetization Dynamics in Ferromagnetic Nanostripes with a Width down to 50 Nm; Nanoscale **7,** 18312 (2015).

[69] C. Banerjee, S. Saha, S. Barman, O. Rousseau, Y. Otani, and A. Barman, Width Dependent Transition of Quantized Spin-Wave Modes in $Ni_{80}Fe_{20}$ Square Nanorings; J. Appl. Phys. **116,** 163912 (2014).
[70] S. Pal, S. Saha, M. V. Kamalakar, and A. Barman, Field-Dependent Spin Waves in High-Aspect-Ratio Single-Crystal Ferromagnetic Nanowires; Nano Res. **9,** 1426 (2016).
[71] J. M. Shaw, T. J. Silva, M. L. Schneider, and R. D. McMichael, Spin Dynamics and Mode Structure in Nanomagnet Arrays: Effects of Size and Thickness on Linewidth and Damping; Phys. Rev. B **79,** 184404 (2009).
[72] R. Mandal, P. Laha, K. Das, S. Saha, S. Barman, A. K. Raychaudhuri, and A. Barman, Effects of Antidot Shape on the Spin Wave Spectra of Two-Dimensional $Ni_{80}Fe_{20}$ Antidot Lattices; Appl. Phys. Lett. **103,** 262410 (2013).
[73] B. K. Mahato, B. Rana, D. Kumar, S. Barman, S. Sugimoto, Y. Otani, and A. Barman, Tunable Spin Wave Dynamics in Two-Dimensional $Ni_{80}Fe_{20}$ Nanodot Lattices by Varying Dot Shape; Appl. Phys. Lett. **105,** 012406 (2014).
[74] R. Mandal, S. Saha, D. Kumar, S. Barman, S. Pal, K. Das, A. K. Raychaudhuri, Y. Fukuma, Y. Otani, and A. Barman, Optically Induced Tunable Magnetization Dynamics in Nanoscale Co Antidot Lattices; ACS Nano **6,** 3397 (2012).
[75] S. Saha, R. Mandal, S. Barman, D. Kumar, B. Rana, Y. Fukuma, S. Sugimoto, Y. Otani, and A. Barman, Tunable Magnonic Spectra in Two-Dimensional Magnonic Crystals with Variable Lattice Symmetry; Adv. Funct. Mater. **23,** 2378 (2013).
[76] R. Mandal, S. Barman, S. Saha, Y. Otani, and A. Barman, Tunable Spin Wave Spectra in Two-Dimensional $Ni_{80}fe_{20}$ Antidot Lattices with Varying Lattice Symmetry; J. Appl. Phys. **118,** 053910 (2015).
[77] S. Pan, S. Mondal, M. Zelent, R. Szwierz, S. Pal, O. Hellwig, M. Krawczyk, and A. Barman, Edge Localization of Spin Waves in Antidot Multilayers with Perpendicular Magnetic Anisotropy; Phys. Rev. B **101,** 014403 (2020).
[78] N. N. Phuoc, S. L. Lim, F. Xu, Y. G. Ma, and C. K. Ong, Enhancement of Exchange Bias and Ferromagnetic Resonance Frequency by using Multilayer Antidot Arrays; J. Appl. Phys. **104,** 093708 (2008).
[79] S. Neusser, B. Botters, and D. Grundler, Localization, Confinement, and Field-Controlled Propagation of Spin Waves in $Ni_{80}Fe_{20}$ Antidot Lattices; Phys. Rev. B **78,** 054406 (2008).
[80] S. Neusser, G. Duerr, H. G. Bauer, S. Tacchi, M. Madami, G. Woltersdorf, G. Gubbiotti, C. H. Back, and D. Grundler, Anisotropic Propagation and Damping of Spin Waves in a Nanopatterned Antidot Lattice; Phys. Rev. Lett. **105,** 067208 (2010).
[81] S. Tacchi, B. Botters, M. Madami, J. W. Kłos, M. L. Sokolovskyy, M. Krawczyk, G. Gubbiotti, G. Carlotti, A. O. Adeyeye, S. Neusser, and D. Grundler, Mode Conversion from Quantized to Propagating Spin Waves in a Rhombic Antidot Lattice Supporting Spin Wave Nanochannels; Phys. Rev. B **86,** 014417 (2012).
[82] K. Vogt, F. Y. Fradin, J. E. Pearson, T. Sebastian, S. D. Bader, B. Hillebrands, A. Hoffmann, and H. Schultheiss, Realization of a Spin-Wave Multiplexer; Nat. Commun. **5,** 3727 (2014).
[83] M. P. Kostylev, A. A. Serga, T. Schneider, B. Leven, and B. Hillebrands, Spin-Wave Logical Gates; Appl. Phys. Lett. **87,** 153501 (2005).
[84] H. Yu, G. Duerr, R. Huber, M. Bahr, T. Schwarze, F. Brandl, and D. Grundler, Omnidirectional Spin-Wave Nanograting Coupler; Nat. Commun. **4,** 2702 (2013).
[85] J. W. Kłos, D. Kumar, J. Romero-Vivas, H. Fangohr, M. Franchin, M. Krawczyk, and A. Barman, Effect of Magnetization Pinning on the Spectrum of Spin Waves in Magnonic Antidot Waveguides; Phys. Rev. B **86,** 184433 (2012).
[86] J. W. Kłos, D. Kumar, M. Krawczyk, and A. Barman, Magnonic Band Engineering by Intrinsic and Extrinsic Mirror Symmetry Breaking in Antidot Spin-Wave Waveguides; Sci. Rep. **3,** 2444 (2013).
[87] Y. Au, M. Dvornik, O. Dmytriiev, and V. V. Kruglyak, Nanoscale Spin Wave Valve and Phase Shifter; Appl. Phys. Lett. **100,** 172408 (2012).

[88] Q. Wang, P. Pirro, R. Verba, A. Slavin, B. Hillebrands, and A. V. Chumak, Reconfigurable Nanoscale Spin-Wave Directional Coupler; Sci. Adv. **4,** e1701517 (2018).
[89] M. A. Abeed and S. Bandyopadhyay, Experimental Demonstration of an Extreme Subwavelength Nanomagnetic Acoustic Antenna Actuated by Spin–Orbit Torque from a Heavy Metal Nanostrip; Adv. Mater. Technol. **5,** 1901076 (2020).
[90] J. Holanda, D. S. Maior, A. Azevedo, and S. M. Rezende, Detecting the Phonon Spin in Magnon–Phonon Conversion Experiments; Nat. Phys. **14,** 500 (2018).
[91] Y. Tabuchi, S. Ishino, T. Ishikawa, R. Yamazaki, K. Usami, and Y. Nakamura, Hybridizing Ferromagnetic Magnons and Microwave Photons in the Quantum Limit; Phys. Rev. Lett. **113,** 083603 (2014).
[92] D. Zhang, X.-Q. Luo, Y.-P. Wang, T.-F. Li, and J. Q. You, Observation of the Exceptional Point in Cavity Magnon-Polaritons; Nat. Commun. **8,** 1368 (2017).
[93] X. Zhang, C.-L. Zou, N. Zhu, F. Marquardt, L. Jiang, and H. X. Tang, Magnon Dark Modes and Gradient Memory; Nat. Commun. **6,** 8914 (2015).
[94] O. V. Dobrovolskiy, R. Sachser, T. Brächer, T. Böttcher, V. V. Kruglyak, R. V. Vovk, V. A. Shklovskij, M. Huth, B. Hillebrands, and A. V. Chumak, Magnon–Fluxon Interaction in a Ferromagnet/Superconductor Heterostructure; Nat. Phys. **15,** 477 (2019).
[95] Q. Wang, M. Kewenig, M. Schneider, R. Verba, F. Kohl, B. Heinz, M. Geilen, M. Mohseni, B. Lägel, F. Ciubotaru, C. Adelmann, C. Dubs, S. D. Cotofana, O. V. Dobrovolskiy, T. Brächer, P. Pirro, and A. V. Chumak, A Magnonic Directional Coupler for Integrated Magnonic Half-Adders; Nat. Electron. **3,** 765 (2020).
[96] A. Mahmoud, F. Ciubotaru, F. Vanderveken, A. V. Chumak, S. Hamdioui, C. Adelmann, and S. Cotofana, Introduction to Spin Wave Computing; J. Appl. Phys. **128,** 161101 (2020).
[97] J. Torrejon, M. Riou, F. A. Araujo, S. Tsunegi, G. Khalsa, D. Querlioz, P. Bortolotti, V. Cros, K. Yakushiji, A. Fukushima, H. Kubota, S. Yuasa, M. D. Stiles, and J. Grollier, Neuromorphic Computing with Nanoscale Spintronic Oscillators; Nature **547,** 428 (2017).
[98] D. Lachance-Quirion, S. P. Wolski, Y. Tabuchi, S. Kono, K. Usami, and Y. Nakamura, Entanglement-Based Single-Shot Detection of a Single Magnon with a Superconducting Qubit; Science **367,** 425 (2020).
[99] P. F. Carcia, A. D. Meinhaldt, and A. Suna, Perpendicular Magnetic Anisotropy in Pd/Co Thin Film Layered Structures; Appl. Phys. Lett. **47,** 178 (1985).
[100] S. Ikeda, K. Miura, H. Yamamoto, K. Mizunuma, H. D. Gan, M. Endo, S. Kanai, J. Hayakawa, F. Matsukura, and H. Ohno, A Perpendicular-Anisotropy CoFeB–Mgo Magnetic Tunnel Junction; Nat. Mater. **9,** 721 (2010).
[101] G.-G. An, J.-B. Lee, S.-M. Yang, J.-H. Kim, W.-S. Chung, and J.-P. Hong, Highly Stable Perpendicular Magnetic Anisotropies of CoFeB/MgO Frames Employing W Buffer and Capping Layers; Acta Mater. **87,** 259 (2015).
[102] T. Liu, Y. Zhang, J. W. Cai, and H. Y. Pan, Thermally Robust Mo/CoFeB/MgO Trilayers with Strong Perpendicular Magnetic Anisotropy; Sci. Rep. **4,** 5895 (2014).
[103] T. Liu, J. W. Cai, and L. Sun, Large Enhanced Perpendicular Magnetic Anisotropy in CoFeB/MgO System with the Typical Ta Buffer Replaced by an Hf Layer; AIP Adv. **2,** 032151 (2012).
[104] M. Gottwald, J. J. Kan, K. Lee, X. Zhu, C. Park, and S. H. Kang, Scalable and Thermally Robust Perpendicular Magnetic Tunnel Junctions for STT-MRAM; Appl. Phys. Lett. **106,** 032413 (2015).
[105] K. Yakushiji, H. Kubota, A. Fukushima, and S. Yuasa, Perpendicular Magnetic Tunnel Junctions with Strong Antiferromagnetic Interlayer Exchange Coupling at First Oscillation Peak; Appl. Phys. Express **8,** 083003 (2015).
[106] I. Dzyaloshinsky, A Thermodynamic Theory of "Weak" Ferromagnetism of Antiferromagnetics; J. Phys. Chem. Solids **4,** 241 (1958).
[107] T. Moriya, Anisotropic Superexchange Interaction and Weak Ferromagnetism; Phys. Rev. **120,** 91 (1960).
[108] X. Z. Yu, Y. Onose, N. Kanazawa, J. H. Park, J. H. Han, Y. Matsui, N. Nagaosa, and Y. Tokura, Real-Space Observation of a Two-Dimensional Skyrmion Crystal; Nature **465,** 901 (2010).

[109] K. Di, V. L. Zhang, H. S. Lim, S. C. Ng, M. H. Kuok, J. Yu, J. Yoon, X. Qiu, and H. Yang, Direct Observation of the Dzyaloshinskii-Moriya Interaction in a Pt/Co/Ni Film; Phys. Rev. Lett. **114,** 047201 (2015).
[110] K. Di, V. L. Zhang, H. S. Lim, S. C. Ng, M. H. Kuok, X. Qiu, and H. Yang, Asymmetric Spin-Wave Dispersion due to Dzyaloshinskii-Moriya Interaction in an Ultrathin Pt/CoFeB Film; Appl. Phys. Lett. **106,** 052403 (2015).
[111] J. Cho, N.-H. Kim, S. Lee, J.-S. Kim, R. Lavrijsen, A. Solignac, Y. Yin, D.-S. Han, N. J. J. van Hoof, H. J. M. Sweagten, B. Koopmans, and C.-Y. You, Thickness Dependence of the Interfacial Dzyaloshinskii–Moriya Interaction in Inversion Symmetry Broken Systems; Nat. Commun. **6,** 7635 (2015).
[112] A. K. Chaurasiya, C. Banerjee, S. Pan, S. Sahoo, S. Choudhury, J. Sinha, and A. Barman, Direct Observation of Interfacial Dzyaloshinskii-Moriya Interaction from Asymmetric Spin-wave Propagation in W/CoFeB/SiO_2 Heterostructures Down to Sub-nanometer CoFeB Thickness; Sci. Rep. **6,** 32592 (2016).
[113] A. K. Chaurasiya, S. Choudhury, J. Sinha, and A. Barman, Dependence of Interfacial Dzyaloshinskii-Moriya Interaction on Layer Thicknesses in Ta/CoFeB/TaOx Heterostructures from Brillouin Light Scattering; Phys. Rev. Appl. **9,** 014008 (2018).
[114] S. Tacchi, R. E. Troncoso, M. Ahlberg, G. Gubbiotti, M. Madami, J. Åkerman, and P. Landeros, Interfacial Dzyaloshinskii-Moriya Interaction in Pt/CoFeB Films: Effect of the Heavy-Metal Thickness; Phys. Rev. Lett. **118,** 147201 (2017).
[115] H. T. Nembach, J. M. Shaw, M. Weiler, E. Jué, and T. J. Silva, Linear Relation between Heisenberg Exchange and Interfacial Dzyaloshinskii–Moriya Interaction in Metal Films; Nat. Phys. **11,** 825 (2015).
[116] X. Ma, G. Yu, C. Tang, X. Li, C. He, J. Shi, K. L. Wang, and X. Li, Interfacial Dzyaloshinskii-Moriya Interaction: Effect of 5d Band Filling and Correlation with Spin Mixing Conductance; Phys. Rev. Lett. **120,** 157204 (2018).
[117] J. D. Fowlkes, R. Winkler, B. B. Lewis, M. G. Stanford, H. Plank, and P. D. Rack, Simulation-Guided 3D Nanomanufacturing via Focused Electron Beam Induced Deposition; ACS Nano **10,** 6163 (2016).
[118] J. Torrejon, J. Kim, J. Sinha, S. Mitani, M. Hayashi, M. Yamanouchi, and H. Ohno, Interface Control of the Magnetic Chirality in CoFeB/MgO Heterostructures with Heavy-Metal Underlayers; Nat. Commun. **5,** 4655 (2014).
[119] I. Gross, L. J. Martínez, J. P. Tetienne, T. Hingant, J. F. Roch, K. Garcia, R. Soucaille, J. P. Adam, J. V. Kim, S. Rohart, A. Thiaville, J. Torrejon, M. Hayashi, and V. Jacques, Direct Measurement of Interfacial Dzyaloshinskii-Moriya Interaction in X\CoFeB\tMgO Heterostructures with a Scanning NV Magnetometer (X=Ta,TaN, W); Phys. Rev. B **94,** 064413 (2016).
[120] S.-G. Je, D.-H. Kim, S.-C. Yoo, B.-C. Min, K.-J. Lee, and S.-B. Choe, Asymmetric Magnetic Domain-Wall Motion by the Dzyaloshinskii-Moriya Interaction; Phys. Rev. B **88,** 214401 (2013).
[121] H. Yang, O. Boulle, V. Cros, A. Fert, and M. Chshiev, Controlling Dzyaloshinskii-Moriya Interaction via Chirality Dependent Atomic-Layer Stacking, Insulator Capping and Electric Field; Sci. Rep. **8,** 12356 (2018).
[122] S. Jaiswal, K. Litzius, I. Lemesh, F. Büttner, S. Finizio, J. Raabe, M. Weigand, K. Lee, J. Langer, B. Ocker, G. Jakob, G. S. D. Beach, and M. Kläui, Investigation of the Dzyaloshinskii-Moriya Interaction and Room Temperature Skyrmions in W/CoFeB/MgO Thin Films and Microwires; Appl. Phys. Lett. **111,** 022409 (2017).
[123] S. Husain, N. Sisodia, A. K. Chaurasiya, A. Kumar, J. P. Singh, B. S. Yadav, S. Akansel, K. H. Chae, A. Barman, P. K. Muduli, P. Svedlindh, and S. Chaudhary, Observation of Skyrmions at Room Temperature in Co_2FeAl Heusler Alloy Ultrathin Film Heterostructures; Sci. Rep. **9,** 1085 (2019).
[124] F. Büttner, I. Lemesh, M. Schneider, B. Pfau, C. M. Günther, P. Hessing, J. Geilhufe, L. Caretta, D. Engel, B. Krüger, J. Viefhaus, S. Eisebitt, and G. S. D. Beach, Field-Free Deterministic Ultrafast Creation of Magnetic Skyrmions by Spin–Orbit Torques; Nat. Nanotechnol. **12,** 1040 (2017).
[125] X. Zhang, J. Xia, Y. Zhou, D. Wang, X. Liu, W. Zhao, and M. Ezawa, Control and Manipulation of a Magnetic Skyrmionium in Nanostructures; Phys. Rev. B **94,** 094420 (2016).

[126] X. Zhang, Y. Zhou, and M. Ezawa, Magnetic Bilayer-Skyrmions without Skyrmion Hall Effect; Nat. Commun. **7,** 10293 (2016).
[127] S. Mizukami, Y. Ando, and T. Miyazaki, Effect of Spin Diffusion on Gilbert Damping for a Very Thin Permalloy Layer in Cu/Permalloy/Cu/Pt Films; Phys. Rev. B **66,** 104413 (2002).
[128] B. Heinrich, Y. Tserkovnyak, G. Woltersdorf, A. Brataas, R. Urban, and G. E. W. Bauer, Dynamic Exchange Coupling in Magnetic Bilayers; Phys. Rev. Lett. **90,** 187601 (2003).
[129] S. N. Panda, S. Mondal, J. Sinha, S. Choudhury, and A. Barman, All-Optical Detection of Interfacial Spin Transparency from Spin Pumping in β-Ta/Cofeb Thin Films; Sci. Adv. **5,** eaav7200 (2019).
[130] S. N. Panda, S. Majumder, A. Bhattacharyya, S. Dutta, S. Choudhury, and A. Barman, Structural Phase-Dependent Giant Interfacial Spin Transparency in W/CoFeB Thin-Film Heterostructures; ACS Appl. Mater. Interfaces **13,** 20875 (2021).
[131] J. C. Rojas-Sánchez, N. Reyren, P. Laczkowski, W. Savero, J. P. Attané, C. Deranlot, M. Jamet, J. M. George, L. Vila, and H. Jaffrès, Spin Pumping and Inverse Spin Hall Effect in Platinum: The Essential Role of Spin-Memory Loss at Metallic Interfaces; Phys. Rev. Lett. **112,** 106602 (2014).
[132] C. T. Boone, H. T. Nembach, J. M. Shaw, and T. J. Silva, Spin Transport Parameters in Metallic Multilayers Determined by Ferromagnetic Resonance Measurements of Spin-Pumping; J. Appl. Phys. **113,** 153906 (2013).
[133] A. Brataas, Y. Tserkovnyak, G. E. W. Bauer, and B. I. Halperin, Spin Battery Operated by Ferromagnetic Resonance; Phys. Rev. B **66,** 060404 (2002).
[134] M. Morota, Y. Niimi, K. Ohnishi, D. H. Wei, T. Tanaka, H. Kontani, T. Kimura, and Y. Otani, Indication of Intrinsic Spin Hall Effect in 4d and 5d Transition Metals; Phys. Rev. B **83,** 174405 (2011).
[135] C.-F. Pai, L. Liu, Y. Li, H. W. Tseng, D. C. Ralph, and R. A. Buhrman, Spin Transfer Torque Devices Utilizing the Giant Spin Hall Effect of Tungsten; Appl. Phys. Lett. **101,** 122404 (2012).
[136] L. Liu, C.-F. Pai, Y. Li, H. W. Tseng, D. C. Ralph, and R. A. Buhrman, Spin-Torque Switching with the Giant Spin Hall Effect of Tantalum; Science **336,** 555 (2012).
[137] A. Ganguly, K. Kondou, H. Sukegawa, S. Mitani, S. Kasai, Y. Niimi, Y. Otani, and A. Barman, Thickness Dependence of Spin Torque Ferromagnetic Resonance in $Co_{75}Fe_{25}$/Pt Bilayer Films; Appl. Phys. Lett. **104,** 072405 (2014).
[138] A. Ganguly, R. M. Rowan-Robinson, A. Haldar, S. Jaisweal, J. Sinha, A. T. Hindmarch, D. A. Atkinson, and A. Barman, Time-Domain Detection of Current Controlled Magnetization Damping in Pt/$Ni_{81}Fe_{19}$ Bilayer and Determination of Pt Spin Hall Angle; Appl. Phys. Lett. **105,** 112409 (2014).
[139] E. Sagasta, Y. Omori, S. Vélez, R. Llopis, C. Tollan, A. Chuvilin, L. E. Hueso, M. Gradhand, Y. Otani, and F. Casanova, Unveiling the Mechanisms of yhe Spin Hall Effect in Ta; Phys. Rev. B **98,** 060410 (2018).
[140] S. Mondal, S. Choudhury, N. Jha, A. Ganguly, J. Sinha, and A. Barman, All-Optical Detection Of the Spin Hall Angle in W/CoFeB/SiO_2 Heterostructures with Varying Thickness of the Tungsten Layer; Phys. Rev. B **96,** 054414 (2017).
[141] F. J. Jedema, A. T. Filip, and B. J. van Wees, Electrical Spin Injection and Accumulation at Room Temperature in an All-Metal Mesoscopic Spin Valve; Nature **410,** 345 (2001).
[142] L. K. Werake and H. Zhao, Observation of Second-Harmonic Generation Induced by Pure Spin Currents; Nat. Phys. **6,** 875 (2010).
[143] M. Montazeri, P. Upadhyaya, M. C. Onbasli, G. Yu, K. L. Wong, M. Lang, Y. Fan, X. Li, P. Khalili Amiri, R. N. Schwartz, C. A. Ross, and K. L. Wang, Magneto-Optical Investigation of Spin–Orbit Torques in Metallic and Insulating Magnetic Heterostructures; Nat. Commun. **6,** 8958 (2015).
[144] J. D. Joannopoulos, S. G. Johnson, J. N. Winn, R. D. Meade, Photonic Crystals – Molding the Flow of Light, 2nd Edn, Princeton University Press, Princeton/Oxford, US/UK (2008).
[145] D. Weiss, K. Richter, A. Menschig, R. Bergmann, H. Schweizer, K. von Klitzing, and G. Weimann, Quantized Periodic Orbits in Large Antidot Arrays; Phys. Rev. Lett. **70,** 4118 (1993).
[146] R. P. Cowburn, A. O. Adeyeye, and J. A. C. Bland, Magnetic Domain Formation in Lithographically Defined Antidot Permalloy Arrays; Appl. Phys. Lett. **70,** 2309 (1997).

[147] S. Wirth, A. Anane, and S. von Molnár, Thermally Activated Magnetization Reversal in Nanometer-Size Iron Particles; Phys. Rev. B **63,** 012402 (2000).
[148] D. H. Y. Tse, S. J. Steinmuller, T. Trypiniotis, D. Anderson, G. A. C. Jones, J. A. C. Bland, and C. H. W. Barnes, Static and Dynamic Magnetic Properties of $Ni_{80}Fe_{20}$ Square Antidot Arrays; Phys. Rev. B **79,** 054426 (2009).
[149] C. Yu, M. J. Pechan, and G. J. Mankey, Dipolar Induced, Spatially Localized Resonance in Magnetic Antidot Arrays; Appl. Phys. Lett. **83,** 3948 (2003).
[150] S. Tacchi, M. Madami, G. Gubbiotti, G. Carlotti, A. O. Adeyeye, S. Neusser, B. Botters, and D. Grundler, Magnetic Normal Modes in Squared Antidot Array With Circular Holes: A Combined Brillouin Light Scattering and Broadband Ferromagnetic Resonance Study; IEEE Trans. Magn. **46,** 172 (2010).
[151] V. Bhat, J. Woods, L. E. De Long, J. T. Hastings, V. V. Metlushko, K. Rivkin, O. Heinonen, J. Sklenar, and J. B. Ketterson, Broad-Band FMR Study of Ferromagnetic Thin Films Patterned with Antidot Lattices; Physica C: Superconductivity **479,** 83 (2012).
[152] A. Barman, Control of Magnonic Spectra in Cobalt Nanohole Arrays: the Effects of Density, Symmetry and Defects; J. Phys. D: Appl. Phys. **43,** 195002 (2010).
[153] R. Zivieri and L. Giovannini, Metamaterial Properties of Ferromagnetic Antidot Lattices; Metamaterials **6,** e127 (2012).
[154] D. Kumar, J. W. Kłos, M. Krawczyk, and A. Barman, Magnonic Band Structure, Complete Bandgap, and Collective Spin Wave Excitation in Nanoscale Two-Dimensional Magnonic Crystals; J. Appl. Phys. **115,** 043917 (2014).
[155] Q. Wang, Z. Zhong, L. Jin, X. Tang, F. Bai, H. Zhang, and G. S. D. Beach, Design of Nanostrip Magnonic Crystal Waveguides with a Single Magnonic Band Gap; J. Magn. Magn. Mater. **340,** 23 (2013).
[156] N. G. Deshpande, M. S. Seo, X. R. Jin, S. J. Lee, Y. P. Lee, J. Y. Rhee, and K. W. Kim, Tailoring of Magnetic Properties of Patterned Cobalt Antidots by Simple Manipulation of Lattice Symmetry; Appl. Phys. Lett. **96,** 122503 (2010).
[157] M. J. Pechan, C. Yu, R. L. Compton, J. P. Park, and P. A. Crowell, Direct Measurement of Spatially Localized Ferromagnetic-Resonance Modes in an Antidot Lattice (invited); J. Appl. Phys. **97,** 10J903 (2005).
[158] S. Neusser, B. Botters, M. Becherer, D. Schmitt-Landsiedel, and D. Grundler, Spin-Wave Localization between Nearest and Next-Nearest Neighboring Holes in an Antidot Lattice; Appl. Phys. Lett. **93,** 122501 (2008).
[159] H. Ulrichs, B. Lenk, and M. Münzenberg, Magnonic Spin-Wave Modes in CoFeB Antidot Lattices; Appl. Phys. Lett. **97,** 092506 (2010).
[160] S. Neusser, H. G. Bauer, G. Duerr, R. Huber, S. Mamica, G. Woltersdorf, M. Krawczyk, C. H. Back, and D. Grundler, Tunable Metamaterial Response of a $Ni_{80}Fe_{20}$ Antidot Lattice for Spin Waves; Phys. Rev. B **84,** 184411 (2011).
[161] S. Pal, J. W. Klos, K. Das, O. Hellwig, P. Gruszecki, M. Krawczyk, and A. Barman, Optically Induced Spin Wave Dynamics in $[Co/Pd]_8$ Antidot Lattices with Perpendicular Magnetic Anisotropy; Appl. Phys. Lett. **105,** 162408 (2014).
[162] A. De, S. Mondal, S. Sahoo, S. Barman, Y. Otani, R. K. Mitra, and A. Barman, Field-Controlled Ultrafast Magnetization Dynamics in Two-Dimensional Nanoscale Ferromagnetic Antidot Arrays; Beilstein J. Nanotechnol. **9,** 1123 (2018).
[163] R. Zivieri, S. Tacchi, F. Montoncello, L. Giovannini, F. Nizzoli, M. Madami, G. Gubbiotti, G. Carlotti, S. Neusser, G. Duerr, and D. Grundler, Bragg Diffraction of Spin Waves from a Two-Dimensional Antidot Lattice; Phys. Rev. B **85,** 012403 (2012).
[164] S. Neusser, G. Duerr, S. Tacchi, M. Madami, M. L. Sokolovskyy, G. Gubbiotti, M. Krawczyk, and D. Grundler, Magnonic Minibands in Antidot Lattices with Large Spin-Wave Propagation Velocities; Phys. Rev. B **84,** 094454 (2011).
[165] S. Choudhury, S. Majumder, S. Barman, Y. Otani, and A. Barman, Active Control of Mode Crossover and Mode Hopping of Spin Waves in a Ferromagnetic Antidot Lattice; Phys. Rev. Appl. **10,** 064044 (2018).

[166] N. Porwal, A. De, S. Mondal, K. Dutta, S. Choudhury, J. Sinha, A. Barman, and P. K. Datta, Observation of Angle-Dependent Mode Conversion and Mode Hopping in 2D Annular Antidot Lattice; Sci. Rep. **9,** 12138 (2019).
[167] R. Zivieri, P. Malagò, L. Giovannini, S. Tacchi, G. Gubbiotti, and A. O. Adeyeye, Soft Magnonic Modes in Two-Dimensional Permalloy Antidot Lattices; J. Phys.: Condens. Matter **25,** 336002 (2013).
[168] S. Choudhury, S. Barman, Y. Otani, and A. Barman, Efficient Modulation of Spin Waves in Two-Dimensional Octagonal Magnonic Crystal; ACS Nano **11,** 8814 (2017).
[169] S. Majumder, S. Choudhury, S. Barman, Y. Otani, and A. Barman, Reconfigurable Spin-Wave Dynamics in Two-Dimensional Quasiperiodic Magnonic Crystals; Phys. E: Low-Dimens. Syst. Nanostructures**,** 114901 (2021).
[170] A. De, K. Dutta, S. Mondal, S. Barman, Y. Otani, and A. Barman, Magnonic Crystals with Complex Geometry; Phys. Rev. B **103,** 064402 (2021).
[171] Q. Wang, L. Jin, X. Tang, F. Bai, H. Zhang, and Z. Zhong, Micromagnetic Simulation of the Dynamic Susceptibility Spectra of Antidot Array Films With Two Sublattices; IEEE Trans. Magn. **48,** 3246 (2012).
[172] J. Ding, D. Tripathy, and A. O. Adeyeye, Dynamic Response of Antidot Nanostructures with Alternating Hole Diameters; EPL (Europhysics Letters) **98,** 16004 (2012).
[173] M. Madami, G. Gubbiotti, S. Tacchi, G. Carlotti, and S. Jain, Study of the Spin Excitations in Antidot Lattices with Line Defects; Physica B: Condensed Matter **435,** 152 (2014).
[174] S. Choudhury, S. Barman, Y. Otani, and A. Barman, Controlled Evolution of Spin Waves in Unconventional Defective Honeycomb Antidot Lattices; J. Magn. Magn. Mater. **489,** 165408 (2019).
[175] T. Schwarze and D. Grundler, Magnonic Crystal Wave Guide with Large Spin-Wave Propagation Velocity in CoFeB; Appl. Phys. Lett. **102,** 222412 (2013).
[176] C. Banerjee, S. Choudhury, J. Sinha, and A. Barman, Pseudo-One-Dimensional Magnonic Crystals for High-Frequency Nanoscale Devices; Phys. Rev. Appl. **8,** 014036 (2017).
[177] A. K. Mondal, C. Banerjee, A. Adhikari, A. K. Chaurasiya, S. Choudhury, J. Sinha, S. Barman, and A. Barman, Spin-Texture Driven Reconfigurable Magnonics in Chains of Connected $Ni_{80}Fe_{20}$ Submicron Dots; Phys. Rev. B **101,** 224426 (2020).
[178] L. Pauling, The Structure and Entropy of Ice and of Other Crystals with Some Randomness of Atomic Arrangement; J. Am. Chem. Soc. **57,** 2680 (1935).
[179] W. F. Giauque and M. F. Ashley, Molecular Rotation in Ice at 10°K. Free Energy of Formation and Entropy of Water; Phys. Rev. **43,** 81 (1933).
[180] A. P. Ramirez, Strongly Geometrically Frustrated Magnets; Annu. Rev. Mater. Sci. **24,** 453 (1994).
[181] L. Balents, Spin liquids in frustrated magnets; Nature **464,** 199 (2010).
[182] M. J. Harris, S. T. Bramwell, D. F. McMorrow, T. Zeiske, and K. W. Godfrey, Geometrical Frustration in the Ferromagnetic Pyrochlore $Ho_2Ti_2O_7$; Phys. Rev. Lett. **79,** 2554 (1997).
[183] C. Castelnovo, R. Moessner, and S. L. Sondhi, Magnetic Monopoles in Spin Ice; Nature **451,** 42 (2008).
[184] R. F. Wang, C. Nisoli, R. S. Freitas, J. Li, W. McConville, B. J. Cooley, M. S. Lund, N. Samarth, C. Leighton, V. H. Crespi, and P. Schiffer, Artificial 'Spin Ice' in a Geometrically Frustrated Lattice of Nanoscale Ferromagnetic Islands; Nature **439,** 303 (2006).
[185] M. Tanaka, E. Saitoh, H. Miyajima, T. Yamaoka, and Y. Iye, Magnetic Interactions in a Ferromagnetic Honeycomb Nanoscale Network; Phys. Rev. B **73,** 052411 (2006).
[186] S. Gliga, G. Hrkac, C. Donnelly, J. Büchi, A. Kleibert, J. Cui, A. Farhan, E. Kirk, R. V. Chopdekar, Y. Masaki, N. S. Bingham, A. Scholl, R. L. Stamps, and L. J. Heyderman, Emergent Dynamic Chirality in a Thermally Driven Artificial Spin Ratchet; Nat. Mater. **16,** 1106 (2017).
[187] R. Macêdo, G. M. Macauley, F. S. Nascimento, and R. L. Stamps, Apparent Ferromagnetism in the Pinwheel Artificial Spin Ice; Phys. Rev. B **98,** 014437 (2018).
[188] A. Farhan, C. F. Petersen, S. Dhuey, L. Anghinolfi, Q. H. Qin, M. Saccone, S. Velten, C. Wuth, S. Gliga, P. Mellado, M. J. Alava, A. Scholl, and S. van Dijken, Nanoscale Control of Competing

Interactions and Geometrical Frustration in a Dipolar Trident Lattice; Nat. Commun. **8,** 995 (2017).
[189] I. Gilbert, Y. Lao, I. Carrasquillo, L. O'Brien, J. D. Watts, M. Manno, C. Leighton, A. Scholl, C. Nisoli, and P. Schiffer, Emergent Reduced Dimensionality by Vertex Frustration in Artificial Spin Ice; Nat. Phys. **12,** 162 (2016).
[190] J. Park, B. L. Le, J. Sklenar, G.-W. Chern, J. D. Watts, and P. Schiffer, Magnetic Response of Brickwork Artificial Spin Ice; Phys. Rev. B **96,** 024436 (2017).
[191] Y. Lao, F. Caravelli, M. Sheikh, J. Sklenar, D. Gardeazabal, J. D. Watts, A. M. Albrecht, A. Scholl, K. Dahmen, C. Nisoli, and P. Schiffer, Classical Topological Order in the Kinetics of Artificial Spin Ice; Nat. Phys. **14,** 723 (2018).
[192] J. Lehmann, C. Donnelly, P. M. Derlet, L. J. Heyderman, and M. Fiebig, Poling of an Artificial Magneto-Toroidal Crystal; Nat. Nanotechnol. **14,** 141 (2019).
[193] C. F. Petersen, A. Farhan, S. Dhuey, Z. Chen, M. J. Alava, A. Scholl, and S. van Dijken, Tuning Magnetic Ordering in a Dipolar Square-Kite Tessellation; Appl. Phys. Lett. **112,** 092403 (2018).
[194] J. Sklenar, Y. Lao, A. Albrecht, J. D. Watts, C. Nisoli, G.-W. Chern, and P. Schiffer, Field-Induced Phase Coexistence in an Artificial Spin Ice; Nat. Phys. **15,** 191 (2019).
[195] G.-W. Chern and P. Mellado, Magnetic Monopole Polarons in Artificial Spin Ices; Europhys. Lett. **114,** 37004 (2016).
[196] A. Farhan, A. Scholl, C. F. Petersen, L. Anghinolfi, C. Wuth, S. Dhuey, R. V. Chopdekar, P. Mellado, M. J. Alava, and S. van Dijken, Thermodynamics of Emergent Magnetic Charge Screening in Artificial Spin Ice; Nat. Commun. **7,** 12635 (2016).
[197] B. Farmer, V. S. Bhat, A. Balk, E. Teipel, N. Smith, J. Unguris, D. J. Keavney, J. T. Hastings, and L. E. De Long, Direct Imaging of Coexisting Ordered and Frustrated Sublattices in Artificial Ferromagnetic Quasicrystals; Phys. Rev. B **93,** 134428 (2016).
[198] E. Y. Vedmedenko, H. P. Oepen, and J. Kirschner, Decagonal Quasiferromagnetic Microstructure on the Penrose Tiling; Phys. Rev. Lett. **90,** 137203 (2003).
[199] S. Ladak, D. E. Read, G. K. Perkins, L. F. Cohen, and W. R. Branford, Direct Observation of Magnetic Monopole Defects in an Artificial Spin-Ice System; Nat. Phys. **6,** 359 (2010).
[200] E. Mengotti, L. J. Heyderman, A. F. Rodríguez, F. Nolting, R. V. Hügli, and H.-B. Braun, Real-Space Observation of Emergent Magnetic Monopoles and Associated Dirac Strings in Artificial Kagome Spin Ice; Nat. Phys. **7,** 68 (2011).
[201] J. P. Morgan, A. Stein, S. Langridge, and C. H. Marrows, Thermal Ground-State Ordering and Elementary Excitations in Artificial Magnetic Square Ice; Nat. Phys. **7,** 75 (2011).
[202] A. Westphalen, A. Schumann, A. Remhof, H. Zabel, M. Karolak, B. Baxevanis, E. Y. Vedmedenko, T. Last, U. Kunze, and T. Eimüller, Magnetization Reversal of Microstructured Kagome Lattices; Phys. Rev. B **77,** 174407 (2008).
[203] Z. Budrikis, K. L. Livesey, J. P. Morgan, J. Akerman, A. Stein, S. Langridge, C. H. Marrows, and R. L. Stamps, Domain Dynamics and Fluctuations in Artificial Square Ice at Finite Temperatures; New J. Phys. **14,** 035014 (2012).
[204] S. Gliga, A. Kákay, R. Hertel, and O. G. Heinonen, Spectral Analysis of Topological Defects in an Artificial Spin-Ice Lattice; Phys. Rev. Lett. **110,** 117205 (2013).
[205] J. Sklenar, V. S. Bhat, L. E. DeLong, and J. B. Ketterson, Broadband Ferromagnetic Resonance Studies on an Artificial Square Spin-Ice Island Array; J. Appl. Phys. **113,** 17B530 (2013).
[206] M. B. Jungfleisch, W. Zhang, E. Iacocca, J. Sklenar, J. Ding, W. Jiang, S. Zhang, J. E. Pearson, V. Novosad, J. B. Ketterson, O. Heinonen, and A. Hoffmann, Dynamic Response of an Artificial Square Spin Ice; Phys. Rev. B **93,** 100401 (2016).
[207] V. S. Bhat, F. Heimbach, I. Stasinopoulos, and D. Grundler, Magnetization Dynamics of Topological Defects and the Spin Solid in a Kagome Artificial Spin Ice; Phys. Rev. B **93,** 140401 (2016).
[208] V. S. Bhat, F. Heimbach, I. Stasinopoulos, and D. Grundler, Angular-Dependent Magnetization Dynamics of Kagome Artificial Spin Ice Incorporating Topological Defects; Phys. Rev. B **96,** 014426 (2017).

[209] X. Zhou, G.-L. Chua, N. Singh, and A. O. Adeyeye, Large Area Artificial Spin Ice and Anti-Spin Ice $Ni_{80}Fe_{20}$ Structures: Static and Dynamic Behavior; Adv. Funct. Mater. **26,** 1437 (2016).
[210] T. Dion, D. M. Arroo, K. Yamanoi, T. Kimura, J. C. Gartside, L. F. Cohen, H. Kurebayashi, and W. R. Branford, Tunable Magnetization Dynamics in Artificial Spin Ice via Shape Anisotropy Modification; Phys. Rev. B **100,** 054433 (2019).
[211] D. M. Arroo, J. C. Gartside, and W. R. Branford, Sculpting the Spin-Wave Response of Artificial Spin Ice via Microstate Selection; Phys. Rev. B **100,** 214425 (2019).
[212] A. Ghosh, F. Ma, J. Lourembam, X. Jin, R. Maddu, Q. J. Yap, and S. Ter Lim, Emergent Dynamics of Artificial Spin-Ice Lattice Based on an Ultrathin Ferromagnet; Nano Lett. **20,** 109 (2020).
[213] Y. Li, G. Gubbiotti, F. Casoli, F. J. T. Gonçalves, S. A. Morley, M. C. Rosamond, E. H. Linfield, C. H. Marrows, S. McVitie, and R. L. Stamps, Brillouin Light Scattering Study of Magnetic-Element Normal Modes in a Square Artificial Spin Ice Geometry; J. Phys. D: Appl. Phys. **50,** 015003 (2016).
[214] S. Mamica, X. Zhou, A. Adeyeye, M. Krawczyk, and G. Gubbiotti, Spin-Wave Dynamics in Artificial Anti-Spin-Ice Systems: Experimental and Theoretical Investigations; Phys. Rev. B **98,** 054405 (2018).
[215] E. Iacocca, S. Gliga, R. L. Stamps, and O. Heinonen, Reconfigurable Wave Band Structure of an Artificial Square Ice; Phys. Rev. B **93,** 134420 (2016).
[216] A. K. Chaurasiya, A. K. Mondal, J. C. Gartside, K. D. Stenning, A. Vanstone, S. Barman, W. R. Branford, and A. Barman, Comparison of Spin-Wave Modes in Connected and Disconnected Artificial Spin Ice Nanostructures Using Brillouin Light Scattering Spectroscopy; ACS Nano **15,** 11734 (2021).
[217] O. M. Volkov, A. Kákay, F. Kronast, I. Mönch, M.-A. Mawass, J. Fassbender, and D. Makarov, Experimental Observation of Exchange-Driven Chiral Effects in Curvilinear Magnetism; Phys. Rev. Lett. **123,** 077201 (2019).
[218] A. Korniienko, V. Kravchuk, O. Pylypovskyi, D. Sheka, J. van den Brink, and Y. Gaididei, Curvature Induced Magnonic Crystal in Nanowires; SciPost Physics **7,** 035 (2019).
[219] A. A. Mistonov, N. A. Grigoryeva, A. V. Chumakova, H. Eckerlebe, N. A. Sapoletova, K. S. Napolskii, A. A. Eliseev, D. Menzel, and S. V. Grigoriev, Three-Dimensional Artificial Spin Ice in Nanostructured Co on an Inverse Opal-Like Lattice; Phys. Rev. B **87,** 220408 (2013).
[220] A. May, M. Hunt, A. Van Den Berg, A. Hejazi, and S. Ladak, Realisation of a Frustrated 3D Magnetic Nanowire Lattice; Commun. Phys. **2,** 13 (2019).
[221] P. A. Popov, A. Y. Sharaevskaya, E. N. Beginin, A. V. Sadovnikov, A. I. Stognij, D. V. Kalyabin, and S. A. Nikitov, Spin Wave Propagation in Three-Dimensional Magnonic Crystals and Coupled Structures; J. Magn. Magn. Mater. **476,** 423 (2019).
[222] C. Jin, C. Zhang, C. Song, J. Wang, H. Xia, Y. Ma, J. Wang, Y. Wei, J. Wang, and Q. Liu, Current-Induced Motion of Twisted Skyrmions; Appl. Phys. Lett. **114,** 192401 (2019).
[223] S. Da Col, S. Jamet, N. Rougemaille, A. Locatelli, T. O. Mentes, B. S. Burgos, R. Afid, M. Darques, L. Cagnon, J. C. Toussaint, and O. Fruchart, Observation of Bloch-Point Domain Walls in Cylindrical Magnetic Nanowires; Phys. Rev. B **89,** 180405 (2014).
[224] M. Schöbitz, A. De Riz, S. Martin, S. Bochmann, C. Thirion, J. Vogel, M. Foerster, L. Aballe, T. O. Menteş, A. Locatelli, F. Genuzio, S. Le-Denmat, L. Cagnon, J. C. Toussaint, D. Gusakova, J. Bachmann, and O. Fruchart, Fast Domain Wall Motion Governed by Topology and OErsted Fields in Cylindrical Magnetic Nanowires; Phys. Rev. Lett. **123,** 217201 (2019).
[225] J.-S. B. Tai and I. I. Smalyukh, Static Hopf Solitons and Knotted Emergent Fields in Solid-State Noncentrosymmetric Magnetic Nanostructures; Phys. Rev. Lett. **121,** 187201 (2018).
[226] C. Donnelly, S. Finizio, S. Gliga, M. Holler, A. Hrabec, M. Odstrčil, S. Mayr, V. Scagnoli, L. J. Heyderman, M. Guizar-Sicairos, and J. Raabe, Time-Resolved Imaging of Three-Dimensional Nanoscale Magnetization Dynamics; Nat. Nanotechnol. **15,** 356 (2020).
[227] C. Xu, X. Wu, G. Huang, and Y. Mei, Rolled-up Nanotechnology: Materials Issue and Geometry Capability; Adv. Mater. Technol. **4,** 1800486 (2019).
[228] S. S. P. Parkin, M. Hayashi, and L. Thomas, Magnetic Domain-Wall Racetrack Memory; Science **320,** 190 (2008).

[229] C. Bran, E. Berganza, J. A. Fernandez-Roldan, E. M. Palmero, J. Meier, E. Calle, M. Jaafar, M. Foerster, L. Aballe, A. Fraile Rodriguez, R. P. del Real, A. Asenjo, O. Chubykalo-Fesenko, and M. Vazquez, Magnetization Ratchet in Cylindrical Nanowires; ACS Nano **12,** 5932 (2018).
[230] A. Fernández-Pacheco, R. Streubel, O. Fruchart, R. Hertel, P. Fischer, and R. P. Cowburn, Three-Dimensional Nanomagnetism; Nat. Commun. **8,** 15756 (2017).
[231] B. S. Lim, A. Rahtu, and R. G. Gordon, Atomic Layer Deposition of Transition Metals; Nat. Mater. **2,** 749 (2003).
[232] M. Daub, M. Knez, U. Goesele, and K. Nielsch, Ferromagnetic Nanotubes by Atomic Layer Deposition in Anodic Alumina Membranes; J. Appl. Phys. **101,** 09J111 (2007).
[233] J. Bachmann, Jing, M. Knez, S. Barth, H. Shen, S. Mathur, U. Gösele, and K. Nielsch, Ordered Iron Oxide Nanotube Arrays of Controlled Geometry and Tunable Magnetism by Atomic Layer Deposition; J. Am. Chem. Soc. **129,** 9554 (2007).
[234] C. Donnelly, M. Guizar-Sicairos, V. Scagnoli, M. Holler, T. Huthwelker, A. Menzel, I. Vartiainen, E. Müller, E. Kirk, S. Gliga, J. Raabe, and L. J. Heyderman, Element-Specific X-Ray Phase Tomography of 3D Structures at the Nanoscale; Phys. Rev. Lett. **114,** 115501 (2015).
[235] S. Tottori, L. Zhang, F. Qiu, K. K. Krawczyk, A. Franco-Obregón, and B. J. Nelson, Magnetic Helical Micromachines: Fabrication, Controlled Swimming, and Cargo Transport; Adv. Mater. **24,** 811 (2012).
[236] A. May, M. Hunt, A. Van Den Berg, A. Hejazi, and S. Ladak, Realisation of a Frustrated 3D Magnetic Nanowire Lattice; Commun. Phys. **2,** 13 (2019).
[237] G. Williams, M. Hunt, B. Boehm, A. May, M. Taverne, D. Ho, S. Giblin, D. Read, J. Rarity, R. Allenspach, and S. Ladak, Two-Photon Lithography for 3D Magnetic Nanostructure Fabrication; Nano Res. **11,** 845 (2018).
[238] M. Albrecht, G. Hu, I. L. Guhr, T. C. Ulbrich, J. Boneberg, P. Leiderer, and G. Schatz, Magnetic Multilayers on Nanospheres; Nat. Mater. **4,** 203 (2005).
[239] R. Streubel, V. P. Kravchuk, D. D. Sheka, D. Makarov, F. Kronast, O. G. Schmidt, and Y. Gaididei, Equilibrium Magnetic States in Individual Hemispherical Permalloy Caps; Appl. Phys. Lett. **101,** 132419 (2012).
[240] F. Balhorn, S. Mansfeld, A. Krohn, J. Topp, W. Hansen, D. Heitmann, and S. Mendach, Spin-Wave Interference in Three-Dimensional Rolled-Up Ferromagnetic Microtubes; Phys. Rev. Lett. **104,** 037205 (2010).
[241] R. Streubel, F. Kronast, U. K. Rößler, O. G. Schmidt, and D. Makarov, Reconfigurable Large-Area Magnetic Vortex Circulation Patterns; Phys. Rev. B **92,** 104431 (2015).
[242] D. Zhou, F. Wang, B. Li, X. Lou, and Y. Han, Glassy Spin Dynamics in Geometrically Frustrated Buckled Colloidal Crystals; Phys. Rev. X. **7,** 021030 (2017).
[243] J. M. De Teresa, A. Fernández-Pacheco, R. Córdoba, L. Serrano-Ramón, S. Sangiao, and M. R. Ibarra, Review of Magnetic Nanostructures Grown by Focused Electron Beam Induced Deposition (FEBID); J. Phys. D: Appl. Phys. **49,** 243003 (2016).
[244] A. Fernández-Pacheco, L. Serrano-Ramón, J. M. Michalik, M. R. Ibarra, J. M. De Teresa, L. O'Brien, D. Petit, J. Lee, and R. P. Cowburn, Three Dimensional Magnetic Nanowires Grown by Focused Electron-Beam Induced Deposition; Sci. Rep. **3,** 1492 (2013).
[245] J. Pablo-Navarro, D. Sanz-Hernández, C. Magén, A. Fernández-Pacheco, and J. M. de Teresa, Tuning Shape, Composition and Magnetization of 3D Cobalt Nanowires Grown by Focused Electron Beam Induced Deposition (FEBID); J. Phys. D: Appl. Phys. **50,** 18LT01 (2017).
[246] J. Pablo-Navarro, C. Magén, and J. M. de Teresa, Purified and Crystalline Three-Dimensional Electron-Beam-Induced Deposits: The Successful Case of Cobalt for High-Performance Magnetic Nanowires; ACS Appl. Nano Mater. **1,** 38 (2018).
[247] M. J. Martínez-Pérez, J. Pablo-Navarro, B. Müller, R. Kleiner, C. Magén, D. Koelle, J. M. de Teresa, and J. Sesé, NanoSQUID Magnetometry on Individual As-grown and Annealed Co Nanowires at Variable Temperature; Nano Lett. **18,** 7674 (2018).
[248] J. Pablo-Navarro, R. Winkler, G. Haberfehlner, C. Magén, H. Plank, and J. M. De Teresa, In Situ Real-Time Annealing of Ultrathin Vertical Fe Nanowires Grown by Focused Electron Beam Induced Deposition; Acta Mater. **174,** 379 (2019).

[249] I. Utke, P. Hoffmann, and J. Melngailis, Gas-Assisted Focused Electron Beam and Ion Beam Processing and Fabrication; J. Vac. Sci. Technol. B: Microelectronics and Nanometer Structures Processing, Measurement, and Phenomena **26,** 1197 (2008).
[250] D. Sanz-Hernández, R. F. Hamans, J.-W. Liao, A. Welbourne, R. Lavrijsen, and A. Fernández-Pacheco, Fabrication, Detection, and Operation of a Three-Dimensional Nanomagnetic Conduit; ACS Nano **11,** 11066 (2017).
[251] T. da Câmara Santa Clara Gomes, J. De La Torre Medina, M. Lemaitre, and L. Piraux, Magnetic and Magnetoresistive Properties of 3D Interconnected NiCo Nanowire Networks; Nanoscale Res. Lett. **11,** 466 (2016).
[252] A. Botman, J. J. L. Mulders, and C. W. Hagen, Creating Pure Nanostructures from Electron-Beam-Induced Deposition Using Purification Techniques: A Technology Perspective; Nanotechnology **20,** 372001 (2009).
[253] S. Maruo, O. Nakamura, and S. Kawata, Three-Dimensional Microfabrication with Two-Photon-Absorbed Photopolymerization; Opt. Lett. **22,** 132 (1997).
[254] R. Thomas, J. Li, S. Ladak, D. Barrow, and P. M. Smowton, In Situ Fabricated 3D Micro-Lenses for Photonic Integrated Circuits; Opt. Express **26,** 13436 (2018).
[255] J. Askey, M. O. Hunt, W. Langbein, and S. Ladak, Use of Two-Photon Lithography with a Negative Resist and Processing to Realise Cylindrical Magnetic Nanowires; Nanomaterials **10** (2020).
[256] M. Hunt, M. Taverne, J. Askey, A. May, A. Van Den Berg, Y.-L. D. Ho, J. Rarity, and S. Ladak, Harnessing Multi-Photon Absorption to Produce Three-Dimensional Magnetic Structures at the Nanoscale; Materials **13** (2020).
[257] C. Andreas, A. Kákay, and R. Hertel, Multiscale and Multimodel Simulation of Bloch-Point Dynamics; Phys. Rev. B **89,** 134403 (2014).
[258] S. Bochmann, D. Döhler, B. Trapp, M. Staňo, O. Fruchart, and J. Bachmann, Preparation and Physical Properties of Soft Magnetic Nickel-Cobalt Three-Segmented Nanowires; J. Appl. Phys. **124,** 163907 (2018).
[259] M. Gavagnin, H. D. Wanzenboeck, S. Wachter, M. M. Shawrav, A. Persson, K. Gunnarsson, P. Svedlindh, M. Stöger-Pollach, and E. Bertagnolli, Free-Standing Magnetic Nanopillars for 3D Nanomagnet Logic; ACS Appl. Mater. Interfaces **6,** 20254 (2014).
[260] P. Vavassori, M. Pancaldi, M. J. Perez-Roldan, A. Chuvilin, and A. Berger, Remote Magnetomechanical Nanoactuation; Small **12,** 1013 (2016).
[261] Y. Gaididei, V. P. Kravchuk, and D. D. Sheka, Curvature Effects in Thin Magnetic Shells; Phys. Rev. Lett. **112,** 257203 (2014).
[262] L. Keller, M. K. I. Al Mamoori, J. Pieper, C. Gspan, I. Stockem, C. Schröder, S. Barth, R. Winkler, H. Plank, M. Pohlit, J. Müller, and M. Huth, Direct-Write of Free-Form Building Blocks for Artificial Magnetic 3D Lattices; Sci. Rep. **8,** 6160 (2018).
[263] A. May, M. Saccone, A. van den Berg, J. Askey, M. Hunt, and S. Ladak, Magnetic Charge Propagation upon a 3D Artificial Spin-Ice; Nat. Commun. **12,** 3217 (2021).
[264] M. Krawczyk and H. Puszkarski, Plane-Wave Theory of Three-Dimensional Magnonic Crystals; Phys. Rev. B **77,** 054437 (2008).
[265] M. Krawczyk, J. Klos, M. L. Sokolovskyy, and S. Mamica, Materials Optimization of the Magnonic Gap in Three-Dimensional Magnonic Crystals with Spheres in Hexagonal Structure; J. Appl. Phys. **108,** 093909 (2010).
[266] S. Mamica, M. Krawczyk, M. L. Sokolovskyy, and J. Romero-Vivas, Large Magnonic Band Gaps and Spectra Evolution in Three-Dimensional Magnonic Crystals Based on Magnetoferritin Nanoparticles; Phys. Rev. B **86,** 144402 (2012).
[267] J. Romero Vivas, S. Mamica, M. Krawczyk, and V. V. Kruglyak, Investigation of Spin Wave Damping in Three-Dimensional Magnonic Crystals Using the Plane Wave Method; Phys. Rev. B **86,** 144417 (2012).
[268] E. Tartakovskaya, W. Kreuzpaintner, and A. Schreyer, Spin Wave Dynamics in Two- and Three-Dimensional Superlattices of Nanosized Ferromagnetic Spheres; J. Appl. Phys. **103,** 023913 (2008).

[269] E. N. Beginin, A. V. Sadovnikov, A. Y. Sharaevskaya, A. I. Stognij, and S. A. Nikitov, Spin Wave Steering in Three-Dimensional Magnonic Networks; Appl. Phys. Lett. **112,** 122404 (2018).
[270] G. Gubbiotti, A. Sadovnikov, E. Beginin, S. Nikitov, D. Wan, A. Gupta, S. Kundu, G. Talmelli, R. Carpenter, I. Asselberghs, I. P. Radu, C. Adelmann, and F. Ciubotaru, Magnonic Band Structure in Vertical Meander-Shaped $Co_{40}Fe_{40}B_{20}$ Thin Films; Phys. Rev. Appl. **15,** 014061 (2021).
[271] G. Gubbiotti, A. Sadovnikov, E. Beginin, S. Sheshukova, S. Nikitov, G. Talmelli, I. Asselberghs, I. P. Radu, C. Adelmann, and F. Ciubotaru, Magnonic Band Structure in CoFeB/Ta/NiFe Meander-Shaped Magnetic Bilayers; Appl. Phys. Lett. **118,** 162405 (2021).
[272] M. Okuda, T. Schwarze, J. C. Eloi, S. E. Ward Jones, P. J. Heard, A. Sarua, E. Ahmad, V. V. Kruglyak, D. Grundler, and W. Schwarzacher, Top-Down Design of Magnonic Crystals from Bottom-up Magnetic Nanoparticles through Protein Arrays; Nanotechnology **28,** 155301 (2017).

Chapter 2

2. Theoretical Background

In a classical electromagnetic picture, magnetism is described by a current carrying loop. Initially, the concept of magnetism was related to the orbital angular momentum of an electron. The findings of magnetism from the s-band electron of a silver atom by Stern-Gerlach [1] gave experimental evidence of the spin degree of freedom. The modern concept of magnetization is based on the spin of the electron and its interaction with the orbital degree of freedom. Depending on the response of a magnetic material to an applied magnetic field, the material can be categorized in diamagnet, paramagnet, ferromagnet, ferrimagnet and antiferromagnet. Among these, ferromagnet and ferrimagnet show spontaneous magnetic behaviour. With the development of quantum mechanical theories, the origin of spontaneous magnetization was described by Heisenberg [2] introducing coupling between neighbouring spins, which is known as Heisenberg's exchange interaction. According to Weiss theory [3], the competition between the exchange interaction and the dipolar interaction (due to free magnetic poles on the surface) leads to the creation of domains in ferromagnets to minimize the free energy. In ferromagnetic nanostructure, besides the exchange and dipolar interaction, the shape also plays an important role in the static and dynamic behaviours of magnetization. This thesis is based on the properties of ferromagnetic thin films and nanostructures, where the above-mentioned interactions play an important role.

In the succeeding paragraphs, an overview of the different energies that influence the dynamics of ferromagnetic nanostructures is given. Subsequently, a description of the magnetization dynamics is given which will be followed by the origin and different ways of manipulating magnetic damping parameter in a ferromagnetic system.

2.1 Different Magnetic Energies

Ferromagnetic systems consist of different energy terms such as Zeeman energy (E_Z), exchange energy (E_{ex}), dipolar energy (E_{dip}), demagnetizing energy (E_{demag}) and anisotropic energy (E_{anis}). The competition between these energies gives rise to interesting static magnetization configurations which, in turn, affect the dynamical properties. The effective energy (E_{eff}) can be written as a sum of all the energies.

$$E_{eff} = E_Z + E_{ex} + E_{dip} + E_{anis} + E_{demag} \quad (2.1)$$

A magnetic system tries to achieve its ground or equilibrium state by minimizing its effective energy at any given condition. A brief discussion of the energy terms is presented below.

2.1.1 Zeeman Energy

In presence of an external magnetic field ($\boldsymbol{H_{ext}}$), the magnetic system experiences a torque that tries to align its magnetization ($\boldsymbol{M}$) along the applied magnetic field direction. This gives rise to an energy term in the magnetic system known as Zeeman energy.

Zeeman energy of a magnetic substance of volume V is given by the equation,

$$E_Z = -\mu_0 \int_0^V \boldsymbol{M} \cdot \boldsymbol{H_{ext}}\, dV \quad (2.2)$$

where μ_0 is magnetic permeability of free space. The parallel configuration of $\boldsymbol{M}$ with $\boldsymbol{H_{ext}}$ archives the minimum energy state.

2.1.2 Exchange Energy

This is a quantum-mechanical short-range magnetic interaction energy which is an outcome of Coulomb interaction and Pauli exclusion principle. The exchange interaction was theorized by Heisenberg based on Heitler-London model for hydrogen atom. It is commonly known as the 'Heisenberg exchange' or isotropic exchange interaction. The magnetic ordering of ferromagnet, ferrimagnet and antiferromagnet systems can be described by this interaction.

The Heisenberg exchange interaction Hamiltonian is given by,

$$H_{ex} = -2 \sum_{i \neq j} J_{ij}\, \boldsymbol{S}_i \cdot \boldsymbol{S}_j \quad (2.3)$$

where $\boldsymbol{S}_i$ and $\boldsymbol{S}_j$ are spin operators of i-th and j-th atoms, respectively, and J_{ij} is the exchange integral between the atoms. For isotropic media J_{ij} becomes site independent, and it can be replaced by J outside the summation. The above Hamiltonian suggests that for parallel spin configuration, i.e., a ferromagnetic ordering $J < 0$ and for antiparallel configuration, i.e., antiferromagnetic ordering $J > 0$. In continuum limit the above equation can be written as:

$$E_{ex} = A \int_0^V (\nabla m)^2\, dV \quad (2.4)$$

where m is the normalized magnetization and A is the exchange stiffness constant. A is related to exchange integral J and is given by, $A = \frac{n_u J S^2}{a}$. Here, a is the lattice constant and n_u is the number of atoms per unit cell of a lattice. For simple cubic (SC), body centre cubic

(BCC) and face centre cubic (FCC) lattices, n_u values are one, two and four, respectively. Exchange interaction is a short-range interaction and the length scale related to it is known as the exchange length (l) which is related to A. For soft magnetic materials, it is given by $l = \sqrt{\frac{2A}{\mu_0 M_S^2}}$. Here M_s is the saturation magnetization of the material. The exchange length plays a crucial role to determine the spin configuration in a confined magnetic structure. Besides direct exchange interaction, there are several types of indirect exchange interactions, such as superexchange interaction [4,5], double exchange interaction [6] and Ruderman-Kittel-Kasuya-Yoshida (RKKY) interaction [7,8]. Superexchange interaction occurs in ionic solids. The non-neighbouring magnetic ions interact via a non-magnetic ion in-between them. Here, two cations interact through a nonmagnetic atom. Depending on the strength of interaction, it can be ferromagnetic or antiferromagnetic. In general, it gives strong antiferromagnetic coupling between magnetic ions. One example is antiferromagnetic ionic solid MnO. Double exchange interaction occurs in some oxides where the magnetic ions exhibit mixed valency. In the mixed valence state, different oxidation states occur which gives rise to a ferromagnetic arrangement. Magnetite (lodestone: Fe_3O_4) is one of the examples of double exchange interaction. RKKY interaction occurs in metals with localized magnetic moment. The exchange is mediated via the valance electrons. This type of exchange possesses long-range coupling, anisotropic and oscillating behaviours. One example is rare earth metals with their localized 4*f* electrons. The asymmetric indirect exchange interaction is known as the Dzyloshinskii-Moriya interaction (DMI) [9,10]. This is known as a three-site exchange interaction where two ferromagnetic atoms interact via a non-magnetic atom. The DMI Hamiltonian is given by, $H_{DM} = -\boldsymbol{D} \cdot (\boldsymbol{S}_i \times \boldsymbol{S}_j)$. Here $\boldsymbol{D}$ is the DMI vector which often leads to canted spin structures by a small angle.

2.1.3 Dipolar Energy

Interaction between two magnetic dipoles gives rise to magnetic dipolar energy. The dipolar energy between two magnetic dipoles with moments $\boldsymbol{m}_1$ and $\boldsymbol{m}_2$ and separated by a vector $\boldsymbol{r}$ term is given by:

$$E_d = \frac{\mu_0}{4\pi r^3}\left[\boldsymbol{m}_1 \cdot \boldsymbol{m}_2 - \frac{3}{r^2}(\boldsymbol{m}_1 \cdot \boldsymbol{r})(\boldsymbol{m}_2 \cdot \boldsymbol{r})\right] \qquad (2.5)$$

where μ_0 is the permeability of free space. The above equation suggests that the energy varies as $1/r^3$ and the energy is minimized for antiparallel configuration between $\boldsymbol{m}_1$ and

$\boldsymbol{m}_2$. This is a long-range interaction, whereas, in the short-range, exchange energy dominates. In ferromagnets, this energy does not contribute to ferromagnetic ordering but plays a crucial role in the formation of domain, demagnetizing field distribution and spin-wave behaviours in long wavelength regime.

2.1.4 Anisotropic Energy

Due to the anisotropy energy magnetization tends to align along some preferred direction which is known as the easy direction of magnetization. On the contrary, the direction along which magnetization is difficult to align is known as the hard direction. The difference between the energy to align magnetization along the hard and easy axis is related to the anisotropy energy of a ferromagnet [11,12]. There are two primary sources of magnetic anisotropy, i.e., the spin-orbit interaction and dipolar interaction. Depending upon the origin, the magnetic anisotropy can be divided into different categories, such as A) magnetocrystalline anisotropy, B) shape or configurational anisotropy, C) volume, surface and interface anisotropy, D) strain-induced anisotropy, E) configurational anisotropy etc. A brief discussion on different anisotropies is given below.

A. Magnetocrystalline Anisotropy

This is an intrinsic magnetic behaviour that mainly originates from two distinct sources, namely, i) single-ion contribution and ii) two ion contributions. The primary source of magnetocrystalline anisotropy is the spin-orbit interaction (SOI) (single-ion contribution) and the secondary source is the dipolar interaction (two ion contributions) among the magnetic dipoles [13]. The single-ion contribution arises from the electrostatic interaction between the orbitals of magnetic electrons with crystal field potential. This interaction tends to align the magnetic moments along a preferred crystallographic direction along with the SOI. Two ion contribution occurs from dipole-dipole interaction. Two different spin configurations of ferromagnetically coupled magnetic moments are shown in Fig. 2.1. The head to tail configuration is energetically favourable and the magnets align along this direction. This contribution is calculated by taking dipole sum over the whole lattices which vanish for certain lattices, including all the cubic lattices. Therefore, this is a source of anisotropic energy in noncubic lattices. The anisotropic exchange can be another source of two-ion contributions. Aforementioned, Heisenberg interaction is ideally isotropic. However, the exchange coupled pairs can have a preferred direction, due to the contribution from SOI in the

higher order corrections. The magnetocrystalline anisotropy energy for a cubic crystal structure (such as iron and nickel) can be written as:

$$E_{cryst} = K_0 + K_1(\alpha_1^2 + \alpha_2^2 + \alpha_3^2) + K_2\alpha_1^2\alpha_2^2\alpha_3^2 + \cdots\cdots \quad (2.6)$$

here, K_i is the i-th magnetocrystalline anisotropy constant, α_i is direction cosine which fulfils the condition: $\alpha_1^2 + \alpha_2^2 + \alpha_3^2 = 1$.

For tetragonal structure:

$$E_{cryst} = K_0 + K_1\alpha_3^2 + K_2\alpha_3^4 + \cdots\cdots \quad (2.7)$$

For hexagonal structure:

$$E_{cryst} = K_0 + K_1(\alpha_1^2 + \alpha_2^2) + K_2(\alpha_1^2 + \alpha_2^2)^2 + \cdots\cdots \quad (2.8)$$

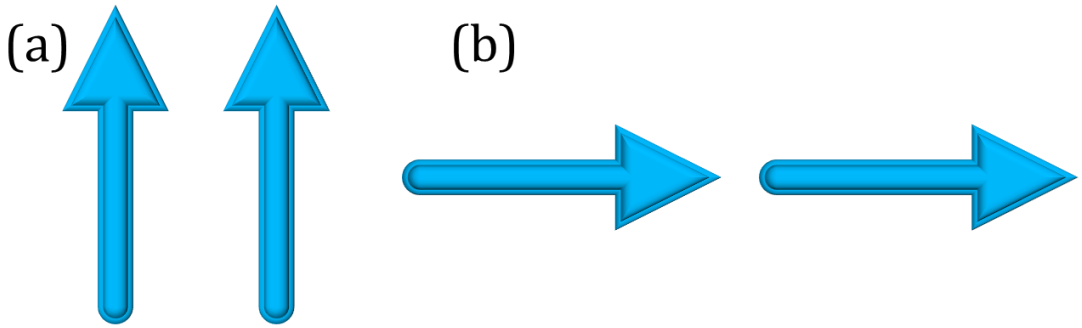

Figure 2. 1. (a) Broadside and (b) head to tail configuration for ferromagnetically coupled magnetic moments. The latter is lower in energy.

B. Shape Anisotropy

When the length scale of a magnetic element is reduced (micro or nanoscale), the shape of the magnetic element plays a crucial role to align its magnetization in a particular direction. Let us consider a polycrystalline ferromagnetic magnetic material (such as permalloy: $Ni_{80}Fe_{20}$), which does not possess any magnetocrystalline anisotropy due to the lack of particular orientations of grains. The isotropic behaviour of such system only holds for a spherical structure. For any other shapes, it might have one or more preferred directions of magnetization. The relationship of magnetic induction ($\boldsymbol{B}$) with the applied magnetic field ($\boldsymbol{H}$) and magnetization ($\boldsymbol{M}$) is $\boldsymbol{B} = \mu_0(\boldsymbol{H} + \boldsymbol{M})$, which is only valid for infinite media. A finite system exhibits free magnetic poles at its surfaces which give rise to the stray magnetic field outside the sample. This stray field gives rise to the demagnetizing field ($\boldsymbol{H}_{dem}$) inside the sample.

The energy corresponding to the stray field is given by:

$$E_{str} = -\frac{1}{2}\int \mu_0 \boldsymbol{M} \cdot \boldsymbol{H}_{dem} dV \quad (2.9)$$

The estimation of $\boldsymbol{H}_{\text{dem}}$ is complicated for arbitrary structure. In case of the homogeneously magnetized ellipsoid, the $\boldsymbol{H}_{\text{dem}}$ is constant as given by:

$$\boldsymbol{H}_{dem} = -N\boldsymbol{M} \quad (2.10)$$

where N is demagnetizing tensor and $Tr(N)$ is 1 (4π) in SI (CGS). Thus, the stray field energy (demagnetizing energy) becomes:

$$E_{str} = \frac{1}{2} V \mu_0 \boldsymbol{M} N \boldsymbol{M} \quad (2.11)$$

where V is the volume of the sample. N strongly depends on sample shape and geometry. Finally, magnetization tries to minimize the stray energy. A non-ellipsoidal shape will be described by an effective demagnetizing factor.

C. Surface and Interface Anisotropies

Broken symmetry in the low dimensional system such as thin films and multilayers, give rise to an effective anisotropy term which contains two contributions, one from volume and one from the surface. The total contribution is given by:

$$K_{eff} = K^V + \frac{2K^S}{t} \quad (2.12)$$

where K^V is the volume related magnetocrystalline anisotropy constant, K^S is the surface-related magnetocrystalline anisotropy constant and t is the thickness of the system. The inverse thickness dependency of K^S suggests its crucial role in the lower thickness of thin films. The factor of two is due to two surfaces of thin films. Below a critical film thickness ($t_c = -\frac{2K^S}{K^V}$) K^S dominates which prefers perpendicular direction of magnetization, known as perpendicular magnetic anisotropy (PMA). PMA can arise from: reduced coordination symmetry, altered electronic structure, localized epitaxial strain at the interface, electronic band structure etc. [14,15].

D. Strain-induced Anisotropy

Magnetic ordering in a crystal can modify its lattice parameters and as a result its volume. This effect is known as magnetostriction. The inverse effect, where applied stress modifies the magnetic property is known as the Villari effect. The key parameter behind the interplay is the magnetoelastic interaction [16-18]. In case of thin films and multilayers, the lattice mismatch between constituent layers gives rise to strain-induced anisotropy [19,20]. The uniaxial stress on ferromagnetic material may cause strain-

induced anisotropy. The elastic energy density for a polycrystalline magnetic material is given by:

$$E_{ms} = -\lambda_S \left(\frac{Y}{2}\right)(3\cos^2\theta - 1)\epsilon + \frac{1}{2}Y\epsilon^2 \quad (2.13)$$

where λ_S is saturation magnetostriction, ϵ is strain, Y is Young's modulus and θ defines the angle between magnetization direction and strain axis. By applying stress, a specific magnetization direction, i.e., uniaxial anisotropy can be induced. The uniaxial anisotropy due to stress is given by:

$$K_U = \frac{3}{2}\lambda_S\sigma \quad (2.14)$$

where σ (= ϵY) is uniaxial stress. Besides the stress, uniaxial anisotropy can be induced by depositions or annealing a disordered alloy in a magnetic field to create some atomic scale texture [21].

E. Configuration Anisotropy

In case of nanomagnetic structure, the competition between exchange and dipolar interaction becomes very critical. Patterning of magnetic structure generally produces non-ellipsoidal elements. In a non-ellipsoidal element, the changes of magnetization from a uniform to a non-uniform state cost huge energy which is known as configurational anisotropy [22,23]. This anisotropy depends on the shape and arrangement of the nanoelements [24,25].

2.2 Magnetization Dynamics

Different magnetization dynamics phenomena occur over a wide range of temporal regimes [26], starting from femtosecond (fs) to picosecond (ps), nanosecond (ns) and microsecond (μs) time scale. The timescales (τ) are estimated from the interaction energies (E) using Heisenberg relation: $\tau = h/E$. The fastest occurring process in fs timescale includes Heisenberg interaction (~ 10 fs), spin-orbit coupling and spin-transfer torque (~10 fs – 1 ps) and pulsed laser-induced ultrafast demagnetization (few hundreds of fs). The magnetization reversal occurs in a few ps to few hundreds of ps. The vortex core switching occurs in few tens of ps to several ns timescale. The precessional magnetization dynamics occurs in few ps to few hundreds of ps and the magnetization damping related to precessional motions occurs in sub ns to tens of ns time. In a ferromagnetic material, the spin-wave propagates in a few hundred ps to tens of ns before getting damped. The domain wall motion occurs within a few ns to hundreds of μs. In this

thesis, the studies are primarily based on precessional magnetization dynamics, damping and corresponding spin-wave modes. A discussion of these phenomena is given below.

2.2.1 Laser Induced Magnetization Dynamics

When a femtosecond laser pulse hits a ferromagnetic sample a sudden drop in its magnetization is observed within a few hundred femtoseconds. This rapid change in magnetization is known as ultrafast demagnetization. The physical origin behind the ultrafast demagnetization is still a topic of intense debate, since its successful demonstration in 1996 by Beaurepaire *et al.* [27]. It was explained by considering a three-temperature model (three thermalized reservoirs for exchanging energy namely, electron, lattice and spin systems). However, this model is not sufficient to describe the microscopic details of this phenomenon. Later on, several thermotical models have been proposed to describe the underlying physical mechanism, such as Elliot-Yafet (EY) scattering [28], Coulomb scattering [29], spin-orbit coupling (SOC) [30], relativistic quantum electrodynamics approach [31], superdiffusive spin transport [32], laser-induced spin flip [33] etc. To date, the microscopic details of ultrafast demagnetization are a topic of debate. Following the ultrafast demagnetization, the system tries to recover its equilibrium state via a remagnetization process. It happens through a fast relaxation process (within few tens of ps) due to the exchange of energy from hot electrons and spins to the lattice which has been phenomenologically described by the three-temperature model [212,221]. Subsequently, there is a slow recovery of magnetization via the diffusion of electron and lattice heat to the surrounding environment [240,241]. In the course of the slow relaxation process, if an external magnetic field is applied along a specific direction, the precessional motion of magnetization can be induced in the system which eventually damps out within a few ns.

2.2.2 Precessional Magnetization Dynamics

In presence of an external magnetic field, the magnetic moments of a ferromagnet align along the field direction. The magnetic moments become parallel to each other in a uniform magnetization configuration. The magnetization of the whole system can be imagined as a giant macrospin or magnetic moment. The combination of the external field with exchange field, dipolar field, anisotropic field and any other fields in a ferromagnet gives an effective field. In the equilibrium state, the magnetization aligns along the effective field. The application of any perturbation such as rf-field, pulsed laser, thermal

energy modifies the effective field term. As a result, the magnetization deviates from the equilibrium position, After the perturbation, the effective field returns to its previous direction and it tries to pull back the magnetization along its direction. As a consequence, it extracts a torque on the magnetization, triggering a precessional motion of magnetization. The precessional motion performs a damped spiral motion with respect to the effective magnetic field. The precessional magnetization dynamics can be described by a phenomenological Landau-Lifshitz-Gilbert (LLG) equation. The LLG equation is a torque equation that was formulated by Landau and Lifshitz in 1935 [34], and later the phenomenological damping term was given by Gilbert [35,36]. In the classical picture, torque (**T**) is given by the rate change of angular momentum ($\boldsymbol{L}$).

$$\mathbf{T} = \frac{d\boldsymbol{L}}{dt} \tag{2.15}$$

The spin degree of freedom is related to spin angular momentum ($\boldsymbol{S}$). So, the above equation can be written as:

$$\mathbf{T} = \frac{d\boldsymbol{S}}{dt} \tag{2.16}$$

The magnetic moment ($\boldsymbol{M}$) is related to the $\boldsymbol{S}$ as $\boldsymbol{M} = -\gamma\boldsymbol{S}$, where γ is the gyromagnetic ratio. The effective magnetic field exerts a torque on $\boldsymbol{M}$ which is given by:

$$\mathbf{T} = \boldsymbol{M} \times \boldsymbol{H}_{eff} \tag{2.17}$$

The effective field term can be written as:

$$\boldsymbol{H}_{eff} = \boldsymbol{H}_{ext} + H_{ex} + \boldsymbol{H}_{demag} + \boldsymbol{H}_{anis} + \boldsymbol{h}(t) \tag{2.18}$$

Where $\boldsymbol{H}_{ext}$ is the external magnetic field, $\boldsymbol{H}_{ex}$ is the exchange field, $\boldsymbol{H}_{demag}$ is the demagnetizing field due to dipolar interactions, $\boldsymbol{H}_{anis}$ is the anisotropic field and $\boldsymbol{h}$(t) is a time-varying magnetic field.

Combining equations (2.16) and (2.17), the torque equation can be written as:

$$\frac{d\boldsymbol{M}}{dt} = -\gamma\left(\boldsymbol{M} \times \boldsymbol{H}_{eff}\right) \tag{2.19}$$

The above equation describes the precessional motion of magnetization without any damping.

In a physical system, the precession cannot exist for an infinite time. It will be damped out after some time. Landau and Lifshitz (LL) modified the torque equation by considering a damping term which is given by:

$$\frac{d\boldsymbol{M}}{dt} = -\gamma\left(\boldsymbol{M} \times \boldsymbol{H}_{eff}\right) - \frac{\lambda}{M_S^2}\boldsymbol{M} \times (\boldsymbol{M} \times \boldsymbol{H}_{eff}) \tag{2.20}$$

where M_S is saturation magnetization and λ is LL damping term with a dimension of sec^{-1}. Gilbert introduced a dimensionless damping parameter (α) and modified the torque term in the LL equation. The equation can be written as:

$$\frac{d\boldsymbol{M}}{dt} = -\gamma\left(\boldsymbol{M} \times \boldsymbol{H}_{eff}\right) + \frac{\alpha}{M_S}\boldsymbol{M} \times \frac{d\boldsymbol{M}}{dt} \tag{2.21}$$

The Gilbert and LL damping parameter are related to each other as $\alpha = \lambda / \gamma M_S$.

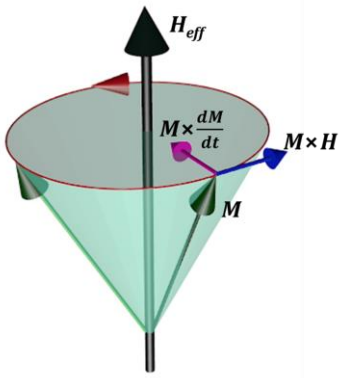

Figure 2. 2. Precessional motion of magnetization ($\boldsymbol{M}$) with respect to effective magnetic field ($\boldsymbol{H}_{eff}$) is shown. Different torque terms of LLG equation are shown.

2.2.3 Spin-wave and Ferromagnetic Resonance

The concept of spin-wave was first introduced by F. Bloch in 1930 [37] to explain the reduction in saturation magnetization with increasing temperature. In the ground state, all the magnetic moments, i.e., spins are parallel to each other. When they are perturbed by external stimuli, a phase difference between two neighbouring spins comes into the picture. In a coupled magnetic system such as ferromagnet, the phase difference propagates as spin-wave. The quanta of spin-wave are known as magnon.

In case of uniform precession, the magnetic moments precess in phase with respect to the external field. As a result, the wavelength (wave vector (k)) becomes nearly infinity (≈ 0). On the other hand, the non-uniform precession can be described as the propagation of a phase difference in the system. It gives a finite wavelength corresponding to finite k. In this thesis, the precessional motion at $k \approx 0$ have been studied which gives rise to the information of uniform spin-wave mode, damping in thin film heterostructures, 2D and 3D confined structure, and different types of standing spin-wave modes in 2D and 3D confined structure. The uniform precessional motion is known as ferromagnetic resonance (FMR). In 1946, Griffiths first observed the FMR in thin films [38]. In 1947, Kittel [39] gave an analytical expression for the spin-wave frequency of FMR or uniform

mode considering the external magnetic field (H_{ext}) and demagnetizing field of the sample. The Kittel equation can be derived from the LLG equation (2.20). For simplicity, the damping part is neglected. For a general ellipsoid with the external bias field along z-direction and $\frac{d\boldsymbol{M_z}}{dt} \approx 0$, the FMR frequency can be written as:

$$f_{FMR} = \frac{\gamma}{2\pi}\sqrt{\left[H_{ext} + \left(N_y - N_z\right)M_S\right]\left[H_{ext} + (N_x - N_z)M_S\right]} \tag{2.22}$$

Where M_S is the saturation magnetization, N_x, N_y and N_z are demagnetizing factors along x-, y- and z-direction, respectively. Depending on the shape of the system the expression of f_{FMR} gets modified. For some basic shapes expression of f_{FMR} is given below:

For a sphere $N_x = N_y = N_z = 4\pi/3$,

$$f_{FMR} = \frac{1}{2\pi}(\gamma H_{ext}) \tag{2.23}$$

For a thin film in x-z plane, $N_x = N_z = 0$ and $N_y = 4\pi$,

$$f_{FMR} = \frac{\gamma}{2\pi}\sqrt{H_{ext}\left[H_{ext} + 4\pi M_S\right]} \tag{2.24}$$

For an infinite circular cylinder with length along z-axis, $N_x = N_z = 2\pi$ and $N_y = 0$

$$f_{FMR} = \frac{\gamma}{2\pi}(H_{ext} + 2\pi M_S) \tag{2.25}$$

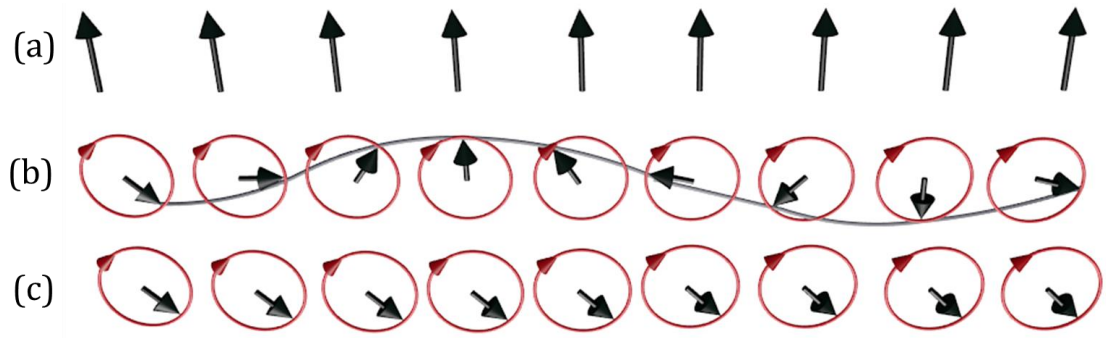

Figure 2. 3. (a) Ground state spin configuration of a ferromagnetic material. (b) Non uniform precessional motion, and (c) uniform precessional motion are shown.

2.3 Damping

Magnetization damping plays a pivotal role to manipulate the precessional dynamics and spin-wave propagation in magnetic thin films and confined structures. Complete control over damping is desirable for future spintronics and magnonic devices [40,41]. Higher damping is required for data storage devices [42] to minimize thermal fluctuations, faster reversal rate and coherent rotation during magnetization reversal. However, lower damping is required for reducing the write current in STT-MRAM devices [43] and long-

distance spin-wave propagation in magnetic nanostructures is a necessity for designing spin-wave based communication devices, where spin-wave acts as information encoder and processor. The damping can be manipulated by different mechanisms, namely, material composition, ion-irradiation, spin pumping, spin current among others. In a magnetic material the coupling between electron spin, electron orbit and lattice are the primary contributors to damping. Damping can originate from intrinsic properties which are inevitable and extrinsic factors that are avoidable. A discussion on the different origins of magnetic damping is given below.

2.3.1 Intrinsic Mechanisms

A. Spin-Orbit Coupling

In a magnetic material, an electron's orbital angular momentum ($\boldsymbol{L}$) and spin angular momentum ($\boldsymbol{S}$) are coupled to each other. Total angular momentum is given by the sum of two momentums: $\boldsymbol{J} = \boldsymbol{L} + \boldsymbol{S}$. In case of ferromagnetic resonance, the spins are excited to a higher energy level and the energy transfer between spin degree and orbital degree occurs. This energy transfer is interrupted by electron-lattice scattering which gives rise to magnetic damping. In 1976, Kambersky [44] proposed a torque correlation model considering intra-band and inter-band transitions to correlate SOC strength (ξ) with damping. The damping is proportional to ξ^2 and ξ^3 in high and low temperatures, respectively.

B. Phonon Drag Mechanism

In 1998, Shul [45] proposed the phonon-drag mechanism for magnetic damping. This mechanism is valid for samples with isotropic magnetization and lattice strain. The phonon drag mechanism contribution to magnetic damping is given by:

$$\alpha_{phonon} = \frac{2n\gamma}{M_S}\left(\frac{B_2(1+\sigma)}{Y}\right)^2 \qquad (2.26)$$

where n is the phonon viscosity, B_2 is the magnetoelastic shear constant, Y is Young's modulus, σ is the Poison ratio, M_s is the saturation magnetization and γ is the gyromagnetic ratio.

C. Eddy Current Mechanism

This mechanism [46] is important for thicker metallic ferromagnetic films with thickness greater than or equal to the skin depth of the microwave field. The magnetization precession induces eddy current in the metallic sample.

The eddy current mechanism contribution to magnetic damping is given by:

$$\alpha_{eddy} = \frac{1}{6} M_S \gamma \left(\frac{4\pi}{c}\right)^2 \sigma_c d^2 \qquad (2.27)$$

where c is the speed of light in vacuum, σ_c is the conductivity of the metal, d is film thickness M_s is saturation magnetization and γ is the gyromagnetic ratio. The d^2 proportionality suggests that the eddy current contribution to magnetic damping for thin films is negligible.

2.3.2 Extrinsic Mechanisms

A. Two Magnon Scattering

In two magnon scattering [47,48], the uniform precessional mode ($k \approx 0$) scatters from inhomogeneous anisotropic or exchange field to two non-uniform precessional modes ($k \neq 0$). Due to the energy conservation, the scattered modes can have the same frequency but the momentum does not conserve due to translational asymmetry. The phase mismatch between the uniform and non-uniform mode leads to dephasing of precessional motion which eventually increases the magnetic damping of the system. The contribution of two magnon scattering increases with an increase in precessional frequency. The number of degenerate magnons increases with increasing frequency which enhances the scattering probability.

B. Magnetic inhomogeneity

In some scenarios [49], the characteristic inhomogeneity field dominates the interaction field which affects the magnetic damping parameter. In case of long wavelength (small k) spin-waves, the damping mainly reflects the large length scale inhomogeneity which is different in nature from two magnon scattering.

2.3.3 Manipulation of Magnetic Damping

In a practical ferromagnetic system, magnetic damping has contributions from intrinsic (α_0) and extrinsic (α_{ext}) sources. The effective damping (α_{eff}) can be written as a sum of both contributions:

$$\alpha_{eff} = \alpha_0 + \alpha_{ext} \qquad (2.28)$$

The static modification of damping includes different phenomena, namely, ion irradiation [50], doping [51], spin pumping [52], etc. In such cases, the modification of damping occurs irreversibly. However, reversible or dynamic control over damping is a necessity

of technological importance. The dynamic manipulation of damping can be achieved by tailoring a pulsed magnetic field [53,54] or injecting spin current in a ferromagnetic thin film. The SHE is an elegant way to generate a pure spin current that affects the magnetization dynamics in a ferromagnetic thin film by exerting torque on the precessional motion. A brief discussion on different Hall effects and the origin of SHE is given below.

A. Ordinary Hall Effect

In presence of an out of plane magnetic field, the electrons of a nonmagnetic current carrying conductor experience the Lorentz force which moves the electron against one side of the conductor. It gives a voltage, known as Hall voltage across the orthogonal direction to the applied current and magnetic field direction. This effect is known ordinary Hall effect. This landmark discovery was made by E. H. Hall in 1879 [55]. The Hall voltage of a metallic slab is given by:

$$V_H = \frac{IB}{neb} \tag{2.29}$$

where I is the amplitude of the current, B is magnetic induction, n is carrier density, e is electron charge value and b is slab width. This Hall voltage measurement gives the information of carrier density in nonmagnetic conductors and semiconductors.

B. Anomalous Hall effect

In 1881, Hall [56] observed a ten times larger voltage in ferromagnetic iron compared to the nonmagnetic conductor. This effect is known as the anomalous Hall effect. In case of a ferromagnet, it can arise in the absence of a magnetic field as well. The total Hall resistance (R_H) is given by:

$$R_H = R_0 B + R_A M \tag{2.30}$$

Where R_0 is the Hall coefficient, R_A is the anomalous Hall resistance, B is magnetic induction and M is magnetization along the applied magnetic field direction.

C. Spin Hall Effect

In some nonmagnet metals, the application of charge current generates the spin polarization dependent deflection to the transverse direction due to spin-dependent scattering via SOI. The spins with opposite polarities deflect to the two different directions and accumulate on two opposite surfaces which create a spin gradient known as spin current. This phenomenon is known as SHE [57]. A schematic of SHE is shown in Fig. 2.4. When an in-plane charge current ($\mathbf{I_c}$) is injected in HM, it generates a spin current

($\mathbf{I_s}$) with polarity $\boldsymbol{\sigma}$ and accumulates at the interface. As a result, the adjacent FM layer experiences SOT. These three vectors are mutually orthogonal to each other and satisfy the equation [58] given below:

$$\mathbf{I_S} = \frac{\hbar}{2e}\theta_{SH}(\mathbf{I_c} \times \boldsymbol{\sigma}) \tag{2.31}$$

where θ_{SH} is the spin Hall angle which defines the charge current to spin current conversion efficiency. As the $\mathbf{I_s}$ along z-direction as shown in the schematic, from the above equation it is clear that in-plane charge current results in an in-plane spin polarization.

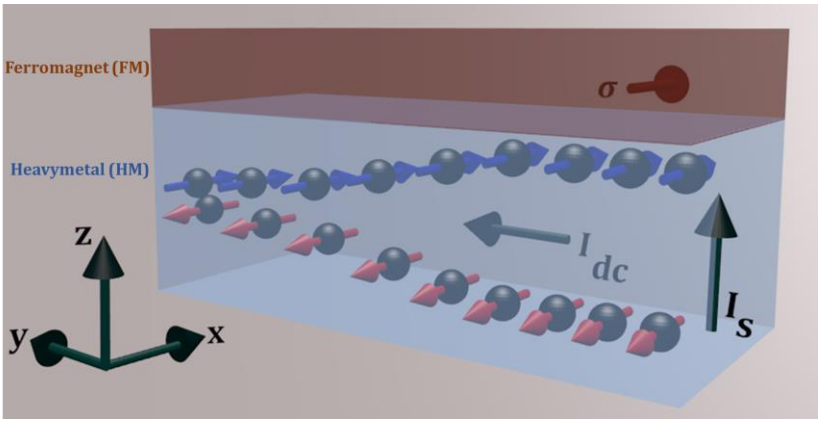

Figure 2. 4. (a) Schematic of bulk spin Hall effect in heavy metal (HM) is shown. Flow of charge current direction (I_{dc}), spin current direction (I_s) are shown.

SHE can have two different origins, namely, intrinsic which relates to the band structure of crystal and extrinsic which relates to spin-dependent scattering of electrons. The extrinsic contribution primarily originates from two mechanisms, skew scattering and side jump. A brief discussion of these mechanisms is given below.

I. Skew Scattering Mechanism

This mechanism is described by Mott scattering in relativistic physics [59]. In an HM with high SOC (like Pt, Ta, W), the skew scattering arises from SOC of disorder potential, scattering of spin-orbit coupled quasiparticle from scaler potential, multiband character due to contribution of sub-bands to disorder potential [60]. When an electron passes through an electric field ($\boldsymbol{E}$) due to impurity, a magnetic field in the transverse direction, $\boldsymbol{B} \sim \boldsymbol{v} \times \boldsymbol{E}$ is experienced by its spin. This magnetic field is inhomogeneous due to disorder in the electric field. Therefore, the electron gets deflected due to the Zeeman effect which depends on spin polarity.

II. Side Jump Mechanism

This mechanism purely has a quantum mechanical origin. In quantum mechanical pictures, electrons are considered as Gaussian wave packets. When a Gaussian wave packet scatters from an impurity with SOI, it experiences a shift in the transverse direction from its previous path [61]. The wave packet experiences an anomalous velocity ($\boldsymbol{v}$) which depends on spin polarity ($\boldsymbol{\sigma}$). It can be derived from Pauli's Hamiltonian (H) with potential due to SOI.

$$H = \frac{p^2}{2m} + eV + V_{so} \tag{2.32}$$

where $V_{so} = \frac{\hbar}{4m^2c^2}(\boldsymbol{\sigma} \times \boldsymbol{\nabla} V).\boldsymbol{p}$.

$$\boldsymbol{v} = \frac{\partial H}{\partial \boldsymbol{p}} = \frac{\boldsymbol{p}}{2m} - \frac{e\hbar}{4m^2c^2}(\boldsymbol{\sigma} \times \mathbf{E}) \tag{2.33}$$

where $\boldsymbol{E}$ is the electric field corresponding to potential V and $\boldsymbol{p}$ is the electron momentum.

References

[1] W. Gerlach and O. Stern, Das magnetische Moment des Silberatoms; Z. Phys. **9,** 353 (1922).
[2] W. Heisenberg, Mehrkörperproblem und Resonanz in der Quantenmechanik; Z. Phys. **38,** 411 (1926).
[3] P. Weiss, L'hypothèse du Champ Moléculaire et la Propriété Ferromagnétique; J. Phys. Theor. Appl. **6,** 661 (1907).
[4] H. A. Kramers, L'interaction Entre les Atomes Magnétogènes dans un Cristal Paramagnétique; Physica **1,** 182 (1934).
[5] P. W. Anderson, Generalizations of the Weiss Molecular Field Theory of Antiferromagnetism; Phys. Rev. **79,** 705 (1950).
[6] C. Zener, Interaction between the d-Shells in the Transition Metals. II. Ferromagnetic Compounds of Manganese with Perovskite Structure; Phys. Rev. **82,** 403 (1951).
[7] T. Kasuya, Electrical Resistance of Ferromagnetic Metals; Prog. Theor. Phys. **16,** 58 (1956).
[8] M. A. Ruderman and C. Kittel, Indirect Exchange Coupling of Nuclear Magnetic Moments by Conduction Electrons; Phys. Rev. **96,** 99 (1954).
[9] I. Dzyaloshinsky, A Thermodynamic Theory of "Weak" Ferromagnetism of Antiferromagnetics; J. Phys. Chem. Solids **4,** 241 (1958).
[10] T. Moriya, Anisotropic Superexchange Interaction and Weak Ferromagnetism; Phys. Rev. **120,** 91 (1960).
[11] P. Bruno and J. P. Renard, Magnetic Surface Anisotropy of Transition Metal Ultrathin Films; Appl. Phys. A **49,** 499 (1989).
[12] P. Bruno and J. Seiden, Theoretical Investigations on Magnetic Surface Anisotropy; Le Journal de Physique Colloques **49,** C8 (1988).
[13] J. M. D. Coey, Magnetism and Magnetic Materials (Cambridge University Press, 2010).
[14] S.-i. Iwasaki and K. Ouchi, Co-Cr Recording Films with Perpendicular Magnetic Anisotropy; IEEE Trans. Magn. **14,** 849 (1978).
[15] N. Nakajima, T. Koide, T. Shidara, H. Miyauchi, H. Fukutani, A. Fujimori, K. Iio, T. Katayama, M. Nývlt, and Y. Suzuki, Perpendicular Magnetic Anisotropy Caused by Interfacial Hybridization via Enhanced Orbital Moment in Co/Pt Multilayers: Magnetic Circular X-Ray Dichroism Study; Phys. Rev. Lett. **81,** 5229 (1998).
[16] R. C. O'Handley and S. W. Sun, Strained Layers and Magnetoelastic Coupling; J. Magn. Magn. Mater. **104,** 1717 (1992).
[17] E. R. Callen and H. B. Callen, Static Magnetoelastic Coupling in Cubic Crystals; Phys. Rev. **129,** 578 (1963).
[18] W. F. Brown Jr, Theory of Magnetoelastic Effects in Ferromagnetism; J. Appl. Phys. **36,** 994 (1965).
[19] D. Sander, The Correlation between Mechanical Stress and Magnetic Anisotropy in Ultrathin Films; Rep. Prog. Phys. **62,** 809 (1999).
[20] S. W. Sun and R. C. O'handley, Surface Magnetoelastic Coupling; Phys. Rev. Lett. **66,** 2798 (1991).
[21] G. S. Cargill Iii and T. Mizoguchi, Dipolar Mechanisms for Magnetic Anisotropy in Amorphous Ferrimagnetic Alloys; J. Appl. Phys. **49,** 1753 (1978).
[22] R. P. Cowburn, A. O. Adeyeye, and M. E. Welland, Configurational Anisotropy in Nanomagnets; Phys. Rev. Lett. **81,** 5414 (1998).
[23] M. E. Schabes and H. N. Bertram, Magnetization Processes in Ferromagnetic Cubes; J. Appl. Phys. **64,** 1347 (1988).
[24] B. K. Mahato, S. Choudhury, R. Mandal, S. Barman, Y. Otani, and A. Barman, Tunable Configurational Anisotropy in Collective Magnetization Dynamics of $Ni_{80}Fe_{20}$ Nanodot Arrays with Varying Dot Shapes; J. Appl. Phys. **117,** 213909 (2015).
[25] S. Jain, Y. Ren, A. O. Adeyeye, and N. Singh, Configurational Anisotropy and Control of Magnetic Vortex Chirality in Arrays of Circular $Ni_{80}Fe_{20}$ Nanoscale Dots; Phys. Rev. B **80,** 132401 (2009).

[26] A. Barman and A. Haldar, in Solid State Phys.; Vol. 65, edited by R. E. Camley and R. L. Stamps (Academic Press, 2014), p. 1.
[27] E. Beaurepaire, J. C. Merle, A. Daunois, and J. Y. Bigot, Ultrafast Spin Dynamics in Ferromagnetic Nickel; Phys. Rev. Lett. **76,** 4250 (1996).
[28] F. Dalla Longa, J. T. Kohlhepp, W. J. M. de Jonge, and B. Koopmans, Influence of Photon Angular Momentum on Ultrafast Demagnetization in Nickel; Phys. Rev. B **75,** 224431 (2007).
[29] M. Krauß, T. Roth, S. Alebrand, D. Steil, M. Cinchetti, M. Aeschlimann, and H. C. Schneider, Ultrafast Demagnetization of Ferromagnetic Transition Metals: The Role of the Coulomb Interaction; Phys. Rev. B **80,** 180407 (2009).
[30] G. P. Zhang and W. Hübner, Laser-Induced Ultrafast Demagnetization in Ferromagnetic Metals; Phys. Rev. Lett. **85,** 3025 (2000).
[31] J.-Y. Bigot, M. Vomir, and E. Beaurepaire, Coherent Ultrafast Magnetism induced By Femtosecond Laser Pulses; Nat. Phys. **5,** 515 (2009).
[32] M. Battiato, K. Carva, and P. M. Oppeneer, Superdiffusive Spin Transport as a Mechanism of Ultrafast Demagnetization; Phys. Rev. Lett. **105,** 027203 (2010).
[33] G. Malinowski, F. Dalla Longa, J. H. H. Rietjens, P. V. Paluskar, R. Huijink, H. J. M. Swagten, and B. Koopmans, Control of Speed and Efficiency of Ultrafast Demagnetization by Direct Transfer of Spin Angular Momentum; Nat. Phys. **4,** 855 (2008).
[34] L. Landau and E. Lifshitz, On the Theory of The Dispersion of Magnetic Permeability in Ferromagnetic Bodies; Phys. Z. Sowjetunion **8,** 153 (1935).
[35] T. L. Gilbert, A Phenomenological Theory of Damping in Ferromagnetic Materials; Phys. Rev. **100,** 1235 (1955).
[36] T. L. Gilbert, A Phenomenological Theory of Damping in Ferromagnetic Materials; IEEE Trans. Magn. **40,** 3443 (2004).
[37] F. Bloch, Zur Theorie des Ferromagnetismus; Z. Phys. **61,** 206 (1930).
[38] J. H. E. Griffiths, Anomalous High-frequency Resistance of Ferromagnetic Metals; Nature **158,** 670 (1946).
[39] C. Kittel, On the Theory of Ferromagnetic Resonance Absorption; Phys. Rev. **73,** 155 (1948).
[40] A. Barman, G. Gubbiotti, S. Ladak, A. O. Adeyeye, M. Krawczyk, J. Gräfe, C. Adelmann, S. Cotofana, A. Naeemi, V. I. Vasyuchka, B. Hillebrands, S. A. Nikitov, H. Yu, D. Grundler, A. V. Sadovnikov, A. A. Grachev, S. E. Sheshukova, J. Y. Duquesne, M. Marangolo, G. Csaba, W. Porod, V. E. Demidov, S. Urazhdin, S. O. Demokritov, E. Albisetti, D. Petti, R. Bertacco, H. Schultheiss, V. V. Kruglyak, V. D. Poimanov, S. Sahoo, J. Sinha, H. Yang, M. Münzenberg, T. Moriyama, S. Mizukami, P. Landeros, R. A. Gallardo, G. Carlotti, J. V. Kim, R. L. Stamps, R. E. Camley, B. Rana, Y. Otani, W. Yu, T. Yu, G. E. W. Bauer, C. Back, G. S. Uhrig, O. V. Dobrovolskiy, B. Budinska, H. Qin, S. van Dijken, A. V. Chumak, A. Khitun, D. E. Nikonov, I. A. Young, B. W. Zingsem, and M. Winklhofer, The 2021 Magnonics Roadmap; J. Phys.: Condens. Matter **33,** 413001 (2021).
[41] A. V. Chumak, V. I. Vasyuchka, A. A. Serga, and B. Hillebrands, Magnon Spintronics; Nat. Phys. **11,** 453 (2015).
[42] A. Hoffmann and S. D. Bader, Opportunities at the Frontiers of Spintronics; Phys. Rev. Appl. **4,** 047001 (2015).
[43] J.-G. Zhu, Y. Zheng, and G. A. Prinz, Ultrahigh Density Vertical Magnetoresistive Random Access Memory (invited); J. Appl. Phys. **87,** 6668 (2000).
[44] V. Kamberský, On Ferromagnetic Resonance Damping in Metals; Czechoslovak Journal of Physics B **26,** 1366 (1976).
[45] H. Suhl, Theory of the Magnetic Damping Constant; IEEE Trans. Magn. **34,** 1834 (1998).
[46] W. S. Ament and G. T. Rado, Electromagnetic Effects of Spin Wave Resonance in Ferromagnetic Metals; Phys. Rev. **97,** 1558 (1955).
[47] M. Sparks, R. Loudon, and C. Kittel, Ferromagnetic Relaxation. I. Theory of the Relaxation of the Uniform Precession and the Degenerate Spectrum in Insulators at Low Temperatures; Phys. Rev. **122,** 791 (1961).
[48] R. Arias and D. L. Mills, Extrinsic Contributions to the Ferromagnetic Resonance Response of Ultrathin Films; Phys. Rev. B **60,** 7395 (1999).

[49] D. J. Twisselmann and R. D. McMichael, Intrinsic Damping and Intentional Ferromagnetic Resonance Broadening in Thin Permalloy Films; J. Appl. Phys. **93,** 6903 (2003).
[50] A. Ganguly, S. Azzawi, S. Saha, J. A. King, R. M. Rowan-Robinson, A. T. Hindmarch, J. Sinha, D. Atkinson, and A. Barman, Tunable Magnetization Dynamics in Interfacially Modified $Ni_{81}Fe_{19}$/Pt Bilayer Thin Film Microstructures; Sci. Rep. **5,** 17596 (2015).
[51] W. Bailey, P. Kabos, F. Mancoff, and S. Russek, Control of Magnetization Dynamics in $Ni_{81}Fe_{19}$ Thin Films Through the Use if Rare-Earth Dopants; IEEE Trans. Magn. **37,** 1749 (2001).
[52] S. Mizukami, Y. Ando, and T. Miyazaki, Effect of Spin Diffusion on Gilbert Damping for a Very Thin Permalloy Layer in Cu/Permalloy/Cu/Pt Films; Phys. Rev. B **66,** 104413 (2002).
[53] M. Bauer, R. Lopusnik, J. Fassbender, and B. Hillebrands, Suppression of Magnetic-Field Pulse-Induced Magnetization Precession by Pulse Tailoring; Appl. Phys. Lett. **76,** 2758 (2000).
[54] T. Gerrits, H. A. M. van den Berg, J. Hohlfeld, L. Bär, and T. Rasing, Ultrafast Precessional Magnetization Reversal by Picosecond Magnetic Field Pulse Shaping; Nature **418,** 509 (2002).
[55] E. H. Hall, On a New Action of the Magnet on Electric Currents; American Journal of Mathematics **2,** 287 (1879).
[56] R. Karplus and J. M. Luttinger, Hall Effect in Ferromagnetics; Phys. Rev. **95,** 1154 (1954).
[57] M. I. Dyakonov and V. I. Perel, Current-Induced Spin Orientation of Electrons in Semiconductors; Phys. Lett. A **35,** 459 (1971).
[58] G. Y. Guo, S. Murakami, T. W. Chen, and N. Nagaosa, Intrinsic Spin Hall Effect in Platinum: First-Principles Calculations; Phys. Rev. Lett. **100,** 096401 (2008).
[59] N. F. Mott, The Scattering of Fast Electrons by Atomic Nuclei; Proceedings of the Royal Society of London. Series A, Containing Papers of a Mathematical and Physical Character **124,** 425 (1929).
[60] J. Sinova, S. O. Valenzuela, J. Wunderlich, C. H. Back, and T. Jungwirth, Spin Hall effects; Rev. Mod. Phys. **87,** 1213 (2015).
[61] S. Takahashi and S. Maekawa, Spin Current, Spin Accumulation and Spin Hall Effect; Sci. Technol. Adv. Mater. **9,** 014105 (2008).

Chapter 3

3. Methods

In this chapter, a brief discussion of the methods used in sample fabrication, characterization and numerical analysis is presented. Nanofabrication [1] is the core of nanoscience and nanotechnology [2]. It relies on the continuous improvements and upgrades of the fabrication process of thin films and confined nanostructures while maintaining the purity of the base materials and minimizing the structural defects in a cost-effective manner. Over the years, several thin film depositions and nanopatterning methods have been developed for the fabrication of thin film heterostructures and two dimensional (2D) confined structures. Recently, different three dimensional (3D) lithographic techniques are combined with thin film deposition techniques to fabricate high quality 3D nanostructures [3,4] while maintaining material purity. Here, we have used dc and rf sputtering technique for the fabrication of thin film heterostructures. The electron beam lithography (EBL) and two photon lithography (TPL) have been used to write the 2D and 3D patterned structures, respectively. Thin film deposition techniques (electron beam evaporation and thermal evaporation) and electrochemical deposition techniques have been used to deposit the magnetic materials for the fabrication of the patterned structures. The intrinsic features of magnetic material at the nanoscale mainly rely upon the crystalline and chemical ordering as well as the quality of the surface of the patterned structure. Therefore, detailed characterization is necessary to characterize and optimize the magnetic parameters of the nanostructures. The characterizations to determine the crystal structure, surface imaging and morphology, and the chemical compositions of these heterostructures and structured magnetic materials have been performed by X-ray diffraction (XRD) [5], scanning electron microscopy (SEM) [6], atomic force microscopy (AFM) [7] and energy dispersive X-ray (EDX) spectroscopy [8]. The static and quasistatic magnetic characterizations have been probed by magnetic force microscopy (MFM) [9], static magneto-optical Kerr effect (static-MOKE) [10]. Further, the state-of-the-art optical techniques employed to measure the magnetization dynamics in time and frequency domain are time-resolved magneto-optic Kerr effect (TRMOKE) magnetometer, and Brillouin light scattering (BLS) spectroscopy [11]. The

techniques are based on light-mater interaction, which can excite and detect the magnetization dynamics with appreciable spatio-temporal resolution. Micromagnetic simulation is an efficient numerical tool for studying a wide variety of magnetic phenomena including magnetization reversal and dynamics. The reproduction of experimentally observed phenomena in micromagnetic simulations is a powerful way to validate and understand the observed magnetic properties. Researchers have developed a series of micromagnetic simulators. In this thesis, we have used the object oriented micromagnetic framework (OOMMF), MuMax3, and LLG micromagnetic simulator. In the succeeding paragraphs, the aforementioned techniques are briefly discussed.

3.1 Sample Fabrication

3.1.1 Electron-beam Lithography

EBL [12] is widely used for 2D nanostructure fabrication. It can produce feature size varies from submicron to few nanometres. In this process, an electron sensitive resist is exposed to electron beams to write a pattern on a clean substrate (bottom to top approach) or a thin film (top to bottom). The pattern structure is generated by using a computer aided design (CAD) which also controls the writing on the resist. This feature makes it a maskless pattern generator. Depending on the resist the exposed area becomes soluble (+ve resist) or insoluble (-ve resist) to the developer solvent. Here, a bilayer (PMMA/MMA) or monolayer (PMMA) positive resist was spun on a pre-cleaned substrate (thin film) using a spin coater before preparing the resist pattern on the thin film or substrate using EBL. Subsequently, the resist is immersed in a developer (compatible with the resist) to develop the pattern. In this thesis, a bilayer resists (PMMA/MMA) pattern on $Ni_{80}Fe_{20}/Al_2O_3$ thin film (deposited on self-oxidized Si (100)) and a monolayer (PMMA) resist pattern on self-oxidized Si (100) substrate were designed using EBL for the fabrication of connected nanodot (CND) and square artificial spin ice (ASI) structure, respectively.

3.1.2 Two-photon Lithography

TPL is a widely used technique in photonic and micromechanics [13-15] to produce 3D nanostructure with sub-micron feature size. Recently, the TPL technique has been adapted to fabricate nanoscale 3D magnetic nanostructures [16-19]. In case of TPL, the resist is polymerized by simultaneous absorption of two photons of a long wavelength beam usually in infrared (IR) regime. The insignificant linear absorption of IR by common

resist and the quadratic variation of polymerization rate with light intensity make TPL the only available technique with intrinsic 3D nanofabrication and 3D spatial resolution capability. In TPL, fs laser pulses are focused using a microscope objective (MO) onto a photoresist to write a 3D pattern.

In this thesis, TPL was used to write tetrapod structures inside a positive photoresist (AZ9260) and to prepare a scaffold of 3D diamond bond lattice (3D-ASI) on a negative tone photoresist (IPL-780).

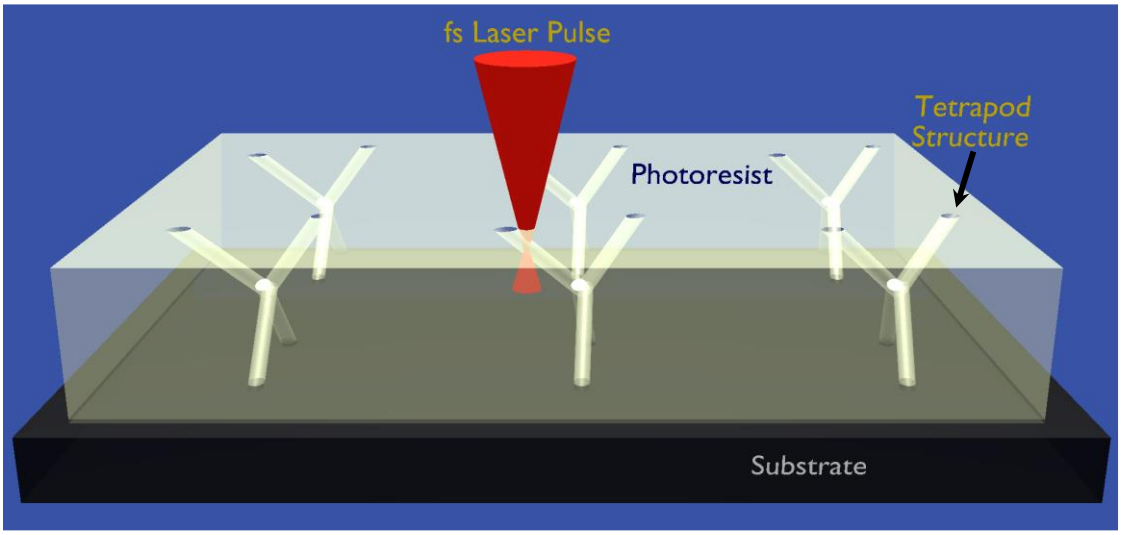

Figure 3. 1. Schematic of a two-photon lithography (TPL).

3.1.3 Electrodeposition

Electrodeposition [17,20-24] is a process to coat a surface (usually metallic coating) by electric current via oxidation and reduction method. Here, the electrolyte solution of a salt of the desired metal is used to deposit the metal on the surface. The depositing (substrate) surface is placed in the cathode and the inert metal (platinum, graphite etc.) or the coating metal can be used as an anode. In case of inert metal as the anode, the electrolyte has to be added to maintain the solution concentration. In this thesis, cobalt was deposited into the holes of the 3D resist pattern of tetrapod using electrodeposition. The 3D resist pattern was developed on a glass/ITO (700 nm) substrate. The electrolyte solution of cobalt sulphate (90 g), cobalt chloride (27 g), boric acid (14 g) and sodium lauryl sulphate (1 g) was used in a standard Watts bath (600 ml). The deposition was

performed at a constant current of 1 mA with a cobalt anode. A schematic of the electrodeposition process is shown in Fig. 3.2.

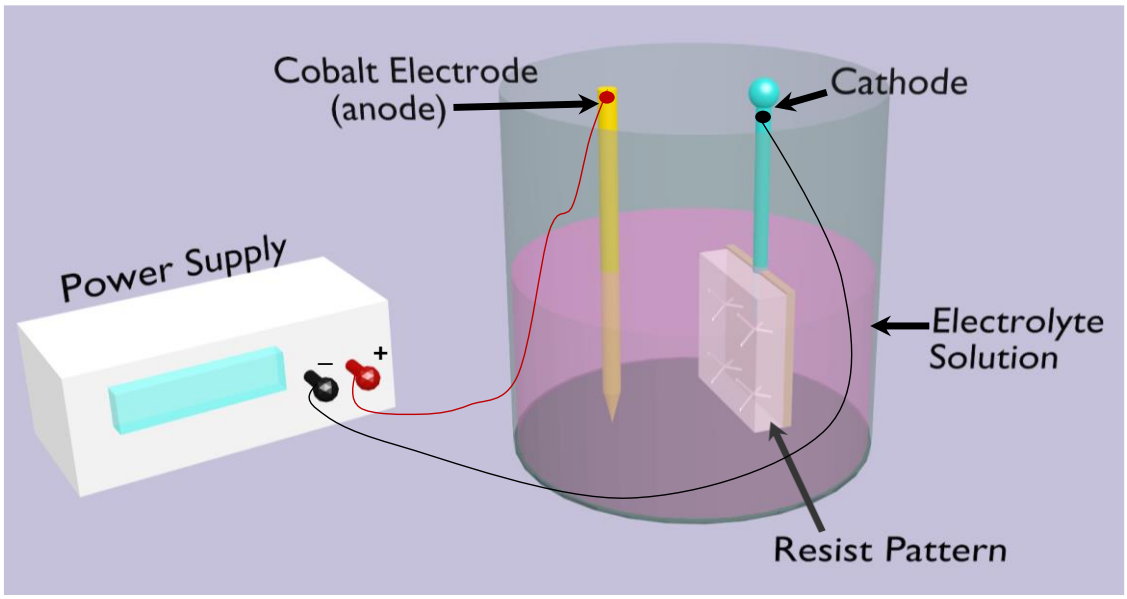

Figure 3. 2. Schematic of electrodeposition.

3.1.4 Thermal Evaporation

We have also used the thin film deposition techniques to deposit the magnetic thin films. Three most commonly used thin film deposition techniques are thermal evaporation, electron beam evaporation and sputtering. These are also known as the physical vapour deposition (PVD) technique [25] in accordance with its deposition process. In order to maintain the high purity of the material, the depositions are carried out in a high vacuum chamber to avoid impurity from the air molecules.

In the thermal evaporation process, the source material is placed in a vessel, known as a boat. The sample is heated up using a restive heating process by passing a large amount of current through the boat. As a result, the source material melts and forms a gaseous state. In the high vacuum chamber, the gas atoms of the source material evaporate and hit the substrate by travelling through the vacuum chamber. On the substrate surface, the evaporated atoms condensate and make a thin layer of the source material. The thickness of the thin layer is monitored in real time using a crystal monitor sensor. In this thesis, the 99.99 % pure 50-nm-thick $Ni_{81}Fe_{19}$ was deposited on the 3D scaffold of diamond bond lattice, in a thermal evaporator (aluminium boat) at a base pressure below 1×10^{-6} with a deposition rate of 0.2 nm/s [26]. For the fabrication of square ASI, a 25-nm-thick $Ni_{80}Fe_{20}$ film was deposited on an EBL-developed patterned structure by using thermal

evaporation at a base pressure of 9.7 × 10^{-7} Torr [27]. A schematic of the thermal evaporation process is shown in Fig. 3.3.

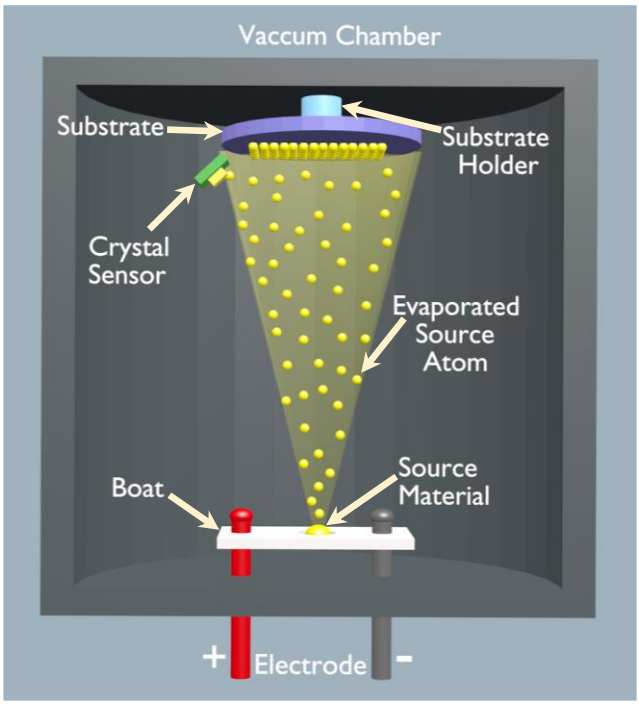

Figure 3. 3. Schematic of thermal evaporation.

3.1.5 Electron-beam Evaporation

The electron-beam evaporation [28] is similar to thermal evaporation. Here, the source material is heated up differently by focusing the stream of electrons generated by an electron gun [29] (from a filament due to thermionic emission). The source material is placed on a crucible and heated up by the electron beam from the electron gun which is accelerated using a high voltage electrode and focused on the material using magnets. The source material melts and evaporates. The evaporated material strikes the substrate and condensates to form a thin layer of the source material. Here, different materials can be kept in separate crucibles which are then be placed on a linear/circular train. Therefore, multiple materials can be deposited in an electron-beam evaporation chamber without breaking the vacuum or venting. In the thesis, the electron-beam evaporation was used to deposit $Ni_{80}Fe_{20}$ (20-nm-thick) film coated with Al_2O_3 (60-nm-thick) at a base pressure of 2 × 10^{-8} Torr on top of commercially available self-oxidized Si (100) substrate to fabricate CND structure. Also, the contact pads of chromium/gold were deposited for the application charge current to the heterostructures of Ta/CoFeB/SiO_2.

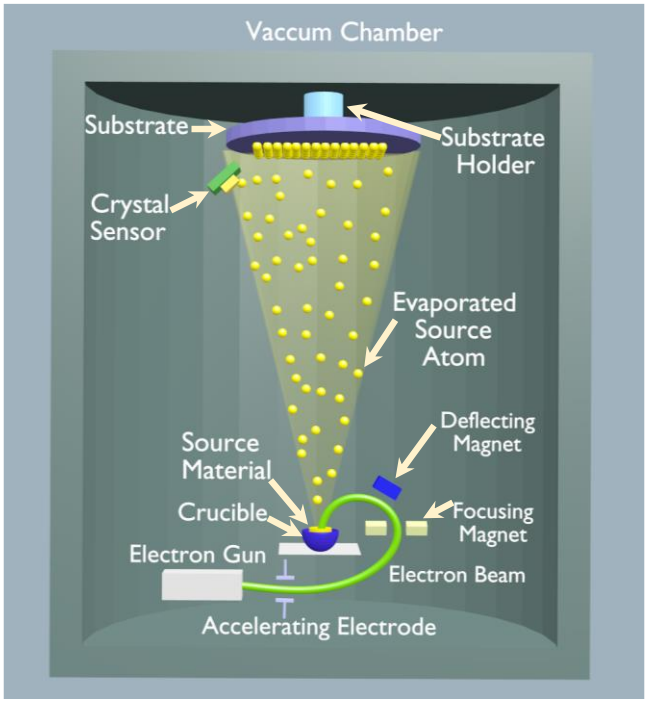

Figure 3. 4. Schematic of electron-beam evaporation.

3.1.6 Sputtering

The working principle of sputtering is different from the above two thin film deposition techniques. Here, the target material is placed in a high vacuum chamber. Then an inert gas (generally Argon: Ar [30]) is inserted into the chamber. Subsequently, a high negative voltage is applied to the target material and the positive part is connected to the substrate holder. The voltage is high enough to pull out an electron from the Ar atoms to form an Ar^+ ion close to the target material. The free electron tries to move away from the negatively charged cathode. In case of magnetron sputtering, permanent magnets are placed below the target material. Then the electrons travel in a circular path towards magnets and collide with neutral Ar molecules to generate more Ar^+ ions. As a result, Ar plasma forms inside the vacuum chamber. Due to the high negative voltage at the target material, the Ar^+ ions accelerate and travel towards the material with higher velocity and dislodge the source material. This method is known as sputtering [31]. The sputtered atoms travel in a typical line-of-sight cosine path and, as a result, they get deposited on the substrate. A sputtering system can have more than one source material. It can deposit single or multilayer thin films. The DC and RF voltage sources can be used in sputtering. The former is preferred for metal substances while the latter is preferred for the insulators to avoid charge accumulation at the surface of the source material. In this

thesis, the Ta/CoFeB/SiO_2 heterostructures were deposited using RF-DC magnetron sputtering [32,33] at a base pressure of 2.0×10^{-7} Torr and argon pressure of about 1.0 mTorr at a deposition rate of 0.2 Å/s.

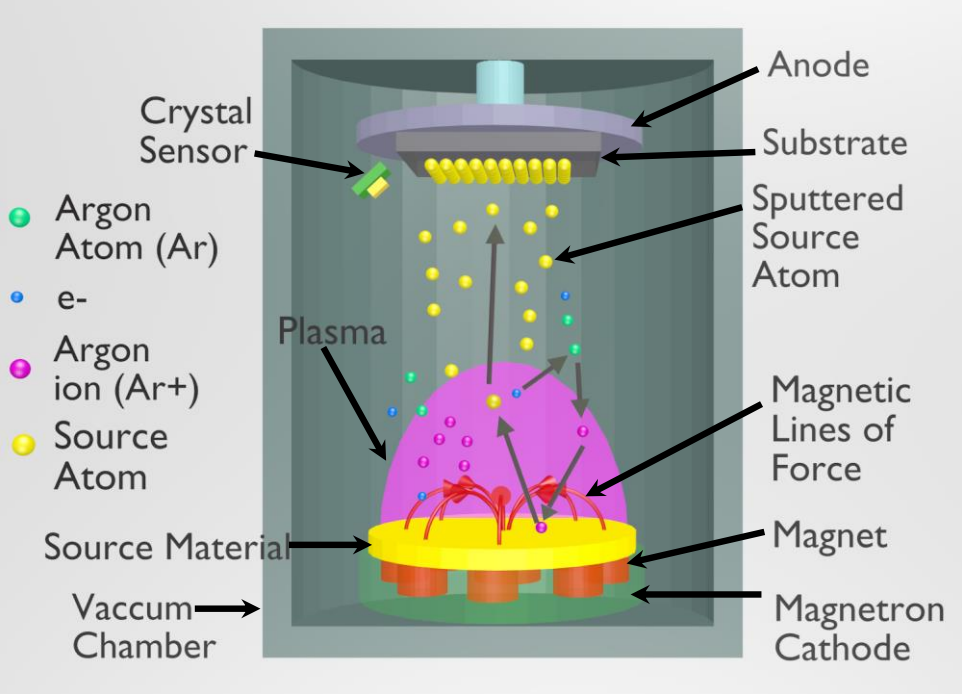

Figure 3. 5. Schematic of RF-DC magnetron sputtering.

3.1.7 Ion Milling and Lift off Process

Ion milling [34,35] is extensively used to fabricate patterned structures using the top-down approach. The ions of an inert gas (Ar) from an ion beam source which is accelerated towards the sample to remove the materials from desired places. Here, the substrate is placed in a vacuum chamber on a rotation stage. The sample stage is kept at a tilted position to the ion source to increase the etch rate compared to normal incidence. In this thesis, the holes of CND structures were drilled using an ion milling system at a base pressure of 1×10^{-4} Torr with a beam current of 60 mA for 6 min.

After the fabrication of the nanostructures using the top-down or bottom-up approach, the residual resist is removed by using the lift-off process. Here, the whole patterned system is immersed in a resist soluble solvent (e.g., acetone) for few minutes (1-5 min). Then it is kept in an ultrasonic bath to assist the removal of resist after immersion in the solution. Subsequently, the isopropyl alcohol and deionized water rinsing process are performed to clean the substrate after resist removal. In case of the 3D tetrapod

structure, after removing the resist using acetone the sample was subjected to oxygen plasma treatment for 1h to remove the leftover of the resist [17].

3.2 Sample Characterization

3.2.1 Scanning Electron Microscopy

SEM imaging is used to verify the lift-off completion and check the sample surface morphology and topography. Here a beam of the electron is produced by cathode either by using thermionic emission [36] or an electric field (field emission SEM: FESEM [37,38]) and focused on the sample using electromagnetic lenses. The electron beam can detect feature size from 1-2 nm to 1-2 mm due to its very short wavelength. The electron beam interacts with the sample in different manners such as secondary electrons (ejected from the sample), backscattered electrons, transmitted electrons, absorbed electrons (heat), characteristic X-rays, and elastically and inelastically scattered electrons. When the numbers of incoming and outgoing electrons are not the same, then the sample builds up a charge (charging effect) and it affects the image quality.

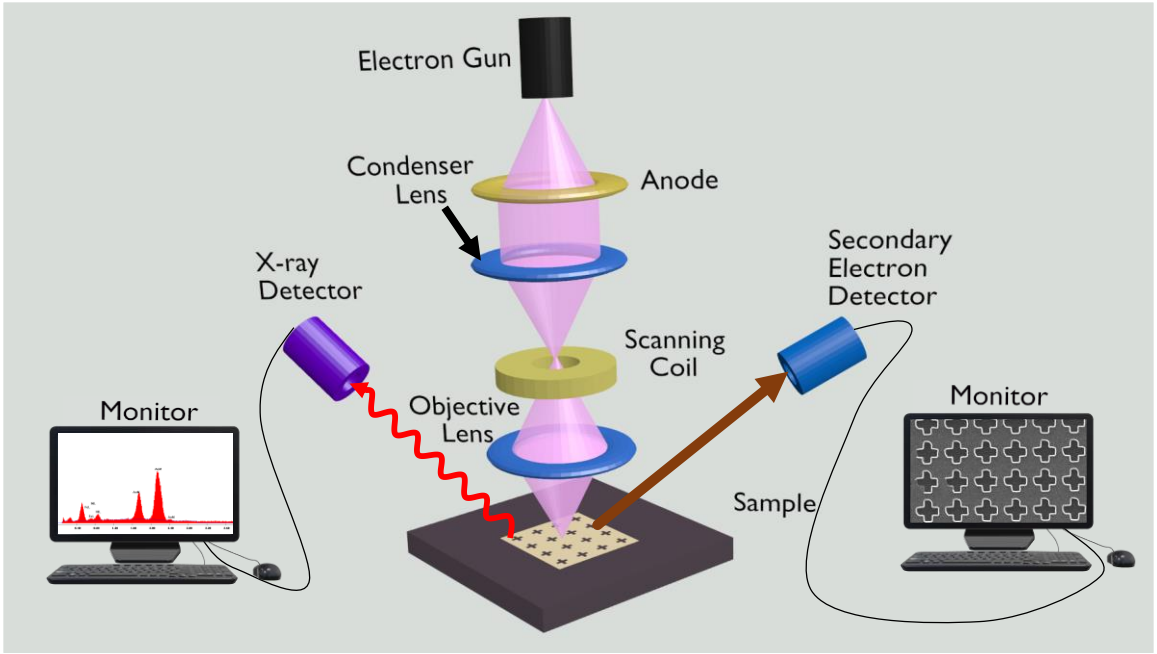

Figure 3. 6. Schematic of scanning electron microscope (SEM) and energy dispersive X-ray (EDX) is shown. The monitor at right and left captures the SEM image and EDX spectra, respectively.

To avoid charging, the samples (generally insulators) are coated with a thin layer of a metallic film. In most cases, the secondary electrons are detected by electron sensitive detector to produce SEM images. The secondary electrons explore the surface feature of

the sample which gives 3D features. In this thesis, FEI Quanta 200 (at SNBNCBS) and Hitachi Regulus 8230 (at Cardiff University) SEMs were used to image 2D and 3D nanostructures.

3.2.2 Energy Dispersive X-ray

The EDX is a non-destructive analytical tool [38] for elemental analysis and chemical characterization of the materials present in a sample. Generally, it is used in conjunction with SEM and detected using a special EDX detector and spectrum analyzer software. The basic principle of EDX is based upon the phenomenon that each element has a unique atomic structure that corresponds to the unique characteristic X-ray of the elements. When high energy of charged particles (like electrons, protons) hits the sample, it excites and ejects out electrons from an inner shell and creates an electron hole at that position. To stabilize the atom, electrons from the outer shell with higher energy jump into the inner shell to fill the electron-hole and emits an X-ray. The energy of the X-ray is equal to the difference between the energy of the outer and inner shell. This emitted X-ray is detected by an EDX detector to generate EDX spectra.

3.2.3 X-ray Diffraction

The X-ray wavelength is comparable to the lattice constant of the material which makes it a suitable candidate for the study of material structure. The XRD [5] technique is used to investigate the crystalline material structure, including atomic arrangement, crystallite size and imperfections. Here a beam of X-rays (wavelength ~1.5418 Å: the K_α radiation (X-ray) from a copper target) is incident on the sample and is diffracted by the atoms' electron of a crystal. A crystal can be treated as a regular array of atoms that can elastically scatter electromagnetic waves, like X-rays. The scattered beams from the electrons form secondary spherical waves. A periodic or crystalline structure produces the secondary wave in a periodic manner. Most of the waves interfere destructively and the constructive interference occurs according to Bragg's condition:

$$2d\ sin\ \theta = n\lambda \qquad (3.1)$$

where d is the distance between the atomic planes, θ the incident angle, n any integer and λ the wavelength of the X-ray. The above equation suggests that the diffraction spots appear at certain angles of incidence for a particular lattice structure (related to d). During the measurements, the incident angle of X-ray is varied over a range of angles in small steps and the corresponding reflected intensities are measured as a function of the

angle of the reflected beam with respect to the direction of the incident beam (2θ). The diffraction peaks are converted to *d*-spacings to identify the elements present in the sample. Typically, this is done by matching the data with standard reference patterns (i.e., Inorganic Crystal Structure Database (ICSD) or International Centre for Diffraction Data (ICDD)).

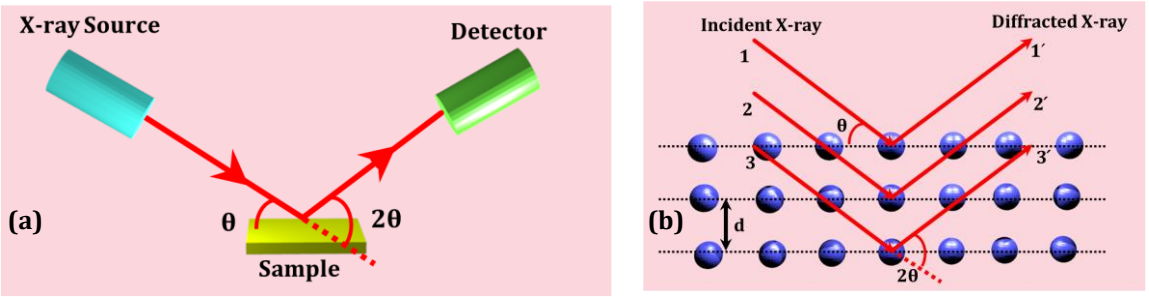

Figure 3. 7. Schematic of (a) X-ray diffractometer and (b) diffraction of X-ray from the atomic planes are shown.

3.2.4 Atomic Force Microscopy

The AFM has been designed to probe the local properties such as morphology, roughness etc. The sample or the probe is mounted on a piezoelectric stage which enables small and accurate movements at the nanoscale to perform a raster scan. The information is derived from the interaction between probe and sample. The AFM probe is consisting of a flexible cantilever (generally coated with Co-Cr, Pt-Ir etc.) and a sharp tip (coated with Co-Cr, Pt-Ir or doped diamond etc.) at its end (see Fig. 3.8). When the tip is brought close to the sample surface, it experiences vertical and lateral deflection due to different forces such as van der Waals force, force due to chemical bonding, capillary force and electrostatic force. This deflection is mapped with the help of a laser beam and four-quadrant photodetectors to extract the local properties of the sample. A laser beam is pointed on the top surface and the reflected beam is placed at the centre of four-quadrant photodetectors. Any deflection of the cantilever causes the change in the photodetector signal which is mapped using software to get information on local parameters.

Depending upon the sample surface and interaction force between the probe and the sample surface, AFM can be used in three different modes, namely, i) contact mode, ii) non-contact mode and iii) tapping mode. In case of contact mode, the tip scans the sample in close contact with the sample surface and maintains a constant repulsive between the probe and the surface. A feedback loop is employed to maintain this criterion by

providing a feedback voltage to the piezoelectric stage. Here, cantilevers with low stiffness values are used to achieve a large deflection signal (tens to hundreds of nm) while keeping the interaction force within the safe limit to avoid any damage or scratch over the sample surface and the probe. In case of non-contact mode, the tip scans over few tens of Å above the sample surface. A weak attractive force like Van der Waals force is probed to construct the topographical image of its surface. The small forces between the tip and the sample are measured by calculating the modulation in amplitude, phase or frequency of the oscillation of the cantilever in response to the force gradients from the sample. The tapping mode is commonly used in AFM. Here, the cantilever oscillates at or near its resonance frequency with the help of piezoelectric actuators. The tip is brought close to the sample until it slightly touches or taps the sample surface. The irregular contact with the sample surface affects the oscillation due to energy losses. The resulting change in oscillation amplitude is recorded to map the surface topography.

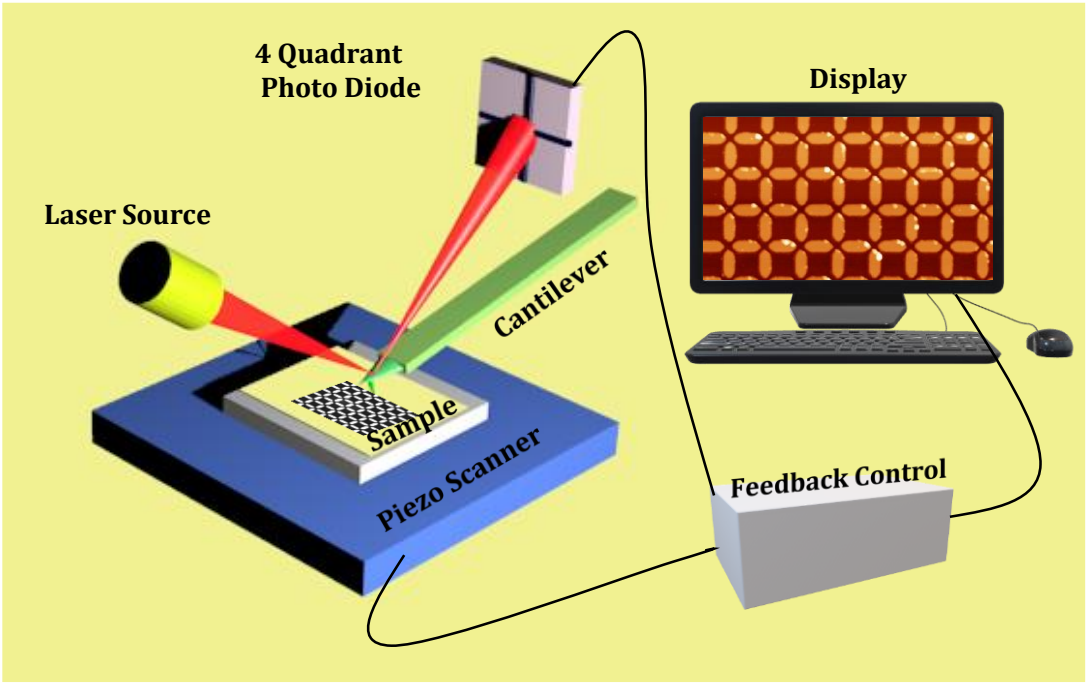

Figure 3. 8. Schematic of atomic force microscopy(AFM).

3.2.5 Magnetic Force Microscopy

In magnetic force microscopy (MFM) the magnetic texture formed within a magnetic sample can be probed by studying the magnetic interactions between the tip and the sample. Here, the tip is coated with a thin magnetic layer (e.g., Co, Co-Cr) with high

coercivity so that the magnetization state of the tip remains unaltered during the imaging. When the tip is brought close to the sample surface, it experiences magnetic forces as well as atomic and electrostatic forces. During the measurements to get a better MFM image, the AFM image is first captured. Subsequently, the tip is lifted by a certain distance and scanned over the surface at a particular height to record the out-of-plane magnetic stray field. The magnetic signal is extracted using software to get information on the magnetic texture. Depending on the stray field strength originating from the magnetic sample the MFM scan can be performed in static and dynamic mode. In this thesis, the discussed surface morphology and the magnetic texture of the samples were measured using Veeco (diInnova) system.

3.2.6 Magneto Optic Kerr Effect

The discovery of different magneto-optic effects [39] showed that the magnetic moment strongly influences the polarization of the light. As a consequence, magneto-optic effect based techniques emerged as detection tools for static and dynamic magnetic phenomena. Initially, it was observed that the plane of polarization of a linearly polarized light is rotated when the light travels through a magnetic medium. This effect is known as Faraday's effect [40]. Later on, a similar effect was observed in the reflected light from a magnetic system. When a linearly polarized light is reflected from an ordered ferromagnetic material, its plane of polarization rotates and it becomes an elliptically polarized light. This effect is known as the magneto-optic Kerr effect [41,42]. This effect is quantified by two parameters related to the major and minor axis of the ellipse, namely, Kerr rotation (θ_k: angle between major axis with the direction of the linearly polarized light) and Kerr ellipticity (ε_k: related to the inverse tangent of the minor and major axis of the ellipse). The θ_k and ε_k are linearly related to magnetization and both change their sign with the reversal of the magnetization. The Kerr effect originates from magnetic circular birefringence (responsible for ε_k) and magnetic circular dichroism (responsible for θ_k). The quantum mechanical explanation suggests that the interaction between the electric field ($\mathbf{E} = -\nabla V$) of incident light with the magnetization (spin: $\mathbf{s}$) of the sample gives rise to an effective vector potential ($\mathbf{A} \sim \mathbf{s} \times \nabla V$) which affects the electron motion due to spin-orbit interaction. In case of ferromagnetic material, the imbalance between up and down spins gives rise to the Kerr effect. Depending on the relative orientation between the magnetization direction of a ferromagnetic material and the plane of the

incident light, the Kerr effect can be categorized in three different geometries (shown in Fig. 3.9), namely, polar, longitudinal and transverse. In the polar Kerr effect, the magnetization is along the out-of-plane direction of the sample and parallel to the plane of incidence of the beam. When the magnetization lies in the plane of the sample and also parallel to the plane of incidence the effect is known as the longitudinal Kerr effect. In the transverse Kerr effect, the magnetization lies in the plane of the sample and perpendicular to the plane of incidence.

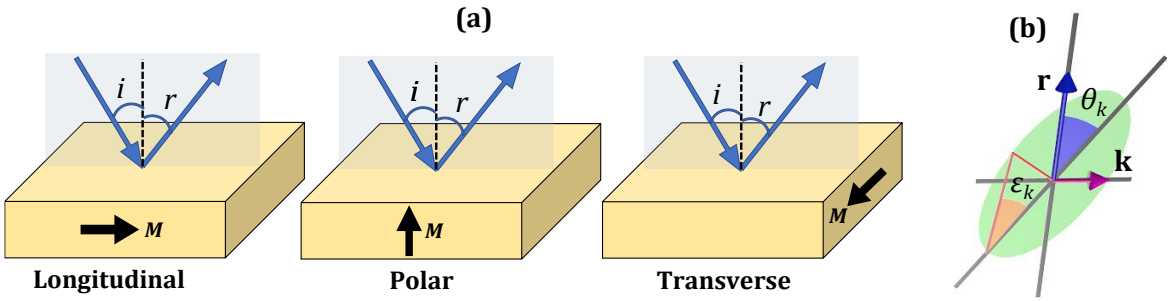

Figure 3. 9. (a) Schematic of longitudinal, polar and transverse Kerr geometries, and (b) Kerr rotation (θ_k), Kerr ellipticity (ε_k) and two orthogonal components of electric field (***r*** and ***k***) in the ellipsoid are shown.

The transverse electric (s-polarized) and transverse magnetic (p-polarized) polarization of light can show the longitudinal and polar Kerr effect. However, the transverse Kerr effect occurs only for the p-polarized light, because the electric field of the incident light becomes parallel to magnetization for s-polarized light which results in a zero Lorentz force. The transverse effect does not show any change in the light polarization, due to the induced polarization being along the same direction of the polarization of the incident light. Instead, the transverse Kerr effect shows a change in the intensity of the reflected light related to a change in magnetization orientation. The Kerr effect in all the geometries changes with the incidence angle of the light. The Kerr effect in transverse and longitudinal geometry vanish for normal incidence of light due to vanishing Lorentz force or induced polarization being along the incident-light direction. The Kerr effect in polar geometry shows maximum effect in the normal incidence of light which makes it useful in the magneto-optic recording.

A. Static Magneto Optic Kerr Effect Magnetometer

The static-MOKE magnetometer is a non-invasive tool to measure the hysteretic behaviour of ferromagnetic thin films and patterned nanostructures. The static-MOKE is a surface-sensitive technique that allows measuring localized magnetic properties in a

nonuniformly distributed system (like wedge shape film). The static-MOKE can be measured in all three geometries, i.e., polar, longitudinal and transverse. However, the change in polarization of incident light can be observed in polar and longitudinal geometries as mentioned in the previous section. The static-MOKE in our laboratory at S.N. Bose National Centre for Basic Sciences is based on longitudinal geometry where the magnetic field is applied in the plane of the sample to keep the magnetization parallel to the incidence plane of light.

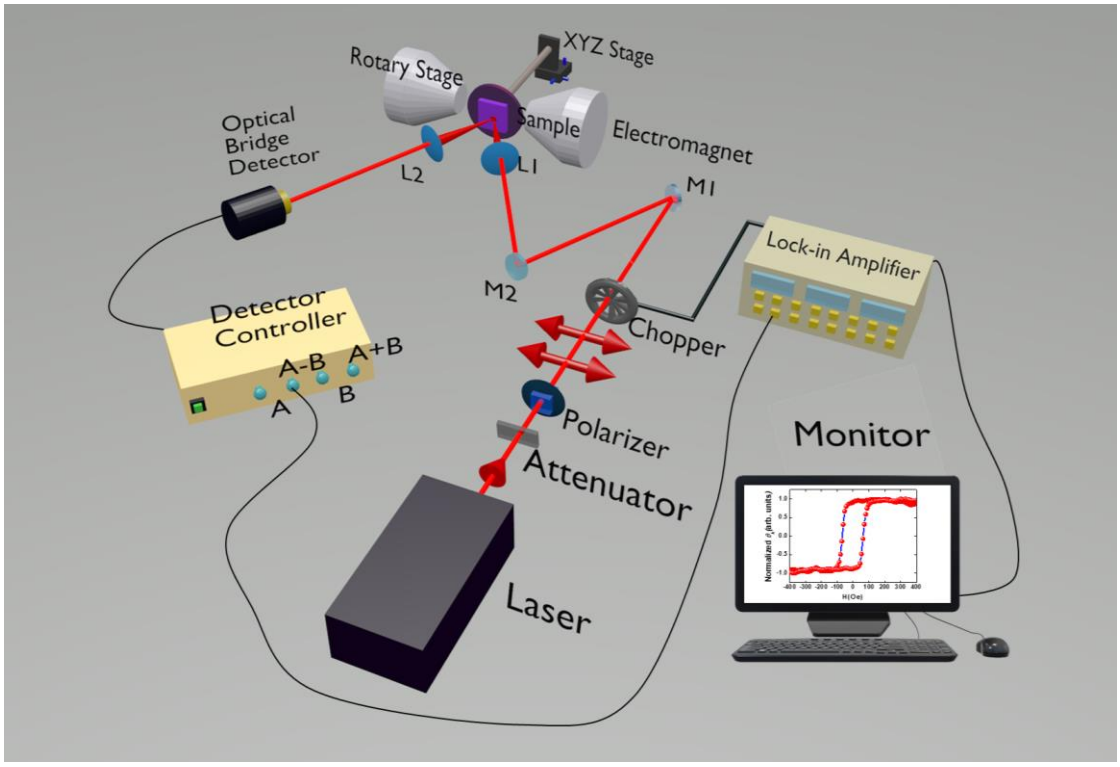

Figure 3. 10. Schematic of the static-MOKE system present in our laboratory at S.N. Bose national centre for Basic Sciences.

A continuous-wave laser beam from a He-Ne laser (output power ~ 30 mW) of a wavelength of 632.8 nm is used to probe the Kerr effect. The beam is passed through a Glan-Thompson polarizer to obtain high-quality s-polarized light. The polarized beam is chopped at a 2 kHz frequency by using a mechanical chopper. Then it is steered through different mirrors and focused on the sample using a convex lens (L1). The sample is placed in between two pole pieces of an electromagnet. The field is reversed by reversing the current through the pole pieces using a bipolar power supply. Then the reflected light is collected by another convex lens (L2) and guided towards the detector. Here, we use a special type of detector, namely, a balanced photodiode detector or optical bridge detector (OBD). The photodiodes in the OBD convert the optical signal to an electrical

signal which is measured by using a lock-in amplifier. A reference signal from the chopper controller is fed to a lock-in amplifier to measure the signal in a phase-sensitive manner to obtain a better signal to noise ratio. The OBD consists of a polarized beam splitter and two photodiodes. The polarized beam splitter is placed at 45° with respect to the reflected light direction. Therefore, a linearly polarized light in absence of any Kerr effect splits equally into two orthogonal parts of polarization giving rise to the balanced condition in the OBD. Any change in polarization in light due to Kerr rotation gives a finite electrical signal at the output (~ (A-B)) of the OBD.

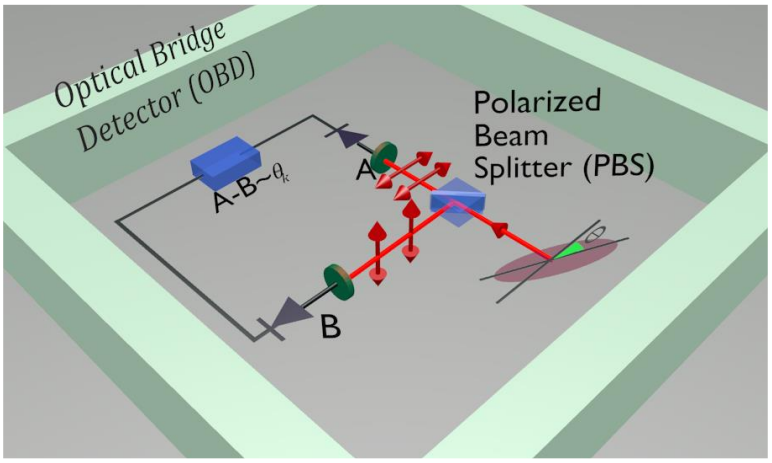

Figure 3. 11. Schematic of the optical bridge detector (OBD).

3.3 Experiment Tools for Magnetization Dynamics

3.3.1 Time-Resolved Magneto Optic Kerr Microscope

To measure the magnetization dynamics, we have used the TRMOKE technique. Here, a two-colour pump-probe technique is exploited where the pump beam excites the dynamics and the time-delayed probe beam captures the time evolution of magnetization. This is an all-optical technique that does not require any sophisticated waveguide design like all-electrical measurements [11,43,44]. The non-invasive nature makes it a puissant tool to measure magnetization dynamics in thin films and magnetic nanostructures. In a broad sense, the collinear set-up consists of an fs pulsed laser system, a second harmonic generator (SHG), a motorized delay stage, different guiding optics and a detection system. The fs oscillator system consists of two laser systems (Millennia eV and Tsunami of Spectra Physics). A brief discussion on the different components of the colinear TRMOKE is given in the succeeding paragraphs.

A. Millennia eV

The Millennia eV 10S model of Spectra Physics (Newport) is a sophisticated laser that consists of three basic components: i) water-cooled laser head, ii) 48 V DC utility unit and iii) controlling software.

The laser head of Millennia eV [45] consists of an optical cavity that uses folded cavity resonator. In this architecture, the pump beam of the fibre-coupled output from a diode module is focused into a vanadate crystal using a telescope and a dichroic fold mirror. The diode laser pumps the vanadate crystal which absorbs the laser beam and emits its laser at 1064 nm. The crystal is the driving engine of the Millennia eV. The dichroic mirror is highly transparent to the diode pump beam wavelength and highly reflective to the vanadate laser beam. Then the laser beam is resonated and confined inside the Millennia eV cavity. A non-critically phase-matched lithium triborate (LBO) crystal is placed inside the cavity to convert the laser beam of 1064 nm to 532 nm (green) laser beam via frequency doubling mechanism. In order to get optimized output power of 532 nm, the LBO crystal is kept on a compact temperature regulating oven to maintain the crystal temperature and to maintain a suitable phase-matching condition. The LBO crystal has a smaller nonlinear coefficient [46] compared to other crystals. However, the large acceptance angle of the LBO crystal makes it suitable for the stability of the Millennia eV cavity in case of slight misalignment. Further, the advanced 'Quiet Multi-Axial Mode Doubling' technology provides extremely stable and high amplitude of the laser beam by managing the number of axial modes, gain, nonlinear conversion, excited-state lifetime and suppressing the noise. An output coupler consisting of a dichroic mirror allows the 532 nm beam to exit from the cavity while confining the 1064 nm beam inside the cavity. A small portion of the output beam is sampled using a beam splitter and a photodiode to give feedback to the diode pump system to obtain a constant output (within ± 1% of the setpoint) in the power mode operation. A shutter is placed outside the cavity enclosure which is controlled using a software. A recirculating chiller from Polyscience at a fixed temperature of 20 ^{o}C is used to cool the laser head during the lasing process. The output power of the Millenia eV is kept fixed at 8 W (maximum power 10 W) in our system.

B. Tsunami

The output of Millennia eV is fed to the Tsunami laser system through Brewster's window. It can produce continuously tunable outputs in near-IR wavelength ranging from 690 nm to 1080 nm with pulse width around 80 fs [47]. The laser system consists of Ti:sapphire

rod, pump beam mirrors, rod focusing mirrors, an output coupler, a high reflector beam folding mirrors, dispersion control elements, and tuning elements. The Ti:sapphire rod is the active lasing medium which is a Titanium ion (Ti^{3+}) doped sapphire (Al_2O_3) crystal. The optics form a resonator cavity inside the Tsunami enclosure. The pump beam is collinearly aligned with the cavity mode using guiding mirrors and illuminates on the rod. A high inversion population is required to overcome the total loss for lasing operation of the rod. The continuous population inversion in the long length laser rod is achieved by a longitudinal pumping mechanism where the pump beam and optical cavity mode are focused as well as overlapped at a narrow line within the rod. The pump beam is then collimated and expanded back to the normal diameter. The generation of mode locked laser with a higher repetition rate (around 80 MHz) requires a longer cavity compared to a continuous-wave laser source. To achieve the long length cavity within the minimal space of the Tsunami enclosure, a ten-fold mirror cavity is used. This introduces an unavoidable astigmatism issue for aligning the focusing mirror other than the normal incidence of the beam. It is avoided by carefully aligning the focusing mirrors and the rod length at Brewster's angle. After passing through the optics the beam is fed into an acousto-optic modulator (AOM) for active mode locking. The AOM is placed at Brewster's angle and driven by the regenerative mode locking process by using an rf signal which can handle a slight change in the cavity length by adjusting the driving signal to the AOM. The output wavelength of the Tsunami laser is tuned by using a four-prism sequence and a tuning slit in between them. By changing the slit width, the spectral width is controlled which modifies the temporal width (related through Heisenberg uncertainty relation) of the pulsed laser. The output of Tsunami is fixed at a wavelength of 800 nm (due to its high sensitivity to Si photodiode) and the pulse width is maintained around 80 fs by adjusting the full width half maxima of spectra at around 12 nm (wavelength domain) using wavelength selection and group velocity dispersion (GVD) knobs (by tuning the prisms position and the slit width). The Ti:sapphire rod temperature is kept fixed using a chiller unit for stable output over a long period. The cavity is constantly purged with clean and dry N_2 gas to maintain humidity by removing dust and water vapour.

C. Second Harmonic Generator

The SHG (Model no. – 3980-4) from Spectra Physics is designed for frequency doubling which converts the one part of the Tsunami's output beam of 800 nm to a wavelength of

400 nm which is used as the pump beam in our system. The second harmonic generation is based on the nonlinearities of the optical parameters of a material [48]. The dielectric polarization of a dielectric material consists of nonlinear higher order terms besides the linear term of the electric field. The second harmonic generation which is a coherent optical process of radiation of dipoles in a material depends on the second order electric field term in the expansion of the polarization. When a dipole of a non-centrosymmetric crystal oscillates in presence of an oscillatory electric field of frequency ω, it can emit a frequency of 2ω apart from the fundamental frequency ω. Therefore the near-IR light converts to near-UV light. Here, the SHG employed a non-linear β-barium borate (BBO) optical crystal which produces a second harmonic of the fundamental laser pulse. The second harmonic beam becomes parallelly polarized whereas the fundamental beam remains vertically polarized. The BBO crystal has higher SHG conversion efficiency compared to the LBO crystal and also it does not require any heating arrangements like the LBO crystal. The SHG conversion efficiency is inversely proportional to the spot size of the beam. Therefore, the beam waist is optimized by using a telescopic arrangement of two lenses. A thin BBO crystal is used to minimize the pulse broadening due to GVD. It can also achieve phase matching over the entire tunable wavelength range (690-1080 nm). To protect the BBO crystal from air moisture due to its hydrographic nature, it is sealed within a cylindrical case with antireflection coated windows and filled with an index matching fluid. The second harmonic and fundamental beam are separated by using a prism with a highly reflective coating for the fundamental beam. The second harmonic beam diffracts through a pair prism which compensates the beam shape distortion and horizontal displacement due to the SHG crystal. Finally, both the beams exit the SHG unit through two different output paths.

D. Experimental Set-up of TRMOKE Microscopy

The customised TRMOKE microscope present in our laboratory at the S. N. Bose National Centre for Basic Sciences relies upon a two-colour collinear pump-probe geometry, where the axes of both pump beam (the second harmonic output with wavelength λ_{pump}

= 400 nm) and probe beam (the fundamental beam with wavelength λ_{probe} = 800 nm) are superposed before they are made incident collinearly on the sample.

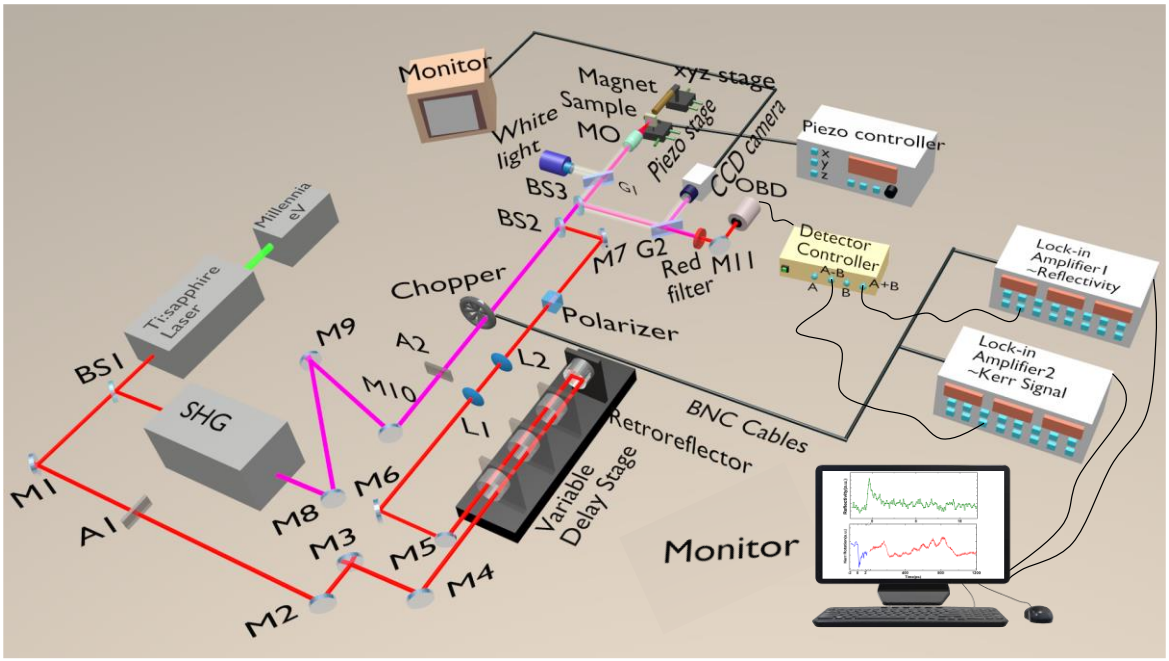

Figure 3. 12. Schematic of the colinear TRMOKE system present in our laboratory at S.N. Bose National Centre for Basic Sciences.

The fundamental beam from the Titanium (Ti): sapphire pulsed laser source is divided into two parts by a 70:30 beam splitter. The intense part goes through the SHG to produce the pump beam, which is then guided towards the sample with the help of steering mirrors. The other part (the fundamental probe beam) goes through a retro-reflector (RR) fixed on an automated variable delay stage in the path of the probe beam. By moving the RR back and forth it is possible to introduce the desired optical path difference between the pump and the probe beams, which corresponds to the time delay in this experiment. Subsequently, both the beams are spatially overlapped using a beam combiner and are collinearly focused onto the sample using a single MO (M-40X with numerical aperture 0.65). The MO focuses the probe beam to a diffraction limited spot size (~ 800 nm) on the sample surface while the pump beam becomes slightly defocused with a spot size of ~ 1 μm because of chromatic aberration. The higher intensity of the pump beam perturbs the equilibrium magnetization of the sample, thereby inducing the dynamics. The dynamics affect the Kerr rotation of the reflected probe beam, which is, in turn, dependent on the time delay between the pump and the probe pulses. By changing the retroreflector position on the delay stage by small steps, the time evolution of the

magnetization dynamics (along with the total reflectivity signal) is measured in a phase-sensitive manner by using an OBD and two lock-in amplifiers (to record Kerr signal and reflectivity data; Model: SR830 DSP, Stanford Research Systems). The direction of the applied bias magnetic field is slightly tilted with respect to the magnetic anisotropy direction, to get a finite demagnetizing field along the direction of the pump pulse.

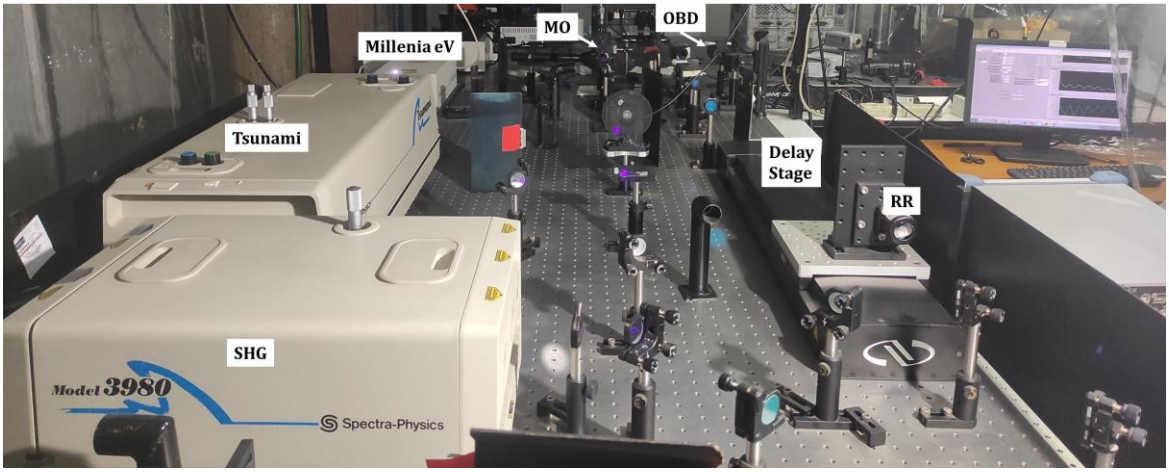

Figure 3. 13. Photograph of the TRMOKE microscopy set-up present in our laboratory at S.N. Bose National Centre for Basic Sciences.

E. Routine Alignments during Experiment

The collinear alignment of the pump and probe beam is very vital in our TRMOKE microscope. Therefore, some routine alignment steps are performed regularly:

1. Firstly, the power of the Tsunami output is maximized using external micrometer controllers of Tsunami, and simultaneously the spectrum is optimized for desired central wavelength (λ_{probe} = 800 ± 2 nm) and FWHM (~ 12 nm or more).

2. The RR alignment is checked by observing the position of the beam after RR. If the beam moves with the movement of the RR, mirrors before RR are adjusted to remove the shift.

3. The overlap between the pump and probe beams is checked after the beam combiner. If the alignment is correct, both the beams will follow the same path (i.e., in collinear geometry).

4. Next, we check whether the beams are co-axial with the MO. For that, we check the beam positions at the back aperture of MO. Any misalignment of the beams is adjusted by changing the tilts of the respective mirrors. The adjustment is fine-tuned by monitoring the pump and probe beam spots falling onto a substrate by a CCD camera. The MO is moved back and forth about the position of its focal point and any consequent movement

of the centre(s) of the pump and/or probe spot(s) on the screen implies that the beam is not co-axial with the MO.

5. Finally, the alignment of the OBD is adjusted by superposing the back-reflected beam from OBD with the incident beam.

6. After adjusting the optical components, the time-resolved reflectivity data from a standard Si substrate is recorded and its relaxation rate is compared with the standard data to verify the alignment of the pump and probe beam. This is followed by the acquisition of the data from the magnetic specimen is being started.

3.3.2 Non Colinear Time-resolved Magneto Optic Kerr Magnetometry

This setup is based on an amplified femtosecond laser system where a fundamental beam having a wavelength of 800 nm and pulse width of about 40 fs is generated by using a regenerative amplification method. The laser pulse is again split using a beam splitter. One part of this fundamental laser beam is attenuated and collimated to use as the probe beam. Another part is frequency doubled using an SHG and is used as the pump beam to excite the electron and spin dynamics in the sample. The pump and probe beams are made to incident non-collinearly on the sample surface using wavelength specific lens arrangements. The probe is incident normally on the sample plane so that the reflected probe beam can be used to detect the time-resolved Kerr rotation in the polar Kerr geometry in addition to the simultaneous detection of time-resolved reflectivity signal. The procedure of generation of the amplified femtosecond laser pulse is extremely sophisticated and complicated. The entire amplifier (Libra) system from Coherent consists of the following units: ultrafast oscillator (Vitesse), diode-pumped solid-state pump laser (DPSS, Evolution), regenerative cavity, stretcher and compressor grating arrangements, synchronized delay generator etc. In the following subsections, we will discuss those units briefly.

A. Vitesse

Vitesse is a compact DPSS (Verdi)-pumped ultrafast oscillator that produces mode-locked sub-100 fs pulses at 80 MHz repetition rate with an output power of about 200 mW at 800 nm wavelength [24]. Three main units associated with it are the laser diode system, Verdi and the Verdi-pumped ultrafast laser unit (VPUF).

i. Laser diode system: The Verdi is pumped by the continuous output produced by laser diodes. The power supply box for the laser diode contains a commercial power supply, two laser diodes, electrical circuits, monitors and a cooling fan. Light generated by the laser diode assembly is transported by fiber array package (FAP) and is used to pump the gain medium of Verdi. The main components of diode laser assembly are FAP I and FAP II, each of which contains a laser diode bar capable of efficiently converting the electrical energy to optical energy. It is desirable to operate the FAPs at low temperatures and sufficient drive currents. The wavelength of the emitted light is temperature dependent. Proper heat sink and cooling fans are there to maintain the optimum temperature.

ii. Verdi: This resonator consists of a unidirectional single-frequency ring cavity with the facility of intra-cavity SHG to produce multi-watt level green (532 nm) output. Intra-cavity etalon enables the single frequency selectivity. This pump resonator is an 'end-pump design' where light travels along the optical axis of Nd:YVO_4 (Vanadate) gain medium. Verdi absorbs energy from 808 nm input and produces strong single line emission of 1064 nm which is later frequency doubled. As it is known that an optically pumped laser rod can act as a lens, it is important to maintain the temperature of Vanadate to minimize the thermal focusing and hence astigmatism. The LBO crystal used for frequency doubling can act as an output coupler. The tower temperature for this crystal is maintained at 150°C to have 90° phase matching between the fundamental beam (1064 nm) and its second harmonic (532 nm). After exiting the resonator, the 532-nm-beam is steered by a mirror towards the VPUF. A piezoelectric transducer driven lever controls the tilt for maintaining the optimum pump beam alignment into VPUF. Hence, this system is known as a power track mirror arrangement.

iii. VPUF: Ti:sapphire is the active medium in this laser unit. The multiple negative dispersive mirrors provide a negative dispersion for producing sub-100 fs pulses. Mode locking is automatically achieved by using Kerr lensing. For suitable material, the irradiation of high intensity laser beam can create distortion of the atoms due to high electric field. This effect is known as the optical Kerr effect which can affect the refractive index of the material. Thus, a laser beam having higher intensity at the central part can set a gradient of refractive index in the material. This lensing narrows the beam waist. A slit is used to only allow the narrow mode-locked beams after blocking the continuous-wave laser. Finally, it provides the real driving force for further and continuous mode

locking. Different wavelengths of a beam can travel with different velocities due to the wavelength-dependent refractive index of optical components. This causes the GVD which introduces reshaping of pulse or spectral chirp (either positive or negative). Also, due to Kerr lensing, the frequency components of a pulse get phase-shifted differently. This is called self-phase modulation which causes temporal chirping by leading towards pulse broadening. To compensate for these GVD and chirping, multiple negative dispersion mirrors (which are Fabry-Perot etalons) are employed to bring the net GVD of the cavity down to zero.

B. Evolution

Evolution-30 is a diode-pumped Q-switched Nd:YLF laser capable of producing average energy of more than 20 mJ for a 527-nm-beam having a 1 kHz repetition rate. The components are described below:

i. Power supply and laser diode: Evolution employs laser diode pumping to excite the laser gain medium. High efficiency results in low power electrical and cooling utility requirements with thousands of hours promised lifetime.

ii. Nd:YLF gain medium: Nd:YLF or Nd:$LiYF_4$ is used because of its long upper-state lifetime (470 μs). It provides efficient energy storage for high-pulse energy operation at low repetition rates. Its low thermal lensing and natural birefringence avoid the loss of beam quality. An intra-cavity polarizer gives the freedom to select 1047 nm or 1053 nm transitions during pumping. The output beam of Evolution is the frequency-doubled part of the 1053 nm laser.

iii. Acousto-optic Q-switching: If a transparent material (here silica) is subjected to ultrasonic vibration, the photo-elastic effect couples the strain field of ultrasonic wave to the refractive index of the material. Now if the laser falls on the grating created by this effect, then a part of the light is diffracted in different directions. This energy loss is sufficient to destroy the 'Q' of the cavity. Generally, a piezoelectric transducer is used to convert the electrical signal to ultrasonic sound. The laser can be returned to the high 'Q' state after switching off the voltage applied to the transducer. If the ultrasonic vibration is stopped, then the fused silica block emits a Q-switched laser pulse.

iv. Frequency doubling component: A nonlinear crystal, e.g., LBO, is used as an output coupler to frequency double the Q-switched beam. A heater maintains the tower temperature usually at 327.5 °F (164 °C). This crystal can efficiently work at the

temperature range between 157 °C and 171 °C range for noncritical phase matching with a 1053 nm laser and it emits about 527 nm in the output.

C. Working Principle of Libra

The physical phenomena that are associated with the regenerative amplification of femtosecond laser within Libra are described briefly in the following section:

i. Chirped pulse amplification (CPA): This is a technique for amplifying an ultrashort laser pulse up to extremely high pulse energy with the laser pulse being stretched out temporally and spectrally before amplification. Sometimes highly intense laser beam can lose its energy within a very short path length due to unwanted self-focusing. CPA can avoid this obstacle. Initially, a weak but short duration pulse is generated. The peak power is reduced significantly after stretching. The pulse is then amplified without any self-focusing. Finally, the amplified pulse is compressed to its original pulse duration. Libra employs CPA to stretch a weak pulse by 10,000 times with the help of a grating and amplifies by a factor of 106 by using Ti:sapphire crystal.

ii. Pulse stretching and compressing: A diffraction grating which reflects different wavelengths of a beam at different angles can introduce a varying delay for different wavelengths. This stretches or compresses the pulse temporally. In a stretcher grating, the in-build configuration is such that the higher frequency components (blue side of the spectrum) have to travel far to become time delayed with respect to the redder components. The pulse thus has a positive GVD due to this stretching which is known as a positively chirped pulse. In a compressor grating, the scenario is just the opposite. The bluer frequency components are made to travel faster in order to compensate for the delay with respect to the redder part and thus the pulse achieves its desired temporal width again.

iii. Regenerative amplification (RGA): For a Ti:sapphire crystal absorptive transition takes place between 400 and 600 nm. However, the short wavelength side of the fluorescence spectrum merges with this transition wavelength. Thus, the actual range of lasing becomes limited in the IR range. This crystal has large gain bandwidth, exploited for pulse amplification. In the RGA cavity of Libra, Ti:sapphire crystal rod is used to amplify a single nJ pulse (selected from the mode-locked train of seed laser emitted from Vitesse) to mJ pulse. This amplification for a single pass within the crystal is very small.

RGA cavity offers a multipass trip to the seed laser so that a very high overall gain can be achieved.

D. Two Color Optical Pump-Probe Setup in Noncollinear Geometry

The s-polarized fundamental laser beam from the output of the amplifier (Libra) is guided by a set of five mirrors before being split into two equal parts using a 50:50 beam splitter (see Fig. 3.14). A portion of this fundamental laser beam is fed into the SHG. After the frequency doubling (λ = 400 nm) we obtain the pump beam. The other part of the fundamental laser beam (λ = 800 nm) is heavily attenuated being used as the probe beam. This beam is steered by several mirrors into a motorized scanning delay stage (Newport, with motion controller: model number-EPS301) with the RR assembly to introduce a variable time delay. Before entering into the RR, the probe beam is collimated using a pair of plano-convex lenses of focal lengths 10 cm and 15 cm. As a result, the beam-waist are reduced to ~5 mm. The probe beam coming out from the RR is guided to the sample using few mirrors before being focused on the sample surface by using a plano-convex lens. A GT polarizer (GTH5M, Thorlabs) with an extinction ratio of 100000:1 is placed in the path of the probe beam to ensure a high degree of polarization of the incident probe beam. Three irises are kept in the path of the probe beam to monitor the vertical and lateral shifts of the probe beam on a regular basis. The pump beam is guided onto the sample by using a set of five mirrors which are adjusted to compensate the optical path length with respect to the probe path. A variable attenuator is used for adjusting the probe power falling onto the sample. The pump and probe beams are made to incident non-collinearly onto the sample surface. The pump beam is kept slightly defocused on the sample surface to avoid any damage to the sample by the high irradiation of the pump beam. The probe beam is tightly focused on the sample surface and placed carefully at the centre of the pump beam so that the dynamics are probed from the uniformly excited part of the sample. The pump and probe beams have spot sizes of 200 μm and 100 μm, respectively. The sample is mounted on a holder placed on the top of a translational x-y-z stage. A viewing arrangement is made using a white light source and a CCD camera for monitoring the overlap of the pump and probe beams as well as their positions on the sample surface. The reflected pump beam is blocked. The reflected probe beam is split into two parts with a beam splitter. One part is fed directly into a Si detector which measures the total reflectivity. The other part passes through another GT polarizer (analyzer). Then it is fed

to a Si detector to measure the Kerr rotation of the probe beam. The analyzer is set at a very small angle from the extinction so that it measures the Kerr rotation on a minimal background of reflectivity. The bias magnetic field is applied by using permanent magnets in the desired configuration. The pump beam is chopped by using an optical chopper (Thorlabs, MC2000B). The detectors measure the reflectivity and Kerr rotation by two lock-in amplifiers (SR830, Stanford Research System) in a phase sensitive manner using a reference beam from the optical chopper output. The temperature and humidity of the TRMOKE laboratory are maintained at ~22°C and ~30%, respectively.

E. Routine Alignments during Experiment

The regenerative cavity remains stable if the temperature, humidity and dust level in the air is maintained carefully. However, after few months a significant movement of the laser path at the output of Libra is generally observed resulting in a change in the entire optical path. In this setup, there are few crucial places where special care is taken to align the pump and probe beams on a regular basis.

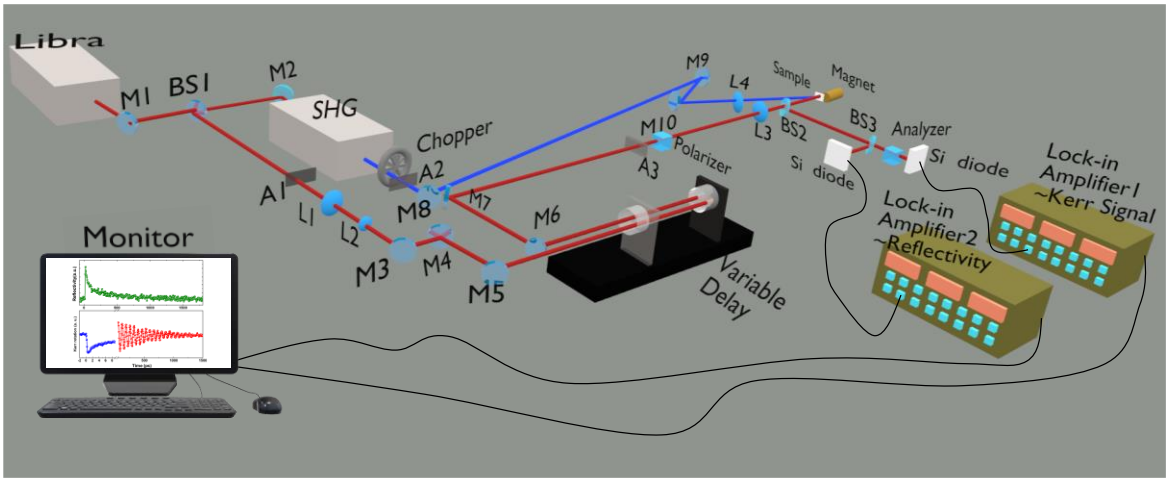

Figure 3. 14. Schematic of the noncolinear TRMOKE system present in our laboratory at S.N. Bose National Centre for Basic Sciences.

1. Monitoring of the parameters at the output of Libra – The power, wavelength, and FWHM of the fundamental laser beam (800 nm) is monitored daily. There is no external control provided for the user to align the cavity on a daily basis. If any significant deviation from the standard values is observed then involved alignment of the cavity is necessary.

2. Alignment before RR – The beam shift from the output of Libra can be checked by monitoring the path of the beam in a couple of irises before RR. Any unwanted shift can be adjusted by tweaking the tilt of mirrors placed before these irises. The RR is moved to

and fro by the delay stage to check any horizontal and vertical shift of the probe spot. By moving the RR in between two extreme ends on the delay stage the beam position can be checked using a height tool or the iris placed after the RR. The Beam movement can be nullified by using a set of mirrors placed before the RR.

3. Alignment after RR – There are three irises through which the probe beam can pass maintaining the desired horizontal and vertical positions. Any unwanted deviation of the probe beam in the path can be adjusted by a set of mirrors placed after RR.

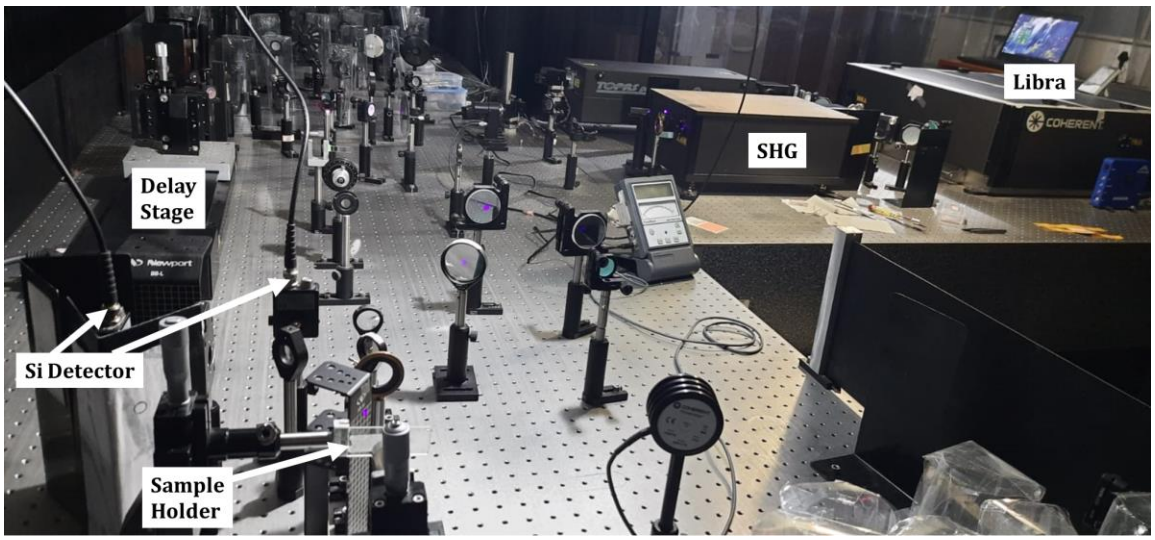

Figure 3. 15. Photograph of the noncolinear TRMOKE system present in our laboratory at the S.N. Bose National Centre for Basic Sciences.

4. Alignment of the pump beam – There is no external control of the SHG unit and usually the pump beam remains stable. Any slight misalignment of the pump beam is adjusted by changing the tilts of the respective mirrors placed in the pump path. The coarse overlap of the pump and the probe spots on the sample surface is achieved by monitoring them on a CCD camera, whereas the fine adjustment is done by maximizing the reflectivity signal at the zero-delay position of RR on the delay stage.

5. Finally, the alignments of the two detectors are checked by viewing the probe spot position at the centre of the sensor by using an IR viewer. After adjusting the optical components, the time-resolved reflectivity data from a test Si-substrate is recorded and its relaxation rate is compared with the standard data to verify the alignment condition and pump-probe overlap.

3.3.3 Brillouin Light Scattering Technique

BLS relies on the interaction between photons with quasiparticles such as phonon, plasmon, magnon etc. Here, a monochromatic laser beam is incident on a sample surface. Most part of the beam goes through reflection or absorption, whereas a small part of it scatters from the surface. In case of elastic scattering, the photon energy or frequency remains the same. However, a change in photons angular frequency is observed due to inelastic scattering which is the principle behind the spin-wave detection using BLS. The BLS measurement in this thesis was performed in backscattered geometry where the scattered light is collected by the same lens used for focusing the incident beam within a solid angle (defined by the numerical aperture of the lens) in the opposite direction of the incident beam. This geometry maximizes the wave vector of the spin-wave involved in the scattering process. The scattered beam is analyzed using a tandem Fabry-Pérot interferometer (TFPI) to extract information of the surface and bulk magnons. BLS technique has some salient features such as; detection of the thermally excited spin wave at room temperature without any external excitation, measurements of spin-wave dispersion in different possible geometry. Over the last few decades, different variants of BLS have been designed to study the spin-wave with frequency, time, spatial and phase resolution. In this thesis, we have employed the BLS for the measurements of collective spin-wave behaviour from an interconnected 3D network. In the succeeding paragraphs, the key components and instrumentation of BLS have been discussed.

A. Laser

A monochromatic solid-state laser source of wavelength 532 nm from Spectra Physics (Excelsior) is used for the precise measurement of spin-wave frequency. Here, the crystal of Nd^{3+} ions doped yttrium vanadate (Nd: YVO_4) is pumped using a diode laser source. The crystal emits infra-red laser light of wavelength 1064 nm. Further, it is converted to visible light by passing through a nonlinear LBO crystal for frequency doubling. It gives a green laser beam of wavelength 532 nm. The output of the laser beam has a diameter of around 670 μm and a divergence of 1.03 mrad. Overall, the laser system gives very stable output power and it does not require any external adjustments in day to day uses.

B. Tandem Fabry- Pérot Interferometer

The TFPI is the heart of BLS measurements. A sophisticated arrangement of two Fabry-Pérot interferometers (FPIs) is used in TFPI to achieve high spectral resolution for the

detection of spin-waves. Generally, the spin-wave frequency lies within 300 GHz, which corresponds to a wavenumber of around 10 cm^{-1}. This is almost 10^5 times smaller than the typical laser excitation frequency. Also, the cross section of inelastically scattered photons is much smaller than that of elastically scattered photons. Therefore, a highly sensitive detection technique is required with a high signal to noise ratio, which is able to pick up the signal from a small fraction of the incident laser beam. These conditions are achieved in TFPI bypassing the scattered beam three times through each FPI placed in tandem configuration. The transmission of light through a single FPI and TFPI is briefly discussed in the following sections.

i. Fabry-Pérot Interferometer

An FPI (etalon) consists of two partially reflective planar mirrors, mounted parallel to each other at a certain distance (L). The light enters the FPI and experiences multiple back and forth reflections, and transmissions. The transmitted lights interfere with each other. The condition for constructive interference for normal incidence is given by:

$$L = \frac{n\lambda}{2} \tag{3.2}$$

where n is an integer (transmission order) and λ is the wavelength of light. The frequency gap (Δf) between two consecutive orders is given by:

$$\Delta f = \frac{c}{2L} \tag{3.3}$$

where c is the velocity of light in vacuum. The inter-order spacing is defined as the free spectral range (FSR). The finesse (F) of the interferometer is related to the FSR.

$$F = \frac{\Delta f_{FSR}}{\Delta f_{FWHM}} \tag{3.4}$$

Where Δf_{FWHM} is the full width half maxima of the transmitted spectra. The finesse affects the intensity of transmitted light as given by the expression below.

$$\Delta I_t = \frac{I_0}{1+\left(\frac{4F^2}{\pi^2}\right)\sin^2\frac{2\pi L}{\lambda}} \tag{3.5}$$

Where I_0 is the incident light intensity. The above equation is also known as the Airy function which describes the periodicity of transmitted light intensity with mirror spacing and frequency. The finesse is the measure of the quality of the instrument which is connected to the reflectivity (R) of the mirror of FPI and is given by:

$$F = \frac{\pi\sqrt{R}}{(1-R)} \tag{3.6}$$

From the above equation, it is clear that higher reflectivity enhances the finesse of the FPI. The increment of finesse increases the FSR (eqn. 3.3) as Δf_{FWHM} decreases. On the other hand, if R is fixed, the increment in L decreases the FSR which enhances frequency resolution as the finesse is maintained at a fixed value. The contrast (C) of an FPI is given by:

$$C = 1 + \frac{4R}{(1-R)^2} \tag{3.7}$$

The contrast of the n-pass interferometer is the n-th power of that of the single pass interferometer contrast. For example, for a three-pass interferometer, the contrast will be a minimum of three orders of magnitude higher than the single pass interferometer.

ii. Tandem Operation

In case of one FPI, the periodicity of transmitted intensity as a function of mirror spacing is the major problem for identifying the frequencies of a scattered beam. For example, two wavelengths (λ_1 and λ_2) can satisfy the transmittance condition of different orders (m_1 and m_2) in an FPI of mirror spacing L.

$$L = m_1\lambda_1 = m_2\lambda_2 \tag{3.8}$$

As the reference beam determines the order of the transmitted beam. The order of the second wavelength (does not match with the reference beam) remains inaccessible.

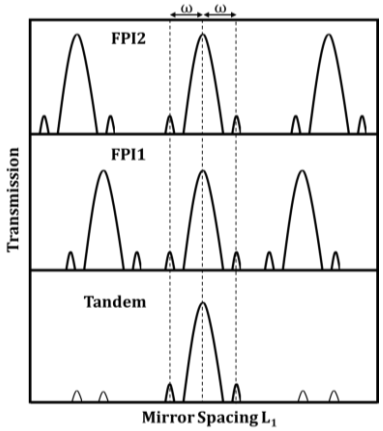

Figure 3. 16. Transmission Spectra of FPI1 and FPI2 and in tandem operation. The transmitted spectra consist of an intense elastic peak (frequency: ω_L) and two weaker sidebands ($\omega_L \pm \omega$).

Also, in case of a scattered beam, it is not possible to exactly identify the Stokes peak of a specific order or the anti-Stokes peak of the previous order. The tandem configuration is capable to solve this ambiguity. Here, the light passes through two consecutive FPIs placed at an angle α. This arrangement was developed by John Sandercock in 1971 [49,50]. The right mirror of each FPI is placed on a translational stage and the other one

on a separate angular orientation device. The scanning translational stage can move the right mirror of each FPIs along the optical axis of FPI1. A change in mirror spacing by an amount of d in FPI1 causes a change in FPI2, which is given by:

$$\Delta L_2 = \Delta L_1 \cos(\alpha) \tag{3.9}$$

where $\Delta L_1 = d$.

This also satisfies a synchronized condition:

$$\frac{\delta L_1}{\delta L_2} = \frac{L_1}{L_2} \tag{3.10}$$

This synchronization condition is employed to suppress the intermixing of different orders. Both the FPIs are adjusted for the transmission separately before the scanning on the linear stage. Though the FPIs transmit different orders, in combination they transmit a centre mode by suppressing the others which can be adjusted by changing the mirror spacing of FPI2. This arrangement enhances the FSR of the resultant spectra without affecting the spectral resolution. The light passes thrice through each FPIs to enhance the contrast. Subsequently, the six-pass beam is fed into a photomultiplier tube which counts the number of photons as a function of the mirror spacing and the ensuing frequency shift. In order to obtain this, the scanning stage constantly sweeps the distance corresponding to the required frequency window and the data is acquired for a long time to attain sufficient statistics. As a result, the acquired BLS intensity is proportional to the spin-wave intensity at any given frequency.

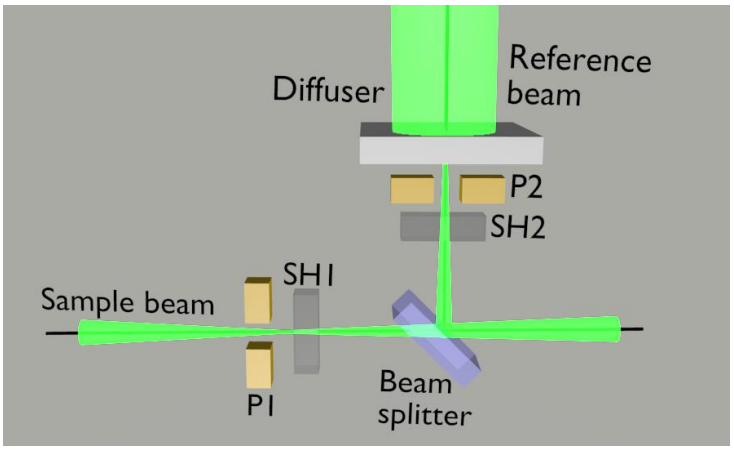

Figure 3. 17. Schematic of the pinhole and light modulator arrangement inside the TFPI of the BLS system.

C. Light Modulator

The light modulator is a double pinhole system that is placed at the light entrance path of TFPI as shown in Fig.3.17. With the synchronization with TFPI operation, the shutter SH1 and SH2 are alternatively opened to control the light intensity to protect the single photon counter detector from the intense elastic light. Here, Fig. 3.18(a) presents the spectrum of the scattered signal captured by the first pinhole (P1), while, Fig. 3.18(b) shows that of the reference beam passing through the second pinhole (P2). During the scanning of the elastic peak (i.e., region I, IV and V), P1 is closed and P2 is opened, allowing the reference beam to enter through it. This small intensity reference beam is further used to maintain the stabilization of the angular orientation of the FPIs. On the contrary, during the scanning for the Brillouin shifts (i.e., in regions II and III), P2 is closed but P1 is opened.

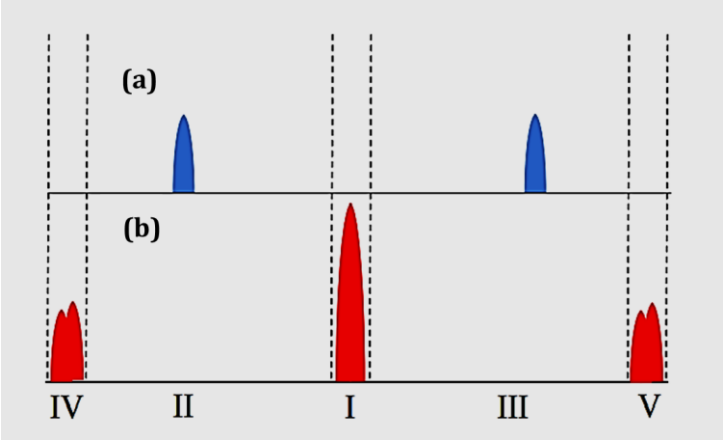

Figure 3. 18. A schematic of the part of the BLS spectrum which passes through shutter (SH), (a) SH1 and (b) SH2 when another shutter remains closed. A superposition of the spectra in (a) and (b) is acquired when SH1 and SH2 operate in synchronization.

D. Experimental Setup

The monochromatic continuous laser beam of wavelength 532 nm splits into two parts (90:10) using a beam splitter. The less intense part is guided using M1 and M2 toward the TFPI where it acts as a reference beam. The reference beam plays a crucial role during measurements. Firstly, it stabilizes the mirror spacing of the FPIs and helps to maintain it throughout the measurement. It also helps to determine the frequency shift in scattered beams with respect to the incident light frequency. On the other hand, the intense part passes through a half wave plate (introduce a π phase) and a polarized beam splitter to make the beam fully polarized (perpendicularly polarized). Then the beam is guided by the mirrors M3, M4, M5, M6 and a prism-mirror towards the sample which is placed in

between two pole pieces of an electromagnet. The electromagnet is used to apply an external magnetic field to the sample. A variable attenuator is used in between M3 and M4 to control the laser beam intensity to avoid sample overheating. The prism mirror is chosen in a small shape to minimize the blockage of backscattered light from the sample. The beam is focused on the sample using an achromatic doublet lens (L: numerical aperture 0.26). The backscattered beam is also collected by the lens. The inelastically scattered beams carry information of spin-wave frequency and wavevector which is given by the conservation of energy and momentum. The conservation of energy (frequency) and momentum (wave vector) due to interaction between incident photon and magnon (spin-wave: angular frequency ω and wave vector k) is given by:

$$\hbar\omega_S = \hbar\omega_i \pm \hbar\omega \tag{3.11}$$

$$\hbar k_S = \hbar k_i \pm \hbar k \tag{3.12}$$

where + (-) sign stands for anti-Stokes (Stokes) process and ω_i, k_i and ω_s, k_s are the angular frequency and wave vector of the incident and scattered light, respectively.

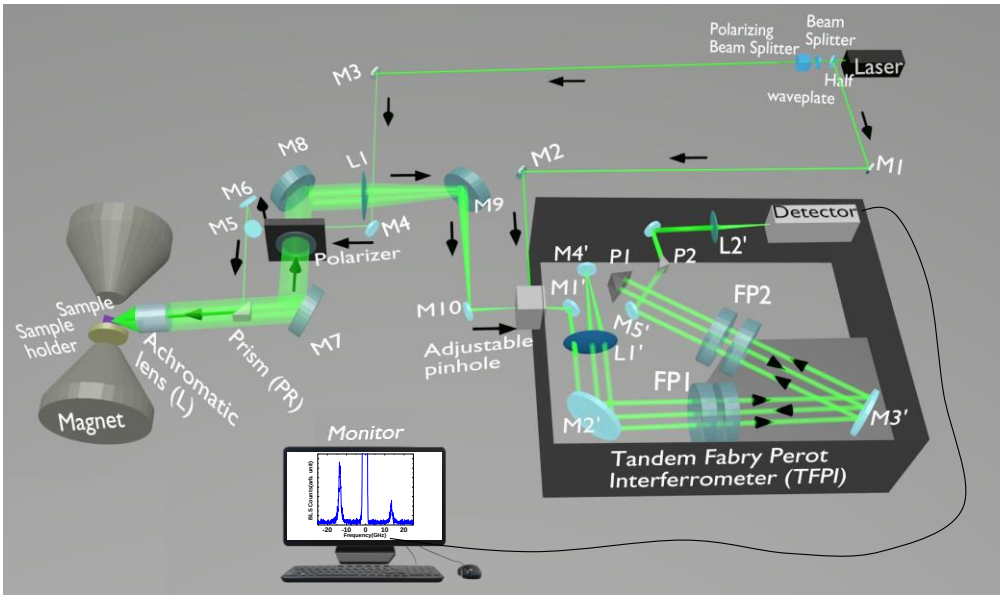

Figure 3. 19. Schematic of the BLS setup present in our laboratory at S.N. Bose National Centre for Basic Sciences.

The conservation of q is valid for in-plane components as during the scattering the conservation of perpendicular component does not hold good due to the translational broken symmetry. For an incidence angle of θ, the conservation of momentum eqn. (3.12) can be simplified as:

$$|k| = |k_i \sin\theta - k_s \sin\theta| = 2|k_i \sin\theta| \tag{3.13}$$

The sample is mounted on a high precision rotational stage (resolution: 1°) to change the incident angle of the laser light which gives access to different wave vectors as given by the above equation. In our measurement, the θ was kept fixed around 0° to probe the coherent spin-wave behaviour. The measurements were performed for the various magnetic fields by changing the current through the coil of the electromagnet. The backscattered light is guided by M7 towards an analyzer (P) which allows the magnetic information to pass through it and blocks the nonmagnetic signal (such as elastic information and phonons) by exploiting the cross-polarization relations between them.

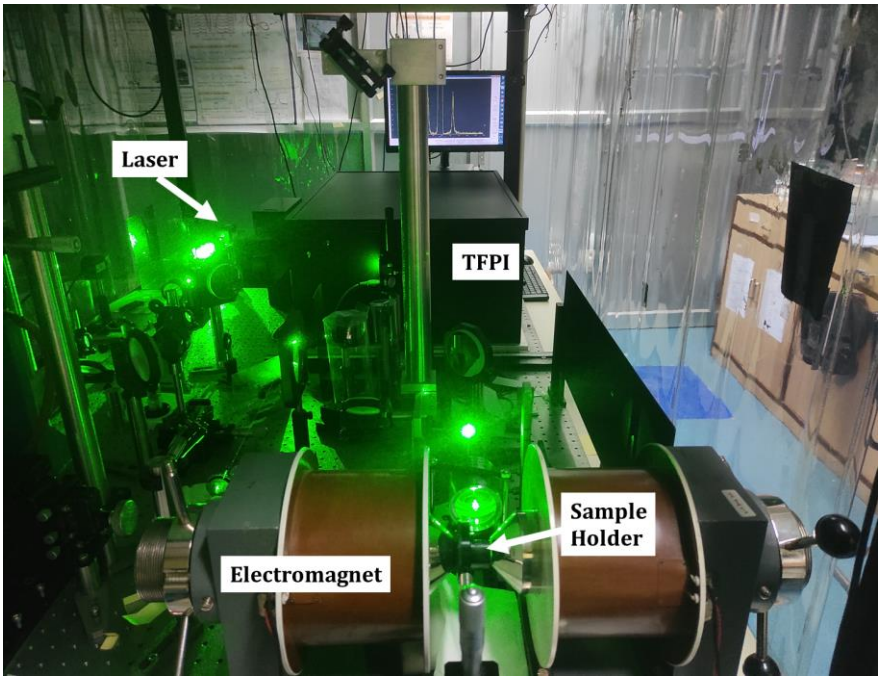

Figure 3. 20. Photograph of the BLS setup present in our laboratory at S.N. Bose National Centre for Basic Sciences.

Afterwards, the beam is guided by M8, M9, M10 and focused by L1 (placed between M8 and M9) at the entrance pinhole of the 3+3 pass TFPI for analyzing the spin-wave frequency. Inside the TFPI, the beam is guided by a mirror M1' which then reaches FP1 by passing through lens L1' and mirror M2'. After that, the beam reflects from M3' and passes through FP2. Subsequently, the beam is reflected from one prism (PR1') and it traces back its path via FP2 and FP1 and reaches M4'. The beam is once again reflected at M4', and thus, it gets redirected, passes through FP1 and FP2 for the third time and completes its 3+3 pass path. Finally, the beam reaches the single-photon counter (D) after passing through a prism (PR2'), two mirrors (M5' and M6') and one lens (L2'). Here, the

resulting light has a very low intensity which is detected by a single photon counter. The signal is analyzed and stored using software (GHOST).

3.4 Numerical Methods

The macrospin formalism can describe the magnetic behaviour of a single domain structure or a uniformly magnetized thin film. Here, the non-linear differential equation, i.e., Landau-Lifshitz-Gilbert equation is solved by linearizing it under a small angle approximation to understand the magnetization dynamics. In case of confined magnetic structures, the uncompensated spins at the boundary give rise to demagnetizing fields which affect the magnetic textures as well as magnetization dynamics, and hence, the calculations are not straightforward. The analytical solutions become more complicated for non-ellipsoidal shapes. Several analytical efforts have been made to determine the demagnetizing field distributions in such nanostructures in all of the three dimensions. However, the theoretical reproduction of experimentally observed behaviour becomes more complicated in a practical structure where the fabrication artifacts add more complexity in the shape in form of defects and deviations for ideal shape among others. Therefore, the development of micromagnetic modelling and different other numerical methods emerged to address these issues. The micromagnetic simulation has become a popular tool to explore the magnetization behaviour of nanostructures in 1D, 2D and 3D due to the availability of different open-source and commercial software packages.

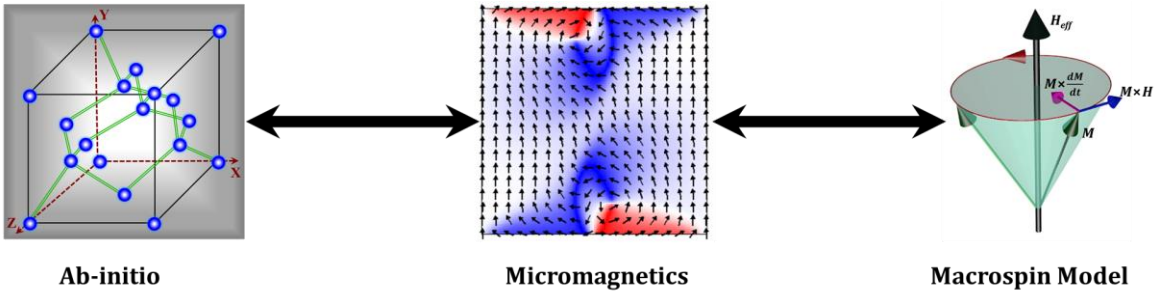

Figure 3. 21. Correlation between micromagnetics with ab-initio and macrospin model.

Micromagnetism is a continuum theory where the magnetic parameters vary continuously in space. In the micromagnetic simulation, the sample is divided into a number of unit cells each of which consists of a magnetic moment (macrospin) which interacts with the neighbouring cell's moment by short-range exchange and long-range dipolar interactions, under the influence of anisotropy fields, and in presence of external magnetic fields, where additional field terms can also be introduced (simplified form of

ab-initio or first principle calculations). At a particular position, the magnitude of magnetization, i.e., saturation magnetization is fixed. However, it can freely rotate in a 3D spherical coordinate. Based on the discretization scheme of the sample, micromagnetic simulation can be divided into two classes, namely, the finite difference method where the sample is discretized into a number of regular parallelepiped cells and the finite element method where the sample is discretized into different geometric shapes like triangles, squares or rectangles in 2D, and tetrahedrons, cubes or hexahedra in 3D.

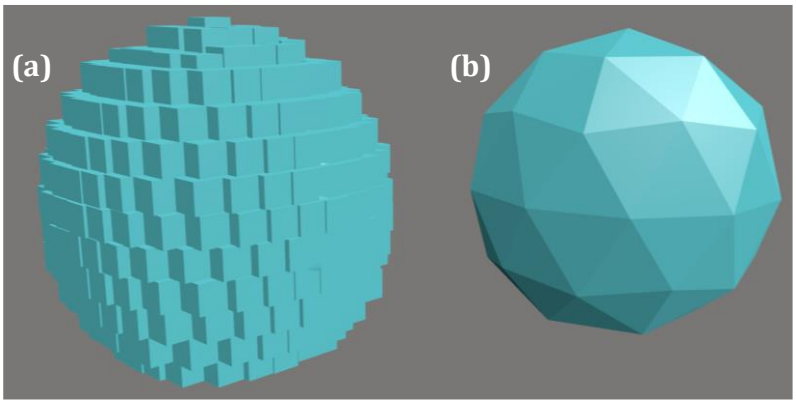

Figure 3. 22. Generation of spherical shape in – (a) finite difference method (cuboidal cell) and (b) finite element method (tetrahedral cell).

The finite element method is useful for the reproduction of any arbitrary shape in the simulation. However, the computational speed is much faster in case of the finite difference method. The main time-consuming part of the micromagnetic simulation is the calculation of the long-range dipole-dipole interaction term (demagnetization field). In case of the finite difference method, due to its regular grid structure, the demagnetizing field is computed using convolution via fast Fourier transformation which is not possible for irregular grid-based finite element methods. This makes the finite difference method a faster computational process compared to the finite element method. Examples of various finite element method-based simulators are NMAG [51], MAGPAR [52], MicroMagnum [53], TetraMag [54], FEELLGOOD [55], FastMag [56] etc. Few examples of finite difference method-based simulators are Object Oriented Micromagnetic Frameworks (OOMMF) [57], LLG micromagnetic simulator [58], MicroMagus [59], MuMax3 [60], Boris [61], Magsimus [62], GoParallel [61] etc. The micromagnetic simulations are valid for timescale >1ps and length scale greater than the atomic scale [63]. In this thesis, we have used the finite difference method-based OOMMF, LLG micromagnetic simulator and MuMax3 software. We have also used a custom-built

DotMag software to calculate the spin-wave mode profiles using the dynamic output files of the micromagnetic simulators. Brief descriptions of the software packages are given below.

3.4.1 OOMMF

OOMMF is an open-source CPU based micromagnetic simulator developed at the National Institute of Standards and Technology (NIST) by M. J. Donahue and D. G. Porter [57]. The core engine code is written in C++ and the interface is written in Tcl and Tk language on top of the source code. The OOMMF package is available on all popular computer platforms, i.e., Unix, Windows and Mac. It utilizes an ordinary differential equation solver to relax spins on a quasi-two-dimensional mesh of square cells. Anisotropy, applied field, and initial magnetization can be varied point wise and arbitrarily shaped elements can be modelled. In case of 2D structures, the geometry can be introduced via an image in '.bmp' picture format which gives the freedom to draw and mimic any possible shape. Besides, the sample geometry can be defined using a script by a set of equations. The system can also be discretized in all three dimensions. The simulations are performed at T = 0 K in OOMMF. The problem is defined with all the required input parameters and initial conditions in a '.mif' file. The intrinsic energies such as exchange energy and magnetocrystalline energy can be specified by providing the numerical values of the exchange constant, anisotropy constant and the direction of anisotropy field in the cartesian coordinate. All the material parameters are provided in the SI unit. It is crucial to set the proper evolver in the script. There are two types of evolvers: time evolvers to take care of LLG dynamics and energy minimization evolvers to locate the local minimum in the energy surface by using a direct minimization technique. Evolvers are mainly controlled by their compatible drivers (i.e., time and minimization drivers). The drivers provide a magnetization configuration to the evolvers with an indication of advancing the configuration by one step (also called 'iteration'). The drivers determine when a simulation stage (or run) is completed using a specified stopping criterion as defined in the input MIF file. For preparing magnetic ground state the minimization evolver is generally used to obtain reliable results. The convergence criterion in the simulation is created by setting the stopping value of d$\boldsymbol{m}$/dt or time. At the stopping time, the maximum value of d$\boldsymbol{m}$/dt across all spins reduces below the set value. The maximum torque should go well below 10^{-6} A/m then. The final magnetization state obtained as the

equilibrium state is then specified as the initial magnetization in the dynamic simulation file. Providing an external perturbation in terms of the additional field the magnetization dynamics is simulated. The time dependent components of magnetization, magnetic field and energies can be extracted in the output file with '.omf', '.ohf' or '.ovf' formats. OOMMF also offers the user to set a periodic boundary condition (PBC) in different dimensions for simulating realistic systems with finite a smaller sample geometry.

3.4.2 MuMax3

MuMax3 [60] is another open source, GPU accelerated micromagnetic simulator, which requires high performance graphics card. GPU-based acceleration provides speeding up by 100x as compared to the CPU-based micromagnetic simulation and can simulate around 16-million-unit cells using 2GB of GPU RAM. The software package is available on Unix, Windows and Mac platforms. The package was developed at the DyNaMat group of Prof. Van Waeyenberge at Ghent University. The package is written in Go language and it uses CUDA C kernel for faster processing. The simulation is performed using a Windows power shell and the progress can be monitored in a web-based user interface. The output is obtained in form of '.ovf' data format which is compatible with the postprocessing and viewing tools for OOMMF. The code is written in a text file in '.mx3' or '.go' format. The sample geometry can be defined by inserting an image in PNG format. The MuMax3 provides some basic 2D and 3D shapes. These shapes can be easily arranged in complex geometry using 3D rotational, translational, scaling functions along with the Boolean operations available in the package, i.e., AND, OR, XOR. These features make it suitable for designing a complex three-dimensional structure. The combination of the ability to the reproduction of complex geometry with the capability of handling a large number of cells with high performance speed makes the MuMax3 software a powerful tool for micromagnetic simulation study in complex 3D nanoscale structures. In a unit cell, the volumetric quantities (M, K etc.) are defined at the middle of the cells, whereas coupling quantities are specified at the faces of the cells. MuMax3 offers several types of Runge-Kutta methods (RK45, RK23, RK12 etc.) to solve the LLG equation with different convergence criteria and error estimation. The solver can be easily defined in the code by defining the solver number. MuMax3 provides relax and minimize function that can find the energy minimum of the system. The relax function tries to closely obtain the minimum energy. These functions prevent all excitations (such as temperature, current, time

dependent magnetic field) during the energy minimization. To make the numerical experiments more realistic, a system with finite geometry can be repeated with the help of PBC and simulation can be performed using the macro-geometry approach. This is different from what is generally being used in OOMMF. The user can set the number of repetitions in which the image can be copied on each side of the simulation box.

3.4.3 LLG Simulator

LLG simulator is a commercially available package that was developed and licensed by M. R. Scheinfein [58]. It has three modules of functionality that are specified in terms of defining the solution. Those maintain consistency with the Windows event-driven programming interface. These modules are briefly described below.

• Input phase: This is used to define the parameters and design customized simulations. Though it increases the risk of input errors, the process is user friendly. As a countermeasure LLG performs exhaustive error checking. Since the program solves the LLG equations using finite differences for exchange energies and fields, as well as boundary elements for magnetostatic self-energies and fields, the object must be defined as a grid. This simulator uses rectangular pixels on a cartesian grid. After setting up the environment, LLG initializes all of the arrays to start computing the demagnetization field coupling tensors. It calculates the field for any boundary conditions. As the simulation phase begins the user is prompted to store the simulation parameters in several files.

• Simulation phase: In this phase, the desired simulation is performed based on the solution of the differential equations (LLG Simulation Sheet).

• Review phase: This phase helps in reviewing the results by re-playing them through a graphically animated movie (LLG Movie Viewer) or the user can view a domain or field file in the viewer control.

The LLG supports four integrators to solve an ordinary differential equation. The most primitive one is the Euler Cartesian method, which is the fastest but least accurate. The Rotation Matrices method is the integrator of choice for solutions where damping is greater than 0.5. This is used to study the magnetic ground state configurations in our systems. The Cartesian Predictor-Corrector integrator is the most accurate and also faster when damping is about 0.01. The Gauss-Seidel Stable method is a semi-implicit first-order integration scheme. The integration time steps can be much larger on fine grids using this method. The study of quasistatic magnetization reversal is more

authentic here. In this thesis, the results are obtained using the 2.50 version of the LLG simulator which works with a single processor and is currently unable to perform parallel computation.

3.4.4 DotMag

The dynamic simulations using OOMMF and MuMax3 software generates '.omf' and '.ovf' files, respectively, which contain the information of the spatial distribution of magnetization (*M(t,x,y,z)*) at a particular given time which can be analyzed to extract the information of superposed multiple resonant modes. In order to extract the power and phase profiles of the multiple resonant modes, we analyzed the '.omf' and '.ovf' files using our home-built post-processing code DotMag [64,65]. To calculate the power and phase profiles in the frequency domain, it takes the fast Fourier transformation of time-domain data along a plane of the sample by keeping one of the coordinates fixed (either x or y or z). If we fix a plane at z = z_1 then the FFT is taken along the x-y plane: $\widetilde{M}^{z_1}(f,x,y) = FFT\left(M^{z_1}(t,x,y)\right)$. Then the power and phase are calculated for a resonant mode of particular frequency $f = f_1$ which can be written as:

Power: $$P^{z_1 f_1}(x,y) = 20log_{10}\left|\widetilde{M}^{z_1}(f_1,x,y)\right| \quad (3.14)$$

and

Phase: $$\phi^{z_1 f_1}(x,y) = \text{atan2}\left(Im\left(\widetilde{M}^{z_1}(f_1,x,y)\right), Re\left(\widetilde{M}^{z_1}(f_1,x,y)\right)\right) \quad (3.15)$$

The power is presented usually in terms of dB and phase in radian. MATLAB is used to run and control this code, and the output is obtained with the plot of space-dependent power and phase at discrete frequencies. The frequency resolution necessarily depends upon the total simulation time and the spatial resolution of calculated power and phase maps depends upon the discretization of the sample (or the number of cells) during micromagnetic simulation.

References

[1] B. Ziaie, A. Baldi, and M. Z. Atashbar, in Springer Handbook of Nanotechnology (Springer, 2010), p. 231.
[2] K. E. Drexler, Engines of Creation: The Coming Era of Nanotechnology (Eric Dresler, 2000).
[3] P. Fischer, D. Sanz-Hernández, R. Streubel, and A. Fernández-Pacheco, Launching a New Dimension with 3D Magnetic Nanostructures; APL Materials **8,** 010701 (2020).
[4] A. Fernández-Pacheco, R. Streubel, O. Fruchart, R. Hertel, P. Fischer, and R. P. Cowburn, Three-Dimensional Nanomagnetism; Nat. Commun. **8,** 15756 (2017).
[5] V. S. Ramachandran and J. J. Beaudoin, Handbook of Analytical Techniques in Concrete Science and Technology: Principles, Techniques and Applications (Elsevier, 2000).
[6] D. McMullan, Scanning Electron Microscopy 1928–1965; Scanning **17,** 175 (1995).
[7] G. Binnig, C. F. Quate, and C. Gerber, Atomic Force Microscope; Phys. Rev. Lett. **56,** 930 (1986).
[8] J. Goldstein, D. E. Newbury, D. C. Joy, C. E. Lyman, P. Echlin, E. Lifshin, L. Sawyer, and J. R. Michael, Scanning Electron Microscopy and X-Ray Microanalysis: Third Edition (Springer US, 2012).
[9] H. Hopster and H. P. Oepen, Magnetic Microscopy of Nanostructures (Springer, 2005).
[10] Z. Q. Qiu and S. D. Bader, Surface Magneto-Optic Kerr Effect; Rev. Sci. Instrum. **71,** 1243 (2000).
[11] A. Barman and J. Sinha, Spin Dynamics and Damping in Ferromagnetic Thin Films and Nanostructures (Springer International Publishing, 2017).
[12] C. Vieu, F. Carcenac, A. Pepin, Y. Chen, M. Mejias, A. Lebib, L. Manin-Ferlazzo, L. Couraud, and H. Launois, Electron Beam Lithography: Resolution Limits and Applications; Appl. Surf. Sci. **164,** 111 (2000).
[13] H.-B. Sun, S. Matsuo, and H. Misawa, Three-Dimensional Photonic Crystal Structures Achieved with Two-Photon-Absorption Photopolymerization of Resin; Appl. Phys. Lett. **74,** 786 (1999).
[14] H.-B. Sun, T. Tanaka, and S. Kawata, Three-Dimensional Focal Spots Related to Two-Photon Excitation; Appl. Phys. Lett. **80,** 3673 (2002).
[15] H.-B. Sun, T. Kawakami, Y. Xu, J.-Y. Ye, S. Matuso, H. Misawa, M. Miwa, and R. Kaneko, Real Three-Dimensional Microstructures Fabricated by Photopolymerization of Resins through Two-Photon Absorption; Opt. Lett. **25,** 1110 (2000).
[16] C. Donnelly, M. Guizar-Sicairos, V. Scagnoli, M. Holler, T. Huthwelker, A. Menzel, I. Vartiainen, E. Müller, E. Kirk, S. Gliga, J. Raabe, and L. J. Heyderman, Element-Specific X-Ray Phase Tomography of 3D Structures at the Nanoscale; Phys. Rev. Lett. **114,** 115501 (2015).
[17] G. Williams, M. Hunt, B. Boehm, A. May, M. Taverne, D. Ho, S. Giblin, D. Read, J. Rarity, R. Allenspach, and S. Ladak, Two-Photon Lithography for 3D Magnetic Nanostructure Fabrication; Nano Res. **11,** 845 (2018).
[18] A. May, M. Hunt, A. Van Den Berg, A. Hejazi, and S. Ladak, Realisation of a frustrated 3D magnetic nanowire lattice; Commun. Phys. 2, 13 (2019).
[19] M. Hunt, M. Taverne, J. Askey, A. May, A. Van Den Berg, Y.-L. D. Ho, J. Rarity, and S. Ladak, Harnessing Multi-Photon Absorption to Produce Three-Dimensional Magnetic Structures at the Nanoscale; Materials **13** (2020).
[20] A. Fert and L. Piraux, Magnetic Nanowires; J. Magn. Magn. Mater. **200,** 338 (1999).
[21] S. Pal, S. Saha, D. Polley, and A. Barman, Magnetization Reversal Dynamics in Co Nanowires with Competing Magnetic Anisotropies; Solid State Commun. **151,** 1994 (2011).
[22] S. Pal, S. Saha, M. V. Kamalakar, and A. Barman, Field-Dependent Spin Waves in High-Aspect-Ratio Single-Crystal Ferromagnetic Nanowires; Nano Res. **9,** 1426 (2016).
[23] S. Sharma, A. Barman, M. Sharma, L. R. Shelford, V. V. Kruglyak, and R. J. Hicken, Structural and Magnetic Properties of Electrodeposited Cobalt Nanowire Arrays; Solid State Commun. **149,** 1650 (2009).

[24] M. R. Karim, D. Panda, A. Adhikari, P. Sharangi, P. Mandal, S. Ghosh, S. Bedanta, A. Barman, and I. Sarkar, Electrodeposited Heusler Alloy Films with Enhanced Magneto-Optical Property; Mater. Today Commun. **25,** 101678 (2020).
[25] J. E. Mahan, Physical Vapor Deposition of Thin Films (Wiley-VCH, 2000).
[26] A. May, M. Hunt, A. Van Den Berg, A. Hejazi, and S. Ladak, Realisation of a Frustrated 3D Magnetic Nanowire Lattice; Commun. Phys. **2,** 13 (2019).
[27] A. K. Chaurasiya, A. K. Mondal, J. C. Gartside, K. D. Stenning, A. Vanstone, S. Barman, W. R. Branford, and A. Barman, Comparison of Spin-Wave Modes in Connected and Disconnected Artificial Spin Ice Nanostructures Using Brillouin Light Scattering Spectroscopy; ACS Nano **15,** 11734 (2021).
[28] M. W. Pyun, E. J. Kim, D.-H. Yoo, and S. H. Hahn, Oblique Angle Deposition of TiO_2 Thin Films Prepared by Electron-Beam Evaporation; Appl. Surf. Sci. **257,** 1149 (2010).
[29] K. Masood, M. Iqbal, and M. Zakaullah, Emission characteristics of the thermionic electron beam sources developed at EBSDL; Nucl. Instrum. Methods Phys. Res. A: Accel. Spectrom. Detect. Assoc. Equip. **584,** 9 (2008).
[30] J. Yang, W. Cui, Y. Li, G. Xie, N. Zhang, R. Wang, T. Hu, and H. Zhang, Investigation of Argon Ion Sputtering on the Secondary Electron Emission from Gold Samples; Appl. Surf. Sci. **382,** 88 (2016).
[31] S. Swann, Magnetron Sputtering; Physics in technology **19,** 67 (1988).
[32] A. K. Chaurasiya, S. Choudhury, J. Sinha, and A. Barman, Dependence of Interfacial Dzyaloshinskii-Moriya Interaction on Layer Thicknesses in Ta/CoFeB/TaOx Heterostructures from Brillouin Light Scattering; Phys. Rev. Appl. **9,** 014008 (2018).
[33] S. N. Panda, S. Mondal, J. Sinha, S. Choudhury, and A. Barman, All-Optical Detection of Interfacial Spin Transparency from Spin Pumping in β-Ta/CoFeB Thin Films; Sci. Adv. **5,** eaav7200 (2019).
[34] Y. Kitade, H. Komoriya, and T. Maruyama, Patterned Media Fabricated by Lithography and Argon-Ion Milling; IEEE Trans. Magn. **40,** 2516 (2004).
[35] Y. Kamata, A. Kikitsu, H. Hieda, M. Sakurai, and K. Naito, Ar Ion Milling Process for Fabricating CoCrPt Patterned Media Using a Self-Assembled PS-PMMA Diblock Copolymer Mask; J. Appl. Phys. **95,** 6705 (2004).
[36] G. D. Danilatos, Introduction to the ESEM Instrument; Microsc. Res. Tech. **25,** 354 (1993).
[37] S. Fan, M. G. Chapline, N. R. Franklin, T. W. Tombler, A. M. Cassell, and H. Dai, Self-Oriented Regular Arrays of Carbon Nanotubes and Their Field Emission Properties; Science **283,** 512 (1999).
[38] A. A. Talin, K. A. Dean, and J. E. Jaskie, Field Emission Displays: A Critical Review; Solid·State Electron. **45,** 963 (2001).
[39] P. N. Argyres, Theory of the Faraday and Kerr Effects in Ferromagnetics; Phys. Rev. **97,** 334 (1955).
[40] M. Faraday, Faraday's Diary: Being the Various Philosophical Notes of Experimental Investigation Made by Michael Faraday, During the Years 1820-1862 and Bequeathed by Him to the Royal Institution of Great Britain, Vol. 1 (G. Bell and sons, Limited, 1932).
[41] J. Kerr, XLIII. On Rotation of the Plane of Polarization by Reflection from the Pole of a Magnet; London, Edinburgh Dublin Philos. Mag. J. Sci. **3,** 321 (1877).
[42] A. Kundt, XXXV. On the Electromagnetic Rotation of the Plane of Polarization of Light by Means of Iron, Cobalt, and Nickel; London, Edinburgh Dublin Philos. Mag. J. Sci. **18,** 308 (1884).
[43] S. Mondal, S. Choudhury, N. Jha, A. Ganguly, J. Sinha, and A. Barman, All-Optical Detection of The Spin Hall Angle in W/CoFeB/SiO_2 Heterostructures with Varying Thickness of the Tungsten Layer; Phys. Rev. B **96,** 054414 (2017).
[44] A. Ganguly, R. M. Rowan-Robinson, A. Haldar, S. Jaiswal, J. Sinha, A. T. Hindmarch, D. A. Atkinson, and A. Barman, Time-Domain Detection of Current Controlled Magnetization Damping in Pt/$Ni_{81}Fe_{19}$ Bilayer and Determination of Pt Spin Hall Angle; Appl. Phys. Lett. **105,** 112409 (2014).

[45] User's Manual, Millenia eV: Diode-Pumped, CW Visible Laser System, (Spectra-Physics, California, USA, 2017).
[46] A. Yariv, P. E. E. A. Yariv, P. Yeh, and P. Yeh, Optical Waves in Crystals: Propagation and Control of Laser Radiation (Wiley, 1984).
[47] User's Manual, Tsunami: Mode-locked Ti:sapphire Laser, (Spectra-Physics, California, USA, 2002).
[48] L. J. Singh, Z. H. Barber, A. Kohn, A. K. Petford-Long, Y. Miyoshi, Y. Bugoslavsky, and L. F. Cohen, Interface Effects in Highly Oriented Films of the Heusler Alloy Co_2MnSi on GaAs (001); J. Appl. Phys. **99,** 013904 (2006).
[49] M. Balkanski, Proceedings of the Second International Conference on Light Scattering in Solids (Paris, July 19-23, 1971) (Flammarion Sciences, 1971).
[50] J. Sandercock and W. Wettling, Light Scattering from Thermal Magnons in Iron and Nickel; IEEE Trans. Magn. **14,** 442 (1978).
[51] T. Fischbacher, M. Franchin, G. Bordignon, and H. Fangohr, A Systematic Approach to Multiphysics Extensions of Finite-Element-Based Micromagnetic Simulations: Nmag; IEEE Trans. Magn. **43,** 2896 (2007).
[52] W. Scholz, J. Fidler, T. Schrefl, D. Suess, H. Forster, and V. Tsiantos, Scalable parallel micromagnetic solvers for magnetic nanostructures; Comput. Mater. Sci. **28,** 366 (2003).
[53] C. Abert, L. Exl, G. Selke, A. Drews, and T. Schrefl, Numerical Methods for the Stray-Field Calculation: A Comparison of Recently Developed Algorithms; J. Magn. Magn. Mater. **326,** 176 (2013).
[54] A. Kakay, E. Westphal, and R. Hertel, Speedup of FEM Micromagnetic Simulations with Graphical Processing Units; IEEE Trans. Magn. **46,** 2303 (2010).
[55] FEELLGOOD, http://feellgood.neel.cnrs.fr./.
[56] J.-K. Byun, I. Volvach, and V. Lomakin, Fast Optimal Design of Micromagnetic Devices Using FastMag and Distributed Evolutionary Algorithm; IEEE Trans. Magn. **52,** 1 (2016).
[57] M. Donahue and D. G. Porter, OOMMF User's guide, version1.0, Interagency Report NISTIR 6376; National Institute of Standard and Technology: Gaithersburg, MD, U.S.A.; (1999).
[58] LLG Micromagnetics Simulator, http://llgmicro.home.mindspring.com/.
[59] MicroMagus, http://www.micromagus.de/home.html.
[60] A. Vansteenkiste, J. Leliaert, M. Dvornik, M. Helsen, F. Garcia-Sanchez, and B. Van Waeyenberge, The Design and Verification of MuMax3; AIP Adv. **4,** 107133 (2014).
[61] S. Lepadatu, Boris Computational Spintronics—High Performance Multi-Mesh Magnetic and Spin Transport Modeling Software; J. Appl. Phys. **128,** 243902 (2020).
[62] J. O. Oti, A General-Purpose Phenomenological Micromagnetic Model for Modern Giant Magnetoresistive Devices; IEEE Trans. Magn. **46,** 2338 (2010).
[63] S.-K. Kim, Micromagnetic Computer Simulations of Spin Waves in Nanometre-Scale Patterned Magnetic Elements; J. Phys. D: Appl. Phys. **43,** 264004 (2010).
[64] D. Kumar, O. Dmytriiev, S. Ponraj, and A. Barman, Numerical Calculation of Spin Wave Dispersions in Magnetic Nanostructures; J. Phys. D: Appl. Phys. **45,** 015001 (2011).
[65] G. Venkat, D. Kumar, M. Franchin, O. Dmytriiev, M. Mruczkiewicz, H. Fangohr, A. Barman, M. Krawczyk, and A. Prabhakar, Proposal for a Standard Micromagnetic Problem: Spin Wave Dispersion in a Magnonic Waveguide; IEEE Trans. Magn. **49,** 524 (2013).

Chapter 4

4. Nanochannels for Spin-Wave Manipulation in $Ni_{80}Fe_{20}$ Nanodot Arrays

4.1 Introduction

Periodically patterned thin film magnetic nanostructures, commonly known as magnonic crystals, is an interesting research field since its inception in 1970s [1,2] due to its potential applications in wave-based computing, on-chip GHz frequency data communication, processing, low energy nanoelectronics devices among others. Spin-wave is the propagation of perturbed energy from the equilibrium state energy in the form of phase in a magnetically coupled system, which acts as information carrier in magnonics [3,4]. In addition to the fundamental understanding of spin-wave in various one-, two- and three-dimensional magnonic crystals [5], a number of miniaturized components and devices such as spin-wave based multiplexer [6], interferometer [7], grating [8], waveguides [9,10], phase shifters [11], directional couplers [12], nanomagnetic antenna [13] and neuromorphic computing [14] have been demonstrated during last one decade. More recently strong coupling of magnons with microwave photon [15], phonon [16], magnon [17,18] and superconducting qubits [19] have been explored as hybrid systems for quantum transduction as well energy harnessing from alternative sources. Control of magnon propagation using topological spin texture has landed a new research field of spin-texture controlled magnonics [20].

In essence, complete understanding and control of spin-waves in patterned arrays of nanomagnets is at the core of the research in magnonics. The overwhelming progress in nanofabrication and high-frequency measurement techniques have made it possible to explore the spin-wave dynamics in various complex patterned magnetic nanostructures. In the last decade, there have been a large number of studies of spin-wave propagation, localization, hybridization and damping on different types of patterned structures such as physically isolated periodically patterned magnetic structures, namely, dot lattices [21-27], nanowire and nanostripes [28-30], nanochannels (NCs) [31] and connected structures, namely, antidot lattices [32-38]. The main focus of studying patterned magnetic nanostructures is to understand and tune the spin-wave frequency, nature of

modes, mode profiles and damping by varying the element width [22,24,29,39], shape [27,36,37], lattice constant [25,40], lattice symmetry [26,38], base material [37,41] as well as by changing the external bias magnetic field strength and orientation [34-36]. Further, the filled antidot lattices [42] and other forms of bicomponent magnonic crystals [43] offer more freedom to tune the spin-wave properties. There have been a large number of studies on spin-wave dynamics in ferromagnetic antidot lattices. Most of the studies were focused on the variation of diameter, shape, separation and lattice symmetry of antidots, which dealt with magnetic elements connected by irregularly shaped nanochannels. The complex demagnetizing field profiles in such structures made it non-trivial to understand the role of nanochannels on the spin-wave spectra in these systems.

Here, we have investigated the spin-wave dynamics in two-dimensional (2D) square arrays of $Ni_{80}Fe_{20}$ (Permalloy; Py hereafter) nanodots which are physically connected to its neighbouring nanodots by simple rectangular shaped NCs of the same material. We have varied the dot size (S) and the nanochannel length (l) while keeping the nanochannel width (w) constant. The filling fraction (area covered by Py/area of one unit cell) increases with decreasing S and l. We have exploited a custom-built time-resolved magneto-optical Kerr effect (TRMOKE) microscope to reliably measure the local precessional dynamics of the samples. We have observed rich spin-wave spectra in these connected nanodot (CND) arrays. The number of spin-wave modes decreases with increasing filling fraction due to the reduction in the demagnetizing region. All the spin-wave modes are found to be coupled between the dots through the vertical NCs (VNCs: connecting the nanodots perpendicular to the applied magnetic field (H) direction) except the highest frequency mode, which shows a mixed backward volume-Damon Eshbach (BV-DE) behaviour. On the contrary, the power of the highest frequency mode is mainly concentrated inside the horizontal NCs (HNCs: connecting the nanodots parallel to H). Furthermore, using numerical micromagnetic simulations we have shown the role of NCs to modulate the higher frequency modes due to the dipole-exchange coupling between the dots.

4.2 Experimental Details

The square shaped arrays Py CNDs each with a 25 × 25 μm^2 area were fabricated by using a combination of electron-beam evaporation, electron-beam lithography and ion milling

on self-oxidized Si (100) substrate. The 20-nm-thick Py film coated with a 60-nm-thick Al_2O_3 protective layer was deposited in an ultra-high vacuum chamber at a base pressure of 2×10^{-8} Torr on a commercially available self-oxidized Si(100) substrate. Bi-layer poly(methyl methacrylate)/methyl methacrylate (PMMA/MMA) resist was used for e-beam lithography to make the resist pattern on the Py thin film followed by ion milling at a base pressure of 1×10^{-4} Torr with a beam current of 60 mA for 6 min for creating the pattern.

The ultrafast magnetization dynamics of the CND arrays was measured by using an all-optical TRMOKE microscope based on a two-colour collinear pump-probe technique [43]. The second harmonic (λ = 400 nm, pulse-width = 100 fs, fluence = 18 mJ/cm^2) of a Ti-Sapphire oscillator (Tsunami, Spectra-Physics) was used to excite the dynamics, while the time-delayed fundamental beam (λ = 800 nm, pulse-width = 80 fs, fluence = 2 mJ/cm^2) was used to detect the ensuing Kerr rotation as a function of the delay time. The time resolution of the system is a little above 100 fs which is determined by the cross-correlation between the pump and the probe beam. The collinear pump-probe beam is focused on the sample by a single microscope objective (MO) of numerical aperture, N.A. = 0.65. The probe beam is tightly focused with ~800 nm spot size on the sample surface by the MO, where the pump beam becomes slightly defocused with about 1 μm spot size, and they are precisely overlapped and placed on the desired region of the sample by using a piezoelectric x-y-z scanning stage. This ensures the measurement of the magnetization dynamics from the uniformly excited region of the sample. The TRMOKE microscope is equipped with a feedback loop of the scanning stage, a CCD camera and a white light illumination system for better stability and viewing. The same MO collects the back-reflected beams, out of which the pump beam is filtered out and the probe is steered to an optical bridge detector to simultaneously measure the time-resolved Kerr rotation and reflectivity. Two lock-in amplifiers are used to measure the signals separately in a phase sensitive manner by using the electrical output from an optical chopper, which is used to chop the pump beam at a 2 kHz frequency. A static magnetic field is applied at a small angle of about 10° from the sample plane which generates a small out-of-plane demagnetizing field. The in-plane component of this magnetic field is defined as the bias field, *H*. After the laser induced ultrafast demagnetization, the out-of-plane component of the demagnetizing field is modified rapidly, inducing a damped precessional motion in the sample.

4.3 Results and Discussions

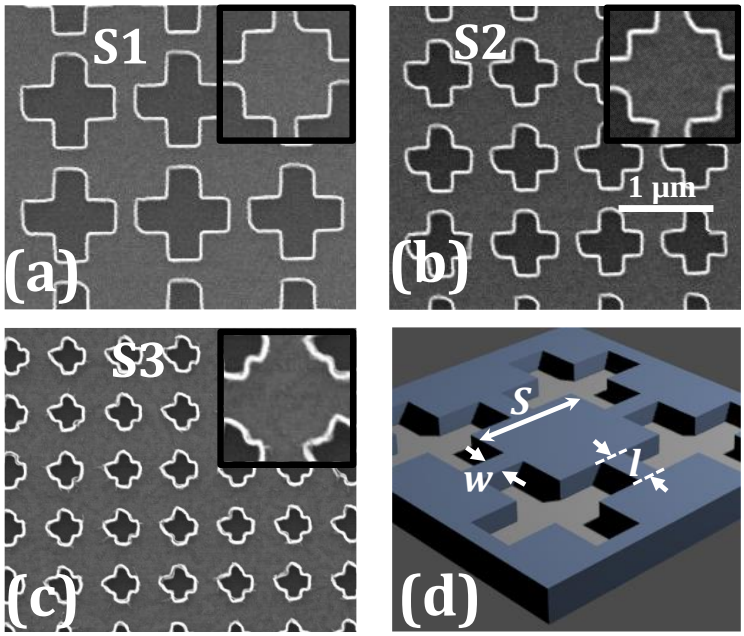

Figure 4. 1. Scanning electron micrographs are shown for (a) S1, (b) S2 and (c) S3. The scale bar is common to three samples, as shown in (b). A magnified view of the constituent nanodot with the four nanochannels is shown at the inset of each image. (d) A schematic of sample is shown where the dot size (S), and nanochannels length (l) and width (w) are marked.

Figure 4.1 (a), (b) and (c) show the scanning electron micrographs of the CND arrays with variable S(l) of 865 nm(320 nm), 660 nm(210 nm) and 465 nm(105 nm) nm, denoted as S1, S2 and S3, while w is constant at around 260 nm for all the samples. Up to ± 10 nm deviation is observed in the lateral dimensions of the samples. A schematic of the sample is shown in Fig. 4.1(d) where the sample parameters S, l and w are highlighted.

Table 4. 1 – Filling factor (f_f) for three sample is calculated by taking the ratio of the area covered by material (A_{Py}) within a unit cell (A). $f_f = A_{py}/A$; ($A = D^2 = (l + S)^2$).

Sample	Dot Size (S nm)	Connector length (l nm)	Unit cell size ($A \times 10^5$ nm^2)	Filling factor (A_{py}/A)
S1	865	320	14.04	0.64
S2	660	210	7.57	0.72
S3	465	105	3.25	0.83

The filling fraction and unit cell size are calculated for all the samples and tabulated in Table (4.1). For S3, the edges of nanodots and NCs are slightly deformed. These deviations and deformations have been corroborated in the micromagnetic simulation.

The experimental geometry for the TRMOKE measurement is shown in Fig. 4.2(a). Typical time-resolved reflectivity and Kerr rotational data from S1 at H = 1.67 kOe are shown in Fig. 4.2 (b) and (c), respectively. The bias field is chosen to be large enough to saturate the magnetization of the sample along the applied field direction. The time scale is broken between 3 to 10 ps to highlight the ultrafast magnetization dynamics [44,45] in different temporal regimes. Following the zero delay, the Kerr rotation exhibits a sharp drop due to the laser induced ultrafast demagnetization (Region II), a fast magnetization recovery or fast remagnetization (Region III) and a slow remagnetization (Region IV) superimposed with multimodal damped precessional motion. The ultrafast demagnetization and fast remagnetization data are fitted with an expression derived from the three-temperature model [46], which yields a demagnetization time of ~200 fs and a fast remagnetization time of ~1 ps. The slow remagnetization time is obtained as ~200 ps by fitting the data with an exponential function.

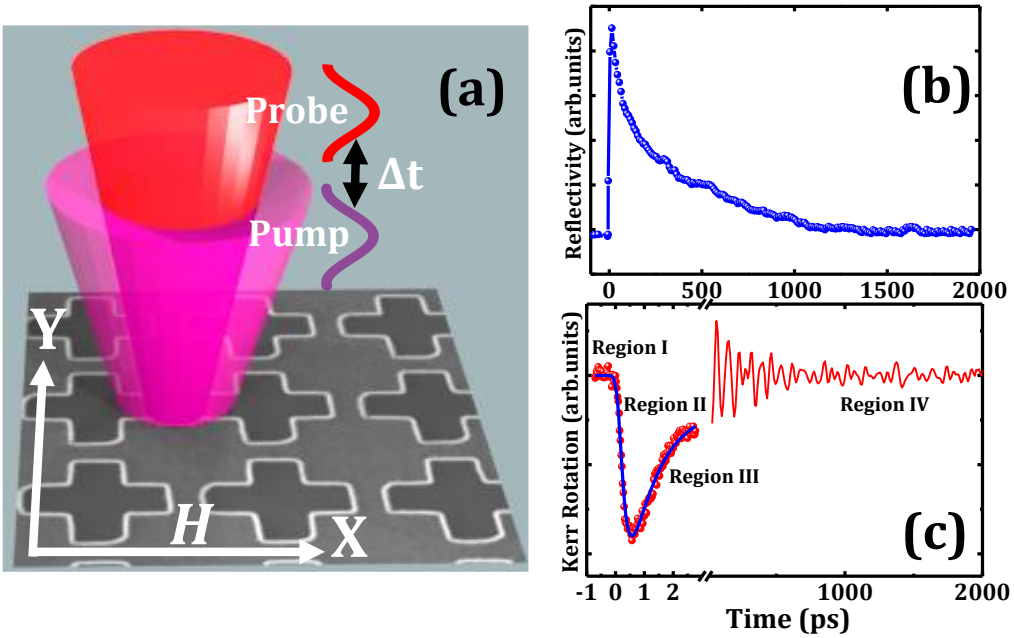

Figure 4. 2. (a) Schematic of experimental geometry is shown. Focusing of pump and probe beam and direction of applied magnetic field (H) are highlighted. Typical time resolved (b) reflectivity and (c) Kerr rotation data of sample S1 are shown at a bias magnetic field of 1.67 kOe.

The background subtracted time-resolved Kerr rotation data for all three samples at H = 1.67 kOe is shown in Fig. 4.3(a). The fast Fourier transformation (FFT) spectra of time-resolved data yield the frequencies of the spin-wave modes (Fig. 4.3(b)). For S1, the highest number of spin-wave modes are observed and the mode number decreases with increasing filling fraction. The decrease in the number of modes is due to the decrease in

the demagnetized region with increasing filling fraction from S1 to S3. The lower frequency modes are suppressed as we move from S1 to S3 and consequently, the spin-wave frequency span narrows down from 6.9 GHz to 3.6 GHz.

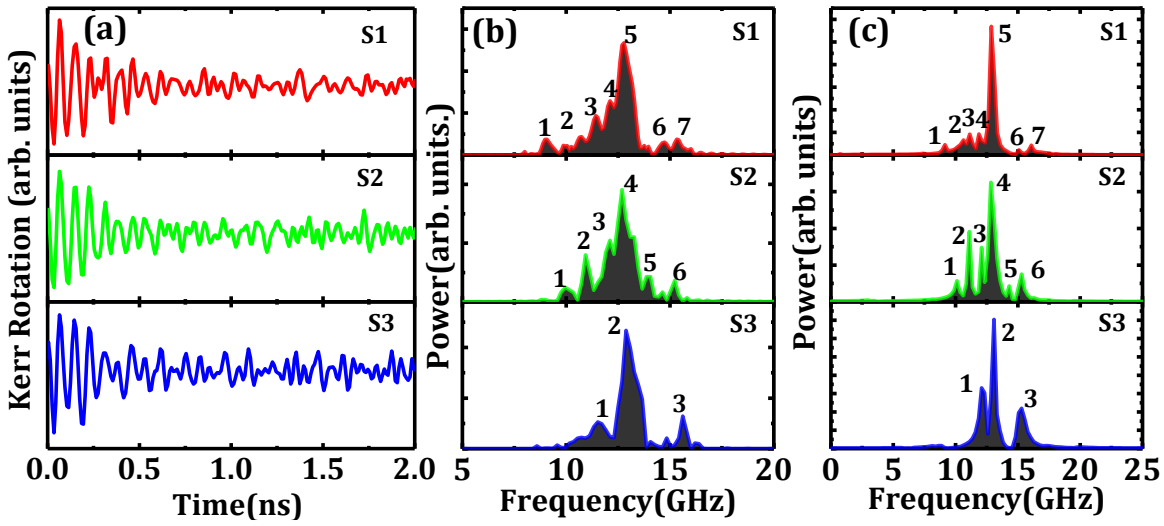

Figure 4. 3. (a) Experimental time-resolved Kerr rotation showing precessional oscillation for all three samples at H = 1.67 kOe. The FFT power spectra of time-resolved (b) experimental and (c) simulated precessional oscillations are shown. Spin wave modes are numbered in the ascending value of frequency.

We have investigated the origin of the spin-wave modes by numerical calculation using Object Oriented Micromagnetic Framework (OOMMF) software [47]. We have considered an array of 4×4 elements with 2D periodic boundary conditions to mimic the large area of the sample compared to the spot size. Subsequently, we have extracted the averaged signal from a 1×1 μm^2 area from the central portion of the array by following the experimental condition. The arrays were divided into cuboidal cells with a size 4 × 4 × 20 nm^3. The lateral cell size is well below the exchange length of Py (≈ 5.2 nm). The observed deformation in shapes was introduced in the simulations and the material parameters were used in the simulation as gyromagnetic ratio γ = 17.6 MHz/Oe, saturation magnetization M_s = 860 emu/cc, anisotropy field H_K = 0 and exchange stiffness constant A_{ex} = 13 × 10^{-6} erg/cm. The material parameters were extracted by fitting the measured bias field dependent precessional frequency of an unpatterned Py thin film with Kittel formula [48] (shown in Appendix A). The value of A_{ex} is obtained from the literature [49]. The equilibrium magnetic states were obtained by relaxing the sample under study at a bias field of 1.67 kOe for a sufficiently long time after reducing it from a larger magnetic field so that the torque on the system goes below 10^{-6} A/m. The damping parameter is artificially made very large at α = 0.99 in order to reach equilibrium quickly. For

simulation of magnetization dynamics, the pump beam in the experiment was mimicked by applying a square shaped pulsed field with a peak amplitude of 20 Oe along z-direction with rise and fall time of both 10 ps and duration of 20 ps, while damping constant α = 0.008 was used from the literature [50]. The FFT of simulated time-resolved out-of-plane magnetization component (m_z), extracted from 1×1 μm^2 area from the central portion of the array is shown in Fig. 4.3(c), revealing the spin-wave modes. The experimentally observed spin-wave modes are qualitatively reproduced in the simulation. The experimental modes can be identified and their frequency spacing is reasonably well reproduced in the simulation. However, the relative powers of the modes are not always reproduced in the simulation.

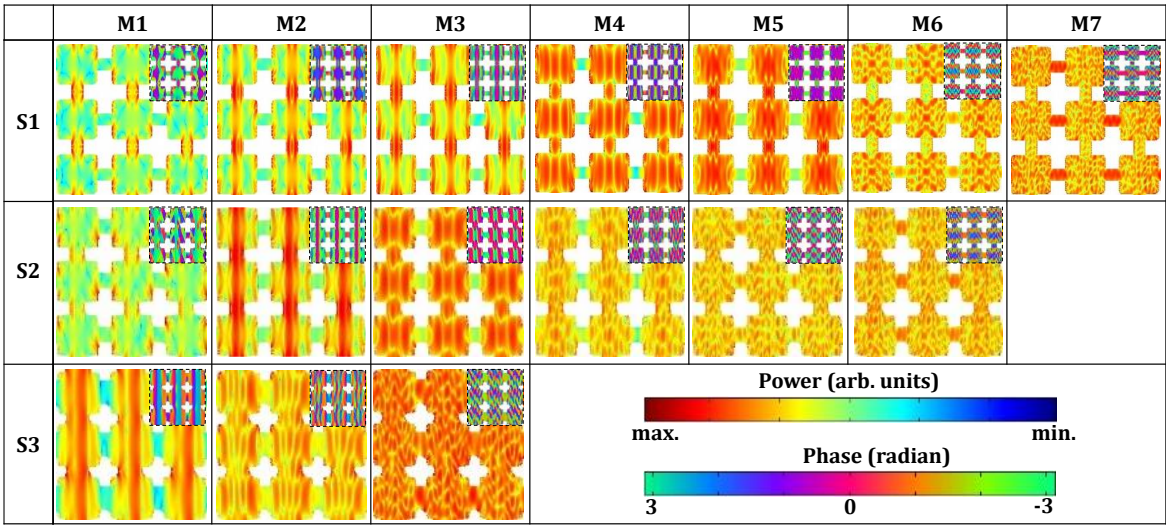

Figure 4. 4. Simulated spatial distributions of power of spin-wave modes are shown. The corresponding phase profiles are shown in the inset.

This is most likely due to the increasing deviation of the actual shape of the sample from the ideal shape, which is not always possible to be fully reproduced in the finite difference method based OOMMF simulation where the samples are divided into cuboidal cells. The cell size cannot be chosen arbitrarily low due to limitations in computational resources. To understand the nature of the spin-wave modes, we have further analyzed the simulated data from OOMMF to calculate the spin-wave mode profiles using a home-built post-processing code, DotMag [51]. The simulated power and phase maps of the spin-wave modes for all three samples are shown in Fig. 4.4. The mode 1 (M1) of S1 and S2 is found to be an edge mode (EM), where the power of spin-wave is concentrated mainly at the edges of VNCs and nanodots. The mode M2 of S1, S2 and M1 of S3 show extended behaviour in a DE-like geometry, i.e., the power of spin-wave mode is extended along

VNCs. The M3, M4 and M5 of S1 all show quantized behaviour in the BV-like geometry, i.e., with quantization axis parallel to the bias magnetic field direction with quantization number n = 5, 7 and 13, respectively. The M3 of S2 and M2 of S3 also show quantized behaviour in BV-like geometry with n = 5 and 7, respectively. The higher frequency modes, i.e., M6 and M7 of S1, M5 and M6 of S2 and M3 of S3 show mixed quantized behaviour in the DE-BV-like geometry. Noticeably here the spin-wave modes are coupled between the nanodots through the VNCs except for the highest frequency modes where modes are coupled through both VNCs and HNCs. It is clear from the power profile that the power of the highest frequency mode (M7) of S1 is concentrated within the HNCs and shows uniform behaviour within HNCs. This behaviour is suppressed for the highest frequency mode of S2 and S3. The spin-wave phase profile of all modes is shown at the top right corner of power maps. The color bars of power and phase profiles are presented at the bottom right corner. To get a deeper insight into the role of NCs in spin-wave mode behaviour, we have performed some additional numerical calculations.

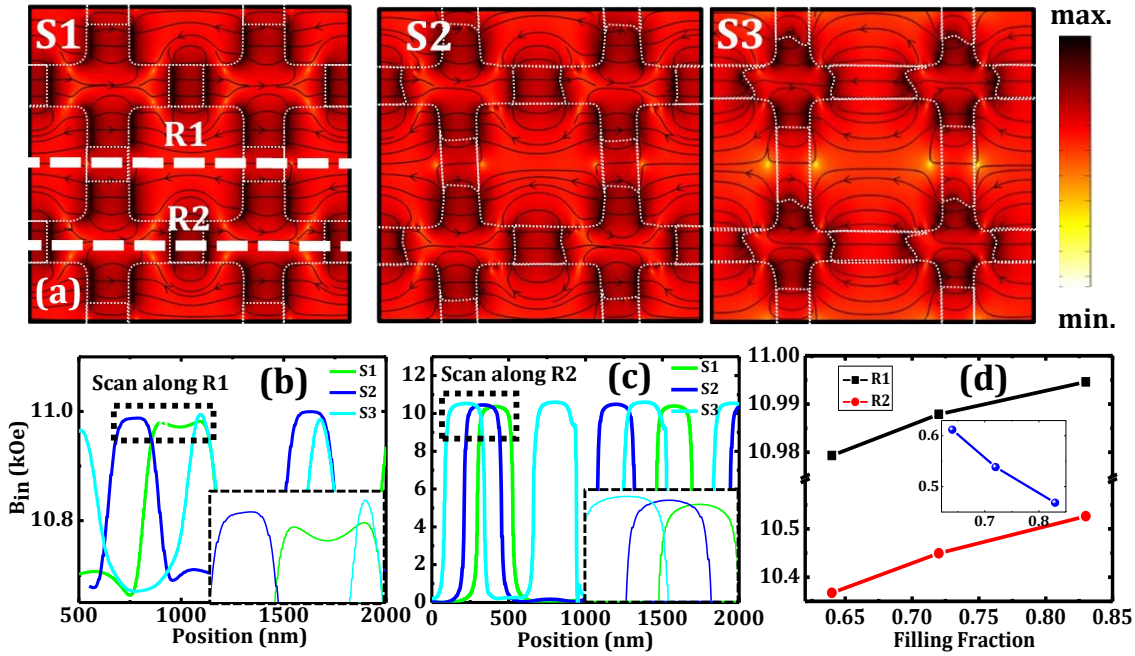

Figure 4. 5. (a) Magnetostatic field distribution of all the samples at H = 1.67 kOe. Linescans of the magnetostatic field distributions taken along (b) horizontal nanochannels: HNCs (R1) and (c) vertical nanochannels: VNCs (R2) as shown by dotted lines on S1 of (a). (d) Variation of magnetostatic field with filling fraction. The difference in B_{in} between HNC and VNC is shown in the inset.

We have calculated the magnetostatic field distribution within the nanodots and NCs using the LLG micromagnetic simulator [52]. The magnetostatic field distribution within the CNDs is shown in Fig. 4.5 (a) for all three samples. Figures 4.5 (b) and (c) show the

line scans of the internal magnetic field (B_{in}) map within the CNDs (as marked by dotted lines R1 and R2 in Fig. 4.5(a)) along x-direction for all three samples. The inset of Figs. 4.5 (b) and (c) show the variation of B_{in} within the HNC and VNC, respectively. The distribution of B_{in} within HNC of S1 shows a central dip, which might be a reason for the concentrated power of the highest frequency mode within HNC of S1. The values of B_{in} within HNC and VNC are plotted as a function of filling fraction in Fig. 4.5(d). With increasing filling fraction, B_{in} also increases indicating a decrease in the demagnetizing field. The numbers of spin-wave modes decrease with increasing filling fraction due to the decrement of exchange decoupled spins at the edges of the holes which suppress the edge modes. The value of B_{in} is always higher in HNC than VNC as the bias field is applied along the HNC direction. Hence, only the higher frequency modes are stabilized within the HNCs. The difference in B_{in} between HNC and VNC is shown in the inset of Fig. 4.5(d). With the increasing filling fraction this difference decrease (it is maximum in S1), which might be another reason that the power of the highest frequency spin-wave mode is concentrated within HNC.

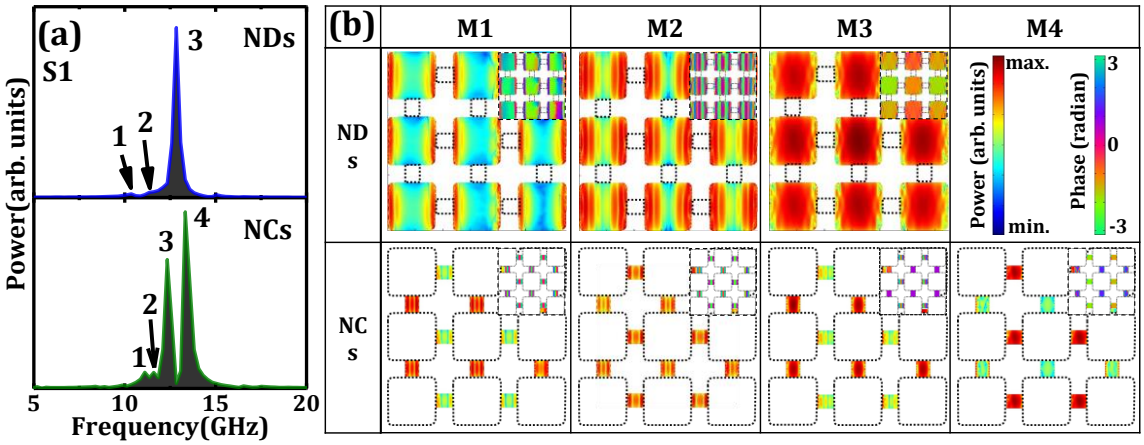

Figure 4. 6. (a) Simulated power spectra of only nanodots and nanochannels of S1 are shown. Modes are marked by numbers in order of ascending frequency value. (b) Simulated spatial distribution of power of spin-wave modes is shown. The corresponding phase profile is presented at the top right corner of each power map. The colour maps of power and phase profiles are shown at the top right side of (b). Black dashed lines are a guide to the eye to show the positions of nanodots or nanochannels.

To explore the origin of the highest frequency modes, we have further simulated the magnetization dynamics of physically isolated nanodots and NCs. The FFT spectra of the simulated time-resolved magnetization of the isolated nanodots and NCs are shown in Fig. 4.6(a) and their corresponding power profiles are shown in Fig. 4.6(b). We observe three spin-wave modes for nanodots and four spin-wave modes for NCs. For isolated dots,

the most intense peak shows uniform precession over the dot area. On the other hand, for the connector-only array, two intense peaks are observed, which are uniform modes in the VNC (lower frequency) or HNC (higher frequency). In the CND array, these connector modes are suppressed while the nanodot modes become more dominant indicating the sacrificial roles of the connectors only to boost the spin-wave propagation between the nanodots. The simulated results of isolated nanodots and NCs of the samples S2 and S3 are shown in Appendix A.

We have further investigated the propagating nature of M3, M5 and M7 of S1 as these modes show distinct behaviour as discussed earlier, which are shown in Figs. 4.7(a) - (c). The spin-wave modes are excited by a sinusoidal point excitation of desired frequency at the centre of the CND array as marked by 'I' in Fig. 4.7.

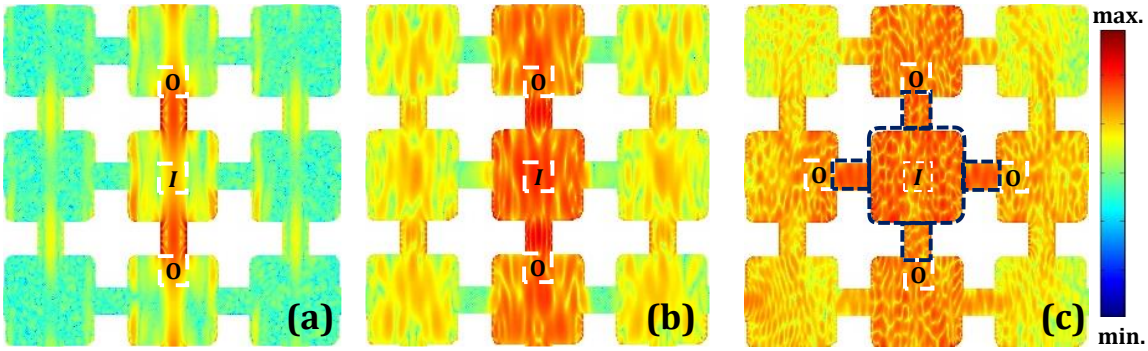

Figure 4. 7. Simulations showing propagating nature of spin-wave modes (a) M3, (b) M5 and (c) M7. Spin wave of desired frequency is excited at the centre (marked by *I*) of the array highlighted by dark blue coloured dashed line as shown in (c). Here 'O' corresponds to the output of the spin-wave propagation through the nanochannels. The colour map of spin-wave power is shown at the right side.

Here, M3 and M5 propagate only through the VNCs along the vertical directions, whereas M7 propagates along all directions through all four NCs from the point of excitation and we obtain outputs at all four points as marked by 'O' in Fig. 4.7(c). This behaviour may be further controlled to construct a circuit analogous to electrical one-to-four demultiplexer logic operations. This remarkable observation of frequency selective spin-wave propagation through nanochannels and potential for the development of demultiplexing-like operation for these special types of nanomagnetic array would be useful for the development of wave-based communications and computing devices.

4.4 Conclusion

In summary, we have investigated the role of magnetic nanochannels to control the spin-wave properties in CND arrays. We have experimentally and numerically studied the time-resolved magnetization dynamics in the CND arrays and explored the effects of NCs, connecting the nanodots on the spin-wave properties through dipole-exchange interaction. The spin-wave properties are found to vary strongly with the length of NCs. With the increase in the filling fraction of the array, the nonuniform demagnetized regions decrease letting the magnetostatic field to increase. Consequently, the number of spin-wave modes also decreases with the increase in filling fraction. The experimental results are qualitatively reproduced by micromagnetic simulations, the latter further aids to identify various spin-wave modes, namely the edge mode, extended mode, quantized mode and mixed quantized mode in the CNDs. The VNCs are found to couple the spin-wave modes between the nanodots, except for the highest frequency mode, for which both NCs act as a coupler. Simulations also reveal that the highest frequency spin-wave mode primarily originates from the HNCs. Additional simulation reveals that the extended mode propagates only through the VNCs, whereas the highest frequency quantized mode propagates through all NCs. These behaviours can be further exploited to construct circuits analogous to a four-way demultiplexer, which can be useful for future spin-wave based communication devices. This study will be helpful for the use of nanochannels in future magnonic devices.

References

[1] C. G. Sykes, J. D. Adam, and J. H. Collins, Magnetostatic Wave Propagation in a Periodic Structure; Appl. Phys. Lett., **29** (1976) 388-391.
[2] J. P. Parekh, and H. S. Tuan, Magnetostatic Surface Wave Reflectivity of a Shallow Groove on a YIG Film; Appl. Phys. Lett., **30** (1977) 667-669.
[3] S. A. Nikitov, P. Tailhades, and C. S. Tsai, Spin Waves in Periodic Magnetic Structures—Magnonic Crystals; J. Magn. Magn. Mater., **236** (2001) 320-330.
[4] V. V. Kruglyak, S. O. Demokritov, and D. Grundler, Magnonics; J. Phys. D: Appl. Phys., **43** (2010) 260301.
[5] M. Krawczyk, and D. Grundler, Review and Prospects of Magnonic Crystals and Devices with Reprogrammable Band Structure; J. Phys.: Condens. Matter, **26** (2014) 123202.
[6] K. Vogt, F.Y. Fradin, J.E. Pearson, T. Sebastian, S.D. Bader, B. Hillebrands, A. Hoffmann, and H. Schultheiss, Realization of a Spin-Wave Multiplexer; Nat. Commun., **5** (2014) 3727.
[7] M.P. Kostylev, A.A. Serga, T. Schneider, B. Leven, and B. Hillebrands, Spin-Wave Logical Gates; Appl. Phys. Lett., **87** (2005) 153501.
[8] H. Yu, G. Duerr, R. Huber, M. Bahr, T. Schwarze, F. Brandl, and D. Grundler, Omnidirectional Spin-Wave Nanograting Coupler; Nat. Commun., **4** (2013) 2702.
[9] J.W. Kłos, D. Kumar, J. Romero-Vivas, H. Fangohr, M. Franchin, M. Krawczyk, and A. Barman; Effect of Magnetization Pinning on the Spectrum of Spin Waves in Magnonic Antidot Waveguides, Phys. Rev. B, 86 (2012) 184433.
[10] J.W. Kłos, D. Kumar, M. Krawczyk, and A. Barman, Magnonic Band Engineering by Intrinsic and Extrinsic Mirror Symmetry Breaking in Antidot Spin-Wave Waveguides; Sci. Rep., **3** (2013) 2444.
[11] Y. Au, M. Dvornik, O. Dmytriiev, and V.V. Kruglyak, Nanoscale Spin Wave Valve and Phase Shifter; Appl. Phys. Lett., **100** (2012) 172408.
[12] Q. Wang, P. Pirro, R. Verba, A. Slavin, B. Hillebrands, and A.V. Chumak, Reconfigurable Nanoscale Spin-Wave Directional Coupler; Sci. Adv., **4** (2018) e1701517.
[13] M.A. Abeed, and S. Bandyopadhyay, Experimental Demonstration of an Extreme Subwavelength Nanomagnetic Acoustic Antenna Actuated by Spin–Orbit Torque from a Heavy Metal Nanostrip; Adv. Mater. Technol., **5** (2020) 1901076.
[14] J. Torrejon, M. Riou, F.A. Araujo, S. Tsunegi, G. Khalsa, D. Querlioz, P. Bortolotti, V. Cros, K. Yakushiji, A. Fukushima, H. Kubota, S. Yuasa, M.D. Stiles, and J. Grollier, Neuromorphic Computing with Nanoscale Spintronic Oscillators; Nature, **547** (2017) 428-431.
[15] Y. Li, T. Polakovic, Y.-L. Wang, J. Xu, S. Lendinez, Z. Zhang, J. Ding, T. Khaire, H. Saglam, R. Divan, J. Pearson, W.-K. Kwok, Z. Xiao, V. Novosad, A. Hoffmann, and W. Zhang, Strong Coupling between Magnons and Microwave Photons in On-Chip Ferromagnet-Superconductor Thin-Film Devices; Phys. Rev. Lett., **123** (2019) 107701.
[16] C. Berk, M. Jaris, W. Yang, S. Dhuey, S. Cabrini, and H. Schmidt, Strongly Coupled Magnon–Phonon Dynamics in a Single Nanomagnet; Nat. Commun., **10** (2019) 2652.
[17] J. Chen, C. Liu, T. Liu, Y. Xiao, K. Xia, G.E.W. Bauer, M. Wu, and H. Yu, Strong Interlayer Magnon-Magnon Coupling in Magnetic Metal-Insulator Hybrid Nanostructures; Phys. Rev. Lett., **120** (2018) 217202.
[18] K. Adhikari, S. Sahoo, A.K. Mondal, Y. Otani, and A. Barman, Large Nonlinear Ferromagnetic Resonance Shift and Strong Magnon-Magnon Coupling in $Ni_{80}Fe_{20}$ Nanocross Array, Phys. Rev. B, **101** (2020) 054406.
[19] Y. Tabuchi, S. Ishino, A. Noguchi, T. Ishikawa, R. Yamazaki, K. Usami, and Y. Nakamura, Coherent Coupling Between a Ferromagnetic Magnon and a Superconducting Qubit; Science, **349** (2015) 405.
[20] S.J. Hämäläinen, M. Madami, H. Qin, G. Gubbiotti, and S. van Dijken, Control of Spin-Wave Transmission by a Programmable Domain Wall; Nat. Commun., **9** (2018) 4853.

[21] G. Gubbiotti, M. Conti, G. Carlotti, P. Candeloro, E.D. Fabrizio, K.Y. Guslienko, A. Andre, C. Bayer, and A.N. Slavin, Magnetic Field Dependence of Quantized and Localized Spin Wave Modes in Thin Rectangular Magnetic Dots; J. Phys.: Condens. Matter, **16** (2004) 7709-7721.
[22] V.V. Kruglyak, A. Barman, R.J. Hicken, J.R. Childress, and J.A. Katine, Picosecond Magnetization Dynamics in Nanomagnets: Crossover to Nonuniform Precession; Phys. Rev. B, **71** (2005) 220409.
[23] P.S. Keatley, V.V. Kruglyak, A. Neudert, E.A. Galaktionov, R.J. Hicken, J.R. Childress, and J.A. Katine, Time-Resolved Investigation of Magnetization Dynamics of Arrays of Nonellipsoidal Nanomagnets with Nonuniform Ground States; Phys. Rev. B, **78** (2008) 214412.
[24] J.M. Shaw, T.J. Silva, M.L. Schneider, and R.D. McMichael, Spin Dynamics and Mode Structure in Nanomagnet Arrays: Effects of Size and Thickness on Linewidth and Damping; Phys. Rev. B, **79** (2009) 184404.
[25] B. Rana, D. Kumar, S. Barman, S. Pal, Y. Fukuma, Y. Otani, and A. Barman, Detection of Picosecond Magnetization Dynamics of 50 nm Magnetic Dots down to the Single Dot Regime; ACS Nano, **5** (2011) 9559-9565.
[26] S. Saha, R. Mandal, S. Barman, D. Kumar, B. Rana, Y. Fukuma, S. Sugimoto, Y. Otani, and A. Barman, Tunable Magnonic Spectra in Two-Dimensional Magnonic Crystals with Variable Lattice Symmetry; Adv. Funct. Mater., **23** (2013) 2378-2386.
[27] B.K. Mahato, B. Rana, D. Kumar, S. Barman, S. Sugimoto, Y. Otani, and A. Barman, Tunable Spin Wave Dynamics in Two-Dimensional $Ni_{80}Fe_{20}$ Nanodot Lattices by Varying Dot Shape; Appl. Phys. Lett., **105** (2014) 012406.
[28] U. Ebels, J.L. Duvail, P.E. Wigen, L. Piraux, L.D. Buda, and K. Ounadjela, Ferromagnetic Resonance Studies of Ni Nanowire Arrays; Phys. Rev. B, **64** (2001) 144421.
[29] S. Saha, S. Barman, Y. Otani, and A. Barman, All-Optical Investigation of Tunable Picosecond Magnetization Dynamics in Ferromagnetic Nanostripes with a Width down to 50 nm; Nanoscale, **7** (2015) 18312-18319.
[30] S. Pal, S. Saha, M.V. Kamalakar, and A. Barman, Field-Dependent Spin Waves in High-Aspect-Ratio Single-Crystal Ferromagnetic Nanowires; Nano Res., **9** (2016) 1426-1433.
[31] S. Choudhury, A.K. Chaurasiya, A.K. Mondal, B. Rana, K. Miura, H. Takahashi, Y. Otani, and A. Barman, Voltage Controlled on-demand Magnonic Nanochannels; Sci. Adv., **6** (2020) eaba5457.
[32] M. Yu, L. Malkinski, L. Spinu, W. Zhou, and S. Whittenburg, Size Dependence of Static and Dynamic Magnetic Properties in Nanoscale Square Permalloy Antidot Arrays; J. Appl. Phys., **101** (2007) 09F501.
[33] S. Neusser, B. Botters, and D. Grundler, Localization, Confinement, and Field-Controlled Propagation of Spin Waves in $Ni_{80}Fe_{20}$ Antidot Lattices; Phys. Rev. B, **78** (2008) 054406.
[34] S. Neusser, G. Duerr, H.G. Bauer, S. Tacchi, M. Madami, G. Woltersdorf, G. Gubbiotti, C.H. Back, and D. Grundler, Anisotropic Propagation and Damping of Spin Waves in a Nanopatterned Antidot Lattice; Phys. Rev. Lett., **105** (2010) 067208.
[35] S. Tacchi, B. Botters, M. Madami, J.W. Kłos, M.L. Sokolovskyy, M. Krawczyk, G. Gubbiotti, G. Carlotti, A.O. Adeyeye, S. Neusser, and D. Grundler, Mode Conversion from Quantized to Propagating Spin Waves in a Rhombic Antidot Lattice Supporting Spin Wave Nanochannels; Phys. Rev. B, **86** (2012) 014417.
[36] R. Mandal, P. Laha, K. Das, S. Saha, S. Barman, A.K. Raychaudhuri, and A. Barman, Effects of Antidot Shape on the Spin Wave Spectra of Two-Dimensional $Ni_{80}Fe_{20}$ Antidot Lattices; Appl. Phys. Lett., **103** (2013) 262410.
[37] S. Pan, S. Mondal, M. Zelent, R. Szwierz, S. Pal, O. Hellwig, M. Krawczyk, and A. Barman, Edge Localization of Spin Waves in Antidot Multilayers with Perpendicular Magnetic Anisotropy; Phys. Rev. B, **101** (2020) 014403.
[38] R. Mandal, S. Barman, S. Saha, Y. Otani, and A. Barman, Tunable Spin Wave Spectra in Two-Dimensional $Ni_{80}Fe_{20}$ Antidot Lattices with Varying Lattice Symmetry; J. Appl. Phys., **118** (2015) 053910.

[39] C. Banerjee, S. Saha, S. Barman, O. Rousseau, Y. Otani, and A. Barman, Width Dependent Transition of Quantized Spin-Wave Modes in $Ni_{80}Fe_{20}$ Square Nanorings; J. Appl. Phys., **116** (2014) 163912.
[40] R. Mandal, S. Saha, D. Kumar, S. Barman, S. Pal, K. Das, A.K. Raychaudhuri, Y. Fukuma, Y. Otani, and A. Barman, Optically Induced Tunable Magnetization Dynamics in Nanoscale Co Antidot Lattices; ACS Nano, **6** (2012) 3397-3403.
[41] N.N. Phuoc, S.L. Lim, F. Xu, Y.G. Ma, and C.K. Ong, Enhancement of Exchange Bias and Ferromagnetic Resonance Frequency by Using Multilayer Antidot Arrays; J. Appl. Phys., **104** (2008) 093708.
[42] S. Choudhury, S. Saha, R. Mandal, S. Barman, Y. Otani, and A. Barman, Shape- and Interface-Induced Control of Spin Dynamics of Two-Dimensional Bicomponent Magnonic Crystals; ACS Appl. Mater. Interfaces, **8** (2016) 18339-18346.
[43] S. Saha, S. Barman, J. Ding, A.O. Adeyeye, and A. Barman, Time-Domain Study of Spin-Wave Dynamics in Two-Dimensional Arrays of Bi-Component Magnetic Structures; Appl. Phys. Lett., **102** (2013) 242409.
[44] A. Barman and J. Sinha, Spin Dynamics and Damping in Ferromagnetic Thin Films and Nanostructures (Springer Publishing AG, Switzerland, 2017).
[45] E. Beaurepaire, J.C. Merle, A. Daunois, and J.Y. Bigot, Ultrafast Spin Dynamics in Ferromagnetic Nickel; Phys. Rev. Lett., **76** (1996) 4250-4253.
[46] G. Malinowski, F. Dalla Longa, J.H.H. Rietjens, P.V. Paluskar, R. Huijink, H.J.M. Swagten, and B. Koopmans, Control of Speed and Efficiency of Ultrafast Demagnetization by Direct Transfer of Spin Angular Momentum; Nat. Phys., **4** (2008) 855-858.
[47] M. Donahue, and D.G. Porter, OOMMF User's guide, version1.0, Interagency Report NISTIR 6376; National Institute of Standard and Technology: Gaithersburg, MD, U.S.A. , (1999).
[48] C. Kittel, On the Theory of Ferromagnetic Resonance Absorption, Phys. Rev., **73** (1948) 155-161.
[49] K.H.J. Buschow, Handbook of Magnetic Materials; Elsevier: Amsterdam, Netherlands, 2009; Vol. 18.
[50] J. Fassbender, J. von Borany, A. Mücklich, K. Potzger, W. Möller, J. McCord, L. Schultz, and R. Mattheis, Structural and Magnetic Modifications of Cr-Implanted Permalloy; Phys. Rev. B, **73** (2006) 184410.
[51] D. Kumar, O. Dmytriiev, S. Ponraj, and A. Barman, Numerical calculation of spin wave dispersions in magnetic nanostructures; J. Phys. D: Appl. Phys., **45** (2011) 015001.
[52] LLG Micromagnetics Simulator, http://llgmicro.home.mindspring.com/.

Chapter 5

5. All-Optical Study of Magnetization Dynamics in a Square Artificial Spin Ice Nanostructure

5.1 Introduction

Periodically patterned magnetic nanostructures are commonly known as magnonic crystals where spin-waves act as information carriers. Over the last decade, magnonic crystals have emerged as a leading candidate for on-chip information carrier and processing devices [1-3], next generation memory devices [4], logic [5], quantum computation [6] and neuromorphic computing [3,7]. A large range of studies has been performed to understand and control magnetization configurations and spin-wave dynamics in different types of magnonic crystals including magnetic dots [8-13], antidots [14-19], bi–component magnonic crystals [20-22], nanostripes and nanowires [23-26], and nanoparticles [27,28]. These lead to the observation of interesting and useful properties such as magnonic bandgap formation and its tunability, magnonic mode splitting, mode hopping, mode crossover, mode anticrossing, creation and annihilation of modes, mode conversion, to name a few [2,26,29-34]. These have serious implications in application for magnonic filter, attenuator, interferometer, transistor, splitter, directional coupler, etc. With the advancement of technology, new types of nanostructures are being fabricated and studied, and new properties are being unveiled leading towards the development of new classes of magnonic crystals. Two-dimensional artificial spin ice (2D-ASI) nanostructures have been one of the latest additions in the league of magnonic crystals.

In 2006, Wang et al. first experimentally demonstrated an artificial geometrically frustrated magnetic structure based on lithographically defined single-domain magnetic islands, the so-called ASI structure [35]. ASIs are generally tailored magnetic nanostructures where magnetic defect states can be manifested. These defect states are known as ‘magnetic monopoles’, which was first observed in natural pyrochlore material [36]. These monopoles are always created or annihilated in pairs to balance the charge distribution and they are connected through ‘Dirac-string’. The back-and-forth movement of monopoles can give rise to a new field named ‘magnetotronics’ [37]. The

high frequency dynamics in the ASI system was first reported numerically by Gilga et al. [38] and experimentally by Sklenar et al. [39] both in 2013. The monopoles were found to introduce a new spin-wave mode and tune its power and frequency with the increase in monopole defects in the system.

Over the last few years, the study of spin-waves in the different form of ASI structures such as square [40-43] and kagome [44-46] lattices have become a vibrant research field. The effects of local defect states on global spin-waves and vice versa can add new functionality to magnonic crystals. The efficient reconfigurability of magnetic microstates in ASI can lead to the development of reconfigurable magnonic crystals, which can fulfil the primary objectives of magnonic crystals. The asymmetric behaviour of spin-wave field dispersion near zero field [40], activation and deactivation spin-wave modes [46], influence of topological defect states controlled by varying the reversal field on spin-wave intensity and field dispersive behaviour [42], and spin texture dependent spin-wave dispersion [47] have been observed in the ASI structures. Recently a comprehensive study of spin-wave mode behaviour and mode selection in connected and disconnected kagome ASI nanostructures have been demonstrated [45]. It is found that the spin-wave mode behaviour is strongly influenced by the ASI geometry. However, in most of those studies [40-46,48], the spin-waves were measured globally using large-area measurement techniques such as ferromagnetic resonance (FMR) and conventional Brillouin light scattering (BLS). The local measurement of spin-wave dynamics in such structure is required to understand the correlation between the local magnetic microstates and the spin-wave modes. However, no such attempts can be found in literature so far.

Here, we are reporting an all-optical study of spin-wave dynamics of a square ASI structure using a custom−built time-resolved magneto-optical Kerr effect (TRMOKE) microscopy technique. The disconnected ASI sample consisting of rectangular shaped nanomagnetic bars arranged in a square lattice was developed by using a combination of e-beam lithography and thermal evaporation. The magnetic force microscopy (MFM) imaging at remanence captures different spin ice states and also multidomain spin texture with vortex state. Rich spin-wave spectra are observed in the system and a detailed spin-wave dispersion with bias magnetic field has been studied experimentally and by numerical simulations. A rich variety of spin-wave modes are observed. However, the micromagnetic simulation results deviate significantly from the experimental spin-

wave mode frequencies in some bias-field range presumably due to the presence of magnetoelastic coupling in the system. Time-resolved reflectivity data shows some clear oscillations with frequencies adjacent to the magnetic modes, which could be reproduced by simple analytical calculations of acoustic modes in this system. The micromagnetic simulation results show a qualitative agreement in the field regimes where magnetic modes dominate and/or have lower overlaps with the acoustic modes. The simulated mode profiles reveal the important roles of the magnetic microstates on spin-wave frequencies and mode profiles. Our, findings can be helpful for designing of reconfigurable magnonics for future communication devices.

5.2 Experimental Details

An array of square ASI structure of a total area of 90 × 90 μm^2 was fabricated by using a combination of electron-beam lithography (EBL), thermal evaporation and lift-off process. The pattern was written onto a single layer polymethyl methacrylate (PMMA) resist (950K) developed on Si/SiO_2 substrate. A 25-nm-thick $Ni_{80}Fe_{20}$ (permalloy, Py hereafter) film and a capping layer of 3.7-nm-thick Al_2O_3 were deposited on the developed pattern using thermal evaporation at a base pressure of 2.6×10^{-6} Torr. The residual resist was removed by the lift-off process to obtain the square ASI structure. The scanning electron microscope (SEM) and atomic force microscope (AFM) imaging were performed on the sample to verify the patterned structure's shape and dimensions. The magnetic hysteresis loop of the sample was measured using the static magneto-optic Kerr (static-MOKE) effect technique by focusing a continuous-wave laser beam (He-Ne laser, wavelength, λ = 632 nm) of spot size 10 μm at the centre of the patterned structure. The MFM image reveals the magnetic microstate of the square ASI at the remanent state. The time-resolved magnetization dynamics of the square ASI sample was measured by using TRMOKE microscopy. The TRMOKE microscope is a collinear two-colour pump-probe technique, where the second harmonic (λ = 400 nm, pulse-width = 100 fs, fluence = 18 mJ/cm^2) of a Ti−Sapphire oscillator (Tsunami, Spectra−Physics, repetition rate = 80 MHz) was used to excite the dynamics, while the time-delayed fundamental beam (λ = 800 nm, pulse-width = 80 fs, fluence = 2 mJ/cm^2) was used to probe the dynamics. The probe laser was tightly focused on the sample surface with spot size ~ 800 nm using a microscope objective (MO) of numerical aperture, N.A. = 0.65, while the pump laser which was passed through the same MO in a collinear geometry with the probe laser becomes slightly

defocused with a spot size of ~ 1μm at the same plane. The pump and probe laser were spatially overlapped with great care so that the probe spot resides exactly at the centre of the pump spot. This ensures that the dynamics are probed from the uniformly excited volume by the pump beam and any small drift of the laser during the measurement does not significantly affect the dynamics. The pump and probe lasers are carefully placed on the desired region of the sample. The back-reflected probe beam from the sample was collected by the same MO. The change of polarization (Kerr rotation) and the total reflectivity in the probe beam were analyzed in a phase sensitive manner using an optical bridge detector and two lock-in amplifiers to probe the spin-wave and the acoustic wave simultaneously. A static magnetic field was applied in the plane of the sample with a slight out-of-plane tilt of ~ 5°. The in-plane component of the magnetic field is defined as *H*.

5.3 Results and Discussions

The AFM and SEM images of the sample are shown in Fig. 5.1(a) and Fig. 5.2(b). The square nanoislands' length (*l*) and width (*w*) are found to be around 480 nm and 180 nm, respectively, and the array periodicity (*D*) and edge to edge separation (*S*) with the first nearest neighbour is around 660 nm and 845 nm respectively. A maximum deviation ±10 nm was found in the dimensions. The AFM analysis confirmed that the sample thickness is very close to the nominal thickness and the surface roughness of the sample was found to be ~0.11 nm. The energy dispersive x-ray (EDX) spectrum of the sample is shown in Fig. 5.1(c). The weight ratio between Ni and Fe was found to be around 4.05 from the EDX spectral analysis, which agrees well with the nominal composition (4.0) of $Ni_{80}Fe_{20}$.

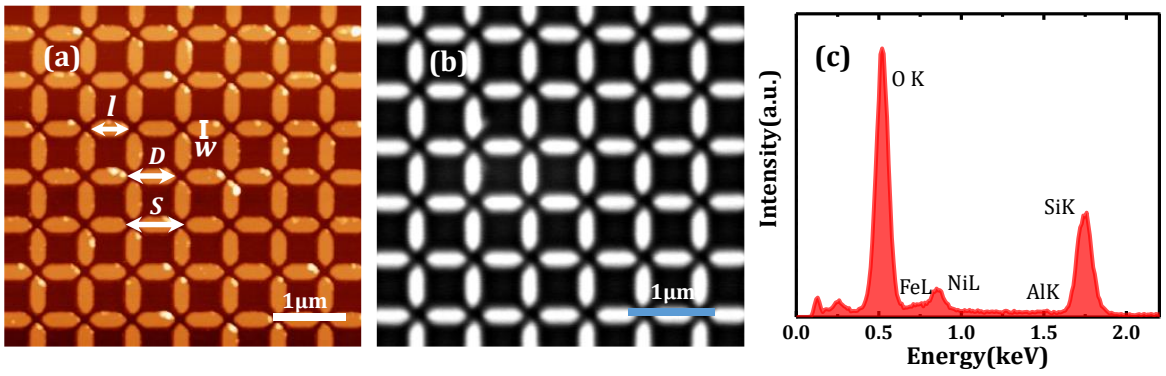

Figure 5. 1. (a) Atomic force microscope and (b) scanning electron microscope images of the Py square ASI structure. The length-scale bars are shown at bottom right corner. Some characteristic structural parameters of the ASI structure are marked in (a). (c) Energy dispersive x-ray spectrum showing elemental composition of the sample. The peak positions of different elements are identified in the spectrum.

The magnetic hysteresis loop of the sample is shown in Fig. 5.2(a), measured using the static-MOKE technique. From there, the coercive field is found to be ~ 315 Oe, which is higher than the reference Py film and the M/M_S ratio is found to be around 0.67 at remanence. The remanent state MFM image is shown in Fig. 5.2(b), which captures different microstates of square ASI such as 2-in-2-out, 3-in-1-out, 1-in-3-out. The experimentally observed hysteresis loop and the MFM contrast have been qualitatively reproduced in micromagnetic simulations as shown in Fig. 5.2(c) and Fig. 5.2(d) respectively. Some nanobars show MFM contrast all over the nanostructure array as observed in the experimental and simulated MFM images. To understand the magnetic configurations of these microstates, we have plotted the simulated magnetization in the remanent state (Fig. 5.2(e)). It shows multi-domain or multi-domain with partial vortex state like spin structures within these nanobars.

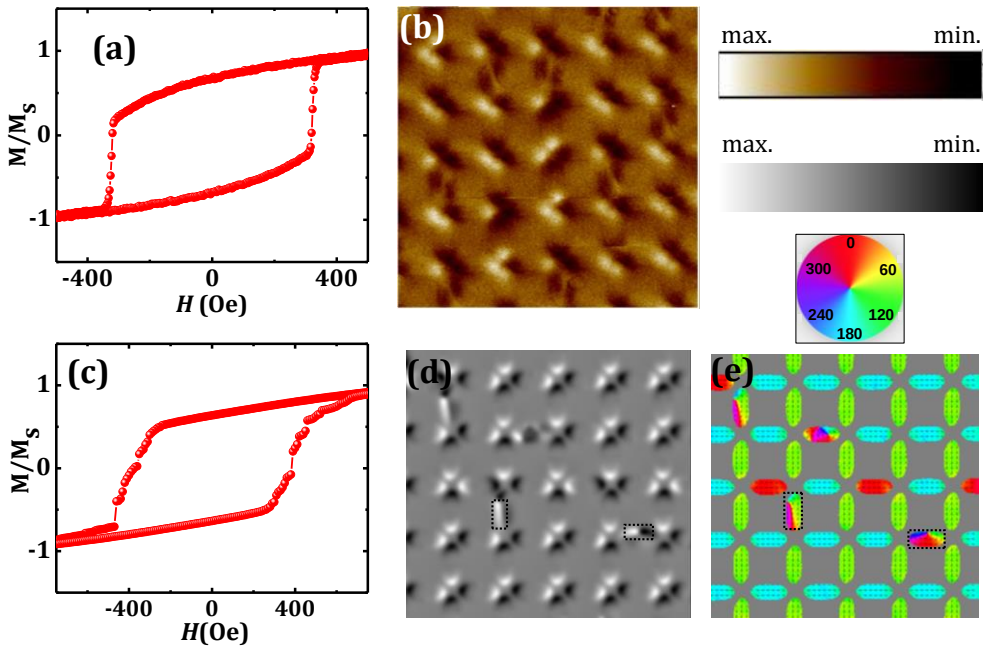

Figure 5. 2. (a) Magnetic hysteresis loop measured by static-MOKE showing the reversal mechanism of Py square ASI. (b) Remanent state MFM image is shown. Simulated (c) magnetic hysteresis loop, (d) remanent state MFM and (e) remanent state magnetization configuration is shown. Multidomain magnetic states are marked by dotted boxes in (d) and (e). The color bars and wheel are shown at top right corner.

Figure 5.3(a) show the typical time-resolved precessional oscillations for four values of *H* measured from the square ASI sample. In the experiment, *H* was varied from +1460 Oe to -1460 Oe to record the precessional data starting at +1460 Oe and gradually decreasing *H* and then reversing the field to reach *H* = -1460 Oe. This was done to capture the effects of the continuous evolution of magnetic microstates in the sample on the ensuing spin-

wave dynamics. A clear beating effect was observed in all the time-dependent precessional oscillations indicating the presence of multiple spin-wave modes. In order to extract the spin-wave frequency components from the time-dependent precessional oscillation, fast Fourier transformation (FFT) was performed as shown in Fig. 5.3(b). The simulated spin-wave power spectra are shown in Fig. 5.3(c). The spin-wave modes are numbered from higher to lower frequency. The spin-wave modes observed only in the simulation are marked as *. A qualitative agreement between experimental and simulated frequencies have been found as discussed later in this chapter.

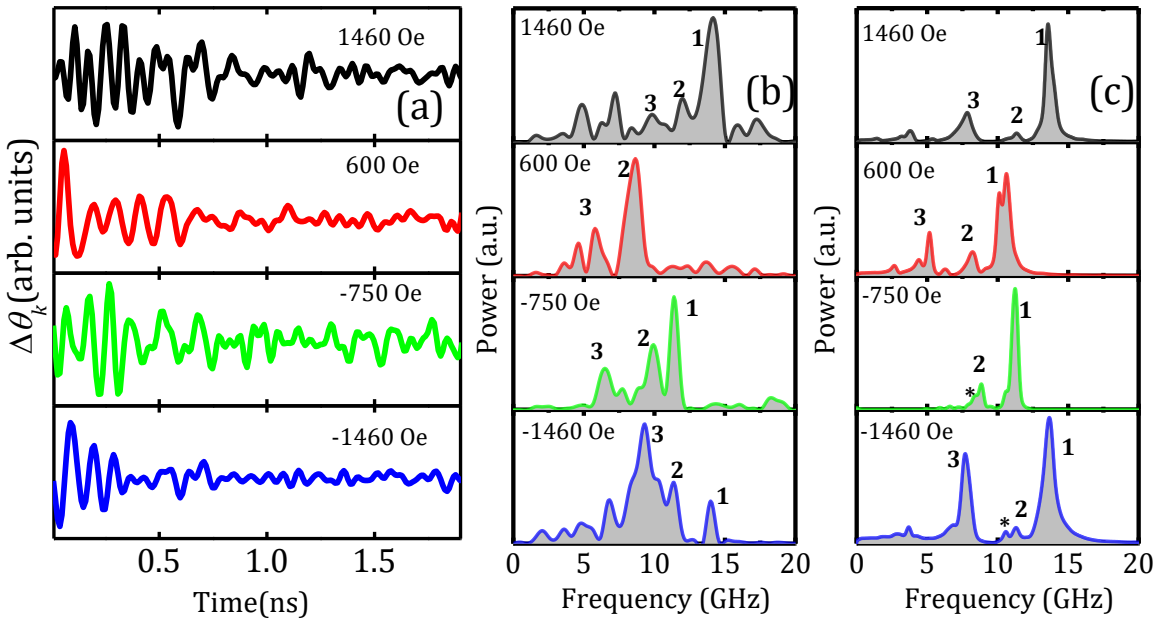

Figure 5. 3. Experimental time-resolved Kerr rotation data is shown for four different bias magnetic field values. The FFT power spectra of the time-resolved (b) experimental and (c) simulated precessional oscillations are shown. The spin-wave modes are numbered in the descending value of frequency. The magnetic field values are mentioned inside each panel. The spin-wave modes only observed in simulation are marked by * in the simulated spectra.

Figures 5.4 (a) and 5.5 show the field dispersion of the extracted spin-wave mode frequencies. A surface plot of the FFT power spectra of the experimental data is shown in Fig. 5.4(a) where the solid data points represent the peak frequencies of the spin-wave modes obtained from Lorentzian multi-peak fits to the power spectra. In Fig. 5.4(b), spin-wave spectra for four different *H* values, as highlighted by the vertical dotted lines on Fig. 5.4(a), are shown to identify different characteristics (discussed later in the chapter) of spin-wave modes. In Fig. 5.5, the experimental spin-wave peak frequencies are plotted again as symbols with simulated spin-wave frequencies (dotted lines) to display their comparison (discussed later in the section). In the experimental data, M1 shows a

monotonic decrement in spin-wave frequency with decreasing field starting from H = +1450 Oe before showing a slight upturn and subsequent fading away. M2, on the other hand, shows a monotonic increase in frequency with an increased bias field in the intermediate positive field range (375 Oe ≤ H ≤ 1050 Oe) before showing a slight downturn in the higher field range (H > 1250 Oe). This behaviour was identified as a magnon mode anticrossing, presumably due to magnon-phonon interaction as discussed later. The spin-wave spectra of the anti-crossing point at H = 1050 Oe is shown in panel 1 of Fig. 5.4(b). The anticrossing gap is found to be around 1.06 GHz. For H < 375 Oe the spin-wave mode frequency becomes invariant with H, which remain invariant even in the negative field range. For H < 1000 Oe M3 regained its power (panel 2 of Fig. 5.4(b)) and shows a monotonic decrease in frequency with H before showing a slight increase and subsequent merging with M2.

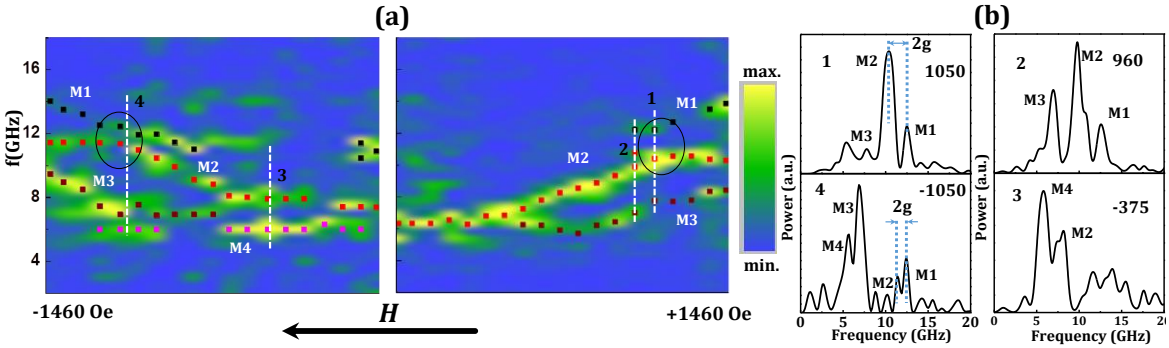

Figure 5. 4. (a) Surface plot of spin-wave power spectra with field (H) is shown. The solid symbols superposed on the surface plot represent peak frequencies of spin-wave modes obtained from the FFT power spectra. The color bar is shown at right. The spin-wave mode anticrossing regions are marked by black solid circles. Four important H values are marked by vertical dashed line on the surface plot whose spin-wave spectra are shown in (b). In panels 1 and 4, the anticrossings and corresponding gaps are shown (b). In panels 2 and 3, M2 starts to show field dispersion.

After the field reversal, the spin-wave modes do not show any significant variation in the frequency with the increase in the magnitude of field up to -375 Oe. M1 reappears at H ≈ -650 Oe and shows a nearly monotonic increase with the increase in the magnitude of H. Initially M2 remains invariant with H but it starts to increase sharply beyond -375 Oe. The corresponding spin-wave spectra are shown in Fig. 5.4(b) - panel 3. For H < -1050 Oe slope of M2 changes drastically as it shows slight decrement with H opening up another anticrossing at around -1050 Oe with a gap of about 0.80 GHz, as shown in panel 4 of Fig. 5.4(b). In this regime, M3 shows qualitatively similar behaviour as for the positive H regime.

To get a deeper insight into the spin-wave dynamics and the spatial characters of the spin-wave modes, we have performed micromagnetic simulations using MuMax3 software [49]. To mimic the large sample area in simulation, an array of 7 × 7 vertexes of square ASI with 2D periodic boundary conditions was considered. The spatially averaged time-domain magnetization was extracted from a 1 μm × 1 μm area from the central portion of the sample following the experimental condition, where the dynamics were measured from a similar area of the sample using the laser spot. The ASI array was divided into cuboidal cells with dimensions 4 × 4 × 20 nm^3. The lateral cell size was taken well below the exchange length of Py (≈5.5 nm). The material parameters used in the dynamic simulations were: gyromagnetic ratio γ = 17.6 MHz/Oe, saturation magnetization M_s = 800 emu/cc, anisotropy field H_K = 0, exchange stiffness constant A_{ex} = 13 × 10^{-6} erg/cm and Gilbert damping parameter α = 0.008. Before studying the magnetization dynamics at a desired magnetic field value, the equilibrium (static) magnetic state was achieved by relaxing the magnetization of the sample at that magnetic field for a long enough time.

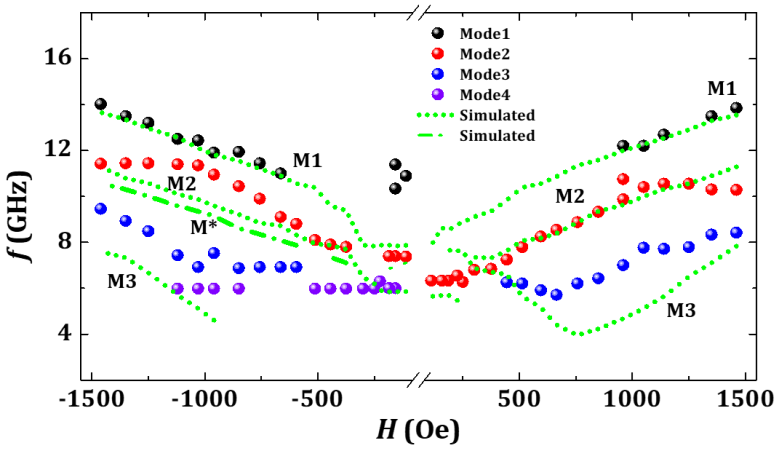

Figure 5. 5. Magnetic field dispersion of experimental and simulated spin-wave frequencies is shown. Solid symbols represent experimental data, which are reproduced from Fig. 5.4(a), while the dotted and dash-dotted lines represent simulated frequencies.

The magnetization dynamics was then simulated by applying a square-shaped pulsed magnetic field, equivalent to optical excitation by the femtosecond laser, of peak amplitude = 20 Oe along the orthogonal direction (along z) of H, having a fall and rise time of 10 ps each and duration of 20 ps. This will produce only the intrinsic spin-wave modes of the ASI system. The simulated spin-wave modes frequencies are shown in Fig. 5.5 by dotted and dash-dotted lines, while the experimental mode frequencies are shown as filled symbols.

It is clear from Fig. 5.5 that despite having a gross qualitative agreement with the experimental spin-wave modes, the simulated modes quantitatively deviate from the experimental modes on several occasions and the qualitative nature of the modes are also not reproduced in some cases. Simulated M1 shows a monotonic decrease with the decrease in the magnitude of H in the regime 110 Oe ≤ H ≤ 1450 Oe. After reversal of H, it remains flat with H up to -375 Oe, beyond which it shows a sudden jump in frequency by ~1.5 GHz. Such a jump is generally related to a change in the magnetic microstate which is also confirmed from the magnetization reversal field in the static-MOKE loop [45]. Beyond this field, the frequency of M1 increases monotonically in the simulation. Therefore, despite the frequency of simulated M1 qualitatively matching with experimental data in some magnetic field range, it starkly deviates from the experimentally observed mode suppression, reappearance and mode repulsion. Hence, we do not observe any spin-wave mode anticrossing in the simulated data. The frequency of M2 is also quantitatively reproduced in the simulation in field regime 375 Oe ≤ H ≤ 1050. In the lower field regime, M2 does not show any significant power in the simulation. In the reversed magnetic field regime, a qualitative agreement between the experimental and simulation frequencies of M2 is observed in the range -375 Oe ≥ H ≥ -665 Oe, beyond which the slopes of the experimental and simulated frequencies differ. While the experimental frequency exhibits a maximum due to anticrossing between M1 and M2 at H = -1050 Oe, the simulated frequency increases almost linearly with the magnitude of H. For M3, although the trends of experimental and simulated frequencies are similar, the simulated frequency is significantly downshifted as opposed to the experimental one. Nevertheless, M3 shows a minimum in frequency at around H = 750 Oe, characteristic of a mode softening behaviour due to the transition of magnetic microstate before getting merged with M2. However, on the negative side of H, the mode softening behaviour is missing in the simulated frequency. The discrepancies between experimental and simulated data will be discussed later in this chapter. Despite the quantitative and some qualitative differences between experimental and simulated data, we will study the spatial maps of the intrinsic spin-wave modes in this system as obtained from the micromagnetic simulations.

To understand the spin-wave mode profiles and the role of magnetic microstates in achieving those profiles, the spin-wave mode profiles have been calculated for three different magnetic field values by using a home-built post-processing code named

DotMag [50]. Before analyzing the spin-wave mode profiles, the equilibrium state magnetization configurations (magnetic microstates) have been studied. The magnetic microstates are shown in Fig. 5.6. It reveals the occurrence of a variety of uniform and nonuniform spin textures. We observe uniform/nearly uniform magnetic microstates at H = 1460, 1050 and -1050 Oe.

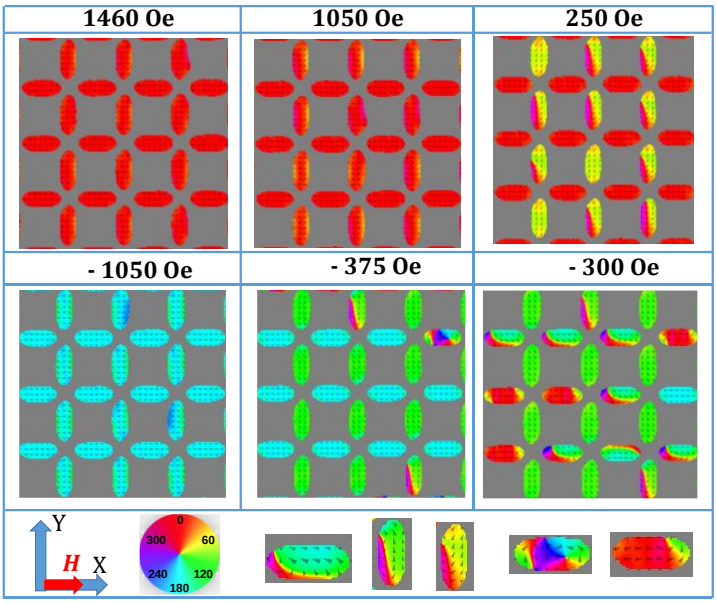

Figure 5. 6. Equilibrium state magnetization configurations at six different magnetic fields (H) are shown. The magnetic field values are mentioned at the top of each image. Magnified views of magnetic microstates are shown in the bottom panels. The color wheel and the magnetic field geometry are shown at the bottom left.

However, in the lower fields, the microstates show large nonuniformities. At H = 250 Oe, the nanobars parallel to the x-axis (horizontal nanobars; HNBs) retain uniform magnetized microstates but those parallel to the y-axis (vertical nanobars; VNBs) show various quasi-uniform C-like microstates. This is because with decreasing H the microstates of VNBs deviate from the direction of H due to dominant shape anisotropy (along y-axis) to form the spin textures. In reversed magnetic field regime, at H = -300 Oe, the microstates display different types of quasi-uniform or multidomain (MD) spin textures in HNBs and VNBs, including C-state and a mixture of the vortex and 180° domains. At H = -375 Oe the magnetization of HNBs starts to reverse and forms S- and C-like states which are reflected in a sudden jump in the simulated spin-wave spectra as shown in Fig. 5.5. The spin-wave mode profiles are influenced by these stark variations of microstates. The calculated spin-wave power and phase profiles are shown in Fig. 5.7 and Fig. 5.8, which show a mixture of uniform and quantized modes. Two different

quantization numbers have been defined for spin-wave modes in backward-volume (BV)-like (n) and Damon-Eshbach (DE)-like (m) geometry. The simulated spin-wave mode profiles at uniform microstates i.e., H = 1460 Oe, 1050 Oe and -1050 Oe, are shown in Figs. 5. 7(a) and 5.7(b).

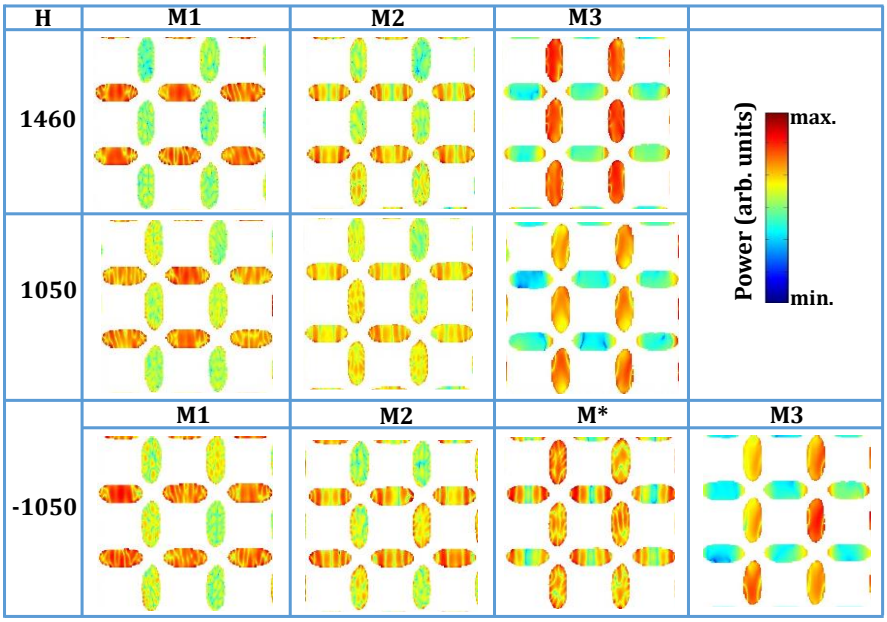

Figure 5. 7. (a) Simulated spin-wave power profiles at different magnetic field values are shown.

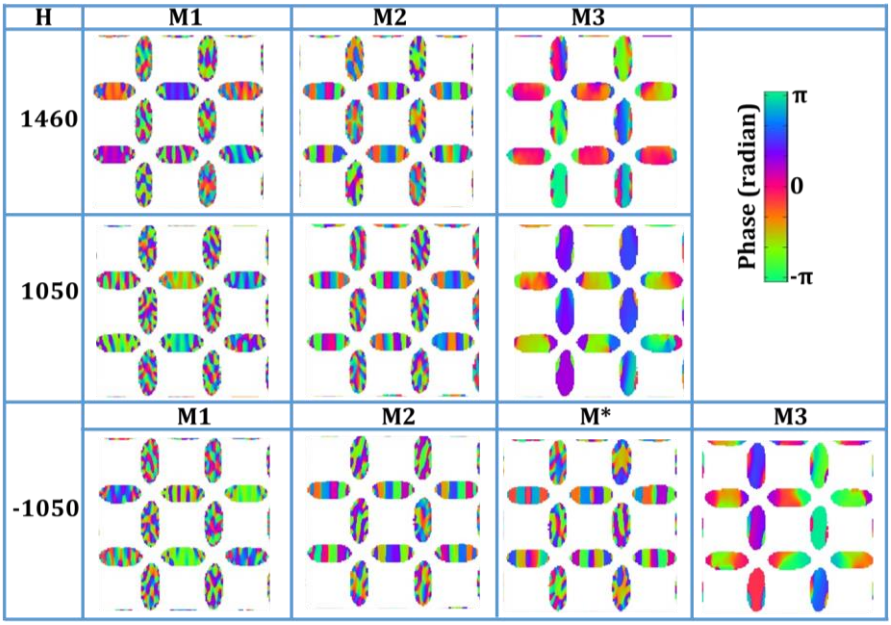

Figure 5. 7. (b) Simulated spin-wave phase profiles at different magnetic field values are shown.

At these field values, the modes show different phase maps while their power is concentrated either in HNBs (M1, M2) or VNBs (M3) or both (M*). The phase profile of

M1 shows n = 9 in HNB and mixed quantized nature in VNBs. The phase profile of M2 shows n = 7 in HNBs and mixed quantized nature in VNBs. M3 shows nearly uniform mode (UM) in VNBs and edge mode (EM) in HNBs. At -1050 Oe, an additional mode (M*) is observed due to mode splitting at around -375 Oe during the field reversal. M* has quantized nature in HNB (n = 5) and mixed quantized nature in VNB, respectively.

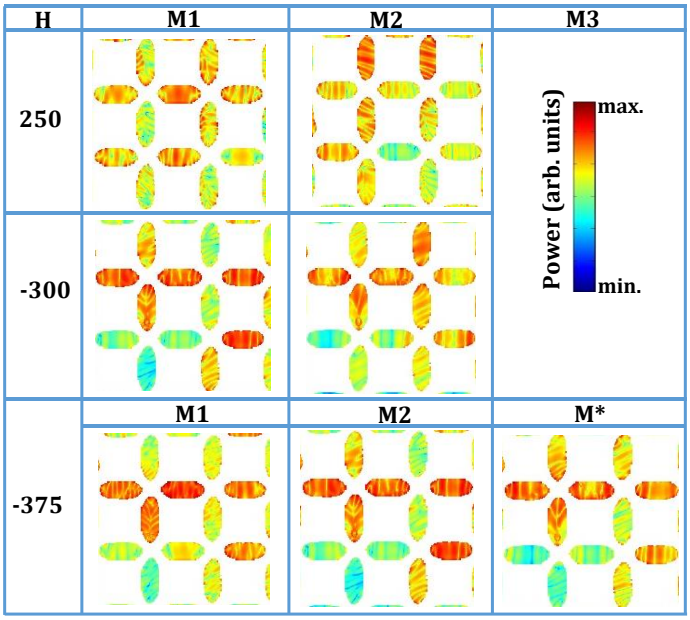

Figure 5. 8. (a) Simulated spin-wave power profiles at different magnetic field values are shown.

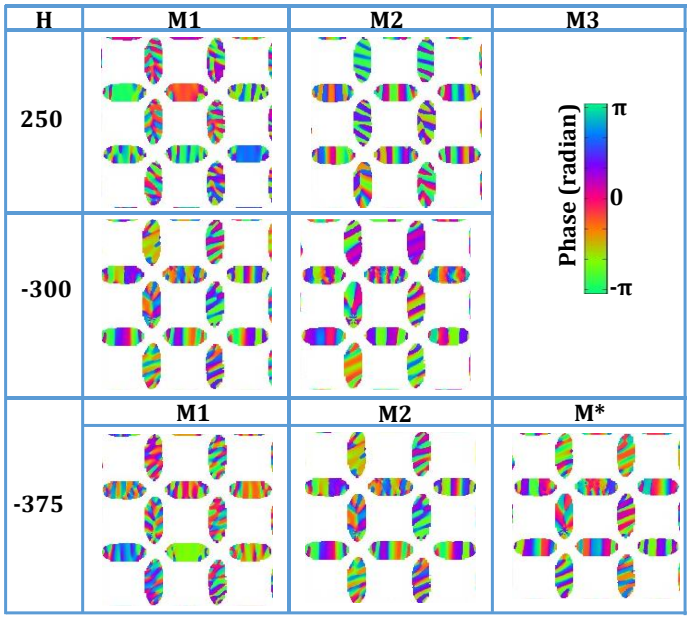

Figure 5. 8. (b) Simulated spin-wave phase profiles at different magnetic field values are shown.

The simulated spin-wave mode profiles at H = 250 Oe, -300 Oe and -375 Oe are shown in Figs. 5.8(a) and 5.8(b). At these fields, the spin-wave power distributions do not follow any set pattern, as they did for the higher fields, but they form some local clusters locally, which may be described from the magnetic microstate distribution. A direct comparison between the microstates and spin-wave mode profiles are presented in Fig. 5.9. At 250 Oe, M1 mainly show power in HNBs and some power in VNBs with MD microstate. Depending on the nearest neighbour magnetization configuration, it shows UM or quantized BV-like mode with n = 9 as shown in Fig. 5.9. M2 shows power in VNBs with quasi uniform state with m = 9.

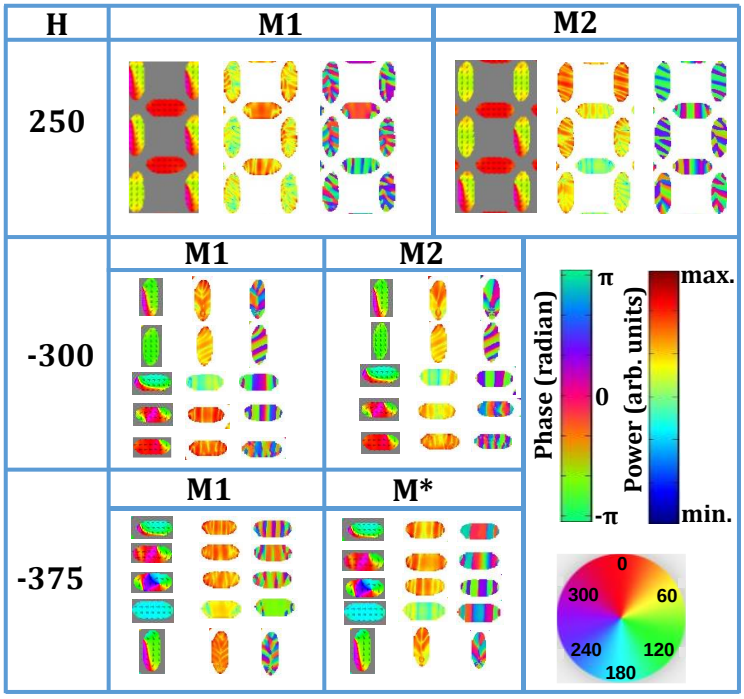

Figure 5. 9. Correlation between magnetic microstates and spin-wave mode profile is shown. Magnetic microstates are shown on the left side and corresponding spin-wave power and phase profiles are presented at middle and right sides of each panel respectively. The colour bars and wheels are presented at bottom right.

Depending on the nearest neighbour magnetization configuration, M2 power in HNBs varies. However, its phase characteristics remain unaltered, i.e., quantized mode with n = 9. At -300 Oe, M1 and M2 mainly show power in HNBs and VNBs with MD configuration. Among the HNBs with MD configuration, it shows power concentrated in those HNBs whose magnetization remained unreversed in most of the nanobars. Both these modes show some power in VNBs with quasi-uniform state and the mode power varies depending on the nearest neighbour magnetization configuration as mentioned before.

M1 shows quantized nature in HNBs with n = 6, mixed quantized nature in VNBs with MD and m = 8 in VNBs with quasi uniform state as presented in Fig. 5.9. M2 shows mixed quantized nature in VNBs with MD state and quantized nature with m = 8 in VNBs with quasi uniform state. It shows diffused power in HNBs with MD configuration with different quantized numbers n = 4, 5 and 6 as shown in Fig. 5.9. At -375 Oe, M1 and M2 mainly show power in HNBs and VNBs with MD configuration. M1 and M2 show mixed quantized nature in VNBs and quantized nature in HNB with MD configuration with n = 9 and 6, respectively. M1 shows some power in a fully reversed state with UM behaviour. M* shows similar power profile behaviours. It shows mixed quantized nature in VNBs with MD state and quantized nature in HNBs with different quantization numbers n = 4, 6, and 5 as shown in Fig. 5.9. In VNBs with quasi uniform state M2 and M* show similar quantized behavior (m = 7) like M2 at H = -300 Oe. From the mode profile analysis, it is evident that the spin-wave mode characteristics remain stable in uniform magnetized state and it is greatly influenced by magnetic microstates which can be introduced during the magnetic field reversal process. Different magnetization configurations favour different spin-wave modes and the mode behaviour changes depending on the microstates as shown in Fig. 5.9. The neighbouring nanobars' microstates can influence spin-wave mode nature and power in a nanobar. Different modes such as uniform mode, quantized mode with different quantization numbers and mixed quantized mode can coexist in an ASI due to the introduction of different microstates during the field reversal.

5.3.1 Magnetoelastic Interaction

As mentioned before, there have been several qualitative and quantitative discrepancies between the experimental and simulated data, particularly the observation of anticrossing behaviour indicating the existence of coupled (hybrid) modes. This is not due to a magnetic interaction-mediated magnon-magnon coupling which would have been reproduced in the micromagnetic simulations without the need of incorporating any external interaction field as observed before [30,51]. We, therefore search for other possibilities responsible for this coupling. Despite the fact that Py has very low magnetostriction it has been shown recently that Py thin films grown on different substrates can develop appreciable magnetostriction [52,53] and ensuing magneto-elastic coupling. Subsequently, we carefully investigate the time-resolved reflectivity data, which show clear oscillations as shown in Fig. 5.10(a). The surface plot of FFT power

spectra of time-resolved reflectivity data as a function of bias magnetic field is shown in Fig. 5.10(b). Four clear frequency components are observed in the surface plot, as marked by horizontal arrows, all of which remain invariant with *H*. This confirms the nonmagnetic origin of the modes. The frequency of the most intense mode is found to be around 6.8 GHz (f_2), while the other three less intense modes have frequencies of 5.2 GHz (f_1), 11.2 GHz (f_3) and 14.2 GHz (f_4). It is known from the literature [54-57] that the irradiation of periodically patterned metallic nanostructures with a pulsed laser can excite surface acoustic waves (SAWs). The rapid increment in temperature of the nanostructures causes impulsive thermal expansion and induces a strain in the substrate, triggering the SAW.

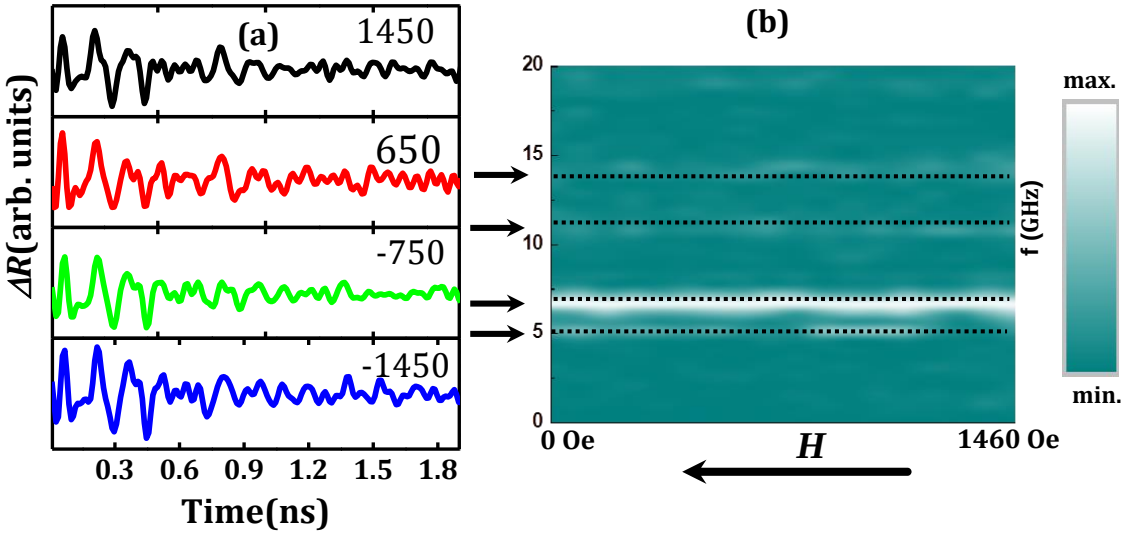

Figure 5. 10. (a) Oscillations in time-resolved reflectivity data are shown for four different applied magnetic fields. (b) Surface plot of FFT power spectra of the time-resolved reflectivity is shown. Positions of different acoustic modes are marked by horizontal arrows, while the color bar is shown at the left side. Calculated acoustic frequencies are shown by dashed lines in (b).

Optically generated SAW has also been observed in the patterned nanostructure of Py on a silicon substrate as reported in the literature [58,59]. As mentioned above, Py has low magneto-elastic coupling due its small magnetostriction [60,61] compare to nickel [62], CoFeB [63] and Co [57,64]. In this study, we chose Py as a base material to avoid the magneto-elastic effect on the spin-wave modes. However, it is evident from the experimental and micromagnetic simulation data that magneto-elastic interaction is present in our sample. The observed SAW frequencies can be analyzed from the elastic properties of the system.

The frequency of SAW related to an array of periodicity D can be given as [58]:

$$\omega = \xi V q \tag{5.1}$$

where the coefficient, $\xi < 1$, depends on the Poisson ratio (σ), the velocity of SAW in the substrate (V) and $q = 2\pi/D$. The velocity of SAW in the substrate is given by the expression:

$$Y = 2\rho(1+\sigma)V^2 \tag{5.2}$$

where Y is Young's modulus and ρ is the density of the material. Considering Y = 130 GPa [65], ρ = 2340 kg/m^3 [58] and σ = 0.27 [58] of silicon, the velocity V is estimated 4670 m/s from eqn. (5.2). For the ASI structure studied here D is ~ 660 nm and the corresponding SAW frequency is found to be ~6.5 GHz (f_{SAW1}) from eqn. (5.1). This frequency agrees well with experimentally observed intense mode (f_2) frequency. Considering the next nearest neighbour edge-to-edge separation of (S) = 845 nm, the SAW frequency is found to be ~5.2 GHz (f_{SAW2}), which is close to the lowest frequency mode (f_1) in the experimental data. This suggests that the intense SAW mode is related to D of the array, while the lowest frequency mode is related to S of the array as marked in Fig. 5.1 (a). The higher frequency mode can be described by [54],

$$\sqrt{h^2 + k^2} f_{SAW} \tag{5.3}$$

where (h,k) are the indices in reciprocal space. The higher-order mode [(1,2) or (2,1)] frequency of f_{SAW1} and f_{SAW2} are found to be ~14.0 GHz and ~11.2 GHz, respectively. These frequency values are close to observed higher order frequency modes f_4 and f_3. Therefore, besides the fundamental SAW modes, higher-order SAW mode is also observed in our studied system.

5.3.2 Overlap Between Magnetic and Elastic Modes

From Fig. 5.4 and Fig. 5.5, it is clear that the signature of acoustic is prominent in the spin-wave field dispersion. Here, M1 is suppressed at a frequency around f_3 at $H \approx$ 1000 Oe and reappears at $H \approx$ -650 Oe close to f_3. M2 and M3 overlap with f_2 at $H \approx$ 400 Oe. M2 overlaps with f3 at $H \approx$ -1000 Oe. The presence of coupling between magnetic and elastic modes is clear from the experimental data as shown in Fig. 5.4. Here, anticrossing behaviour is observed in the vicinity of f3 and f4 of SAW modes. It suggests a strong interaction between magnon and phonon modes. We believe this is the primary reason for the mismatch between the experimental and micromagnetic simulation data without

any stress field. The numerical simulation by introducing an appropriate stress field to reproduce and obtain further understanding of the hybrid magneto-elastic mode will be of interest of future study and presently beyond the scope of this thesis.

5.4 Conclusion

In summary, we have investigated static and dynamic magnetic properties of square ASI system made of nanopatterned Py thin film on silicon substrate using e-beam lithography and thermal evaporation. The MFM imaging of remanent magnetic state has revealed different spin ice microstates and multidomain and magnetic vortex structures. All-optical study of time-resolved magnetization dynamics has revealed rich spin-wave spectra. The field reversal study of the ASI system reveals different novel phenomena such as suppression and reappearance of spin-wave mode, magnon mode anticrossing with high value of anticrossing gap around 1.06 GHz, mode softening, mode merging, field invariant of spin-wave mode in different field regimes. The micromagnetic simulation grossly reproduced spin-wave mode behaviour. In some field regimes, it deviates from experimental data and did not able to qualitatively reproduced the experimental observations. The primary reason behind this discrepancy is the presence of magnetoelastic interaction which has been confirmed from the reflectivity oscillation data. The signature of acoustic mode on the spin-wave field dispersion was clearly observed. The origin of the acoustic mode was understood from analytical calculations. The micromagnetic simulation only gives intrinsic spin-wave modes of ASI structure. The numerical calculation of hybrid magneto-elastic modes is beyond the scope of this study, which will be a topic of future interest. Nevertheless, analyses of intrinsic spin-wave mode profile analysis give an idea about the role of magnetic microstates on the spin-wave dynamics and mode profiles. The spin-wave mode characteristics are greatly influenced by the magnetic microstates which occur during the magnetic field reversal process. Different microstates favour different modes and neighbouring nanobars' microstates can influence the nature of spin-wave modes in a nanobar. During the magnetization reversal, microstates can generate a new spin-wave branch (M2') as observed in simulated data. Finally, this study will be useful for understanding the role of magnetic microstates on spin-wave mode behaviours which can be useful for future ASI-based magnonic devices.

References

[1] H. Yu, G. Duerr, R. Huber, M. Bahr, T. Schwarze, F. Brandl, and D. Grundler, Omnidirectional Spin-Wave Nanograting Coupler; Nat. Commun. **4,** 2702 (2013).
[2] D. Kumar, J. W. Kłos, M. Krawczyk, and A. Barman, Magnonic Band Structure, Complete Bandgap, and Collective Spin Wave Excitation in Nanoscale Two-Dimensional Magnonic Crystals; J. Appl. Phys. **115,** 043917 (2014).
[3] A. Barman, S. Mondal, S. Sahoo, and A. De, Magnetization Dynamics of Nanoscale Magnetic Materials: A Perspective; J. Appl. Phys. **128,** 170901 (2020).
[4] S. S. P. Parkin, M. Hayashi, and L. Thomas, Magnetic Domain-Wall Racetrack Memory; Science **320,** 190 (2008).
[5] M. P. Kostylev, A. A. Serga, T. Schneider, B. Leven, and B. Hillebrands, Spin-Wave Logical Gates; Appl. Phys. Lett. **87,** 153501 (2005).
[6] M. N. Leuenberger and D. Loss, Quantum Computing in Molecular Magnets; Nature **410,** 789 (2001).
[7] A. Barman, G. Gubbiotti, S. Ladak, A. O. Adeyeye, M. Krawczyk, J. Gräfe, C. Adelmann, S. Cotofana, A. Naeemi, V. I. Vasyuchka, B. Hillebrands, S. A. Nikitov, H. Yu, D. Grundler, A. V. Sadovnikov, A. A. Grachev, S. E. Sheshukova, J. Y. Duquesne, M. Marangolo, G. Csaba, W. Porod, V. E. Demidov, S. Urazhdin, S. O. Demokritov, E. Albisetti, D. Petti, R. Bertacco, H. Schultheiss, V. V. Kruglyak, V. D. Poimanov, S. Sahoo, J. Sinha, H. Yang, M. Münzenberg, T. Moriyama, S. Mizukami, P. Landeros, R. A. Gallardo, G. Carlotti, J. V. Kim, R. L. Stamps, R. E. Camley, B. Rana, Y. Otani, W. Yu, T. Yu, G. E. W. Bauer, C. Back, G. S. Uhrig, O. V. Dobrovolskiy, B. Budinska, H. Qin, S. van Dijken, A. V. Chumak, A. Khitun, D. E. Nikonov, I. A. Young, B. W. Zingsem, and M. Winklhofer, The 2021 Magnonics Roadmap; J. Phys.: Condens. Matter **33,** 413001 (2021).
[8] R. P. Cowburn, A. O. Adeyeye, and M. E. Welland, Configurational Anisotropy in Nanomagnets; Phys. Rev. Lett. **81,** 5414 (1998).
[9] G. Gubbiotti, M. Conti, G. Carlotti, P. Candeloro, E. D. Fabrizio, K. Y. Guslienko, A. Andre, C. Bayer, and A. N. Slavin, Magnetic Field Dependence of Quantized and Localized Spin Wave Modes in Thin Rectangular Magnetic Dots; J. Phys.: Condens. Matter **16,** 7709 (2004).
[10] V. V. Kruglyak, A. Barman, R. J. Hicken, J. R. Childress, and J. A. Katine, Picosecond Magnetization Dynamics in Nanomagnets: Crossover to Nonuniform Precession; Phys. Rev. B **71,** 220409(R) (2005).
[11] B. Rana, D. Kumar, S. Barman, S. Pal, Y. Fukuma, Y. Otani, and A. Barman, Detection of Picosecond Magnetization Dynamics of 50 nm Magnetic Dots down to the Single Dot Regime; ACS Nano **5,** 9559 (2011).
[12] S. Saha, R. Mandal, S. Barman, D. Kumar, B. Rana, Y. Fukuma, S. Sugimoto, Y. Otani, and A. Barman, Tunable Magnonic Spectra in Two-Dimensional Magnonic Crystals with Variable Lattice Symmetry; Adv. Funct. Mater. **23,** 2378 (2013).
[13] B. K. Mahato, B. Rana, D. Kumar, S. Barman, S. Sugimoto, Y. Otani, and A. Barman, Tunable Spin Wave Dynamics in Two-Dimensional $Ni_{80}Fe_{20}$ Nanodot Lattices by Varying Dot Shape; Appl. Phys. Lett. **105,** 012406 (2014).
[14] S. Neusser, G. Duerr, H. G. Bauer, S. Tacchi, M. Madami, G. Woltersdorf, G. Gubbiotti, C. H. Back, and D. Grundler, Anisotropic Propagation and Damping of Spin Waves in a Nanopatterned Antidot Lattice; Phys. Rev. Lett. **105,** 067208 (2010).
[15] R. Mandal, P. Laha, K. Das, S. Saha, S. Barman, A. K. Raychaudhuri, and A. Barman, Effects of Antidot Shape on The Spin Wave Spectra of Two-Dimensional $Ni_{80}Fe_{20}$ Antidot Lattices; Appl. Phys. Lett. **103,** 262410 (2013).
[16] S. Pal, J. W. Klos, K. Das, O. Hellwig, P. Gruszecki, M. Krawczyk, and A. Barman, Optically Induced Spin Wave Dynamics in $[Co/Pd]_8$ Antidot Lattices with Perpendicular Magnetic Anisotropy; Appl. Phys. Lett. **105,** 162408 (2014).
[17] R. Mandal, S. Barman, S. Saha, Y. Otani, and A. Barman, Tunable Spin Wave Spectra in Two-Dimensional $Ni_{80}Fe_{20}$ Antidot Lattices with Varying Lattice Symmetry; J. Appl. Phys. **118,** 053910 (2015).

[18] S. Choudhury, S. Barman, Y. Otani, and A. Barman, Efficient Modulation of Spin Waves in Two-Dimensional Octagonal Magnonic Crystal; ACS Nano **11,** 8814 (2017).
[19] S. Sahoo, S. N. Panda, S. Barman, Y. Otani, and A. Barman, Nanochannels for Spin-Wave Manipulation in $Ni_{80}Fe_{20}$ Nanodot Arrays; J. Magn. Magn. Mater. **522,** 167550 (2021).
[20] S. Tacchi, G. Duerr, J. W. Klos, M. Madami, S. Neusser, G. Gubbiotti, G. Carlotti, M. Krawczyk, and D. Grundler, Forbidden Band Gaps in the Spin-Wave Spectrum of a Two-Dimensional Bicomponent Magnonic Crystal; Phys. Rev. Lett. **109,** 137202 (2012).
[21] S. Saha, S. Barman, J. Ding, A. O. Adeyeye, and A. Barman, Time-Domain Study of Spin-Wave Dynamics in Two-Dimensional Arrays of Bi-Component Magnetic Structures; Appl. Phys. Lett. **102,** 242409 (2013).
[22] S. Choudhury, S. Saha, R. Mandal, S. Barman, Y. Otani, and A. Barman, Shape- and Interface-Induced Control of Spin Dynamics of Two-Dimensional Bicomponent Magnonic Crystals; ACS Appl. Mater. Interfaces **8,** 18339 (2016).
[23] U. Ebels, J. L. Duvail, P. E. Wigen, L. Piraux, L. D. Buda, and K. Ounadjela, Ferromagnetic Resonance Studies of Ni Nanowire Arrays; Phys. Rev. B **64,** 144421 (2001).
[24] S. Pal, S. Saha, M. V. Kamalakar, and A. Barman, Field-Dependent Spin Waves in High-Aspect-Ratio Single-Crystal Ferromagnetic Nanowires; Nano Res. **9,** 1426 (2016).
[25] S. Saha, S. Barman, Y. Otani, and A. Barman, All-Optical Investigation of Tunable Picosecond Magnetization Dynamics in Ferromagnetic Nanostripes with a Width down to 50 Nm; Nanoscale **7,** 18312 (2015).
[26] Z. K. Wang, V. L. Zhang, H. S. Lim, S. C. Ng, M. H. Kuok, S. Jain, and A. O. Adeyeye, Nanostructured Magnonic Crystals with Size-Tunable Bandgaps; ACS Nano **4,** 643 (2010).
[27] L. H. F. Andrade, A. Laraoui, M. Vomir, D. Muller, J. P. Stoquert, C. Estournès, E. Beaurepaire, and J. Y. Bigot, Damped Precession of the Magnetization Vector of Superparamagnetic Nanoparticles Excited by Femtosecond Optical Pulses; Phys. Rev. Lett. **97,** 127401 (2006).
[28] B. Rana and A. Barman, Ultrafast Magnetization Dynamics of Chemically Synthesized Ni Nanoparticles; J. Phys. Chem. C **119,** 17444 (2015).
[29] K. Adhikari, S. Barman, R. Mandal, Y. Otani, and A. Barman, Tunable Angle-Dependent Magnetization Dynamics in $Ni_{80}Fe_{20}$ Nanocross Structures of Varying Size; Phys. Rev. Appl. **10,** 044010 (2018).
[30] K. Adhikari, S. Sahoo, A. K. Mondal, Y. Otani, and A. Barman, Large Nonlinear Ferromagnetic Resonance Shift and Strong Magnon-Magnon Coupling in $Ni_{80}Fe_{20}$ Nanocross Array; Phys. Rev. B **101,** 054406 (2020).
[31] S. Tacchi, B. Botters, M. Madami, J. W. Kłos, M. L. Sokolovskyy, M. Krawczyk, G. Gubbiotti, G. Carlotti, A. O. Adeyeye, S. Neusser, and D. Grundler, Mode Conversion from Quantized to Propagating Spin Waves in a Rhombic Antidot Lattice Supporting Spin Wave Nanochannels; Phys. Rev. B **86,** 014417 (2012).
[32] S. Choudhury, S. Majumder, S. Barman, Y. Otani, and A. Barman, Active Control of Mode Crossover and Mode Hopping of Spin Waves in a Ferromagnetic Antidot Lattice; Phys. Rev. Appl. **10,** 064044 (2018).
[33] R. Zivieri, P. Malagò, L. Giovannini, S. Tacchi, G. Gubbiotti, and A. O. Adeyeye, Soft Magnonic Modes in Two-Dimensional Permalloy Antidot Lattices; J. Phys.: Condens. Matter **25,** 336002 (2013).
[34] S. Neusser, G. Duerr, S. Tacchi, M. Madami, M. L. Sokolovskyy, G. Gubbiotti, M. Krawczyk, and D. Grundler, Magnonic Minibands in Antidot Lattices with Large Spin-Wave Propagation Velocities; Phys. Rev. B **84,** 094454 (2011).
[35] R. F. Wang, C. Nisoli, R. S. Freitas, J. Li, W. McConville, B. J. Cooley, M. S. Lund, N. Samarth, C. Leighton, V. H. Crespi, and P. Schiffer, Artificial 'Spin Ice' in a Geometrically Frustrated Lattice of Nanoscale Ferromagnetic Islands; Nature **439,** 303 (2006).
[36] M. J. Harris, S. T. Bramwell, D. F. McMorrow, T. Zeiske, and K. W. Godfrey, Geometrical Frustration in the Ferromagnetic Pyrochlore $Ho_2Ti_2O_7$; Phys. Rev. Lett. **79,** 2554 (1997).
[37] S. T. Bramwell, S. R. Giblin, S. Calder, R. Aldus, D. Prabhakaran, and T. Fennell, Measurement of the Charge and Current of Magnetic Monopoles in Spin Ice; Nature **461,** 956 (2009).

[38] S. Gliga, A. Kákay, R. Hertel, and O. G. Heinonen, Spectral Analysis of Topological Defects in an Artificial Spin-Ice Lattice; Phys. Rev. Lett. **110,** 117205 (2013).
[39] J. Sklenar, V. S. Bhat, L. E. DeLong, and J. B. Ketterson, Broadband Ferromagnetic Resonance Studies on an Artificial Square Spin-Ice Island Array; J. Appl. Phys. **113,** 17B530 (2013).
[40] M. B. Jungfleisch, W. Zhang, E. Iacocca, J. Sklenar, J. Ding, W. Jiang, S. Zhang, J. E. Pearson, V. Novosad, J. B. Ketterson, O. Heinonen, and A. Hoffmann, Dynamic Response of an Artificial Square Spin Ice; Phys. Rev. B **93,** 100401 (2016).
[41] X. Zhou, G.-L. Chua, N. Singh, and A. O. Adeyeye, Large Area Artificial Spin Ice and Anti-Spin Ice $Ni_{80}Fe_{20}$ Structures: Static and Dynamic Behavior; Adv. Funct. Mater. **26,** 1437 (2016).
[42] A. Ghosh, F. Ma, J. Lourembam, X. Jin, R. Maddu, Q. J. Yap, and S. Ter Lim, Emergent Dynamics of Artificial Spin-Ice Lattice Based on an Ultrathin Ferromagnet; Nano Lett. **20,** 109 (2020).
[43] Y. Li, G. Gubbiotti, F. Casoli, F. J. T. Gonçalves, S. A. Morley, M. C. Rosamond, E. H. Linfield, C. H. Marrows, S. McVitie, and R. L. Stamps, Brillouin Light Scattering Study of Magnetic-Element Normal Modes in a Square Artificial Spin Ice Geometry; J. Phys. D: Appl. Phys. **50,** 015003 (2016).
[44] V. S. Bhat, F. Heimbach, I. Stasinopoulos, and D. Grundler, Magnetization Dynamics of Topological Defects and the Spin Solid in a Kagome Artificial Spin Ice; Phys. Rev. B **93,** 140401 (2016).
[45] A. K. Chaurasiya, A. K. Mondal, J. C. Gartside, K. D. Stenning, A. Vanstone, S. Barman, W. R. Branford, and A. Barman, Comparison of Spin-Wave Modes in Connected and Disconnected Artificial Spin Ice Nanostructures Using Brillouin Light Scattering Spectroscopy; ACS Nano **15,** 11734 (2021).
[46] T. Dion, D. M. Arroo, K. Yamanoi, T. Kimura, J. C. Gartside, L. F. Cohen, H. Kurebayashi, and W. R. Branford, Tunable Magnetization Dynamics in Artificial Spin Ice via Shape Anisotropy Modification; Phys. Rev. B **100,** 054433 (2019).
[47] E. Iacocca, S. Gliga, R. L. Stamps, and O. Heinonen, Reconfigurable Wave Band Structure of an Artificial Square Ice; Phys. Rev. B **93,** 134420 (2016).
[48] S. Mamica, X. Zhou, A. Adeyeye, M. Krawczyk, and G. Gubbiotti, Spin-Wave Dynamics in Artificial Anti-Spin-Ice Systems: Experimental and Theoretical Investigations; Phys. Rev. B **98,** 054405 (2018).
[49] A. Vansteenkiste, J. Leliaert, M. Dvornik, M. Helsen, F. Garcia-Sanchez, and B. Van Waeyenberge, The Design and Verification of Mumax3; AIP Adv. **4,** 107133 (2014).
[50] D. Kumar, O. Dmytriiev, S. Ponraj, and A. Barman, Numerical Calculation of Spin Wave Dispersions in Magnetic Nanostructures; J. Phys. D: Appl. Phys. **45,** 015001 (2011).
[51] K. Adhikari, S. Choudhury, S. Barman, Y. Otani, and A. Barman, Observation of Magnon-Magnon Coupling with High Cooperativity in $Ni_{80}Fe_{20}$ Cross-shaped Nanoring Array; Nanotechnology (2021).
[52] R. M. Valletta, G. Guthmiller, and G. Gorman, Relation of Thickness and Some Physical Properties of NiFe Thin Films; J. Vac. Sci. Technol. A **9,** 2093 (1991).
[53] O. Song, C. A. Ballentine, and R. C. O'Handley, Giant Surface Magnetostriction in Polycrystalline Ni and NiFe Films; Appl. Phys. Lett. **64,** 2593 (1994).
[54] Y. Yahagi, B. Harteneck, S. Cabrini, and H. Schmidt, Controlling Nanomagnet Magnetization Dynamics via Magnetoelastic Coupling; Phys. Rev. B **90,** 140405(R) (2014).
[55] Y. Yahagi, C. Berk, B. Hebler, S. Dhuey, S. Cabrini, M. Albrecht, and H. Schmidt, Optical Measurement of Damping in Nanomagnet Arrays Using Magnetoelastically Driven Resonances; J. Phys. D: Appl. Phys. **50,** 17LT01 (2017).
[56] C. Berk, M. Jaris, W. Yang, S. Dhuey, S. Cabrini, and H. Schmidt, Strongly Coupled Magnon–Phonon Dynamics in a Single Nanomagnet; Nat. Commun. **10,** 2652 (2019).
[57] S. Mondal, M. A. Abeed, K. Dutta, A. De, S. Sahoo, A. Barman, and S. Bandyopadhyay, Hybrid Magnetodynamical Modes in a Single Magnetostrictive Nanomagnet on a Piezoelectric Substrate Arising from Magnetoelastic Modulation of Precessional Dynamics; ACS Appl. Mater. Interfaces **10,** 43970 (2018).

[58] A. Comin, C. Giannetti, G. Samoggia, P. Vavassori, D. Grando, P. Colombi, E. Bontempi, L. E. Depero, V. Metlushko, B. Ilic, and F. Parmigiani, Elastic and Magnetic Dynamics of Nanomagnet-Ordered Arrays Impulsively Excited by Subpicosecond Laser Pulses; Phys. Rev. Lett. **97,** 217201 (2006).
[59] C. Giannetti, B. Revaz, F. Banfi, M. Montagnese, G. Ferrini, F. Cilento, S. Maccalli, P. Vavassori, G. Oliviero, E. Bontempi, L. E. Depero, V. Metlushko, and F. Parmigiani, Thermomechanical Behavior of Surface Acoustic Waves in Ordered Arrays of Nanodisks Studied by Near-Infrared Pump-Probe Diffraction Experiments; Phys. Rev. B **76,** 125413 (2007).
[60] R. M. Bozorth and J. G. Walker, Magnetic Crystal Anisotropy and Magnetostriction of Iron-Nickel Alloys; Phys. Rev. **89,** 624 (1953).
[61] C. Rossignol, B. Perrin, B. Bonello, P. Djemia, P. Moch, and H. Hurdequint, Elastic Properties of Ultrathin Permalloy/Alumina Multilayer Films Using Picosecond Ultrasonics and Brillouin Light Scattering; Phys. Rev. B **70,** 094102 (2004).
[62] Y. Yu, H. Bruce, C. Stefano, and S. Holger, In Control of the Magnetization Dynamics in Patterned Nanostructures With Magnetoelastic Coupling, 2015.
[63] D. Froes, M. Arana, L. C. Sampaio, and J. P. Sinnecker, Acoustic Wave Surfing: Spin Waves and Spin Pumping Driven by Elastic Wave; J. Phys. D: Appl. Phys. **54,** 255001 (2021).
[64] A. De, J. L. Drobitch, S. Majumder, S. Barman, S. Bandyopadhyay, and A. Barman, Resonant Amplification of Intrinsic Magnon Modes and Generation of New Extrinsic Modes in a Two-Dimensional Array of Interacting Multiferroic Nanomagnets by Surface Acoustic Waves; Nanoscale **13,** 10016 (2021).
[65] J. J. Wortman and R. A. Evans, Young's Modulus, Shear Modulus, and Poisson's Ratio in Silicon and Germanium; J. Appl. Phys. **36,** 153 (1965).

Chapter 6

6. Ultrafast Magnetization Dynamics in a Nanoscale Three-Dimensional Cobalt Tetrapod Structure

6.1 Introduction

Confined magnetic structures have long been interesting systems due to their interesting spin configuration [1,2], magnetization reversal properties [1,2], spin dynamics [3,4] and damping [5] as well as their potential applications in high density magnetic storage [6], memory [7], logic [8], transistor [9] and communication devices. Consequently, during the last decade, a new research field named as magnonics [10] has rapidly emerged with potential applications in on-chip high-frequency communication and data processing. Magnonic crystals [10,11] are periodically modulated magnetic media, the magnetic counterparts of the photonic [12] and phononic [13] crystals, where spin waves act as information carrier. Ultrafast magnetization dynamics and spin waves of one-dimensional arrays of nanowires [14,15] and two-dimensional arrays of planar ferromagnetic structures such as nanodots [4,16,19] and antidots [20-22] as well as bi-component magnonic crystals [23] have been studied in great detail. In contrast, the study of three-dimensional (3D) magnetic nanostructures is still in its infancy but is gaining intense interest due to the emergence of novel fabrication methods such as focused electron beam induced deposition [24] as well as numerous applications including sensors and actuators [25], ultrahigh density magnetic data storage [26], neuromorphic computer architecture [27], 2.5-dimensional spintronics [25] and 3D magnonic crystals [28]. Recently Chern *et al.* [29] proposed a 3D layered geometry for a 3D artificial spin ice to capture the fully 3D spin-ice behaviour including effective Coulomb interactions between monopoles and they also provide an accessible and flexible, experimentally realizable geometry for the same. However, intensive research to explore the above fields based on 3D micro and nanostructures are missing in the literature. A commonly used technique for 3D structure fabrication is electrodeposition of magnetic material on templates prepared by ion-track etching of polycarbonate membranes, anodization of alumina film, block copolymerization, and focused electron beam milling. However, the fabrication of complex 3D structures of arbitrary shape and

with high precision is difficult using the above techniques. Two-photon lithography [30] (TPL) has recently emerged as a very powerful nanostructuring approach with intrinsic 3D structure fabrication capability and has recently demonstrated the realization of very pure 3D magnetic nanostructures [31].

Here, we have fabricated an array of well-separated 3D cobalt tetrapod structures with sub-micrometre features by using a combination of TPL and electrodeposition. We show, for the first time that such complex 3D magnetic nanostructures can be studied using time-resolved magneto-optical Kerr effect (TRMOKE) microscopy in order to directly observe the ultrafast magnetization dynamics. The time-resolved data show multi-mode precessional oscillations while the fast Fourier transform (FFT) spectra of time-resolved data show two clear precession modes (around 1 and 10 GHz) accompanied by another less intense mode at around 30 GHz. The results have been reproduced by three-dimensional micromagnetic simulations which allowed the mapping of the spatial distribution of precessional modes. The higher frequency mode (30 GHz) shows uniform precession over the major part of the sample, while the other two modes show mixed character.

6.2 Experimental Details

A 100 μm^2 array of three-dimensional cobalt tetrapod structures were fabricated using two-photon lithography (TPL) and electrodeposition [31]. In the TPL technique, a femtosecond laser operating in the infrared frequency range is focused down to a diffraction-limited spot within a conventional photoresist. Common photoresists have negligible linear absorption in the infrared region, and hence the laser can penetrate into the materials and influence its polymerization within the region of interest without perturbing other regions of the resist. A TPL system consisting of a pulsed laser of wavelength = 780 nm, average power = 120 mW, pulse width = 120 fs and repetition rate = 80 MHz was used to build the pattern within the positive photoresist (AZ9260) on glass/indium tin oxide (ITO) substrate. After patterning the resist, electrodeposition was used to fill the channels with Co. A standard Watts bath (600 ml) consisting of cobalt sulphate (90 g), cobalt chloride (27 g), boric acid (14 g) and sodium lauryl sulphate (1 g) was used. A simple two-electrode electrodeposition was used at room temperature with a cobalt anode operating at a constant current of 1 mA. Complete infiltration of the pores was ensured by utilizing deposition rate studies on a number of samples. After

electrodeposition, the resist was removed using acetone, yielding free standing cobalt tetrapod structures. A scanning electron micrograph of the sample is shown in Fig. 6.1. The total array size is approximately 100 μm^2. Each tetrapod structure consists of four wires, each with approximate dimension 657 nm × 782 nm × 10 μm. Only a small amount of variation (60 nm) in nanowire width is seen across the array, with a similar variation in nanowire length (100 nm) also observed. The tetrapod structures are seen to be well fabricated with clean surface morphology. The separation between the tetrapod structures is 10 μm, which ensures that they are not magnetostatically coupled. Further details upon the growth and physical characterisation of these samples can be found elsewhere [31].

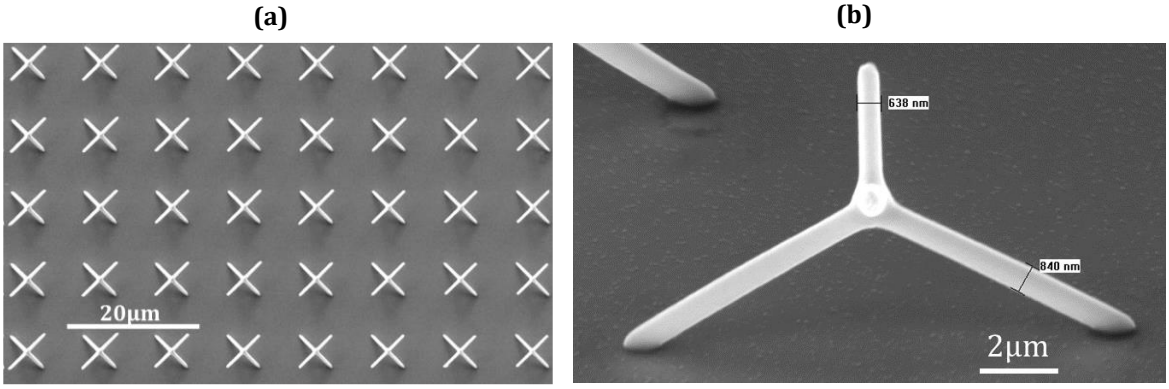

Figure 6. 1. Scanning electron micrograph of (a) an array of tetrapod structures and (b) a single tetrapod structure.

The ultrafast magnetization dynamics from a single tetrapod structure from the array was measured using a custom-built time-resolved magneto-optic Kerr effect (TRMOKE) microscope based on a two-colour collinear pump-probe technique [32]. The second harmonic (λ_{pump} = 400 nm, fluence = 19 mJ/cm^2, pulse width = 100 fs) of the fundamental laser beam from a mode-locked Ti-sapphire laser (Tsunami, Spectra Physics) was used to pump the sample, while the time-delayed fundamental beam (λ_{probe} = 800 nm, fluence = 7 mJ/cm^2, pulse width = 80 fs) is used to probe the polar Kerr rotation by using an optical bridge detection as a function of the time delay between the pump and probe beams. The optical bridge detector isolates the Kerr rotation and the total reflectivity signal to avoid breakthrough of one signal into another and the measurement is done using lock-in amplifiers in a phase sensitive manner to attain high sensitivity. The probe beam is tightly focused (spot diameter = 800 nm) using a microscope objective of numerical aperture of 0.65 at the junction of the tetrapod structure, while the pump beam is slightly defocused

at the focal plane of the probe beam with a spot diameter of about 1 μm. The probe beam is carefully placed at the centre of the pump-beam and the junction of the tetrapod structure using an x-y-z piezoelectric scanning state with a feedback loop and a white-light illumination system. A static magnetic field with varying magnitude is applied at a small angle (~ 15°) to the normal direction of the substrate plane (as shown in Fig. 6.2(a)), the out-of-plane component of which is defined as the bias field *H*.

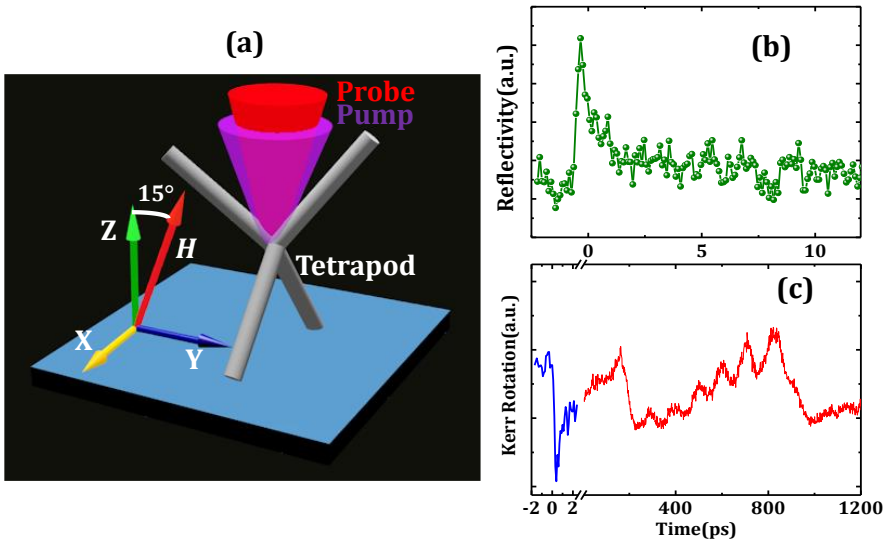

Figure 6. 2. (a) Schematic diagram of the cobalt tetrapod and the experimental geometry. Typical time-resolved (b) reflectivity and (c) Kerr rotation data are shown at H = 3.92 kOe.

Here, we measure the precessional magnetization dynamics from the junction of the Co tetrapod sample, which is a more complicated geometry than a thin film or a vertically standing nanowire. However, after careful alignment of the static bias field angle, we found that this tilt of ~15° is suitable for inducing precessional magnetization dynamics in this sample. A large enough static field is first applied to saturate the sample magnetization followed by reducing it to the desired bias field value for the measurement of the time-resolved dynamic.

6.3 Results and Discussions

Typical time-resolved reflectivity and Kerr rotation data are shown in Figs. 6.2(b) and 6.2(c), respectively. The time-resolved Kerr rotation data show three distinctly different temporal regimes (Fig. 6.2(c)). First, it shows the negative delay followed by ultrafast demagnetization within about 400 fs of the zero delay. This is followed by a fast relaxation within about 700 fs and a slower relaxation superposed with the precession of magnetization. However, the precession shows a complicated profile, which does not

allow the precise determination of the slower relaxation time in this sample. Figure 6.3(a) shows the background subtracted time-resolved Kerr rotation data for three different magnetic field values. The strong beating effect in the precessional oscillation indicates the presence of multiple spin-wave modes in this system.

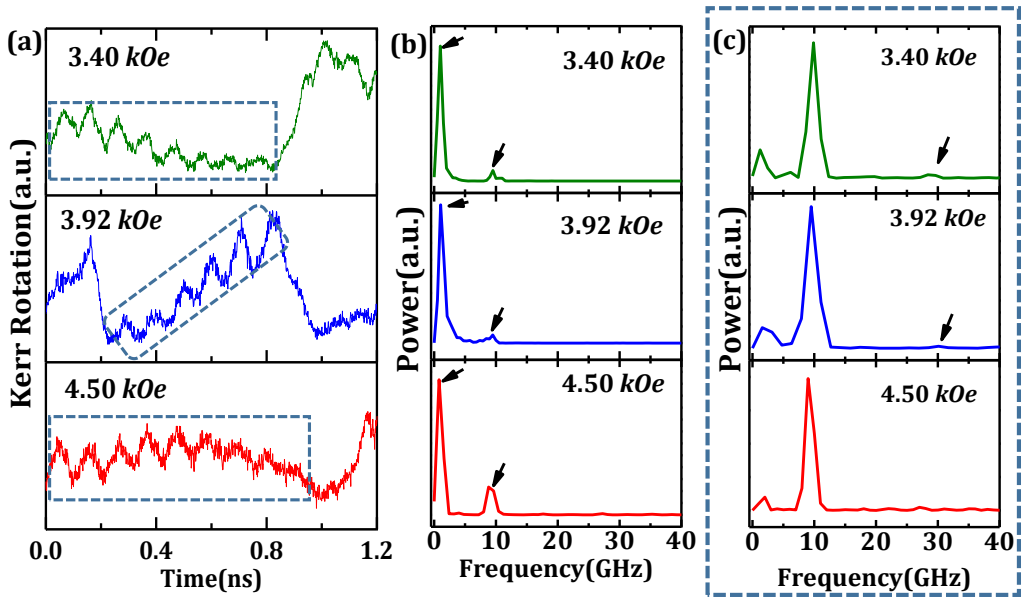

Figure 6. 3. (a) Time-resolved Kerr rotation data for three different bias magnetic field values. (b) Power spectra for the entire time-resolved data. (c) Power spectra for the marked region in time-resolved data. Corresponding values of bias magnetic fields are shown.

The fast Fourier transform (FFT) power spectra of the full time-resolved precessional oscillation data (Fig. 6.3(b)) shows a highly intense mode at around 1 GHz and another less intense mode at around 10 GHz. It is apparent from the precessional data that another higher frequency mode is present in it, and in order to extract that mode clearly from the higher amplitude modes we take FFT of marked part of the precessional data (as shown in Fig. 6.3(c)). The FFT power spectra of partial time-resolved data show a clear mode at around 10 GHz and another lower intensity mode at around 30 GHz. However, for lower bias field values the signal to noise ratio of the magnetization precession data becomes very weak making it difficult for extracting the precessional mode frequencies clearly, and hence we restrict our measurements for three field values only.

To gain more insight into the observed precessional modes, we have performed 3D micromagnetic simulations using MuMax3 [33] software. For 3D visualization of the simulated results, we have used Mayavi [34] and Muview [35] software. In the simulation,

we have considered a tetrapod structure made of four cobalt cylindrical legs of diameters similar to the experimental sample but due to the limited computational resources, we have considered the length of each cylindrical leg as 2.5 μm. This is justified since the experimental time-resolved Kerr rotation data was measured using the focused laser spot placed at the centre of a single tetrapod structure. The sample is discretized into cells of dimensions 25 × 25 × 25 nm^3. We believe the spin-wave modes in structures with such dimensions are primarily governed by the dipolar interaction, so cell size above the exchange length of cobalt can reproduce the observed magnetization dynamics. By simulating a Co tetrapod sample of 2.5 μm leg length allowed us to use cell size of 25 × 25 × 25 nm^3, which correspond to about 40 cells in all three directions at the junction of the tetrapod structure which would be sufficient to resolve the spin configuration and the spin dynamics in this region of space. The magnetic parameters used for the simulation are saturation magnetization M_s = 1400 emu/cc, anisotropy constant K = 0 (justified since the unaixial grains have random orientations [31]), gyromagnetic ratio γ = 17.6 MHz/Oe and exchange stiffness constant A_{ex} = 3.0 × 10^{-5} erg/cm. The external bias field H is applied according to the experimental configuration and a square pulsed field of 10 ps risetime, 200 ps width and peak amplitude of 20 Oe is applied perpendicular to the sample plane. The simulated magnetization dynamics data are acquired from a volume of 1 μm^3 from the tetrapod junction. The FFT power spectra of the simulated time-resolved magnetization (Fig. 6.4(a)) reveals three resonant modes, namely as M1, M2, M3 from higher to lower frequency regime The number of modes and corresponding mode-frequencies obtained from the simulation match qualitatively with the experimental results. The static magnetic configurations of the z-component of magnetization at three different bias field values are shown in Fig. 6.4(b). The colour bar in Fig. 6.4(b) represents normalized magnetization along the z-direction. It is clear from the figure that the z-component of magnetization is increasing with increasing bias field, i.e., the colour is changing from reddish to orange at the ends of the wires and it is changing from violet to gold at the surface of the wires. Though, the increment is not uniform all over the tetrapod structure due to complicated internal field distribution in such a complex 3D structure.

In addition, a slight tilt (15°) in the bias field also introduces an asymmetry in the magnetic configuration in different arms of the tetrapod.

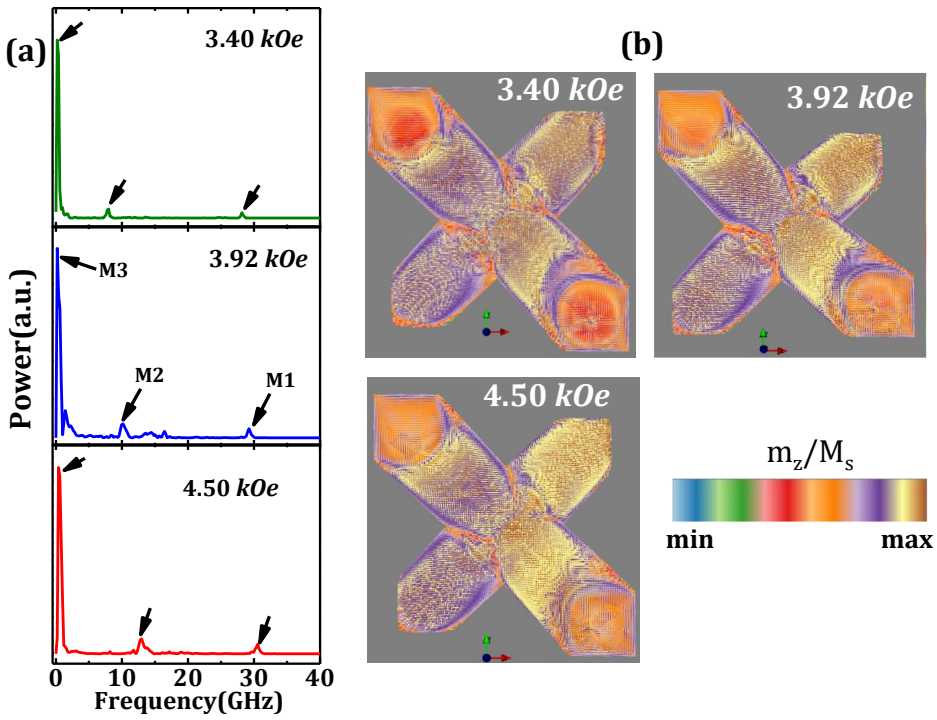

Figure 6. 4. Simulated (a) power spectra and (b) normalized static magnetization configuration (z-component) for ground state at three different bias magnetic fields are shown.

Having achieved this qualitative agreement, we now further simulate the corresponding mode profiles by providing a sinusoidal excitation corresponding to each of the resonance frequencies along z-direction with an amplitude of 20 Oe. This is followed by a long waiting time of more than 100 ns so that all other spurious modes decay down leaving behind only the driven mode at that frequency. The resonant mode profiles are extracted by taking the difference in magnetization between the excited state and the ground state [36]. The difference between z-components is normalized ($m^{z,diff}$) and viewed using Muview software. The spatial profiles of modes M1, M2 and M3 at three different bias fields are shown in Fig. 6.5. The magnetization profiles of the sample at three different magnetic fields show qualitatively similar behaviour although the non-uniformity in the surface magnetization (red contrast) appears to increase with the reduction in the magnetic field (Fig. 6.4(b)). Consequently, the mode profiles of the observed modes at three magnetic field values also show qualitatively the same behaviour (Fig. 6.5), with distinct differences in the mode profiles for the three different modes. Figure 6.6(a) shows the three modes distributed over the whole simulated sample

at a bias field H = 4.50 kOe. It is clearly observed that mode 1 (M1) corresponds to a spatially uniform mode, while mode 2 (M2) and mode 3 (M3) are standing wave modes with increasing number of nodal planes with decreasing frequency.

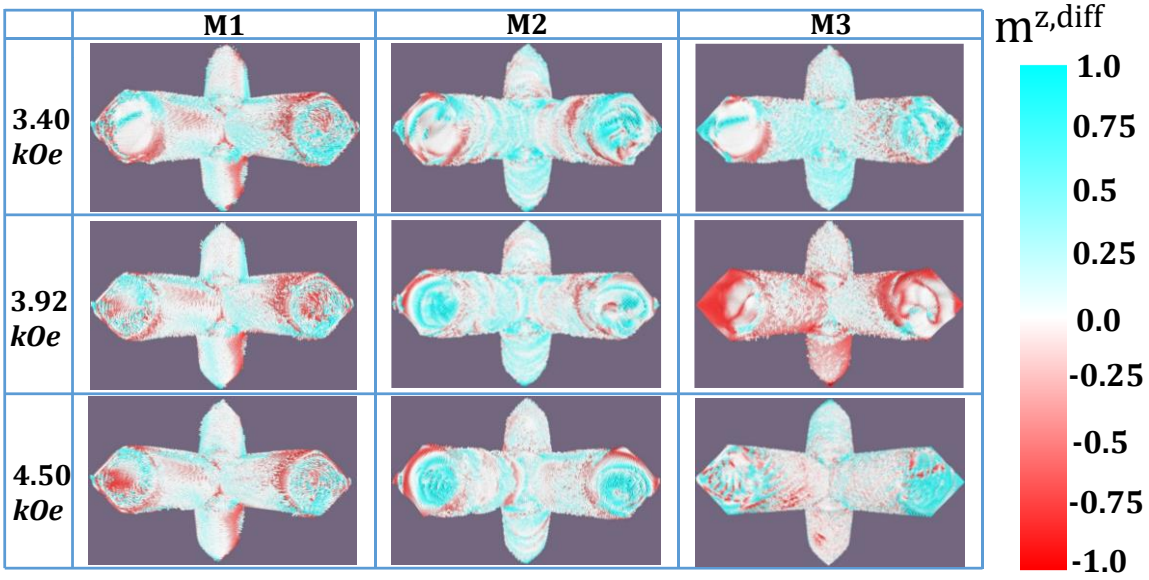

Figure 6. 5. Simulated spin-wave mode profiles for H = 3.40, 3.92 and 4.50 kOe.

Figure 6.6(b) shows slices taken from the junction of the tetrapod for the three modes. From this figure, M2 and M3 are found to have the nature of the mixed mode of dipolar origin with nodal planes spreading along the mutually perpendicular directions of the plane.

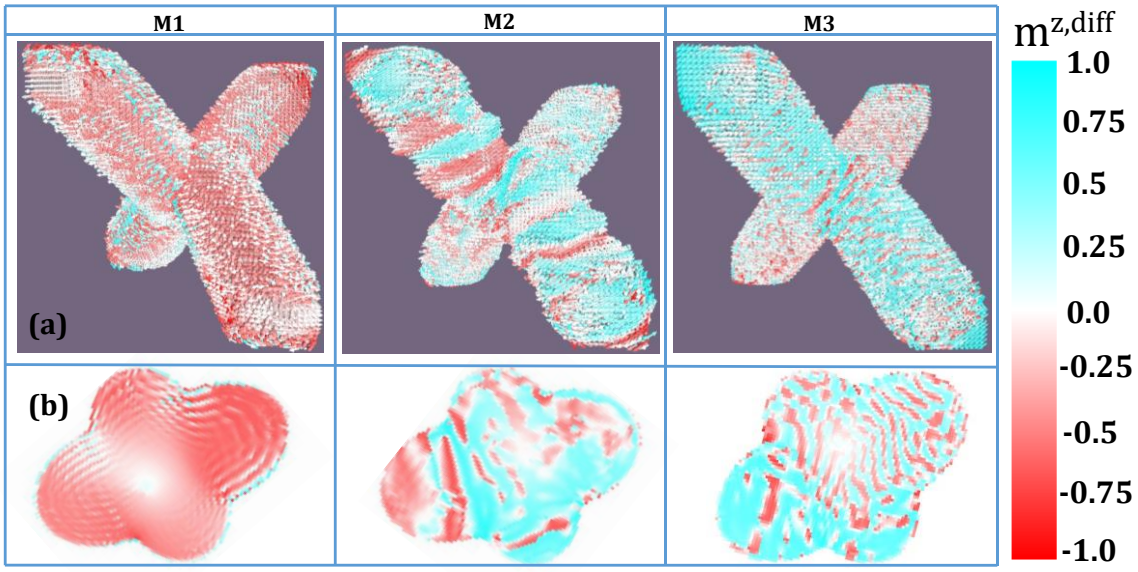

Figure 6. 6. (a) Magnified view of mode profile and (b) sliced view of the tetrapod junction for different modes at H = 4.50 kOe.

The quantization number increases with the decrease in frequency but cannot be clearly counted due to highly complicated spatial nature of the modes. On the other hand, although M1 shows primarily spatially uniform nature it also contains thin fringes along mutually perpendicular direction, indicating standing spin-wave modes of very high mode quantization number.

6.4 Conclusion

In conclusion, we have investigated the ultrafast magnetization dynamics in a three-dimensional cobalt tetrapod structure, by using time-resolved magneto-optical Kerr microscopy. The experimental results along with three-dimensional micromagnetic simulations reveal the existence of three spin-wave modes at around 1, 10 and 30 GHz. With the variation of the bias magnetic field, only small quantitative changes are observed in the modes while the qualitative characters of the modes remain unchanged. Investigation of the spatial nature of the modes over the whole simulated tetrapod sample as well from its junction reveals a spatially uniform mode with thin fringes most likely associated with standing spin-wave mode of high mode quantization number at 30 GHz. However, the two lower frequency modes show dipolar dominated mixed modes with nodal planes spreading along two mutually perpendicular directions. The mode quantization number of the dipolar modes increases with the decrease in frequency. The investigation of ultrafast magnetization dynamics from a complicated three-dimensional magnetic structure and revelation of complex modes in such structures open the possibility of further intensive study in this field for promotion of such structures as building blocks in high-frequency ultra-high-density storage, memory, logic and communication devices.

References

[1] R. Skomski, Nanomagnetics; J. Phys.: Condens. Matter **15**, R841 (2003).
[2] S. D. Bader, Colloquium: Opportunities in Nanomagnetism; Rev. Mod. Phys. **78**, 1 (2006).
[3] A. Barman and A. Haldar, in Solid State Physics, edited by R. E. Camley, and R. L. Stamps (Academic Press, 2014), pp. 1.
[4] V. V. Kruglyak, A. Barman, R. J. Hicken, J. R. Childress, and J. A. Katine, Precessional Dynamics in Microarrays of Nanomagnets; J. Appl. Phys. **97**, 10A706 (2005).
[5] A. Barman, S. Wang, J. Maas, A. R. Hawkins, S. Kwon, J. Bokor, A. Liddle, and H. Schmidt, Size Dependent Damping in Picosecond Dynamics of Single Nanomagnets; Appl. Phys. Lett. **90**, 202504 (2007).
[6] O. Hellwig, A. Berger, T. Thomson, E. Dobisz, Z. Z. Bandic, H. Yang, D. S. Kercher, and E. E. Fullerton, Separating Dipolar Broadening from the Intrinsic Switching Field Distribution in Perpendicular Patterned Media; Appl. Phys. Lett. **90**, 162516 (2007).
[7] S. Tehrani, E. Chen, M. Durlam, M. DeHerrera, J. M. Slaughter, J. Shi, and G. Kerszykowski, High Density Submicron Magnetoresistive Random Access Memory (invited); J. Appl. Phys. **85**, 5822 (1999).
[8] D. A. Allwood, G. Xiong, C. C. Faulkner, D. Atkinson, D. Petit, and R. P. Cowburn, Magnetic Domain-Wall Logic; Science **309**, 1688 (2005).
[9] D. Kumar, S. Barman, and A. Barman, Magnetic Vortex Based Transistor Operations; Sci. Rep. **4**, 4108 (2014).
[10] B. Lenk, H. Ulrichs, F. Garbs, and M. Münzenberg, The Building Blocks of Magnonics; Phys. Rep. **507**, 107 (2011).
[11] M. Krawczyk and D. Grundler, Review and Prospects of Magnonic Crystals and Devices with Reprogrammable Band Structure; J. Phys.: Condens. Matter **26**, 123202 (2014).
[12] H. Kosaka, T. Kawashima, A. Tomita, M. Notomi, T. Tamamura, T. Sato, and S. Kawakami, Superprism Phenomena in Photonic Crystals; Phys. Rev. B **58**, R10096 (1998).
[13] M. S. Kushwaha, P. Halevi, L. Dobrzynski, and B. Djafari-Rouhani, Acoustic Band Structure of Periodic Elastic Composites; Phys. Rev. Lett. **71**, 2022 (1993).
[14] G. Gubbiotti, S. Tacchi, G. Carlotti, N. Singh, S. Goolaup, A. O. Adeyeye, and M. Kostylev, Collective Spin Modes in Monodimensional Magnonic Crystals Consisting of Dipolarly Coupled Nanowires; Appl. Phys. Lett. **90**, 092503 (2007).
[15] Z. K. Wang, V. L. Zhang, H. S. Lim, S. C. Ng, M. H. Kuok, S. Jain, and A. O. Adeyeye, Nanostructured Magnonic Crystals with Size-Tunable Bandgaps; ACS Nano **4**, 643 (2010).
[16] G. Gubbiotti, M. Madami, S. Tacchi, G. Carlotti, and T. Okuno, Normal Mode Splitting in Interacting Arrays of Cylindrical Permalloy Dots; J. Appl. Phys. **99**, 08C701 (2006).
[17] V. V. Kruglyak, P. S. Keatley, A. Neudert, R. J. Hicken, J. R. Childress, and J. A. Katine, Imaging Collective Magnonic Modes in 2D Arrays of Magnetic Nanoelements; Phys. Rev. Lett. **104**, 027201 (2010).
[18] S. Saha, R. Mandal, S. Barman, D. Kumar, B. Rana, Y. Fukuma, S. Sugimoto, Y. Otani, and A. Barman, Tunable Magnonic Spectra in Two-Dimensional Magnonic Crystals with Variable Lattice Symmetry; Adv. Funct. Mater. **23**, 2378 (2013).
[19] B. K. Mahato, B. Rana, D. Kumar, S. Barman, S. Sugimoto, Y. Otani, and A. Barman, Tunable Spin Wave Dynamics in Two-Dimensional $Ni_{80}Fe_{20}$ Nanodot Lattices by Varying Dot Shape; Appl. Phys. Lett. **105**, 012406 (2014).
[20] S. Neusser, B. Botters, and D. Grundler, Localization, Confinement, and Field-Controlled Propagation of Spin Waves in $Ni_{80}Fe_{20}$ Antidot Lattices; Phys. Rev. B **78**, 054406 (2008).
[21] S. Tacchi, B. Botters, M. Madami, J. W. Kłos, M. L. Sokolovskyy, M. Krawczyk, G. Gubbiotti, G. Carlotti, A. O. Adeyeye, S. Neusser, and D. Grundler, Mode Conversion from Quantized to Propagating Spin Waves in a Rhombic Antidot Lattice Supporting Spin Wave Nanochannels; Phys. Rev. B **86**, 014417 (2012).
[22] S. Choudhury, S. Barman, Y. Otani, and A. Barman, Efficient Modulation of Spin Waves in Two-Dimensional Octagonal Magnonic Crystal; ACS Nano **11**, 8814 (2017).

[23] S. Choudhury, S. Saha, R. Mandal, S. Barman, Y. Otani, and A. Barman, Shape- and Interface-Induced Control of Spin Dynamics of Two-Dimensional Bicomponent Magnonic Crystals; ACS Appl. Mater. Interfaces **8**, 18339 (2016).
[24] J. D. Fowlkes, R. Winkler, B. B. Lewis, M. G. Stanford, H. Plank, and P. D. Rack, Simulation-Guided 3D Nanomanufacturing via Focused Electron Beam Induced Deposition; ACS Nano **10**, 6163 (2016).
[25] A. Fernández-Pacheco, R. Streubel, O. Fruchart, R. Hertel, P. Fischer, and R. P. Cowburn, Three-Dimensional Nanomagnetism; Nat. Commun. **8**, 15756 (2017).
[26] S. S. P. Parkin, M. Hayashi, and L. Thomas, Magnetic Domain-Wall Racetrack Memory; Science **320**, 190 (2008).
[27] S. Lequeux, J. Sampaio, V. Cros, K. Yakushiji, A. Fukushima, R. Matsumoto, H. Kubota, S. Yuasa, and J. Grollier, A Magnetic Synapse: Multilevel Spin-Torque Memristor with Perpendicular Anisotropy; Sci. Rep. **6**, 31510 (2016).
[28] S. Mamica, Tailoring of the Partial Magnonic Gap in Three-Dimensional Magnetoferritin-Based Magnonic Crystals; J. Appl. Phys. **114**, 043912 (2013).
[29] G.-W. Chern, C. Reichhardt, and C. Nisoli, Realizing Three-Dimensional Artificial Spin Ice by Stacking Planar Nano-Arrays; Appl. Phys. Lett. **104**, 013101 (2014).
[30] H.-B. Sun, S. Matsuo, and H. Misawa, Three-Dimensional Photonic Crystal Structures Achieved with Two-Photon-Absorption Photopolymerization of Resin; Appl. Phys. Lett. **74**, 786 (1999).
[31] G. Williams, M. Hunt, B. Boehm, A. May, M. Taverne, D. Ho, S. Giblin, D. Read, J. Rarity, R. Allenspach, and S. Ladak, Two-Photon Lithography for 3D Magnetic Nanostructure Fabrication; Nano Res. **11**, 845 (2018).
[32] B. Rana and A. Barman, Magneto-Optical Measurements of Collective Spin Dynamics of Two Dimensional Arrays of Ferromagnetic Nanoelements; SPIN **03**, 1330001 (2013).
[33] A. Vansteenkiste, J. Leliaert, M. Dvornik, M. Helsen, F. Garcia-Sanchez, and B. Van Waeyenberge, The Design and Verification of MuMax3; AIP Adv. **4**, 107133 (2014).
[34] P. Ramachandran and G. Varoquaux, Mayavi: 3D Visualization of Scientific Data; Comput Sci Eng **13**, 40 (2011).
[35] G. Rowlands, Muview2, http://grahamrow.github.io/Muview2/.
[36] M. Donahue and D. G. Porter, OOMMF User's guide, version1.0, Interagency Report NISTIR 6376; National Institute of Standard and Technology: Gaithersburg, MD, U.S.A.; (1999).

Chapter 7

7. Observation of Coherent Spin Waves in a Three-Dimensional Artificial Spin Ice Structure

7.1 Introduction

Patterned magnetic nanostructures have been studied a great deal during the last few decades due to their interesting spin configurations [1-3] and their potential applications in energy-efficient miniaturized spintronics as well as magnonic devices [4-6] where spin-waves may act as information carrier. A large volume of work has been done on one-dimensional (1D) and two-dimensional (2D) magnonic crystals of different forms and geometry [2,7-10]. These include magnetic dot arrays [11], antidot arrays [12], bicomponent magnonic crystal [13], nanowires [14] and nanostripes [15]. During the last few years, three-dimensional (3D) nanomagnetism has emerged as a fascinating research field demonstrating novel physical phenomena such as curvature induced anisotropy [16,17], frustration in 3D artificial spin ice (ASI) systems [18,19], 3D magnonic crystals [17,20], noncollinear spin textures such as twisted skyrmion [21], magnetic singularities e.g., Bloch points [22,23], hopfions [24] and vortex domain walls [25]. On the other hand, 3D magnetic nanostructures have the potential for future applications in magnetic sensors [26], neuromorphic computing [27], ultra-dense data storage devices [28,29] and 2.5D spintronic devices [30]. The main barriers to exploration of 3D magnetic nanostructures [30-33] have been their non-trivial fabrication and characterization techniques. The combination of 3D patterning techniques such as focused electron beam-ion deposition (FEBID) [34], two-photon lithography (TPL) [35-38] with sputtered deposition [39], electrodeposition [40] and thermal evaporation [19,41] have emerged as powerful techniques to fabricate 3D complex magnetic nanostructures for investigation of novel phenomena and development of future magnetic devices. Recently, high quality free-standing tetrapod structures have been made from Co nanowires, by utilizing TPL and electrodeposition [40]. The spin-wave dynamics from the junction of a tetrapod structure was experimentally measured using a time-resolved Kerr microscope [42]. However, the large separation between the tetrapods did not allow the study of coherent magnons in this system. The study of spin-wave dynamics within

interconnected 3D magnetic nanostructures is important to first of all, build an elementary understanding of spin-wave mode behaviours within such complex systems and subsequently to develop future devices which allow the propagation of spin-waves to be controlled in complex 3D circuits. Such structures hold the promise to study coherent magnon states in 3D magnonic crystals due to Bragg scattering in all three spatial directions, as well as investigation of anisotropic magnon minibands and Brillouin zone boundaries along high symmetry directions. Theoretical studies of spin-wave dynamics in prototype of 3D interconnected magnetic nanostructures [20,43] have been reported recently. Finally, the realization of 3D magnetic nanostructures in complex frustrated geometries, such as a 3D-ASI, provides access to a huge number of near degenerate states. Here, previous work has shown the possibility of quasi-3D-ASI systems [44,45] through use of multiple lithography steps. These novel systems show a degenerate ice-rule and have demonstrated the square ice-model, though such systems are currently limited to two-layers. In contrast, harnessing self-assembly techniques and electrodeposition, true 3D geometries have been obtained, which have an inverse opal geometry [18,46]. Two-photon lithography and deposition has recently emerged as a powerful means to produce 3D-ASI systems, taking a diamond-bond lattice geometry [19,47]. A distinct advantage of these systems is the direct-write capability which allows the 3D nanoscale geometry to be written by design. Furthermore, direct magnetic imaging of such structures has now shown the possibility of realizing the full suite of vertex types, as seen in 2D-ASI systems, providing a platform to explore spin-wave dynamics in 3D-ASI for construction of reconfigurable magnonic devices [48].

Here, we report upon the experimental measurement of spin-wave modes in a 3D-ASI composed of interconnected nanowires arranged in diamond bond lattice (DBL) structure using conventional Brillouin light scattering (BLS). The 3D-ASI was fabricated by using a combination of TPL and thermal evaporation. Two clear spin-wave modes were observed in the BLS spectra, each of which showed a systematic variation with the applied magnetic field. These experimental results have been understood in the context of 3D micromagnetic simulations, which show the observed modes can be reproduced in the simulation. The simulated mode profiles revealed complex quantized characters with its power distributed over the entire structure.

7.2 Experimental Details

A 3D array of interconnected nanowires of DBL (3D-DBL) was fabricated by using a three-step process. In the first step, a 3D-DBL structure (50×50×10 μm^3) was fabricated upon glass using TPL and subsequent development. In the second step, a layer of gold (30 nm) was deposited upon the sidewalls of the scaffold nanowires. This was achieved by carrying out four separate Au depositions, whereby the sample was mounted at a 30° tilt and the in-plane angle was rotated by 90° for each deposition. The addition of 4 × 30 nm Au depositions upon the polymer sidewalls allows efficient dissipation of heat for long optical experiments. Finally, a 50-nm-thick $Ni_{81}Fe_{19}$ (Permalloy; Py hereafter) was deposited with the substrate in a flat, zero-tilt position. The deposition of Py on the curved surfaces leads to the formation of nanowires with crescent shaped cross-section [19,47]. Overall, the process yields a DBL of Py which is continuous for four layers, in the y-direction, corresponding to a unit cell in thickness [19].

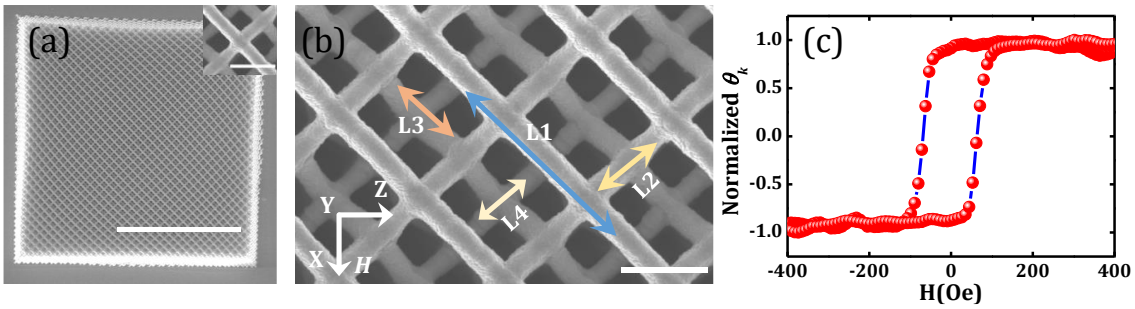

Figure 7. 1. (a) Scanning electron micrograph showing top view of full array of 3D-ASI with size 50×50×10 μm^3, the scale bar is 25 μm. A constituent tetrapod element is shown in the inset by capturing a zoomed view of 3D array where the scale bar is 1 μm (b) A magnified view of the interconnected nanowires in the lattice is shown. Four sub-lattice layers are highlighted. Scale bar in (b) is 2 μm. (c) Magnetic hysteresis loop of the 3D-ASI sample measured using static magneto-optical Kerr effect. Applied magnetic field (H) geometry is shown in (b).

Scanning electron micrographs of the full 3D array are shown in Fig. 7.1(a) and a magnified view (inset of Fig. 7.1(a)) shows a constituent tetrapod element of the interconnected nanowire structure. The four sub-lattice layers are annotated in Fig. 7.1(b). The individual nanowire length is approximately 1000 nm and its width is approximately 260 nm. A deviation up to ±10 nm in the width and up to ±25 nm in the length of the nanowires was observed. More details of fabrication and characterization of the samples can be found elsewhere [19]. Figure 7.1(c) shows the magnetic hysteresis loop (Kerr rotation (θ_K) vs. magnetic field (H)) of the 3D-ASI sample measured using static magneto-optic Kerr effect (static-MOKE) technique, which gives saturation field

and coercive field as ~125 Oe and ~100 Oe, respectively. In the spin-wave measurements, the bias magnetic field was always kept well above the saturation field, ensuring the single-domain state of the sample.

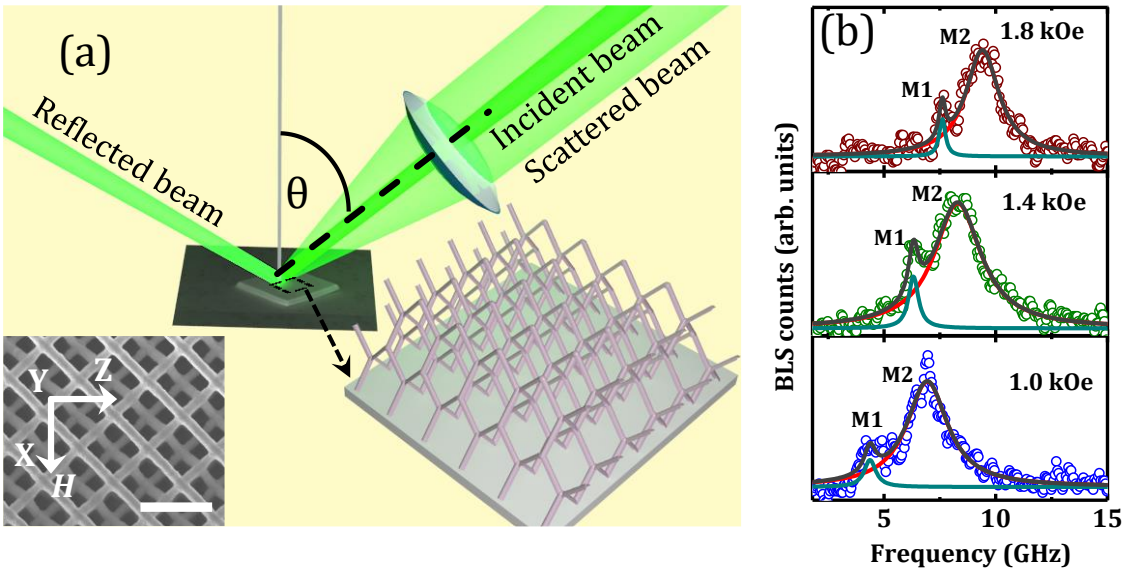

Figure 7. 2. (a) Schematic of BLS measurement geometry. The measurement was performed at θ = 0°. The applied field (*H*) direction is shown in the left inset and the scale bar is 2 μm. The 3D-ASI network is presented by a schematic on the right side of the image. (b) BLS spectra for three different magnetic field values are shown. Open circles present the experimental data points. Here, cyan and red color solid lines present the fitting of individual peak and the grey color solid line presents the resultant of the multi-peak fitting.

The spin-wave dynamics of the 3D array were measured by using conventional BLS [49]. BLS is a popular tool to measure spin-wave dynamics of magnetic thin films and patterned nanostructures. It is a non-contact and thus non-invasive tool to measure thermally excited spin waves at room temperature without any external excitation and under ambient conditions. This technique relies upon the inelastic scattering of light from the sample. The mechanism of inelastic scattering can be quantum mechanically described as a photon–magnon collision, where the creation (Stokes process) and annihilation (anti-Stokes process) of a magnon of wave vector (*k*) and angular frequency (ω) are detected. A continuous wave of monochromatic laser light (wavelength λ = 532 nm, power = 60 mW) was focused on the sample (Fig. 7.2(a)) to a spot size of around 40 μm, which is close to the lateral dimensions of the sample. As a result, the spin waves were measured from almost the entire sample volume. The cross polarization between the inelastically backscattered beam and incident beam was exploited to suppress the phonon contribution. A Sandercock-type six-pass tandem Fabry–Perot interferometer was used to analyze the frequencies of the scattered beam, in order to extract the spin-

wave frequencies. In our experiment, we applied a bias magnetic field (H) parallel to the substrate plane as shown in the inset of Fig. 7.2(a), along a principal axis (x-direction) of the lattice. A high magnetic field was first applied to completely saturate the sample magnetization, which was then gradually decreased to each bias field value for the BLS measurement. A schematic of the experimental geometry is shown in Fig. 7.2(a).

7.3 Results and Discussions

In order to study the spin-wave frequency variation with H, the BLS spectra were measured for the $k \approx 0$ wavevector in the Damon-Eschbach (DE) geometry corresponding to scattering of photon by a surface magnon, for different H values in $0.6 \leq H \leq 2.0$ kOe. Here the momentum will be conserved only in the plane of the sample surface. The $k \approx 0$ geometry will allow us to measure the extended and localized spin-wave over the entire 3D network of connected nanowires but not the spin-wave frequency vs. wave vector dispersion. Some example BLS spectra from the 3D-ASI are shown in Fig. 7.2(b).

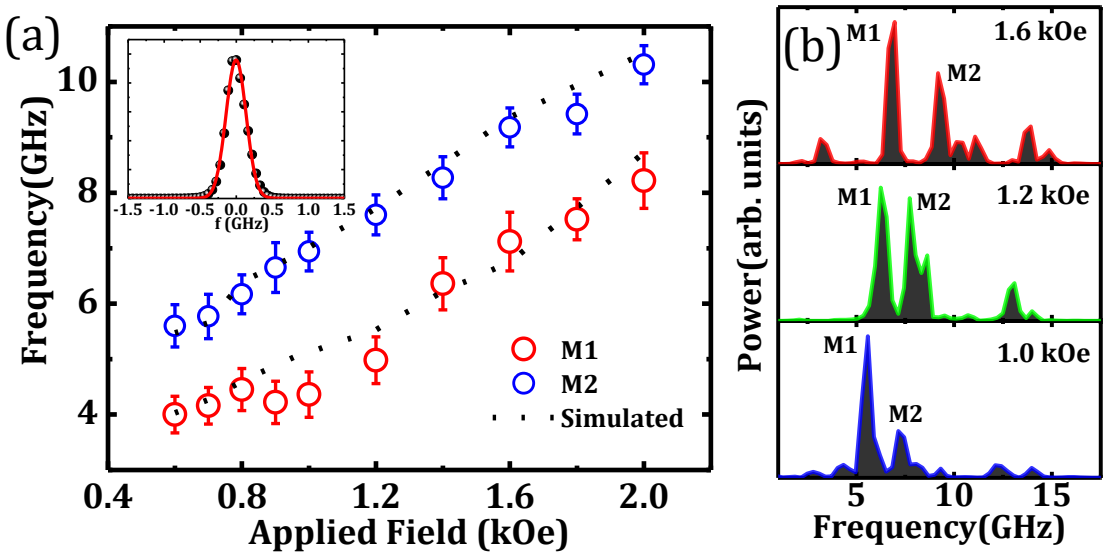

Figure 7. 3. (a) Spin-wave frequencies of mode 1 (M1) and mode 2 (M2) are plotted as a function of applied magnetic field. Here, symbols present the experimentally measured data points. The elastic peak fitted with a Gaussian function is shown at the inset. (b) Simulated spin-wave spectra for three intermediate field values are shown. The dotted lines in (a) present the simulated results.

Two intense spin-wave modes were observed in the spectra which are named as M1 and M2. The lower frequency peak (M1) becomes more prominent at larger values of H. The higher frequency mode (M2) is quite broad apparently due to unresolved modes and/or inhomogeneous line broadening due to defects and inhomogeneous spin textures in the real sample. The BLS spectra were fitted with two-peak Lorentzian functions to extract

the spin-wave frequency values. The bias magnetic field variation of spin-wave frequencies is plotted in Fig. 7.3(a) with combined error bars originating from theoretical fit and the frequency resolution of the BLS setup. The latter is given by the instrumental linewidth, which is ~ 0.3 GHz, determined from the elastic peak as shown at the inset of Fig. 7.3(a). The spin-wave mode frequency increases nearly monotonically with increasing field values suggesting purely magnetic origin of the modes. Despite the complicated structure of the 3D-ASI and the corresponding demagnetizing factors, we have fitted the most intense mode with the Kittel formula, which resulted in a good fit with effective demagnetizing factors at three different axes as presented in section B.1 of Appendix B.

To obtain deeper insight into the behaviour of the observed spin-wave modes, we have numerically simulated the spin-wave dynamics in the 3D-ASI system using the GPU-based MuMax3 software [50]. A schematic of the diamond-lattice unit cell [51] is shown in Fig. 7.4(a) for clarity of understanding of the 3D-ASI structure, where the atoms are non-existent and only the bonds are present. A typical simulated static spin configuration of the 3D-ASI structure is shown in Fig. 7.4(b), which consists of four tetrapod elements, highlighted by different colors. The 3D-ASI structure has been designed to match the geometry of a DBL, as shown in Fig 7.4(a). In order to mimic the experimental sample volume, we considered a unit cell of the 3D-ASI in the simulation and applied a 2D periodic boundary condition in the x-z plane, while along the y-direction the simulated structure contains four layers similar to the experimental sample. The simulated unit cell of the 3D-ASI consists of crescent shaped nanowires (CSN) with dimensions similar to the experimental sample. The sample was divided into cuboidal cells of size $5 \times 5 \times 5$ nm^3. The cell size is taken below the exchange length of Py (≈ 5.2 nm). Further test simulations with lower cell sizes made no significant qualitative changes in the peaks of interest in the simulated spin-wave spectra. The material parameters used in the simulation are: gyromagnetic ratio γ = 17.6 MHz/Oe, saturation magnetization M_s = 860 emu/cc, anisotropy field H_K = 0, and exchange stiffness constant $A_{ex} = 13 \times 10^{-7}$ erg/cm for Py [52]. The equilibrium magnetic states were obtained by relaxing the sample under study at a fixed bias magnetic field along the x-direction as defined in Fig. 7.4(c). The magnetization configuration of the equilibrium state (m_x component) at H = 1.6 kOe is shown in Fig. 7.4(c) which shows a saturated state along the x-direction with very small demagnetized

regions. The magnetization configurations (m_x component) at few other bias magnetic fields are presented in Section B.2 of Appendix B.

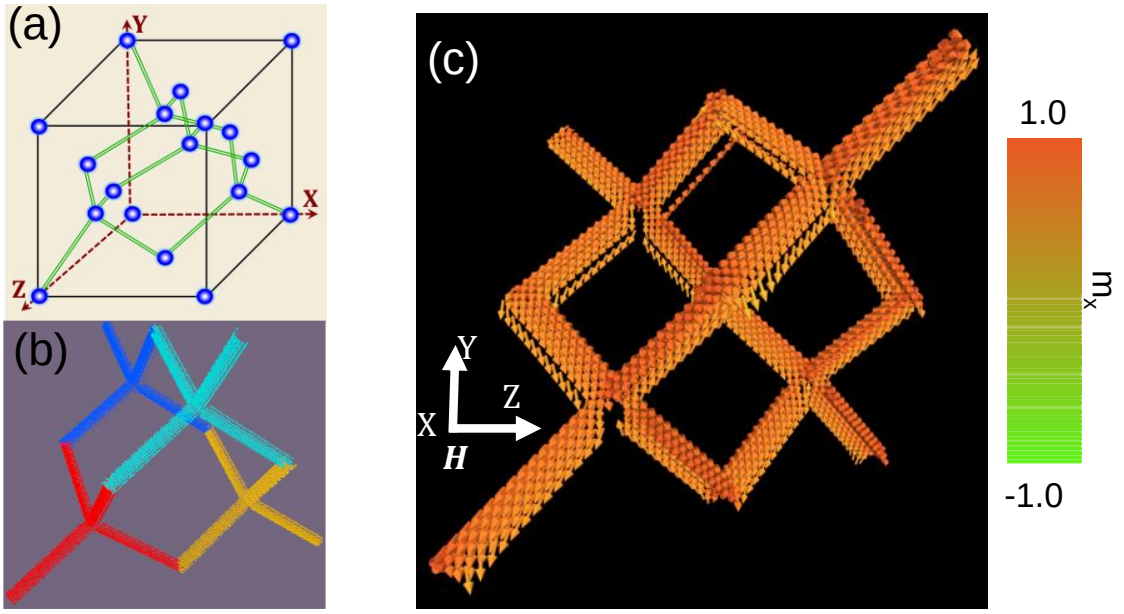

Figure 7. 4. (a) Schematic of diamond-lattice unit cell. Here, the green color double lines present the bond position and blue spheres present the atom position. The dashed lines define the axes. (b) A representative simulated unit cell of 3D-ASI is shown. One unit cell consists of four tetrapod elements, each of them are highlighted by different color for better visualization. A one-to-one correspondence between the diamond bond lattice and 3D-ASI (omitting the atoms) could be found from (a) and (b). (c) Magnetization configuration of the equilibrium state (m_x component) at H = 1.6 kOe (along x-direction; in-plane) is shown. The color bar for m_x is shown next to the image.

The equilibrium state magnetization configuration of the other two components (m_y and m_z) corresponding to Fig. 7.4(c) are shown in Section B.2 of Appendix B. For simulation of the spin-wave dynamics, a square shaped pulsed magnetic field with a peak amplitude of 20 Oe along the y-direction with rising and fall time of both 10 ps and duration of 20 ps, was applied to the equilibrium magnetic state using a Gilbert damping parameter α = 0.008. The spin-wave spectra were calculated by taking fast Fourier transformation (FFT) of the simulated time-domain magnetization (m_y component). Some typical simulated spin-wave spectra are shown in Fig. 7.3(b). The simulated spectra show additional peaks which were either not resolved due to the line broadening or insufficient sensitivity due to their smaller power in the experiment. The peaks adjacent to M2 observed in simulation may have contributed to the broadening of M2 in the BLS spectra as mentioned before. Nevertheless, both the experimental peaks could be identified in the simulation and the variation of their frequencies with bias magnetic field is plotted as dotted lines in Fig. 7.3(a).

A qualitative agreement between the experimental and simulated bias-field variation of spin-wave frequencies is found although the frequency of M1 from BLS shows larger scatter beyond the error bars in lower bias field regime presumably due to its reduced intensity and increased noise in these fields, which pose additional uncertainty in determining its peak frequency. The collective nature of the spin-wave modes has been reconfirmed by test simulations of spin-wave spectra of a single nanowire leg, one tetrapod element and a 3D-ASI structure, which clearly show gradual evolution from spin-wave modes localized in its constituent elements to a 3D-ASI lattice (section B.3 of Appendix B). To understand the spatial nature of the coherent spin-wave modes in the 3D-ASI, we have further analyzed the simulated data from MuMax3 using a home-built post-processing code, DotMag [53]. The mode profiles were calculated by taking slices of 3D-ASI structure along red and black dashed lines, parallel to different planes at positions 1 and 2, respectively, as shown in Fig. 7.5(a). The coordinate system x′y′z′ in Fig. 7.5(a) is defined such that the projections of top and bottom layers on the x'-z' plane become parallel to x′ and z′ axis, respectively. The simulated powermaps of the experimentally observed spin-wave modes are shown in Fig. 7.5(b), 7.5(c) and 7.5(d) for H = 1.6 kOe. The powermaps of additional modes present only in the simulated spectra are presented in the section B.4 of Appendix B. The calculated powermaps along red dashed line parallel to x′-y′ plane at position 1 are shown in Fig. 7.5(b). It captures the lateral view of the top layer and one of bottom layer nanowire's cross-sectional view. The lateral view reveals that the power of M1 is localized at the junction of each bipod but the power of M2 is extended throughout the 3D-ASI nanowire network as shown in Fig. 7.5(b). The phase of the mode M1 and M2 reveal quantized nature with different quantization numbers n = 11 for M1 and n = 5 for M2 as shown by dashed lines in Fig. 7.5(b). The cross-sectional view of CSN in the bottom layer reveals M1 to have quantized nature at the CSN cross-section (n' = 5) with low power, whereas M2 also possesses quantized nature (n' = 2) with reasonably high power as shown in Fig. 7.5(b). To explore the mode profiles further, we took another slice along black dashed line parallel to y′-z′ plane at position 2 (Fig. 7.5(c)). Here, power is distributed over the entire nanowire network for both modes. M1 shows quantized nature with n = 9, while M2 also shows quantized nature with n = 7 in both the connecting nanowires. The mode profile behaviour at CSN cross-section was also

analyzed by taking slice along red dashed line parallel to x′-z′ plane at position 1, as shown in Fig. 7.5(d).

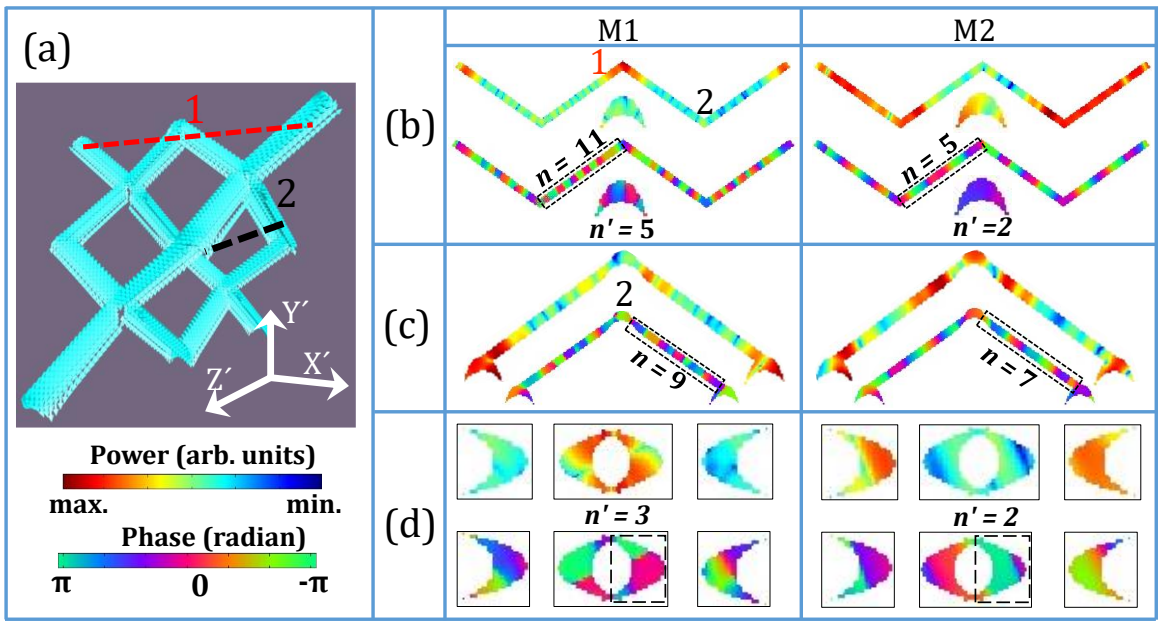

Figure 7. 5. (a) A representative static magnetization profile (m_x component) along with the coordinate system. The red and black dashed lines show the slice taking positions to extract mode profiles parallel to different planes at positions 1 and 2. Spin-wave mode profiles are calculated at different points of 3D-ASI structure at H = 1.6 kOe by taking slice along: (b) x′-y′ plane at point 1, (c) y′-z′ plane at point 2 and (d) x-′z′ plane at point 1. The power profiles are shown in upper panels and corresponding phase profiles in the lower panels. The color bars for power and phase are shown at the bottom left corner.

It captures mode profiles near the junction at position 1 and crescent shaped cross-sections of two adjacent nanowires. Here, M1 forms a quantized mode at CSN cross-section of junction with n' = 3, while M2 also forms a quantized mode with n' = 2. The overall power profile suggests that M1 is primarily localized at the nanowire junctions while M2 is extended over the nanowire networks. The phase profiles reveal the 3D nature of these modes with different quantization numbers along the lateral direction of nanowires and at the cross-sections. We have applied the magnetic field along one principal axis (along x-axis, Fig. 7.4(a)) which is an in-plane symmetry axis for the 3D-ASI structure. However, the crescent cross-section of the nanowires and the 3D geometry of ASI may create a 3D varying magnetic potential within this nanostructure leading to the quantized nature for both spin-wave modes with different quantization number.

7.4 Conclusion

In summary, we have exploited a novel method to fabricate a complex 3D-ASI structure of interconnected nanowires arranged in diamond bond-like lattice using TPL and thermal evaporation. We have studied thermal magnons in this 3D-ASI using BLS spectroscopy which revealed two clear collective spin-wave modes. The spin-wave mode frequencies show good stability and nearly monotonic variation over a broad range of bias magnetic field. We have performed 3D micromagnetic simulations to reproduce the spin-wave spectra and obtained insights into the spatial nature of the spin-wave modes in this 3D-ASI. The spin-wave modes exhibit different spatial characters from localized to extended nature having different mode quantization numbers. Some additional modes in the simulation were either not resolved or detected in the experiment, which called for more precise experiment to detect those. On the other hand, fabrication of even higher quality samples extended equally in all three dimensions will be helpful to understand the spin-wave propagation along all high-symmetry axes in these structures. The collective spin-wave modes in this 3D-ASI system are starkly different from an isolated 3D nanostructure as in the former the coherent spin-wave can extend over all three dimensions along a complex 3D network, promising a very rich magnonic band structure with greater flexibility as opposed to formation of standing spin-waves in an isolated 3D nanostructure. Besides, these spin-waves can be highly reconfigurable due to the possibility of attaining a variety of complex magnetic microstates by varying external magnetic field [47]. To this end, optical exploration of spin-wave modes in this interconnected 3D structure will open the pathway for exciting new possibilities of 3D magnonics for ultrahigh density on-chip communication and processing devices.

References

[1] R. P. Cowburn, D. K. Koltsov, A. O. Adeyeye, M. E. Welland, and D. M. Tricker, Single-Domain Circular Nanomagnets; Phys. Rev. Lett. **83,** 1042 (1999).
[2] S. D. Bader, Colloquium: Opportunities in Nanomagnetism; Rev. Mod. Phys. **78,** 1 (2006).
[3] A. Barman, S. Wang, J. D. Maas, A. R. Hawkins, S. Kwon, A. Liddle, J. Bokor, and H. Schmidt, Magneto-Optical Observation of Picosecond Dynamics of Single Nanomagnets; Nano Lett. **6,** 2939 (2006).
[4] M. P. Kostylev, A. A. Serga, T. Schneider, B. Leven, and B. Hillebrands, Spin-Wave Logical Gates; Appl. Phys. Lett. **87,** 153501 (2005).
[5] J. W. Kłos, D. Kumar, J. Romero-Vivas, H. Fangohr, M. Franchin, M. Krawczyk, and A. Barman, Effect of Magnetization Pinning on the Spectrum of Spin Waves in Magnonic Antidot Waveguides; Phys. Rev. B **86,** 184433 (2012).
[6] H. Yu, G. Duerr, R. Huber, M. Bahr, T. Schwarze, F. Brandl, and D. Grundler, Omnidirectional Spin-Wave Nanograting Coupler; Nat. Commun. **4,** 2702 (2013).
[7] R. Skomski, Nanomagnetics; J. Phys.: Condens. Matter **15,** R841 (2003).
[8] V. V. Kruglyak, S. O. Demokritov, and D. Grundler, Magnonics; J. Phys. D: Appl. Phys. **43,** 264001 (2010).
[9] M. Krawczyk and D. Grundler, Review and Prospects of Magnonic Crystals and Devices with Reprogrammable Band Structure; J. Phys.: Condens. Matter **26,** 123202 (2014).
[10] A. Barman, S. Mondal, S. Sahoo, and A. De, Magnetization Dynamics of Nanoscale Magnetic Materials: A Perspective; J. Appl. Phys. **128,** 170901 (2020).
[11] B. Rana, D. Kumar, S. Barman, S. Pal, Y. Fukuma, Y. Otani, and A. Barman, Detection of Picosecond Magnetization Dynamics of 50 nm Magnetic Dots down to the Single Dot Regime; ACS Nano **5,** 9559 (2011).
[12] S. Choudhury, S. Barman, Y. Otani, and A. Barman, Efficient Modulation of Spin Waves in Two-Dimensional Octagonal Magnonic Crystal; ACS Nano **11,** 8814 (2017).
[13] S. Choudhury, S. Saha, R. Mandal, S. Barman, Y. Otani, and A. Barman, Shape- and Interface-Induced Control of Spin Dynamics of Two-Dimensional Bicomponent Magnonic Crystals; ACS Appl. Mater. Interfaces **8,** 18339 (2016).
[14] S. Pal, S. Saha, M. V. Kamalakar, and A. Barman, Field-Dependent Spin Waves in High-Aspect-Ratio Single-Crystal Ferromagnetic Nanowires; Nano Res. **9,** 1426 (2016).
[15] S. Saha, S. Barman, Y. Otani, and A. Barman, All-Optical Investigation of Tunable Picosecond Magnetization Dynamics in Ferromagnetic Nanostripes with a Width down to 50 nm; Nanoscale **7,** 18312 (2015).
[16] O. M. Volkov, A. Kákay, F. Kronast, I. Mönch, M.-A. Mawass, J. Fassbender, and D. Makarov, Experimental Observation of Exchange-Driven Chiral Effects in Curvilinear Magnetism; Phys. Rev. Lett. **123,** 077201 (2019).
[17] A. Korniienko, V. Kravchuk, O. Pylypovskyi, D. Sheka, J. van den Brink, and Y. Gaididei, Curvature Induced Magnonic Crystal in Nanowires; SciPost Phys. **7,** 035 (2019).
[18] A. A. Mistonov, N. A. Grigoryeva, A. V. Chumakova, H. Eckerlebe, N. A. Sapoletova, K. S. Napolskii, A. A. Eliseev, D. Menzel, and S. V. Grigoriev, Three-Dimensional Artificial Spin Ice in Nanostructured Co on an Inverse Opal-Like Lattice; Phys. Rev. B **87,** 220408 (2013).
[19] A. May, M. Hunt, A. Van Den Berg, A. Hejazi, and S. Ladak, Realisation of a Frustrated 3D Magnetic Nanowire Lattice; Commun. Phys. **2,** 13 (2019).
[20] P. A. Popov, A. Y. Sharaevskaya, E. N. Beginin, A. V. Sadovnikov, A. I. Stognij, D. V. Kalyabin, and S. A. Nikitov, Spin Wave Propagation in Three-Dimensional Magnonic Crystals and Coupled Structures; J. Magn. Magn. Mater. **476,** 423 (2019).
[21] C. Jin, C. Zhang, C. Song, J. Wang, H. Xia, Y. Ma, J. Wang, Y. Wei, J. Wang, and Q. Liu, Current-Induced Motion of Twisted Skyrmions; Appl. Phys. Lett. **114,** 192401 (2019).
[22] S. Da Col, S. Jamet, N. Rougemaille, A. Locatelli, T. O. Mentes, B. S. Burgos, R. Afid, M. Darques, L. Cagnon, J. C. Toussaint, and O. Fruchart, Observation of Bloch-Point Domain Walls in Cylindrical Magnetic Nanowires; Phys. Rev. B **89,** 180405 (2014).

[23] M. Schöbitz, A. De Riz, S. Martin, S. Bochmann, C. Thirion, J. Vogel, M. Foerster, L. Aballe, T. O. Menteş, A. Locatelli, F. Genuzio, S. Le-Denmat, L. Cagnon, J. C. Toussaint, D. Gusakova, J. Bachmann, and O. Fruchart, Fast Domain Wall Motion Governed by Topology and Oersted Fields in Cylindrical Magnetic Nanowires; Phys. Rev. Lett. **123,** 217201 (2019).
[24] J.-S. B. Tai and I. I. Smalyukh, Static Hopf Solitons and Knotted Emergent Fields in Solid-State Noncentrosymmetric Magnetic Nanostructures; Phys. Rev. Lett. **121,** 187201 (2018).
[25] C. Donnelly, S. Finizio, S. Gliga, M. Holler, A. Hrabec, M. Odstrčil, S. Mayr, V. Scagnoli, L. J. Heyderman, M. Guizar-Sicairos, and J. Raabe, Time-Resolved Imaging of Three-Dimensional Nanoscale Magnetization Dynamics; Nat. Nanotechnol **15,** 356 (2020).
[26] C. Xu, X. Wu, G. Huang, and Y. Mei, Rolled-up Nanotechnology: Materials Issue and Geometry Capability; Adv. Mater. Technol. **4,** 1800486 (2019).
[27] J. Torrejon, M. Riou, F. A. Araujo, S. Tsunegi, G. Khalsa, D. Querlioz, P. Bortolotti, V. Cros, K. Yakushiji, A. Fukushima, H. Kubota, S. Yuasa, M. D. Stiles, and J. Grollier, Neuromorphic Computing with Nanoscale Spintronic Oscillators; Nature **547,** 428 (2017).
[28] S. S. P. Parkin, M. Hayashi, and L. Thomas, Magnetic Domain-Wall Racetrack Memory; Science **320,** 190 (2008).
[29] C. Bran, E. Berganza, J. A. Fernandez-Roldan, E. M. Palmero, J. Meier, E. Calle, M. Jaafar, M. Foerster, L. Aballe, A. Fraile Rodriguez, R. P. del Real, A. Asenjo, O. Chubykalo-Fesenko, and M. Vazquez, Magnetization Ratchet in Cylindrical Nanowires; ACS Nano **12,** 5932 (2018).
[30] A. Fernández-Pacheco, R. Streubel, O. Fruchart, R. Hertel, P. Fischer, and R. P. Cowburn, Three-Dimensional Nanomagnetism; Nat. Commun. **8,** 15756 (2017).
[31] S. Mondal, S. Sahoo and A. Barman, "Precessional Magnetization Dynamics and Spin Waves in 3D Ferromagnetic Nanostructures" in Three-Dimensional magnonics, Ed. G. Gubbiotti, CRC Press, ISBN 9789814800730 - CAT# K426145 (2019).
[32] P. Fischer, D. Sanz-Hernández, R. Streubel, and A. Fernández-Pacheco, Launching a New Dimension with 3D Magnetic Nanostructures; APL Materials **8,** 010701 (2020).
[33] A. Barman, G. Gubbiotti, S. Ladak, A. O. Adeyeye, M. Krawczyk, J. Gräfe, C. Adelmann, S. Cotofana, A. Naeemi, V. I. Vasyuchka, B. Hillebrands, S. A. Nikitov, H. Yu, D. Grundler, A. V. Sadovnikov, A. A. Grachev, S. E. Sheshukova, J. Y. Duquesne, M. Marangolo, G. Csaba, W. Porod, V. E. Demidov, S. Urazhdin, S. O. Demokritov, E. Albisetti, D. Petti, R. Bertacco, H. Schultheiss, V. V. Kruglyak, V. D. Poimanov, S. Sahoo, J. Sinha, H. Yang, M. Münzenberg, T. Moriyama, S. Mizukami, P. Landeros, R. A. Gallardo, G. Carlotti, J. V. Kim, R. L. Stamps, R. E. Camley, B. Rana, Y. Otani, W. Yu, T. Yu, G. E. W. Bauer, C. Back, G. S. Uhrig, O. V. Dobrovolskiy, B. Budinska, H. Qin, S. van Dijken, A. V. Chumak, A. Khitun, D. E. Nikonov, I. A. Young, B. W. Zingsem, and M. Winklhofer, The 2021 Magnonics Roadmap; J. Phys.: Condens. Matter **33,** 413001 (2021).
[34] I. Utke, P. Hoffmann, and J. Melngailis, Gas-Assisted Focused Electron Beam and Ion Beam Processing And Fabrication; J. Vac. Sci. Technol. B: Microelectronics and Nanometer Structures Processing, Measurement, and Phenomena **26,** 1197 (2008).
[35] S. Maruo, O. Nakamura, and S. Kawata, Three-Dimensional Microfabrication with Two-Photon-Absorbed Photopolymerization; Opt. Lett. **22,** 132 (1997).
[36] R. Thomas, J. Li, S. Ladak, D. Barrow, and P. M. Smowton, In situ Fabricated 3D Micro-Lenses for Photonic Integrated Circuits; Opt. Express **26,** 13436 (2018).
[37] J. Askey, M. O. Hunt, W. Langbein, and S. Ladak, Use of Two-Photon Lithography with a Negative Resist and Processing to Realise Cylindrical Magnetic Nanowires; Nanomaterials **10** (2020).
[38] M. Hunt, M. Taverne, J. Askey, A. May, A. Van Den Berg, Y.-L. D. Ho, J. Rarity, and S. Ladak, Harnessing Multi-Photon Absorption to Produce Three-Dimensional Magnetic Structures at the Nanoscale; Materials **13** (2020).
[39] C. Donnelly, M. Guizar-Sicairos, V. Scagnoli, M. Holler, T. Huthwelker, A. Menzel, I. Vartiainen, E. Müller, E. Kirk, S. Gliga, J. Raabe, and L. J. Heyderman, Element-Specific X-Ray Phase Tomography of 3D Structures at the Nanoscale; Phys. Rev. Lett. **114,** 115501 (2015).

[40] G. Williams, M. Hunt, B. Boehm, A. May, M. Taverne, D. Ho, S. Giblin, D. Read, J. Rarity, R. Allenspach, and S. Ladak, Two-Photon Lithography for 3D Magnetic Nanostructure Fabrication; Nano Res. **11,** 845 (2018).
[41] D. Sanz-Hernández, R. F. Hamans, J.-W. Liao, A. Welbourne, R. Lavrijsen, and A. Fernández-Pacheco, Fabrication, Detection, and Operation of a Three-Dimensional Nanomagnetic Conduit; ACS Nano **11,** 11066 (2017).
[42] S. Sahoo, S. Mondal, G. Williams, A. May, S. Ladak, and A. Barman, Ultrafast Magnetization Dynamics in a Nanoscale Three-Dimensional Cobalt Tetrapod Structure; Nanoscale **10,** 9981 (2018).
[43] J. Romero Vivas, S. Mamica, M. Krawczyk, and V. V. Kruglyak, Investigation of Spin Wave Damping in Three-Dimensional Magnonic Crystals Using the Plane Wave Method; Phys. Rev. B **86,** 144417 (2012).
[44] Y. Perrin, B. Canals, and N. Rougemaille, Extensive Degeneracy, Coulomb Phase and Magnetic Monopoles in Artificial Square Ice; Nature **540,** 410 (2016).
[45] A. Farhan, M. Saccone, C. F. Petersen, S. Dhuey, R. V. Chopdekar, Y.-L. Huang, N. Kent, Z. Chen, M. J. Alava, T. Lippert, A. Scholl, and S. van Dijken, Emergent Magnetic Monopole Dynamics in Macroscopically Degenerate Artificial Spin Ice; Sci. Adv. **5,** eaav6380 (2019).
[46] C. Kansal, K. Zeissler, B. Illy, S. Walton, A. Cruickshank, S. Felton, W. R. Branford, and M. P. Ryan, Revisiting Electrodeposited Inverse Opals: New Insights into Magnetic Frustration; ECS Meeting Abstracts **MA2020-01,** 1207 (2020).
[47] A. May, M. Saccone, A. van den Berg, J. Askey, M. Hunt, and S. Ladak, Magnetic Charge Propagation upon a 3D Artificial Spin-Ice; Nat. Commun. **12,** 3217 (2021).
[48] J. C. Gartside, S. G. Jung, S. Y. Yoo, D. M. Arroo, A. Vanstone, T. Dion, K. D. Stenning, and W. R. Branford, Current-Controlled Nanomagnetic Writing for Reconfigurable Magnonic Crystals; Commun. Phys. **3,** 219 (2020).
[49] S. O. Demokritov, B. Hillebrands, and A. N. Slavin, Brillouin Light Scattering Studies of Confined Spin Waves: Linear and Nonlinear Confinement; Phys. Rep. **348,** 441 (2001).
[50] A. Vansteenkiste, J. Leliaert, M. Dvornik, M. Helsen, F. Garcia-Sanchez, and B. Van Waeyenberge, The Design and Verification of MuMax3; AIP Adv. **4,** 107133 (2014).
[51] Kittel, Charles. Introduction to Solid State Physics. 18th ed., p. 17: Wiley, 2014.
[52] K. H. J. Buschow; Handbook of Magnetic Materials; Elsevier: Amsterdam, Netherlands, 2009; Vol. 18.
[53] D. Kumar, O. Dmytriiev, S. Ponraj, and A. Barman, Numerical Calculation of Spin Wave Dispersions in Magnetic Nanostructures; J. Phys. D: Appl. Phys. **45,** 015001 (2011).

Chapter 8

8. All-Optical Detection of Spin-Orbit Torque Driven Modulation of Gilbert Damping in Ta/CoFeB/SiO_2 Heterostructures

8.1 Introduction

Gilbert damping of magnetic materials plays a crucial role in controlling its magnetization dynamics. The understanding and manipulation of Gilbert damping are essential for designing future magnonic [1-3] and spintronic devices [4,5]. A high damping value is desirable for magnetic storage and memory devices to minimize the magnetization precession (ringing) during writing [6], while a low damping value is required for energy-efficient magnetoresistive random-access memory (MRAM) [7] to lower the required write current as well as for long-range spin-wave propagation in magnonic devices [8,9] for on-chip transfer and process information. External control over the damping will be pertinent for the development of new-generation energy-efficient magnetic devices. Over the years, there have been various efforts to control damping in ferromagnetic materials [10-12]. These include processes like spin pumping, material doping, ion irradiation and others.

More recently damping has been found to be controlled efficiently and easily by spin-orbit torque (SOT) [13-17] by injecting spin current in a ferromagnetic layer. This ranges from small modulation of damping (MOD) to the attainment of auto-oscillation, where the damping is fully compensated by the SOT [18]. Pure spin current can be generated by using different mechanisms including nonlocal spin injection [19,20], spin pumping [21,22], Rashba effect [23], spin Hall effect (SHE) [24-26] etc. When a charge current is passed through a nonmagnetic metal (NM)/ferromagnet (FM) heterostructure, intrinsic effect (related to Berry curvature) and extrinsic effects like impurity scattering of electrons (skew scattering and side jump mechanism) can cause the generation of pure spin current due to the accumulation of spins having two opposite polarizations at two opposite surfaces by the SHE [27]. The injected pure spin current in the FM layer can manipulate its damping due to SOT [13,28-30]. It has been found that in NM/FM heterostructures, the current induced torques are originated from the spin-orbit coupling

(SOC) within the bulk of the NM (generally heavy metals (HMs)) or at the interface. There can be two types of torques acting simultaneously on the magnetization of an adjacent FM layer: damping-like torque (DLT) and field-like torque (FLT). Their effective magnitudes in a system depend upon several factors: the layer thickness [31], quality of interface in terms of the spin-mixing conductance and interfacial spin transparency [32], electronic properties (such as charge conductivity) [33] and SOC strength of the HM.

Various HM/FM systems have been used to study the MOD due to SHE induced SOT [13,14,34,35]. To this end, Ta-based systems are technologically important due to their reasonably high SHE [36], spin-mixing conductance and interfacial spin transparency of Ta [12], and interfacial Dzyaloshinskii-Moriya interaction [37]. Interestingly, two different structural phases, β-Ta [12,38,39] and α-Ta [36,38,40], can occur depending upon the Ta thickness [38] and deposition conditions [36,40]. Out of those β-Ta is a highly resistive phase with distorted tetragonal crystal structure and has higher SOC. But the stability of this phase at lower thickness regime strongly depends on the deposition condition. At relatively higher thickness the most stable phase of Ta appears with lesser resistivity and lesser SOC strength. Therefore, the study of SOT (DLT and FLT) efficiency over a long thickness regime with stable phase of Ta is required for basic understanding and its effects on future magnonic and spintronic devices.

Here we have demonstrated an all-optical detection of MOD in a β-Ta (t)/CoFeB (3 nm)/SiO_2(2 nm) heterostructure by using time-resolved magneto-optic Kerr (TRMOKE) magnetometer. The thickness of Ta layer has been varied from 3 to 20 nm. Within this wide range, stable β-dominated phase is maintained in Ta. Charge current is applied to the heterostructures using Au electrodes for the generation of SHE in Ta. The pure spin current is thereby generated and transported into the CoFeB layer to exert the SOT while the magnetization precession is excited optically by a femtosecond laser pulse. The damping is modulated by the DLT which is further controlled by varying the magnitude and direction of the charge current. Within the experimentally applied current regime, we have observed a small amount of Joule heating effect in the experimental data. The modulation of frequency (MOF) shows a parabolic variation with the applied current which also confirms the presence of this Joule heating effect in the applied current regime. The FLT and Oersted field contributions are found to be negligible in this study from the observed MOF variation. Therefore, the MOD is calculated for both scenarios, i.e., without/with considering the Joule heating effect. For both cases, DLT efficiency was

found to be around 0.4 over the whole Ta thickness range. It shows the Joule heating effect does not affect the MOD so much as it does for MOF. However, the Joule heating correction gives a higher value of DLT of around 0.41±0.03 (as opposed to 0.38±0.05 without Joule heating correction) with better accuracy. The robustness of DLT over this wide range of Ta thickness (3-20 nm) will be useful for future spintronic and magnonic devices.

8.2 Experimental Details

A series of heterostructures made of Ta (3 nm ≤ t ≤ 20 nm)/$Co_{20}Fe_{60}B_{20}$(3 nm)/SiO_2(2 nm) were deposited by dc/rf magnetron sputtering on Si (100) wafers coated with 100-nm-thick SiO_2. The depositions were carried out at an average base pressure of 2.0×10^{-7} Torr and argon pressure of about 1.0 mTorr at a deposition rate of 0.2 Å/s for all samples. Ta and SiO_2 were deposited with rf power of 40 and 60 W, respectively, while $Co_{20}Fe_{60}B_{20}$ (CoFeB) was deposited with a dc voltage of 380 V. The sample stacks having lateral dimensions of 2 × 2 mm^2 were deposited using a shadow mask. Two contact pads of chromium (5 nm)/gold (25 nm) were deposited to apply charge current to the samples. The atomic force microscopy (AFM) measurements were carried out to check the sample surface roughness. The resistivity of Ta and the grazing-incidence x-ray diffraction (XRD) were measured to determine the crystal phase of Ta over this wide thickness range. The resistivity of Ta was estimated from the sheet resistance measurements of heterostructures. The magnetization dynamics were studied by using a custom-built TRMOKE magnetometer. Here, the second harmonic (λ = 400 nm, repetition rate = 1 kHz, pulse width ≈ 50 fs; pump beam) of an amplified femtosecond laser pulse generated from a regenerative amplifier system (Libra, Coherent) was used to excite the ultrafast dynamics while the time-delayed fundamental laser pulse (λ = 800 nm, repetition rate = 1 kHz, pulse width ≈ 40 fs; probe beam) was used to detect the time-resolved polar Kerr rotation from the sample. The probe beam with spot size ≈ 100 μm was tightly focused on the centre of a slightly defocused pump beam with spot size ≈ 300 μm to measure the uniformly excited magnetic signal. A static magnetic field was applied at a small tilt of ~ 5-10° from the sample plane to produce a finite amount of demagnetize field along the pump beam direction to excite the precessional dynamics. The in-plane component (H = 1.5 kOe) of this field is considered as the bias field applied to the sample. The fluence of the pump and probe beams were kept at 10 mJ/cm^2 and 0.5 mJ/cm^2 to avoid appreciable

effects of laser on magnetic parameters including damping coefficient, and all measurements were done at ambient conditions. A dc charge current was applied along the length of the sample through the electrodes using a source meter (U3606A, Agilent Technologies). The method of all-optical detection of MOD due to SHE generated spin current, employed here, does not require any delicate micro-fabrication techniques for sample preparation. It can eliminate possible experimental artefacts involved in the electrical detection techniques [13,14]. It relies on local measurements over the sample surface and does not suffer from the large area averaging avoiding inhomogeneities and defects present in the sample. The decaying profile of the time-resolved precession oscillations directly gives the magnetic damping coefficient, which is more reliable than competing techniques such as linewidth measurement and analyses using in ferromagnetic resonance (FMR) technique.

8.3 Results and Discussions

Figure 8.1(a) shows the XRD patterns of the heterostructures. In these XRD plots, the peaks corresponding to β-Ta are marked. The high-intensity XRD peak at $\sim$ 33.5° primarily corresponds to the β phase (distorted tetragonal structure) of Ta. We find another peak in the vicinity of 33.5° which is present for all thicknesses of Ta but its origin is unknown. We have not observed any signature of α-Ta phase, to be appeared for 2θ value of $\sim$ 38.5°. The d-value obtained from the β-Ta peak at 33.5° corresponds to $\sim$ 2.6 Å, which ensures the growth of the Ta-thin films is in the tetragonal β phase having a preferential orientation of (002). The stability of the β-phase of Ta in this thickness range is also determined from the electrical resistivity of Ta, by measuring the sheet resistance (R_s) of all the samples. The R_s of the film stack as a function of Ta thickness is plotted in Fig. 8.1(b). We fitted the variation considering 'parallel resistor model' [41] using eqn. (8.1) as charge current distributes in the bilayer stacks according to their individual resistivity.

$$Rs = \left(\frac{\rho_{Ta} \times \rho_{CoFeB}}{t \times d}\right) / \left(\frac{\rho_{Ta}}{t} + \frac{\rho_{CoFeB}}{d}\right) \qquad (8.1)$$

From the slope of the curve, we estimate the average resistivity of Ta (ρ_{Ta}) to be about 248 ± 20 μΩ cm, while for CoFeB (ρ_{CoFeB}) this is found to be 139 ± 20 μΩ cm which matches with reported literature values[13]. Such high resistivity is also reported in the literature for the β phase of Ta [12]. In Fig. 8.1(c), the AFM images for the Sub/Ta (t = 4, 10, 20 nm)/$Co_{20}Fe_{60}B_{20}$(3 nm)/SiO_2(2 nm) heterostructures are presented. From the AFM

analysis, we have obtained the average topographical roughness for the samples ranges from 0.13 nm to 0.25 nm. The roughness values vary by about ~ 10% when measured at various regions of space of the same sample. Overall, the topographical roughness in all film stacks is found to be significantly small irrespective of the Ta thickness. Due to the small thicknesses of the thin film heterostructures, the interfacial roughness will clearly show its signature on the topographical roughness.

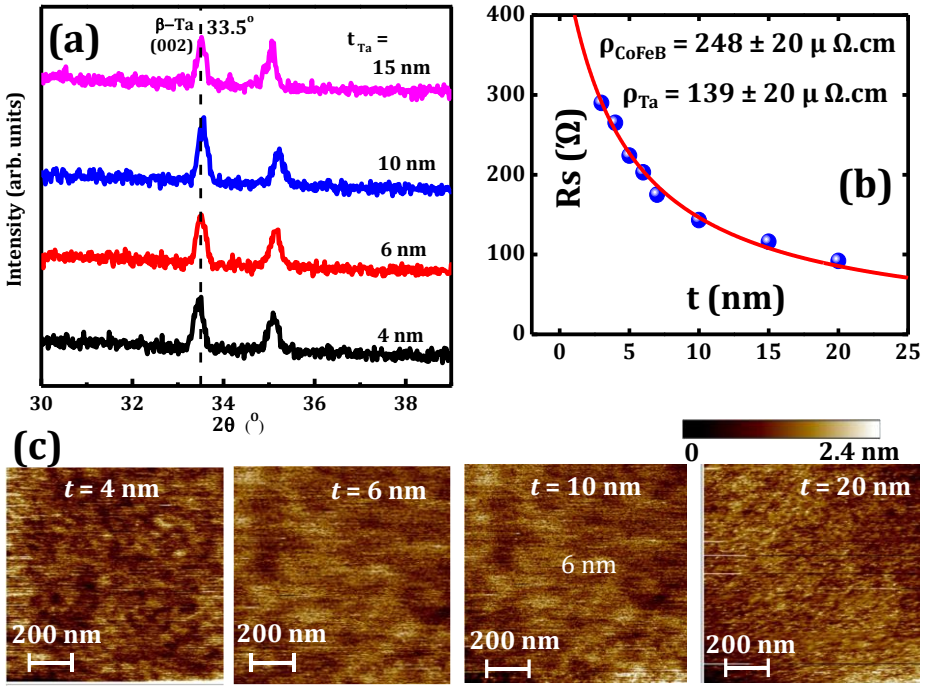

Figure 8. 1. (a) X-ray diffraction patterns measured at grazing angle of incidence from Ta films of thicknesses of 4, 6, 10 and 15 nm are shown. Peaks correspond to β phase of Ta are marked in the plots. (b) Variation of inverse of sheet resistance of Ta(t)/$Co_{20}Fe_{60}B_{20}$(3 nm)/SiO_2(2 nm) as a function of Ta thickness (t) is plotted. (c) Atomic force microscope images showing the surface topography of the Ta(t)/$Co_{20}Fe_{60}B_{20}$(3 nm)/SiO_2(2 nm) samples with t = 4, 6, 10 and 20 nm are presented. The scale bar is same for all samples as shown in the images.

The mechanism of magnetization dynamics in presence of pure spin current has been schematically demonstrated in Fig. 8.2(a). The flow of charge current along x-direction through the Ta layer generates pure spin current along z-direction due to SHE and which is transferred to the CoFeB layer. The spin current gives rise to a SOT (DLT) on magnetization dynamics, which can be described by the modified Landau-Lifshitz-Gilbert equation [13,14] as given by eqn. (8.2).

$$\frac{d\hat{m}}{dt} = -\gamma(\hat{m} \times H_{eff}) + \alpha\left(\hat{m} \times \frac{d\hat{m}}{dt}\right) + \frac{\hbar}{2e\mu_0 M_s d} J_s(\hat{m} \times \hat{\sigma} \times \hat{m}) \qquad (8.2)$$

Here, γ is the gyromagnetic ratio, $\hat{m}$ is magnetization vector, H_{eff} is the effective magnetic field, α is the Gilbert damping constant, d is the ferromagnetic layer thickness, J_s is the

spin current density and $\hat{\sigma}$ is the spin polarization vector. The direction of DLT determined by the third term in eqn. (8.2) acts collinearly with Gilbert damping torque. Hence, it can increase or decrease the effective damping of the system depending on the polarity of the spin polarization vector. The MOD in presence of SOT is related to spin current density, given by eqn. (8.3).

$$\Delta\alpha = \left(\alpha_{eff} - \alpha_0\right) = \frac{\hbar\gamma J_s}{2eM_s d 2\pi f} Sin\theta \qquad (8.3)$$

Here, α_0 and α_{eff} are damping parameters in the absence and presence of charge current, θ is the angle between the magnetic field and charge current direction. The modulation is maximum for θ = 90° as given by eqn. (8.3). Therefore, we kept the directions of applied charge current and H perpendicular to each other throughout the measurements.

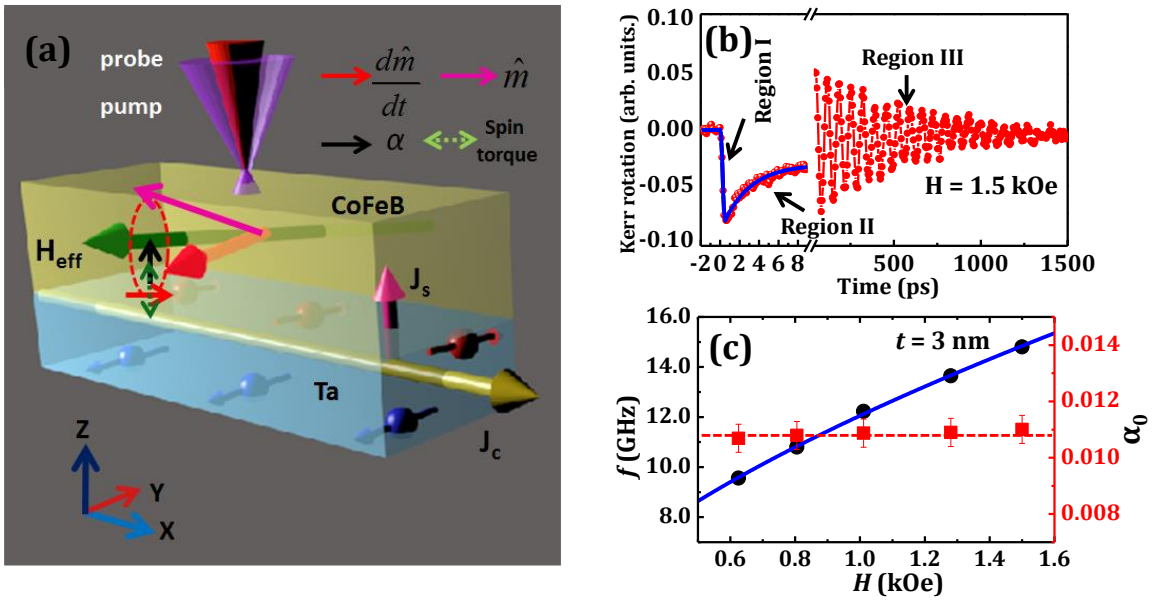

Figure 8. 2. (a) Schematic of the measurement geometry is shown. The applied current (J_c) and magnetic field (H_{eff}) directions are marked (green arrow). (b) A typical time-resolved Kerr rotation data for Ta (3 nm)/$Co_{20}Fe_{60}B_{20}$(3 nm)/SiO_2(2 nm) at H = 1.5 kOe is shown. (c) The bias magnetic field variation of precession frequency (solid black circles) is fitted with Kittel formula (blue solid line). The variation of damping parameter (α_0, solid red squares) with H is shown. The dotted line is a guide to the eye, which shows an invariance of α_0 with H.

The DLT efficiency can be found out from the MOD as given by eqn. (8.4).

$$\xi_{DL} = \frac{2eM_s d 2\pi f \Delta\alpha T}{\hbar\gamma J_c \sin\theta} \qquad (8.4)$$

Here, J_c is the charge current density through the Ta layer, T is the spin transparency at the interface between HM/FM which takes into account all possible effects (i.e., spin pumping, d-d hybridization, spin memory loss etc.). The other parameters have usual meaning as defined earlier. Figure 8.2(b) shows typical time-resolved Kerr rotation data

measured from Ta (3 nm)/$Co_{20}Fe_{60}B_{20}$(3 nm)/SiO_2(2 nm) sample at H = 1.5 kOe without any applied charge current. The ultrafast magnetization dynamics can be divided into three different temporal regions as marked in Fig. 8.2(b). The ultrafast demagnetization occurs within ~ 200 fs (region I) following the pump beam excitation. After this energy rebalancing occurs between electron and spin systems giving rise to a fast relaxation within ~0.6 ps (region II). This is followed by a slow relaxation within ~ 2 ps (region III) along with damped precessional oscillation. Region III is the regime of our interest from where the damped oscillatory Kerr trace is extracted after subtraction of the bi-exponential background. The time-resolved precessional oscillation is fitted with a damped sinusoidal function given by eqn. (8.5).

$$\theta_k(t) = Ae^{-\left(\frac{t}{\tau}\right)}\sin(2\pi ft + \varphi) \tag{8.5}$$

Here, A, τ, f and φ are precession amplitude, relaxation time, frequency and initial phase of oscillation. The precession frequencies at different bias magnetic fields can be plotted and fitted using the following form of the Kittel formula for thin films as given by eqn. (8.6).

$$f = \frac{\gamma}{2\pi}\left(H\left(H + 4\pi M_{eff}\right)\right)^{\frac{1}{2}} \tag{8.6}$$

where $\gamma = g\mu_B/\hbar$, g is the Landé-g-factor, H is the applied bias magnetic field and M_{eff} is the effective magnetization. M_{eff} and g are determined as fitting parameters. In Fig. 8.2(c) The bias magnetic field dependences of precession frequencies for Ta (t = 3 nm)/$Co_{20}Fe_{60}B_{20}$(3 nm)/SiO_2(2 nm) samples are presented. We have obtained M_{eff} ~ 1200 ± 30 emu/cc and g = 2.0 ± 0.05 for these film stacks. The damping of this heterostructure may consist of both intrinsic and extrinsic contributions, and hence, we term it as effective damping parameter (α_{eff}). This can be extracted using the eqn. (8.7).

$$\alpha_{eff} = \frac{1}{\gamma\tau\left(H + \frac{4\pi M_{eff}}{2}\right)} \tag{8.7}$$

This formula can be used to extract effective damping parameter precisely in the moderate bias field regime. For the Ta (t = 3nm)/$Co_{20}Fe_{60}B_{20}$(3 nm)/SiO_2(2 nm), we have observed that α_{eff} remains constant with the variation of H from 0.6 kOe to 1.5 kOe as shown in Fig. 8.2(c). Similar effect is also observed for other samples. This confirms the intrinsic nature of damping for these heterostructures within our experimental magnetic field regime. Due to the insertion of Ta layer, the effective damping of the CoFeB layer has increased slightly in the experimental thickness regime (3 nm ≤ t ≤ 20 nm) for H = 1.5

kOe due to spin pumping. As the spin diffusion length (λ) of Ta, is about 2 nm [12], for $t \geq$ 3 nm the spins accumulated at the Ta/CoFeB interface get fully absorbed in the Ta layer and the backflow is avoided. Thus the enhancement of damping due to spin pumping remains constant for $t \geq 3$ nm. The interface is found not to be fully transparent to the spin current. A detailed analysis of interface transparency is presented elsewhere [12]. Subsequently, the charge current induced MOD has been measured in these heterostructures. Figure 8.3(a) shows the time-resolved Kerr rotation data for Ta (t = 4, 7, 20 nm)/$Co_{20}Fe_{60}B_{20}$(3 nm)/SiO_2(2 nm) samples for two different signs of applied current density, $J_c = \pm 0.5\times10^{10}$ A/m^2.

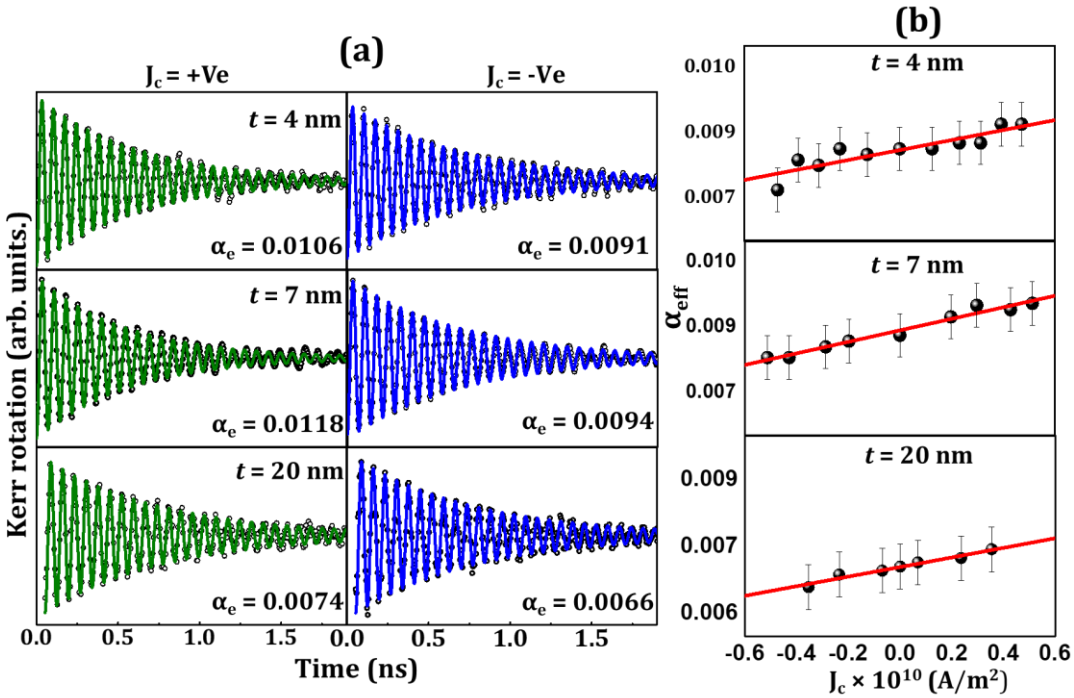

Figure 8. 3. (a) Representative time-resolved precessional oscillations for extraction of damping under the influence of maximum positive and negative charge current densities (J_c) are shown at left and right panels. Here, Ta thickness is mentioned in the left panel. The estimated effective (α_{eff}) damping parameters are also presented inside each panel. Comparison of left and right panel reveals that α_{eff} changes with the polarity of charge current. (b) The MOD plot for Ta thicknesses of 4, 7 and 20 nm are shown. Solid line is a linear fit to the MOD with J_c. Error bars correspond to the fitting error obtained during the estimation of damping.

The effective damping calculated using eqn. (8.7), shows asymmetric linear modulation with the current densities as shown in Fig. 8.3(b). It increases or decreases in two opposite directions of the charge current flow. The relative change in damping values is found to be up to ±10% within the applied current limit ($J_c \leq 0.5\times10^{10}$ A/m^2). Further increase of current density can cause significant Joule heating, enhancement in the

magnetic fluctuation and finally burning of the thin films. For obtaining the MOD, we have fitted the data points with eqn. (8.8).

$$\Delta\alpha = (MOD).J_c \qquad (8.8)$$

From the slope of the fit, we have obtained MOD to be in the order of 1×10^{-13} m^2/A for all the samples. The exact values of MOD are tabulated in Table (8.1) for all samples. The interfacial transparency (T) obtained for these heterostructures is 0.5, which represents a moderately transparent interface [3] in comparison to several other HM/FM interfaces. By using eqn. (8.4), relatively large value to DLT efficiency $\xi_{DL} \sim 0.38\pm0.05$ is found for these samples.

Table 8.1. Values of MOD for different Ta thicknesses.

Ta thickness (nm)	MOD (m^2/A)
3	1.47×10^{-13}
4	1.15×10^{-13}
5	1.15×10^{-13}
6	1.38×10^{-13}
7	1.32×10^{-13}
10	1.20×10^{-13}
15	1.42×10^{-13}
20	1.09×10^{-13}

8.3.1 Modulation of Precessional Frequency in Presence of Charge Current

Significant modulation of precession frequency (MOF) is also observed in some of these samples with the charge current. The possible contributions to MOF come from the Oersted field, Joule heating, and the FLT. The measured MOFs for the samples with t = 6 and 10 nm are shown in Fig. 8.4(a) and 8.4(c), which are fitted with a parabolic function. In the fitting formula, the current through the CoFeB layer is considered by introducing a suitable weight factor with J_c. The symmetric and parabolic variation of frequency with J_c, as shown by the solid line in Fig. 8.4(a) and 8.4(c), suggests that the MOF mainly occurs from the Joule heating effect. We have not observed any significant contribution from the FLT [30,34,42] and Oersted field in the MOF. The MOF can be explained by considering

the change in effective magnetization (M_{eJ}) due to magnetic fluctuations [14,43] because of Joule heating. The change in M_{eJ} can be estimated from eqn. (8.6).

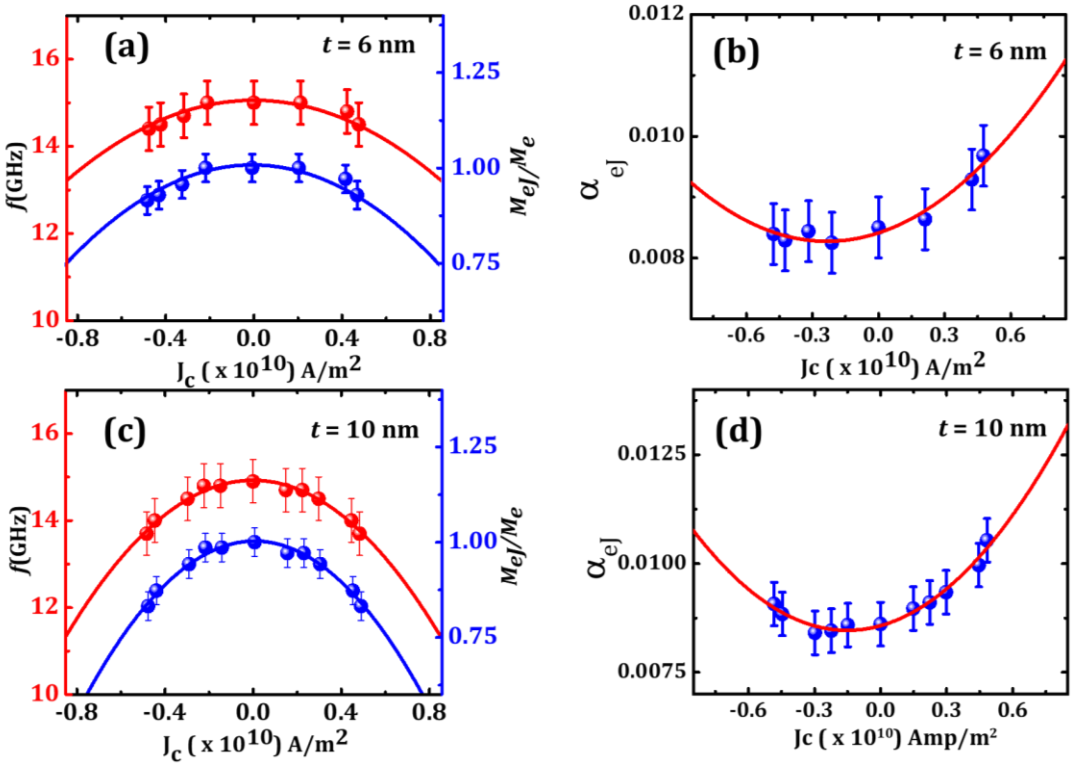

Figure 8. 4. The modulation of frequency (MOF) for t = 6 nm (a) and 10 nm (c) are shown. The solid red line represents the parabolic fit of MOF with J_c. The corresponding change in normalized effective magnetization (M_{eJ}/M_e) is plotted (blue solid circles). The blue solid line represents parabolic fitting. The modulation of damping (MOD) considering Joule heating effect (α_{eJ}) is plotted for t = 6 nm (b) and 10 nm (d). The solid red line represents the fit with a function: a + bJ_c + cJ_c^2. The parameter b gives the MOD due to damping-like torque (DLT).

The variation of M_{eJ} with J_c is shown in Fig. 8.4(a) and 8.4(c) and its fit with a parabolic function of J_c as mentioned earlier. This confirmed the presence of the Joule heating effect in M_{eJ}. From eqn. (8.7), it is evident that the change in effective magnetization will affect the effective damping parameter. We have recalculated the Joule heating induced effective damping (α_{eJ}) considering M_{eJ} and plotted it in Fig. 8.4(b) and 8.4(d) for Ta thickness 6 and 10 nm, respectively. The asymmetric parabolic nature of α_{eJ} with J_c confirms the presence of both Joule heating and DLT. The modified MOD is fitted with a function: + bJ_c + cJ_c^2. Here, b represents MOD due to DLT. The values of b for all samples are found to be around 1.2 ×10^{-13} m^2/A as tabulated in Table (8.2). By using eqn. (8.4), the average value to DLT efficiency is found to be around ξ'_{DL} ~ 0.41±0.03 for all samples.

Table 8.2. The MOD for different Ta thicknesses considering Joule heating effect.

Ta thickness (nm)	MOD considering Joule heating (m^2/A)
3	1.27×10^{-13}
4	1.42×10^{-13}
5	1.30×10^{-13}
6	1.25×10^{-13}
7	1.46×10^{-13}
10	1.42×10^{-13}
15	1.48×10^{-13}
20	1.36×10^{-13}

Figure 8.5 shows the variation of ξ_{DL} and ξ'_{DL} over a broad range of Ta thickness studied here, which shows an invariant behaviour within the error bars. The Joule heating correction gives a higher value of DLT efficiency with better accuracy. However, the DLT efficiency is found to be robust at around 0.4 from both the calculation methods. This robustness of DLT efficiency will be helpful for the development of future spin-orbitronic and magnonic devices where SOT will be applicable.

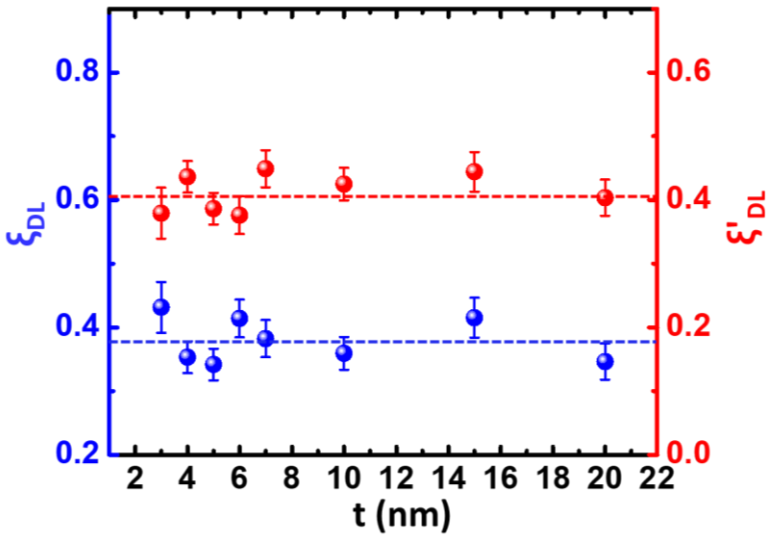

Figure 8. 5. Variation of DLT efficieny without (ξ_{DL}: solid blue circles) and with (ξ'_{DL}; solid red circles) Joule heating effect as a function of Ta thickness. The DLT efficiency remains invariant with Ta thickness. The dotted lines are a guide to the eye.

8.4 Conclusion

In summary, we have investigated the modulation of damping (MOD) in Ta(t)/$Co_{20}Fe_{60}B_{20}$(3 nm)/SiO_2(2 nm) heterostructures in presence of charge current using an all-optical time-resolved magneto-optical Kerr effect technique. The all-optical detection scheme adopted here is a noninvasive and unambiguous method for the reliable determination of spin-orbit effects in HM/FM systems. The XRD and dc resistivity measurements have revealed that the β phase of Ta is stable over a broad range of thickness (t = 3 to 20 nm). We have found the effective damping parameter to remain invariant with the bias magnetic field, confirming the intrinsic nature of damping for these heterostructures within the experimental field regime. We have observed a discernible amount of Joule heating effect from a parabolic variation of MOF in the higher charge current range. The field-like torque (FLT) and Oersted field contributions are found to be negligible in this study as confirmed from the MOF. Subsequently, we have calculated MOD in both scenarios, i.e., without/with Joule heating effect. For both cases, DLT efficiency has been found to be around 0.4 over the whole Ta thickness range. This assures that the Joule heating effect does not mask or smear the MOD as much as it does in MOF. However, the Joule heating correction gives a slightly higher value of DLT of around 0.41±0.03 (in comparison to 0.38±0.05 without Joule heating correction). The large value of DLT and its robustness over a wide range of Ta thickness will be useful for the development of future spin-orbitronic and magnonic devices.

References

[1] M. Krawczyk and D. Grundler, Review and Prospects of Magnonic Crystals and Devices with Reprogrammable Band Structure; J. Phys.: Condens. Matter **26,** 123202 (2014).
[2] A. V. Chumak, V. I. Vasyuchka, A. A. Serga, and B. Hillebrands, Magnon Spintronics; Nat. Phys.**11,** 453 (2015).
[3] A. Barman, G. Gubbiotti, S. Ladak, A. O. Adeyeye, M. Krawczyk, J. Gräfe, C. Adelmann, S. Cotofana, A. Naeemi, V. I. Vasyuchka, B. Hillebrands, S. A. Nikitov, H. Yu, D. Grundler, A. V. Sadovnikov, A. A. Grachev, S. E. Sheshukova, J. Y. Duquesne, M. Marangolo, G. Csaba, W. Porod, V. E. Demidov, S. Urazhdin, S. O. Demokritov, E. Albisetti, D. Petti, R. Bertacco, H. Schultheiss, V. V. Kruglyak, V. D. Poimanov, S. Sahoo, J. Sinha, H. Yang, M. Münzenberg, T. Moriyama, S. Mizukami, P. Landeros, R. A. Gallardo, G. Carlotti, J. V. Kim, R. L. Stamps, R. E. Camley, B. Rana, Y. Otani, W. Yu, T. Yu, G. E. W. Bauer, C. Back, G. S. Uhrig, O. V. Dobrovolskiy, B. Budinska, H. Qin, S. van Dijken, A. V. Chumak, A. Khitun, D. E. Nikonov, I. A. Young, B. W. Zingsem, and M. Winklhofer, The 2021 Magnonics Roadmap; J. Phys.: Condens. Matter **33,** 413001 (2021).
[4] A. Hoffmann and S. D. Bader, Opportunities at the Frontiers of Spintronics; Phys. Rev. Appl. **4,** 047001 (2015).
[5] D. Houssameddine, U. Ebels, B. Delaët, B. Rodmacq, I. Firastrau, F. Ponthenier, M. Brunet, C. Thirion, J. P. Michel, L. Prejbeanu-Buda, M. C. Cyrille, O. Redon, and B. Dieny, Spin-Torque Oscillator Using a Perpendicular Polarizer and a Planar Free Layer; Nat. Mater. **6,** 447 (2007).
[6] M. Tang, W. Li, Y. Ren, Z. Zhang, S. Lou, and Q. Y. Jin, Magnetic Damping and Perpendicular Magnetic Anisotropy in Pd-Buffered $[Co/Ni]_5$ and $[Ni/Co]_5$ Multilayers; RSC Adv. **7,** 5315 (2017).
[7] J.-G. Zhu, Y. Zheng, and G. A. Prinz, Ultrahigh Density Vertical Magnetoresistive Random Access Memory (invited); J. Appl. Phys. **87,** 6668 (2000).
[8] H. Yu, G. Duerr, R. Huber, M. Bahr, T. Schwarze, F. Brandl, and D. Grundler, Omnidirectional Spin-Wave Nanograting Coupler; Nat. Commun. **4,** 2702 (2013).
[9] D. Kumar, S. Barman, and A. Barman, Magnetic Vortex Based Transistor Operations; Sci. Rep. **4,** 4108 (2014).
[10] G. Woltersdorf, M. Kiessling, G. Meyer, J. U. Thiele, and C. H. Back, Damping by Slow Relaxing Rare Earth Impurities in $Ni_{80}Fe_{20}$; Phys. Rev. Lett. **102,** 257602 (2009).
[11] A. Ganguly, S. Azzawi, S. Saha, J. A. King, R. M. Rowan-Robinson, A. T. Hindmarch, J. Sinha, D. Atkinson, and A. Barman, Tunable Magnetization Dynamics in Interfacially Modified $Ni_{81}Fe_{19}$/Pt Bilayer Thin Film Microstructures; Sci. Rep. **5,** 17596 (2015).
[12] S. N. Panda, S. Mondal, J. Sinha, S. Choudhury, and A. Barman, All-Optical Detection of Interfacial Spin Transparency from Spin Pumping in β-Ta/CoFeB Thin Films; Sci. Adv. **5,** eaav7200 (2019).
[13] S. Mondal, S. Choudhury, N. Jha, A. Ganguly, J. Sinha, and A. Barman, All-Optical Detection of the Spin Hall Angle in W/CoFeB/SiO_2 Heterostructures with Varying Thickness of the Tungsten Layer; Phys. Rev. B **96,** 054414 (2017).
[14] A. Ganguly, R. M. Rowan-Robinson, A. Haldar, S. Jaiswal, J. Sinha, A. T. Hindmarch, D. A. Atkinson, and A. Barman, Time-Domain Detection of Current Controlled Magnetization Damping in Pt/$Ni_{81}Fe_{19}$ Bilayer and Determination of Pt Spin Hall Angle; Appl. Phys. Lett. **105,** 112409 (2014).
[15] B. Kaviraj and J. Sinha, Relativistic Torques Induced by Currents in Magnetic Materials: Physics and Experiments; RSC Adv. **8,** 25079 (2018).
[16] A. Capua, T. Wang, S.-H. Yang, C. Rettner, T. Phung, and S. S. P. Parkin, Phase-Resolved Detection of the Spin Hall Angle by Optical Ferromagnetic Resonance in Perpendicularly Magnetized Thin Films; Phys. Rev. B **95,** 064401 (2017).
[17] A. Soumyanarayanan, N. Reyren, A. Fert, and C. Panagopoulos, Emergent Phenomena Induced by Spin–Orbit Coupling at Surfaces and Interfaces; Nature **539,** 509 (2016).
[18] T. Wimmer, M. Althammer, L. Liensberger, N. Vlietstra, S. Geprägs, M. Weiler, R. Gross, and H. Huebl, Spin Transport in a Magnetic Insulator with Zero Effective Damping; Phys. Rev. Lett. **123,** 257201 (2019).

[19] Y. Fukuma, L. Wang, H. Idzuchi, S. Takahashi, S. Maekawa, and Y. Otani, Giant Enhancement of Spin Accumulation and Long-Distance Spin Precession in Metallic Lateral Spin Valves; Nat. Mater. **10,** 527 (2011).
[20] V. E. Demidov, S. Urazhdin, R. Liu, B. Divinskiy, A. Telegin, and S. O. Demokritov, Excitation of Coherent Propagating Spin Waves by Pure Spin Currents; Nat. Commun. **7,** 10446 (2016).
[21] H. Jiao and G. E. W. Bauer, Spin Backflow and ac Voltage Generation by Spin Pumping and the Inverse Spin Hall Effect; Phys. Rev. Lett. **110,** 217602 (2013).
[22] M. Jamali, J. S. Lee, J. S. Jeong, F. Mahfouzi, Y. Lv, Z. Zhao, B. K. Nikolić, K. A. Mkhoyan, N. Samarth, and J.-P. Wang, Giant Spin Pumping and Inverse Spin Hall Effect in the Presence of Surface and Bulk Spin−Orbit Coupling of Topological Insulator Bi_2Se_3; Nano Lett. **15,** 7126 (2015).
[23] I. Mihai Miron, G. Gaudin, S. Auffret, B. Rodmacq, A. Schuhl, S. Pizzini, J. Vogel, and P. Gambardella, Current-Driven Spin Torque Induced by the Rashba Effect in a Ferromagnetic Metal Layer; Nat. Mater. **9,** 230 (2010).
[24] J. E. Hirsch, Spin Hall Effect; Phys. Rev. Lett. **83,** 1834 (1999).
[25] J. Sinova, S. O. Valenzuela, J. Wunderlich, C. H. Back, and T. Jungwirth, Spin Hall Effects; Rev. Mod. Phys. **87,** 1213 (2015).
[26] W. Han, Y. Otani, and S. Maekawa, Quantum Materials for Spin and Charge Conversion; npj Quantum Mater. **3,** 27 (2018).
[27] M. I. Dyakonov and V. I. Perel, Current-Induced Spin Orientation of Electrons in Semiconductors; Phys. Lett. A **35,** 459 (1971).
[28] K. Ando, S. Takahashi, K. Harii, K. Sasage, J. Ieda, S. Maekawa, and E. Saitoh, Electric Manipulation of Spin Relaxation Using the Spin Hall Effect; Phys. Rev. Lett. **101,** 036601 (2008).
[29] A. Ganguly, K. Kondou, H. Sukegawa, S. Mitani, S. Kasai, Y. Niimi, Y. Otani, and A. Barman, Thickness Dependence of Spin Torque Ferromagnetic Resonance in $Co_{75}Fe_{25}$/Pt Bilayer Films; Appl. Phys. Lett. **104,** 072405 (2014).
[30] Y. Takeuchi, C. Zhang, A. Okada, H. Sato, S. Fukami, and H. Ohno, Spin-Orbit Torques in High-Resistivity-W/CoFeB/MgO; Appl. Phys. Lett. **112,** 192408 (2018).
[31] P. M. Haney, H.-W. Lee, K.-J. Lee, A. Manchon, and M. D. Stiles, Current Induced Torques and Interfacial Spin-Orbit Coupling: Semiclassical Modeling; Phys. Rev. B **87,** 174411 (2013).
[32] W. Zhang, W. Han, X. Jiang, S.-H. Yang, and S. S. P. Parkin, Role of Transparency of Platinum–Ferromagnet Interfaces in Determining the Intrinsic Magnitude of the Spin Hall Effect; Nat. Phys. **11,** 496 (2015).
[33] E. Sagasta, Y. Omori, M. Isasa, M. Gradhand, L. E. Hueso, Y. Niimi, Y. Otani, and F. Casanova, Tuning the Spin Hall Effect of Pt from the Moderately Dirty to the Superclean Regime; Phys. Rev. B **94,** 060412 (2016).
[34] K. Ishibashi, S. Iihama, Y. Takeuchi, K. Furuya, S. Kanai, S. Fukami, and S. Mizukami, All-Optical Probe of Magnetization Precession Modulated by Spin–Orbit Torque; Appl. Phys. Lett. **117,** 122403 (2020).
[35] S. Saha, P. Flauger, C. Abert, A. Hrabec, Z. Luo, J. Zhou, V. Scagnoli, D. Suess, and L. J. Heyderman, Control of damping in perpendicularly magnetized thin films using spin-orbit torques; Phys. Rev. B **101,** 224401 (2020).
[36] A. Kumar, R. Bansal, S. Chaudhary, and P. K. Muduli, Large Spin Current Generation by the Spin Hall Effect in Mixed Crystalline Phase Ta Thin Films; Phys. Rev. B **98,** 104403 (2018).
[37] A. K. Chaurasiya, S. Choudhury, J. Sinha, and A. Barman, Dependence of Interfacial Dzyaloshinskii-Moriya Interaction on Layer Thicknesses in Ta/CoFeB/TaOx Heterostructures from Brillouin Light Scattering; Phys. Rev. Appl. **9,** 014008 (2018).
[38] R. Yu, B. F. Miao, L. Sun, Q. Liu, J. Du, P. Omelchenko, B. Heinrich, M. Wu, and H. F. Ding, Determination of Spin Hall Angle and Spin Diffusion Length in Beta-Phase-Dominated Tantalum; Phys. Rev. Mater. **2,** 074406 (2018).
[39] D. Tiwari, N. Behera, A. Kumar, P. Dürrenfeld, S. Chaudhary, D. K. Pandya, J. Åkerman, and P. K. Muduli, Antidamping Spin-Orbit Torques in Epitaxial-Py(100)/β-Ta; Appl. Phys. Lett. **111,** 232407 (2017).

[40] E. O. Nasakina, M. A. Sevostyanov, A. B. Mikhaylova, A. S. Baikin, K. V. Sergienko, A. V. Leonov, and A. G. Kolmakov, Formation of Alpha and Beta Tantalum at the Variation of Magnetron Sputtering Conditions; IOP Conference Series: Materials Science and Engineering **110,** 012042 (2016).
[41] Y.-T. Chen, S. Takahashi, H. Nakayama, M. Althammer, S. T. B. Goennenwein, E. Saitoh, and G. E. W. Bauer, Theory of Spin Hall Magnetoresistance; Phys. Rev. B **87,** 144411 (2013).
[42] K. Garello, I. M. Miron, C. O. Avci, F. Freimuth, Y. Mokrousov, S. Blügel, S. Auffret, O. Boulle, G. Gaudin, and P. Gambardella, Symmetry and Magnitude of Spin–Orbit Torques in Ferromagnetic Heterostructures; Nat. Nanotechnol **8,** 587 (2013).
[43] V. E. Demidov, S. Urazhdin, E. R. J. Edwards, M. D. Stiles, R. D. McMichael, and S. O. Demokritov, Control of Magnetic Fluctuations by Spin Current; Phys. Rev. Lett. **107,** 107204 (2011).

Chapter 9

9. Summary and Outlook

9.1 Summary

In this dissertation, we have explored the quasi-static and dynamic magnetization parameters in nanoscale two- and three-dimensional (2D and 3D) confined structures and thin film heterostructures. Here, we have used RF & DC sputtering for the deposition of thin film heterostructures. The electron beam lithography and two-photon lithography (TPL) were used to write the 2D and 3D patterned structures respectively. Thin film deposition techniques (i.e., electron beam evaporation and thermal evaporation) and electrodeposition techniques have been used to deposit the magnetic materials to prepare the patterned nanostructures. The characterizations for the determination of the crystal structure, surface imaging, morphology and the chemical compositions of these heterostructures and patterned structures of magnetic materials have been studied by using X-ray diffraction (XRD), scanning electron microscopy (SEM), atomic force microscopy (AFM) and energy-dispersive X-ray spectroscopy (EDX). The static and quasistatic magnetic parameters have been probed by magnetic force microscopy (MFM) and the static magneto-optical Kerr effect (static-MOKE) technique. Further, the optical techniques i.e., time-resolved magneto-optic Kerr effect (TRMOKE) magnetometer and Brillouin light scattering (BLS) spectroscopy have been employed to measure the magnetization dynamics in the time and frequency domain respectively. These techniques are based on light-mater interaction, which can excite and detect the magnetization dynamics with appreciable spatial and/or having temporal resolution. Micromagnetic simulations have been exploited for the reproduction of experimentally observed phenomena. In this thesis, we have used object oriented micromagnetic framework (OOMMF), MuMax3, and LLG micromagnetic simulator.

We have experimentally and numerically investigated the role of the regular shaped nanochannels on spin-wave dynamics in the connected nanodot (CND) array. Three CND arrays of square shaped nanodots which are physically connected to its neighbouring nanodots by simple rectangular shaped nanochannels through exchange-dipole interaction, each with 25 × 25 μm^2 areas with the varying filling factor (area covered by

Py/area of one unit cell) of 0.64(S1), 0.72(S2) and 0.83(S3) were fabricated by using a combination of electron-beam evaporation, electron-beam lithography and ion milling. The experimentally observed time-resolved magnetization dynamics revealed the presence of multiple spin-wave modes in the CND arrays. The mode numbers were found to be decreasing with increasing filling fraction. This is because of the decrement in the demagnetized region with the gradual growing filling fraction from S1 to S3. It was also confirmed from the numerical calculations of internal field distribution. Further numerical studies explored various spin-wave modes, namely, the edge mode, extended mode, quantized mode and mixed quantized mode in the CNDs. The vertical nanochannels are found to couple the spin-wave modes between the nanodots except for the highest frequency mode which couples the dots through both the nanochannels. Interestingly, the mode profile of the highest frequency mode (M7) shows an intense power in horizontal nanochannels in the case of S1. This might be due to the formation of local minima and/or the higher value of the internal field in the horizontal nanochannel in comparison to vertical nanochannels as found from the internal field calculations. Further simulations of isolated dots and nanochannels revealed that the modes in isolated dots dominate in the connected system with some additional modes, whereas the nanochannels play a sacrificial role only to boost the spin-wave propagation between the neighbouring nanodots. It also revealed that the highest frequency spin-wave mode primarily originates from the horizontal nanochannels. The additional simulation revealed that the quantized mode (M3) and extended mode (M5) propagate only through the vertical nanochannels, whereas the highest frequency mixed-quantized mode (M7) propagates through all the nanochannels. These behaviours can be further exploited to construct circuits analogous to a four-way demultiplexer, which can be useful for future spin-wave based communication devices. This study will be helpful for the use of nanochannels in future magnonic devices.

Later on, we have investigated the effect of microstates on spin-wave dynamics in a new class of emerging 2D magnonic crystals; square artificial spin ice (ASI) system. The rectangular bar shaped nanopatterned of $Ni_{80}Fe_{20}$ (Py) thin film arranged in a square geometry on silicon substrate was fabricated by using e-beam lithography and thermal evaporation. The experimental and numerical quasistatic characterization of remanent magnetic state has unveiled different spin ice microstates, multidomain and vortex spin textures. The field dispersion study of spin-wave modes revealed different novel physical

phenomena such as suppression and reappearance of spin-wave mode, magnon mode anticrossing with high value of anticrossing gap around 1.06 GHz, mode softening, mode merging, field invariant of spin wave mode in different field regime. A gross qualitative agreement between experiment and micromagnetic simulation results have been found. In some field regime, the simulated data deviated from experimental data and did not able to qualitatively reproduced the experimental observations. The presence of magnetoelastic interaction is the primary reason for the deviation of the experimental data from the simulated results. The acoustic mode originates from the mismatching of stress which is generated due to the transient heating of metallic nanostructures by fs pulsed laser, between the interface of the nanostructures and substrate. The frequency of surface acoustic modes is related to the periodicity of the patterned structure. However, the analyses of intrinsic spin-wave mode profile give an idea about the role of magnetic microstates on the spin wave dynamics and mode profiles. In the saturated regime, different modes such as edge mode, uniform mode and quantized mode were observed. In the lower regime, the magnetization configuration deviates from its saturation state due to competition between magnetic energies such as the shape anisotropy and Zeeman energy. It formed different microstates which affected the spin-wave mode profiles. Instead of forming global distribution of power profile like the higher filed (saturated state) regime, at the lower fields the power distributions form some local clusters which are related to the magnetic microstates' distribution. The spin wave mode characteristics were greatly influenced by the magnetic microstates which appeared at lower fields. Different microstates favoured different modes and neighbouring nanobars' microstates can influence the nature of spin-wave modes in a nanobar. During the magnetization reversal, microstates can generate new spin-wave branch as observed in the simulated data. This tunability of spin wave mode profiles by the introducing magnetic microstate will be useful to control the spin wave behaviours for designing of future spin-wave based magnonic devices.

Further, we have directly investigated the ultrafast magnetization dynamics in a 3D cobalt tetrapod structure, by using all optical TRMOKE microscopy. The 3D structure was fabricated by implementing a novel method, combining TPL and electrodeposition. A single tetrapod structure consists of four wires, each with approximate dimension 657 nm × 782 nm × 10 μm. The separation between the tetrapod structures is around 10 μm, which ensured that they are not magnetostatically coupled. The experimental results

which have been measured from the junction of a tetrapod revealed the presence of two clear modes around 1 and 10 GHz along with a less intense mode around 30 GHz. The 3D micromagnetic simulations explored the mode characteristics. The modes showed a small quantitative change with the variation of bias magnetic field, while the qualitative characters of the modes remained unchanged. The simulated mode profile from the whole simulated structure and the tetrapod junction revealed the spatially uniform mode with thin fringes most likely associated with standing spin-wave mode of high quantization number at 30 GHz. The two lower frequency modes showed dipolar dominated mixed modes with nodal planes spreading along the two mutually perpendicular directions. The mode quantization number of the dipolar modes increased with the decrease in frequency. This first-ever investigation of ultrafast magnetization dynamics of a complicated 3D magnetic nanoscale structure opens the possibility of further intensive study in this field for the promotion of such structures as building blocks in high-frequency ultra-high-density storage, memory, logic and communication devices.

Subsequently, we have extended our study in 3D nanostructures by exploring the spin-wave characteristics in a 3D-ASI structure of interconnected nanowires arranged in diamond bond-like lattice geometry. A novel method was used to fabricate a complex 3D-ASI structure by using a combination of TPL and thermal evaporation. Two clear collective spin-wave modes were revealed by measuring thermal magnons using BLS spectroscopy. The mode frequencies showed good stability and nearly monotonic variation over a broad range of bias magnetic fields. The collective nature of the spin-wave modes was confirmed by simulating a constituent element and a unit cell of the 3D-ASI. The 3D micromagnetic simulations qualitatively reproduced the experimentally observed spin-wave spectra. The spin-wave mode profiles have been calculated along different planes of the 3D-ASI structure which showed different spatial characters from localized to extended nature having different mode quantization numbers. Besides, these spin waves can be highly reconfigurable due to the possibility of attaining a variety of complex magnetic microstates by varying external magnetic fields. Thus, optical exploration of spin-wave modes in this interconnected 3D structure will open the pathway for exciting new possibilities of 3D magnonics for ultrahigh density on-chip communication and processing devices.

We have also investigated the variation damping like torque (DLT) efficiency with varying Ta thickness in a β-Ta(t)/$Co_{20}Fe_{60}B_{20}$(3 nm)/SiO_2(2 nm) heterostructures by employing an all-optical TRMOKE technique. The all-optical detection scheme adopted here is a non-invasive and unambiguous method for the reliable determination of spin-orbit effects in heavy-metal/ferromagnet systems. The XRD and dc resistivity measurements have shown that the β phase of Ta is stable over a broad range of thickness (t = 3 nm to 20 nm). We have found the effective damping parameter to remain invariant with bias magnetic field, ensuring the intrinsic nature of damping for these heterostructures within the experimental field regime. The symmetric and parabolic nature of modulation of frequency (MOF) with the charge current ensures that the MOF primarily originates from the Joule heating effect whereas the contributions from field-like torque (FLT) and Oersted field are very negligible. Subsequently, we have calculated modulation of damping (MOD) in both scenarios, i.e., without/with the Joule heating effect. For both cases, DLT efficiency is around 0.4 over the whole Ta thickness range. This confirms that the Joule heating effect does not mask or suppress the MOD as much as it does in MOF. However, the Joule heating correction gives a slightly higher value of DLT of around 0.41±0.03 (in comparison to 0.38±0.05 without Joule heating correction). The large value of DLT and its robustness over a wide range of Ta thickness will be useful for the development of future spin-orbitronic and magnonic devices.

9.2 Outlook

The ferromagnetic thin films and confined nanostructures are the potential candidate for future storage devices with higher storage density (compared to current storage) with faster processing speed and energy-efficient communication devices. The current hard disk drives (HDDs) are mainly based on magnetic storage media where the storage and sensor parts are based on the magnetic structure. In recent years, solid-state drives (SSDs) are becoming popular in storage devices due to their faster processing speed. However, magnetic HDDs are still useful for bulk storage due to their lowered cost. To fulfil the ever-growing demand for higher data storage devices with faster processing speed, different schemes have been proposed for magnetic storage devices such as vertical stacking of magnetic thin films, race track architecture and others. As a result, 3D magnetic nanostructures have emerged as a potential candidate for future storage devices. The 3D magnetic structures can be used in 3D optical data storage devices where

the Kerr effect mechanism is being used to read and write data. The main hurdles behind these are the lack of tools for the fabrication and characterization of 3D magnetic nanostructures. The study of spin-wave dynamics in such systems not only enhances the fundamental understanding but also can resolve the issue of huge energy loss in form of heat due to the Joule heating effect in current complementary metal-oxide-semiconductor (CMOS) based devices. Thus, understanding and control over spin-waves are required for the designing of spin-wave based different future information carrier and processing devices. As a result, the magnonics research field emerged to study the propagation, excitation, control and detection of spin-waves in periodically arranged magnetic patterned structures. With the progress in nanofabrication and the development of sophisticated state of the art, the spin-wave dynamics in the different forms of magnonic crystals in different dimensions, majorly in 1D and 2D have been explored which leads to the designing of different prototypes of magnetic logic and circuit elements. However, optimization, further understanding and new functionalities are required for the designing of spin-wave based communication devices. As mentioned in the previous section, the highest frequency mode in the CND array can propagate through the four nanochannels from one nanodot to four neighbouring nanodots which is like a 1-input-4-output magnetic circuit. This behaviour can be further tuned by introducing new parameters such as rotatable external magnetic field, asymmetric spin-wave propagation in presence of Dzyloshiskii Moriya interaction (DMI) to design a demultiplexer logic device like the electronic circuit. In the case of the ASI array, the presence of magnetoelastic coupling between the spin-wave modes and surface acoustic wave makes it a suitable system for hybrid magnonics where the interplay between magnon with other quasiparticles such as phonon, optical and microwave photon, spin ensemble, fluxons are studied to achieve more than one tunning parameters to control spin-wave dynamics. The numerical study of spin-wave dynamics in the magneto-elastically coupled system can explore the effect of the surface acoustic wave on the microstates and spin-wave modes characteristics of an ASI which will give the inside of the interacting mechanism in such hybrid systems. Also, the spin-wave propagation through the monopoles in an ASI is very fascinating to explore by using imaging techniques such as micro-focused BLS, X-ray tomography, which can add some new functionalities by modifying spin-wave intensity and/or frequency. The exploration of spin dynamics in 3D nanostructures opens the path for further intensive study in this

field for their potential applications in high-frequency ultra-high-density storage, logic and communication devices. The study of spin-wave dispersion along the different symmetric axes is required for fundamental understanding, as well as it can give rise to different novel phenomena such as bandgap opening and variable bandgap at Brillouin zone along the different symmetry axis direction, appearance and disappearance of spin-wave mode, modification of spin-wave characteristics, just to name a few. The study of spin-wave propagation through a connected 3D structure will be interesting where the spin-wave can propagate through different constituent elements and interfere at the junction of the connected structure. Also, the connected 3D structure can form the 3D-ASI structure where the propagation of monopoles in the 3D network through Dirac string will be useful to study to enrich the fundamental understanding. The dynamic control over the magnetic damping parameter is essential to achieve the higher value of magnetic damping for suppressing the 'ringing' effect during the writing process in the magnetic memory devices and obtain a longer propagation length in a confined structure by lowering the effective magnetic damping parameter. The stability of damping like torque efficiency over the wide thickness regime of Ta makes it a suitable candidate for the fabrication of magnetic confined structures on top of it. The study of spin-wave dynamics in such nanopatterned heterostructures will not only enhance the propagation length of spin-wave modes but also can affect the spin-wave properties by modulating its intensity as well as frequency.

These studies will help to build a foundation for future all-magnon circuits, spin-wave based computing, neuromorphic and quantum computing devices with an ultimate goal to design all magnetic computers which will be based on the magnetic elements (thin films, nanoelements: confined structures) i.e., primary storage (magnetic random-access memory (MRAM)), secondary storage (magnetic HDD) and magnetic circuits (logic, transistor, transducer, RF components).

Appendix A: Chapter 4

A.1. Extraction of Magnetic Parameters of the $Ni_{80}Fe_{20}$ Thin Film

To extract the material parameters for micromagnetic simulations, we have measured the bias magnetic field dependence (H) of spin-wave frequency (f) of an unpatterened $Ni_{80}Fe_{20}$ (Py) thin film of 20 nm thickness. The measured variation of f vs. H is fitted using Kittel formula given by equation (A.1) and shown in Fig. A.1.

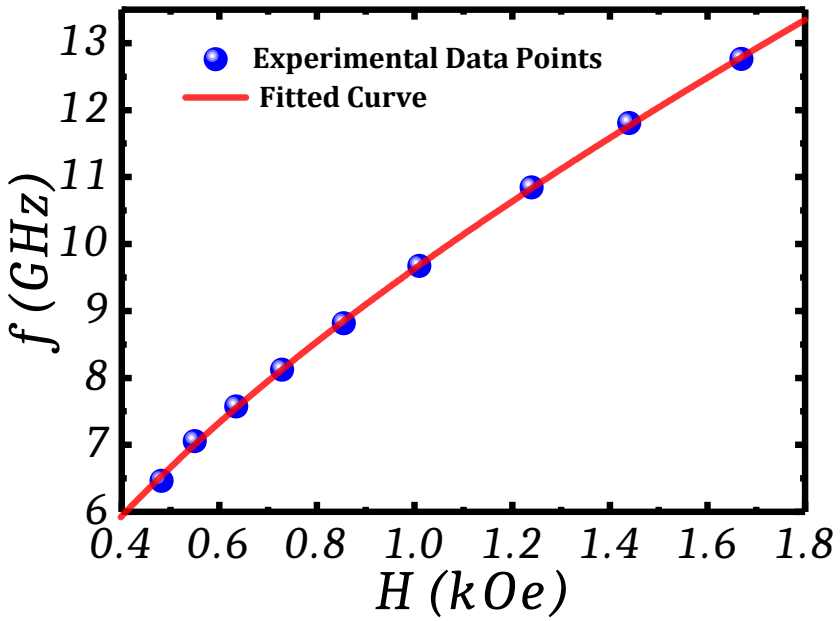

Figure A. 1. Bias field dependence of precession frequency of an unpatterned Py thin film is shown. The symbols represent experimental frequency values, whereas the solid line represents theoretical fit using equation A.1.

$$f = \frac{\gamma}{2\pi}\sqrt{(H + H_k)(H + H_k + 4\pi M_s)} \qquad \text{(A.1)}$$

From the fitted curve we extracted the magnetic parameters as gyromagnetic ratio γ = 17.6 MHz/Oe, saturation magnetization M_s = 860 emu/cc and anisotropy field H_K = 0.

A.2. Spin-Wave in Isolated Nanodots and Nanochannels

We have further simulated the spin-wave dynamics in isolated nanodots (NDs) and nanochannels (NCs) of S2 and S3. The fast Fourier transform (FFT) of the simulated time-resolved data at an applied field of H = 1.67 kOe and the corresponding power profiles of spin-wave modes are shown in Fig. A.2 and Fig. A.3 for sample S2 and S3, respectively. The results of connected dots (CNDs) are reproduced from Fig. 4.3 of Chapter 4 for the

convenience of ready comparison of the results with isolated NDs and NCs. For S2, NDs show three modes, where M1 is an edge mode, M2 is a quantized mode in BV-geometry (n = 5) and M3 is a uniform mode. The NCs also show three spin-wave modes. The M1 and M2 originate from horizontal NCs (HNCs) and M3 originates from the vertical NCs (VNCs).

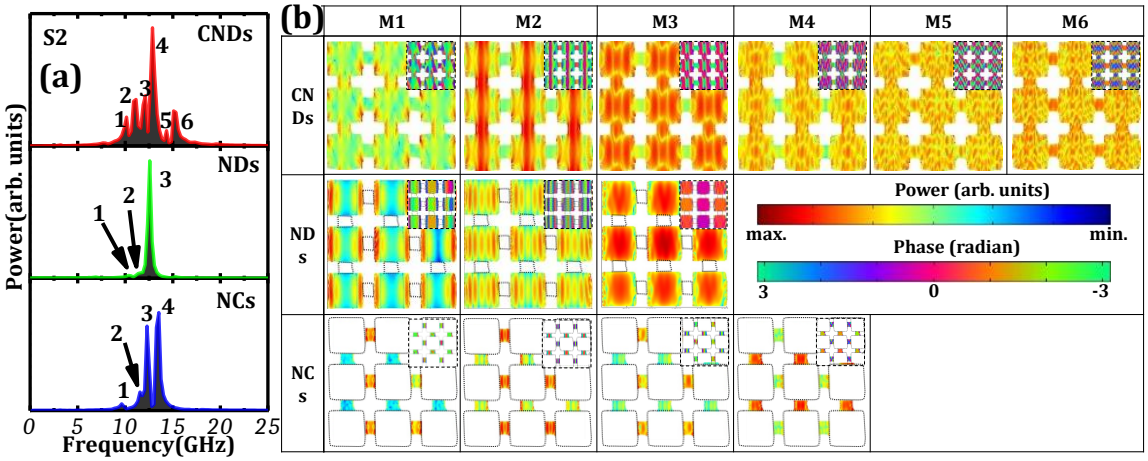

Figure A. 2. (a) Simulated power spectra of connected nanodots (CNDs), isolated nanodots (NDs) and isolated nanochannels (NCs) are shown for sample S2 at an applied bias magnetic field of H = 1.67 kOe. (b) Spatial distributions of spin-wave mode powers are shown, whereas the phase profiles are presented at the insets of corresponding power profiles. In isolated cases, black dashed lines are to guide the positions of the NDs and NCs.

For S3, NDs show two modes. The lower frequency mode is a quantized mode in BV-geometry (n = 5) whereas the higher frequency mode is a uniform mode. Here, the edge mode is supressed because the separation between the NDs is significantly reduced and as a result the dipolar coupling enhances. The NCs show three modes whose behaviours are similar to the previous ones. In CNDs the spin-wave mode characteristics and numbers are remarkably modified from the isolated NDs. The edge mode of NDs and NCs appear as edge mode to CNDs also in the case of S1. The uniform mode of NDs transforms into a quantized mode in CNDs.

The mode profiles of NCs show distinct behaviour for S1, whereas it shows similar behaviour for S2 and S3. The highest frequency mode originates from HNC for S1 and from VNC for S2 and S3. This is due to the modification of shape anisotropy of NCs from S1 to S2. The aspect ratio (w/l) of HNC for the three sample varies as 0.78 (S1), 1.19 (S2) and 2.38 (S3). With this change in aspect ratio of HNC, the direction of easy axis also changes from HNC (for S1) to VNC (for S2 and S3). Therefore, the highest frequency mode prefers HNC for S1 and VNC for

S2 and S3. For S1, the easy direction of HNCs resonates with the easy directions of NDs, and as a result, the highest frequency mode of CNDs shows an intense power within HNC.

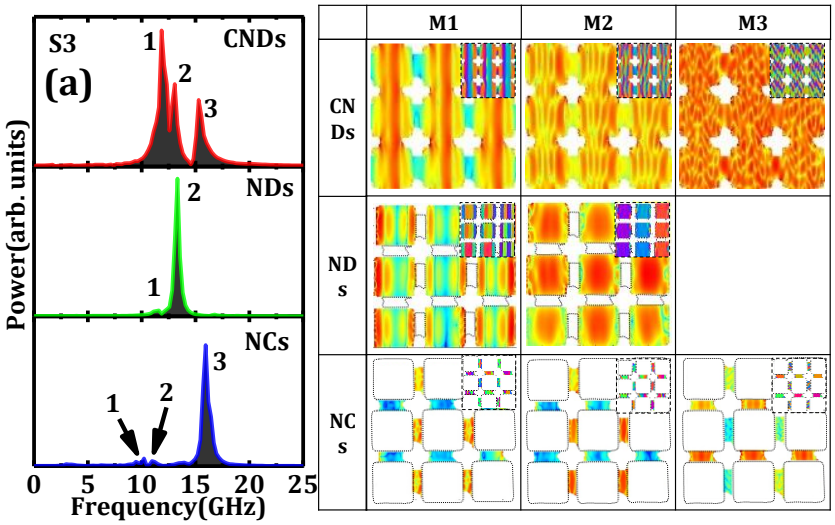

Figure A. 3. (a) Simulated power spectra of connected nanodots (CNDs), isolated nanodots (NDs) and isolated nanochannels (NCs) are shown for sample S3 at an applied bias magnetic field of H = 1.67 kOe. (b) Spatial distributions of spin-wave mode powers are shown, whereas the phase profiles are presented at the insets of corresponding power profiles. In isolated cases, black dashed lines are to guide the positions of the NDs and NCs.

Appendix B: Chapter 7

B.1. Bias Field Dependent of Spin-Wave Frequency

Despite the complex structure of the 3D-ASI studied in this work, we attempted to fit the bias field dependent frequency of the dominant spin-wave mode of the studied structure with Kittel formula. Considering the applied bias magnetic field along x direction and zero magneto-crystalline anisotropy in our sample we write the Kittel formula as:

$$f = \frac{\gamma}{2\pi}[(H + H_{d1})(H + H_{d2})]^{\frac{1}{2}} \quad \text{(B.1)}$$

Here, γ is gyromagnetic ratio, H is external applied magnetic field, $H_{d1} = (N_z - N_x)M_s$ and $H_{d2} = (N_y - N_x)M_s$ are the effective demagnetizing fields originating from the shape of the studied structure, and M_s is saturation magnetization. Here, N_x, N_y and N_z are the demagnetizing factors along x, y and z direction, respectively. The fitted curve is shown in Fig. B.1.

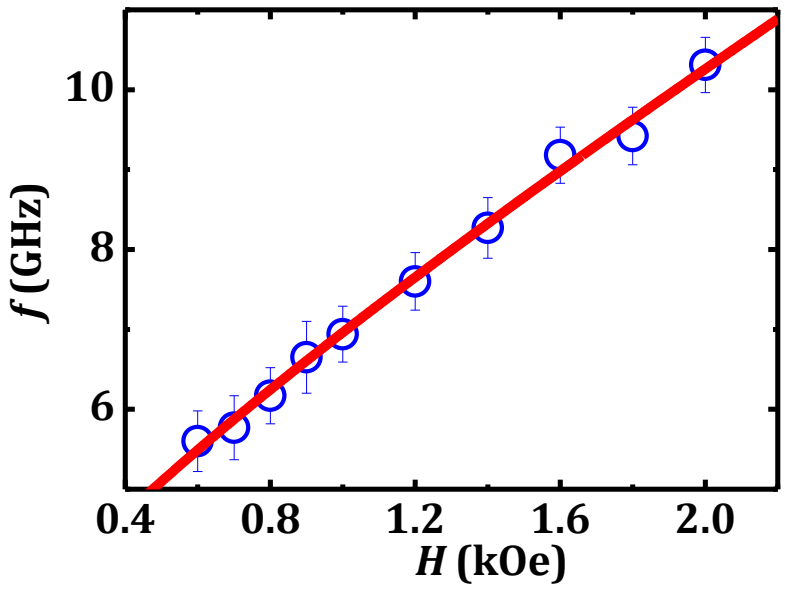

Figure B. 1. Experimental data of bias field dependent spin-wave frequency (open symbols) fitted with Kittel formula of equation B.1 (solid line).

The experimental data was replotted from Fig. 7.3(a) of Chapter 7. From the fit we find the values of demagnetizing factor as N_x = 2.54, N_z = 2.82 and N_y = 7.2 considering the values of γ = 17.6 MHz/Oe and M_s = 860 emu/cc. The extracted values of demagnetizing factors suggest that our sample has a relatively high demagnetization contribution along out-of-plane direction (along y, shown in Fig. B.3).

B.2. Static Magnetization Configuration of the Sample

The simulated magnetization configuration (m_x component) of 3D-ASI sample at different bias field is shown in Fig. B.2. The magnetization profiles show saturated state in applied field regime from 0.6 kOe to 2 kOe. All the measurements were done in the saturated state of the sample.

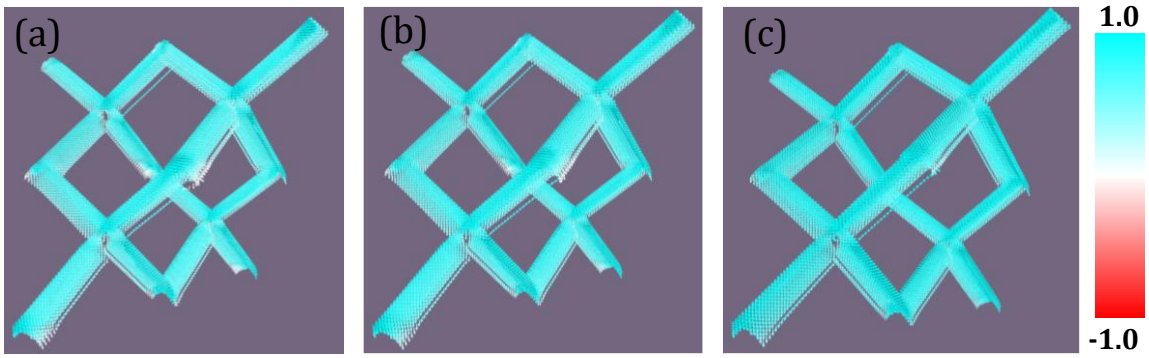

Figure B. 2. Static magnetization configurations (m_x component) of the sample at bias magnetic field (H) of (a) 0.6 kOe, (b) 1.0 kOe and (c) 2.0 kOe are shown.

The equilibrium state (static) magnetization configuration of two orthogonal components (m_y and m_z) at H = 1.6 kOe applied along x direction (m_x is shown in Fig. 7.4(c) of Chapter 7) is presented in Fig. B.3. Two orthogonal components show prominent demagnetized regions in the magnetization configuration.

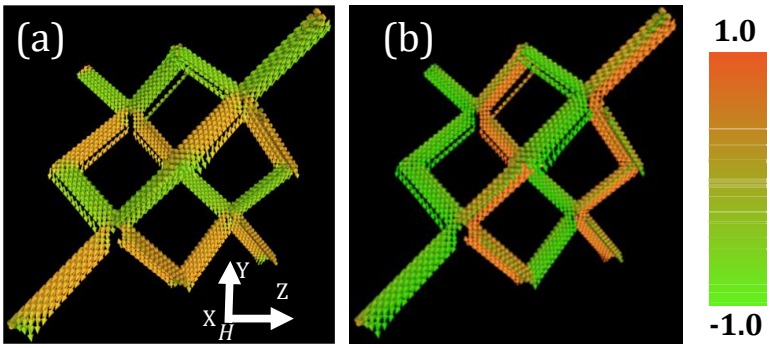

Figure B. 3. Static magnetization configuration of (a) m_z component and (b) m_y component of the 3D-ASI sample at H = 1.6 kOe applied in the plane of the sample (along x direction).

A distinct difference in the spin structures in the out-of-plane component (m_y component), including the demagnetization regions between intra- and inter-nanowires branches is observed. The out-of-plane configuration (m_y) shows more dominant demagnetized state compared to the in-plane configuration (m_z) which also validates the extracted results of higher demagnetizing factor (N_y) along the out-of-plane direction as presented in B.1.

B.3. Collective Nature of Spin-Wave Modes

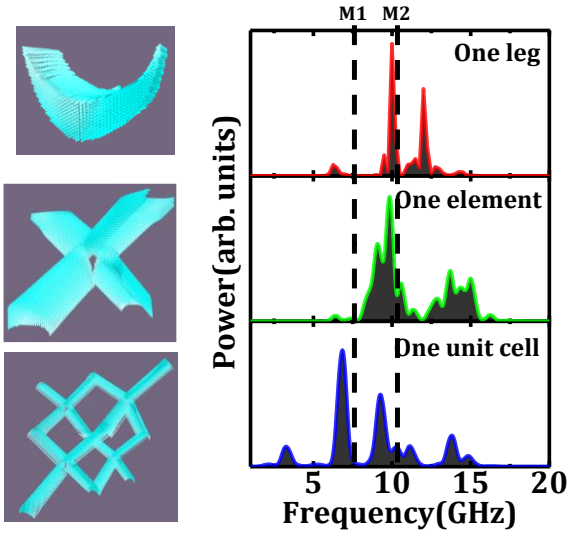

Figure B. 4. Simulated spin-wave spectra for one leg, one element and one unit cell of 3D-ASI at H = 1.6 kOe are shown. The positions of M1 and M2 are marked by black dashed lines.

In order to check the collective nature of the spin-wave modes, we have simulated the spin-wave spectra at H = 1.6 kOe for a single nanowire leg, one tetrapod element and a unit cell of 3D-ASI structure as shown in Fig. B.4. The simulated spin-wave spectra of all three-test structures show distinct behaviours in spin-wave frequency peaks and a gradual evolution from a single nanowire to 3D-ASI structure. These test simulations reassure the collective spin-wave dynamics of the 3D-ASI structure observed in our experiment and simulation.

B.4. Calculated Spin-Wave Mode Profiles of Additional Modes Observed Only in the Simulation

In the simulated spin-wave spectra, we have observed some additional modes, which were either not resolved or detected due to limitations in resolution and/or detection sensitivity. However, these modes are fundamentally important, as they are characteristic modes of this structure. Hence, we have simulated the profiles of these modes too for completeness of study. These modes are numbered from lower to higher frequencies (Fig. B.5). Figure B.5 is repeated from Fig. 7.3 (b) of the Chapter 7 for ready correlation with the simulated mode profiles. The spin-wave mode profiles are presented in Fig. B.6. Here, M1* shows quantized nature with quantization number n = 11 (Fig. B.6(a)) and 11 (Fig. B.6(b)). The cross-sectional view shows that it also forms quantized

mode along the nanowire cross section (Fig. B.6(a)) and at the junction (Fig. B.6(c)) with n' = 4 and 3, respectively. Furthermore, M2* and M3* also show quantized behaviour with power distributed over the entire 3D-ASI structure (Fig. B.6(a) and B.6(b)).

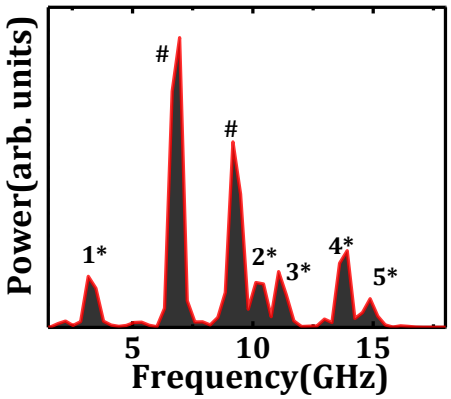

Figure B. 5. Simulated spin-wave spectra of the 3D-ASI sample at H = 1.6 kOe. The experimentally observed modes are marked by '#' while the additional modes observed explicitly in simulation are numbered as 'digit*' from lower to higher frequencies.

The quantization number is found to be n = 5 and 7 for M2* and n = 7 and 6 for M3*, as shown in Fig. B.6(a) and B.6(b), respectively. The cross-sectional view shows the quantized nature of the modes with n' = 2, 2 and 4, 2 for M2* and M3*, respectively, at the cross section (Fig. B.6(a)) and the junction (Fig. B.6(c)). The two higher frequency modes also show the quantized nature along the lateral directions of the connected nanowires (Fig. B.6(d) and B.6(e)) with n = 12 and 12 for M4* and n = 11 and 15 for M5*. The cross-sectional view of the nanowire (Fig. B.6(d)) shows quantized nature of M4* with quantization number n' = 6, while M5* shows a uniform mode. The cross- sectional view at the junction (Fig. B.6(f)) shows the quantized nature with n' = 3 and 3 for M4* and M5*, respectively. The analyses of spin-wave mode profiles reveal primarily quantized nature of these observed additional modes in simulated spectra with significant amount of power distributed over the entire 3D-ASI structures. The phase profiles reveal the 3D nature of these modes with different quantization number and nature along the different lateral directions and cross sections of the connected nanowires of the 3D-ASI structure.

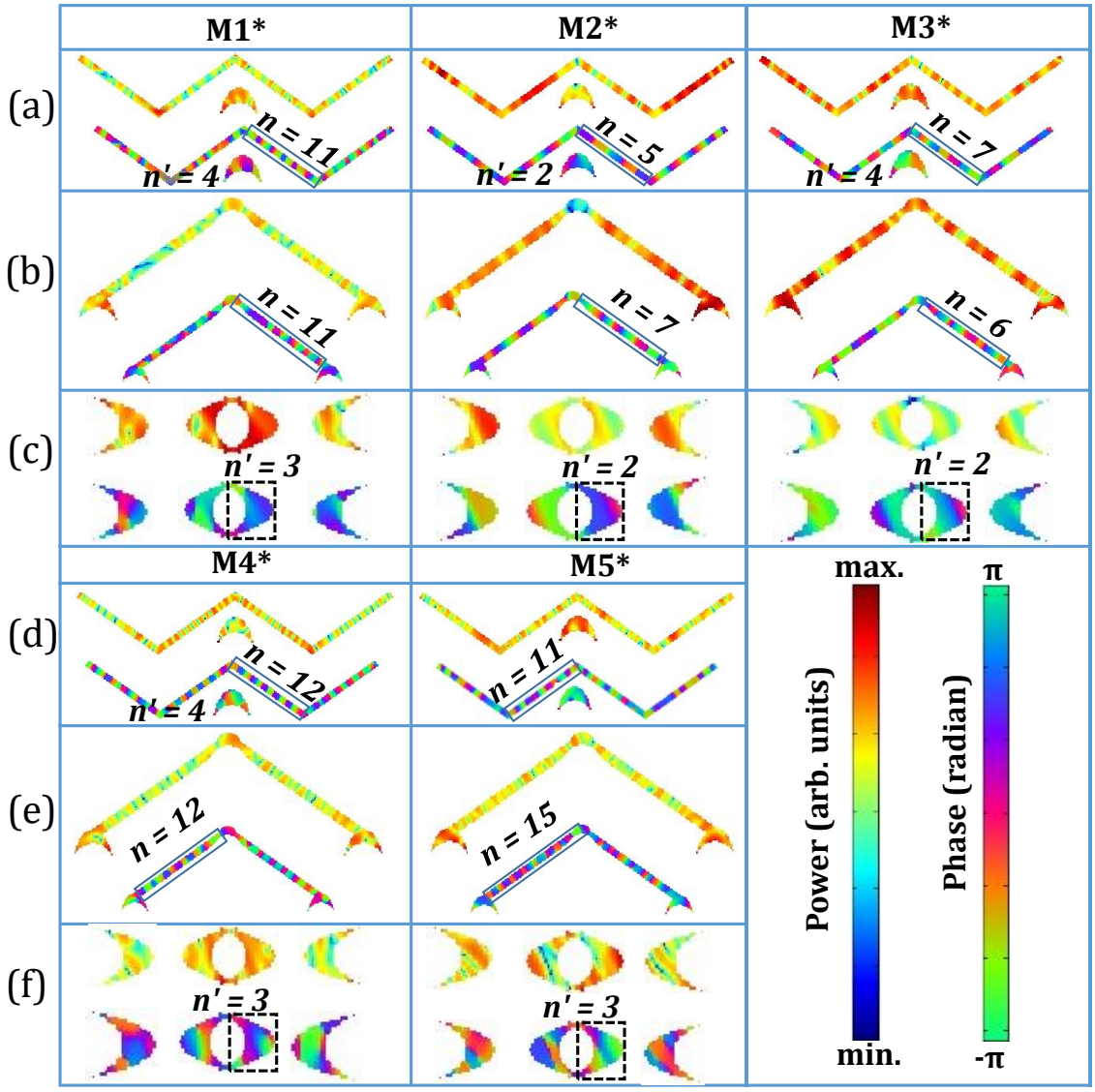

Figure B. 6. Spin-wave mode profiles calculated at different points of 3D-ASI structure at H = 1.6 kOe by taking slice along (a), (d) x′-y′ plane at point 1, (b), (e) y′-z′ plane at point 2 and (c), (f) x′-z′ plane at point 1. The mode profiles of M1, M2 and M3 are shown in (a), (b) and (c), while (d), (e) and (f) show the mode profiles of M4* and M5*. The x′-y-′z′ coordinate and positions (1 and 2) are presented in Fig. 7.5(a) of Chapter 7. The power profiles are shown in upper part and corresponding phase profiles in lower part of each panel. The color bars are presented at bottom right corner.